Seismic array analysis of ocean induced microseisms

by

Martin Gal

School of Physical Sciences, Earth Sciences

Submitted in fulfilment of the requirements for the degree of Doctor of Philosophy

University of Tasmania December, 2016

Declaration of originality

This thesis contains no material which has been accepted for a degree or diploma by the University or any other institution, except by way of background information and duly acknowledged in the thesis, and to the best of my knowledge and belief no material previously published or written by another person except where due acknowledgement is made in the text of the thesis, nor does the thesis contain any material that infringes copyright.

Authority of access

This thesis may be made available for loan and limited copying and communication in accordance with the Copyright Act 1968.

Statement regarding published work contained in thesis

The publishers of the papers comprising Chapter 2, 3 and 4 hold copyright for that content, and access to the material should be sought from the respective journals.

Martin Gal
October 2016

Statement of Co-Authorship

The following people and institutions contributed to the publication of the work undertaken as part of this thesis:

Martin Gal, School of Physical Science – Earth Sciences	= **Candidate**
Anya Reading, University of Tasmania	= **Author 1**
Simon Ellingsen, University of Tasmania	= **Author 2**
Keith Koper, University of Utah	= **Author 3**
Relu Burlacu, University of Utah	= **Author 4**
Lucia Gualtieri, Lamont-Doherty Earth Observatory	= **Author 5**
Hrvoje Tkalčić, Australian National University	= **Author 6**
Steven Gibbons, NORSAR	= **Author 7**
Sven Peter Näsholm, NORSAR	= **Author 8**
Mark Hemer, CSIRO	= **Author 9**

Author details and their roles:

Paper 1, **Improved implementation of the fk and Capon methods for array analysis of seismic noise*:***
Located in chapter 2
Candidate was the primary author and with author 1 and author 3 contributed to the idea
Candidate performed analysis and evaluation of results
Author 7 and author 8 contributed the development and improvement of the technique
Author 1 and author 2 contributed to refinement and presentation

Paper 2, Deconvolution enhanced direction of arrival estimation using one- and three-component seismic arrays applied to ocean induced microseisms:
Located in chapter 3
Candidate was the primary author and with author 1 and author 2 contributed to the idea
Candidate is sole contributor to implementation and extension of technique
Authors 1, 2, 3, 4 & 7 contributed to refinement and presentation

Paper 3, The frequency dependence and locations of short-period microseisms generated in the Southern Ocean and West Pacific:
Located in chapter 4:
Candidate was the primary author and author 1 contributed to the idea
Candidate performed analysis and evaluation of results
Authors 1, 3, 4 & 5 contributed to the development of the manuscript
Author 9 contributed with the ocean hindcast data and assistance in its use
Author 6 contributed with seismic data
Author 1, 2 & 6 contributed with refinement and presentation

Statement of Co-Authorship

Paper 4, Microseism wavefield decomposition using deconvolution enhanced three-component beamforming:
Located in chapter 5:
Candidate was the primary author and author 1 contributed to the idea
Candidate performed analysis and evaluation of results
Authors 1, 2 ,3 and 4 contributed with refinement and presentation

Signed:

Anya M. Reading
Supervisor
School Of Physical
Sciences (Earth Sciences)
University of Tasmania

John Dickey
Head of School
School Of Physical
Sciences
University of Tasmania

Date: 14 Sept 2016

Abstract

Microseisms are weak continuous oscillations of the solid Earth. These oscillations form the background signal on all seismograms, hence the alternative name 'ambient noise'. In the period range 0.5 - 20 seconds, these vibrations are generated in the oceans and their presence can be attributed to two generation mechanisms. Primary microseisms are directly correlated to the period of the ocean waves, and are generated close to coastal areas with a shallow and sloping sea bottom topography. Secondary microseisms show frequencies of double that of their ocean wave sources and are generated in the deeper oceans along storm paths and in coastal areas. An improved understanding of the ambient noise wavefield therefore advances seismological techniques with wide potential applicability, e.g. to ocean wave studies in areas with limited direct observation.

A popular technique to study the weak ambient noise wavefield is plane wave beamforming, which utilizes all sensors in a seismic array simultaneously to improve the detection of coherent seismic energy. Beamforming allows estimatation of the directional and slowness dependent seismic wave propagation present in the wavefield. The accuracy of such analysis is governed by the size and configuration of the seismic array and the beamforming technique. To date, the most commonly used plane wave beamforming technique is frequency wavenumber analysis, which was invented over half a century ago. Given that the number of seismic arrays suitable for the analysis of microseisms is limited, the resolution of the frequency wavenumber analysis has been restricted to the detection of the strongest sources only. Improving the beamforming technique has the potential to improve the estimation of weaker signals in the wavefield and allow the application of beamforming to a wider range of arrays.

This thesis is divided into two parts, the improvement of beamforming techniques for the array analysis of ocean induced microseisms and the application of these new implementations to seismic arrays in Australia. In the first part, multiple beamforming algorithms and preprocessing schemes are evaluated to design an optimal beamforming framework for the analysis of ocean induced microseisms. The emphasis is on the accurate detection of multiple simultaneous seismic waves, the overall improvement of the beamforming power spectrum resolution and the extension from narrow to broadband (in terms of observed frequency range). This task is achieved by using the minimum variance distortionless response (Capon) beamformer supported by diagonal loading in an 'incoherently averaged' signal approach, hence the name, IAS Capon. The performance is evaluated using data from multiple seismic arrays and is found to be superior to the existing standard techniques. Further, the CLEAN algorithm originally developed in radio astronomy and the Richardson-Lucy deconvolution from visible light astronomy are explored, to further enhance

the resolution capabilities of plane wave beamformers in seismology. Deconvolution is used to remove the imprint of the array response function, which is a result of the geometrical configuration of the array stations. It reduces the bias of weaker sources in the power spectrum and also reduces artefact/ghost sources. The best performance is achieved with a modified implementation of the CLEAN algorithm and demonstrated with multiple seismic arrays. CLEAN, as implemented here, iteratively removes energy from the strongest source in the power spectrum. As the parameters of the removed energy are known, it can be placed into a separate 'clean' power spectrum without any array response contributions. Hence, the algorithm is able to decompose the wavefield into its most fundamental signal contributions. The technique is successfully extended to three components and is capable to accurately decompose the three dimensional microseism wavefield into its fundamental energy contributions.

In the second part, the research presented in this thesis makes use of the newly implemented algorithms to analyse secondary microseisms in the southern hemisphere and western Pacific, which have received relatively little attention with regard to generation locations and seasonal patterns of the microseism wavefield. Over two decades of ambient noise data from the Warramunga array in Northern Territory, Australia, are evaluated with the IAS Capon approach. This is carried out on an hourly basis for multiple microseismic sources over a broad frequency range. P wave generation regions are found to be frequency dependent and display seasonal patterns. For surface waves, a transition from Rayleigh to L_g waves is observed. A correlation with an ocean hindcast strengthens confidence in the accurate retrieval of weaker sources with IAS Capon. Finally, the CLEAN approach is used to decompose the three dimensional wavefield with the Pilbara array located in Western Australia, for a full calendar year (2013). The analysis allows the separation of multiple types of surface waves and a mean power representation is given. Special emphasis is placed on Love waves, as their generation mechanism in the secondary microseism range has not yet been established. The results shed new light on the generation regions of Love waves and suggest conversion from Rayleigh waves at sedimentary basin boundaries.

Acknowledgements

I would like to express my utmost gratitude towards my supervisor Anya Reading, who was always a helping hand in need and has equipped me with the skill set required for my future academic career. She always made time for me and was always happy to teach me valuable knowledge of being a successful scientist. I can not thank Anya enough for trusting me with flexible PhD hours that allowed me to chase after ocean swells, which resulted in me having a balanced, memorable and enjoyable life during my PhD. Further thanks goes to my second supervisor Simon Ellingsen, who was a great help in shaping my words in an understandable manner during the period of my PhD.

I would like to acknowledge the help of Keith Koper and Relu Burlacu, who have been great co-authors, contributing with knowledge and insight into the field of ambient noise. Further thanks goes to Hrvoje Tkalčić, who made me feel very welcome during my ANU visit and has cooked some of the most delicious food I have eaten during my candidature.

A shoutout to all the post graduate students at Earth Sciences and CODES, especially the geophys group, that made the working atmosphere really pleasant. Special thanks goes to Auntie Jane, who was very helpful with all my application and bureaucracy related questions (I wonder if they ever fix the cold water issue). An honourable mention goes to the soccer physics master Sam Holt, and the two surf shredders Calum Cunningham and Ivan Belousov the dominator.

The process and completion of this work can largely be attributed to the helping hand of my fiancée Doreen Melari Warjri, who possesses an infinite amount of patience for me. Her care and love have given me happiness and motivation to work through my candidature.

Contents

List of Tables

List of Figures

Abbreviations

1C	one component
2D	two dimensional
3C	three component
ARF	array response function
ASAR	Alice Springs Array
CAS	coherently averaged signal
CLEAN	deconvolution algorithm
CLEAN-3C	three component waveform deconvolution algorithm
DL	diagonal loading
DOA	direction of arrival
fk	frequency wavenumber
H	horizontal component
IAS	incoherently averaged signal
IMS	International Monitoring System
ISC	International Seismological Centre
LASA	Large Aperture Seismic Array
LPDF	long period double frequency
LQ wave	Love wave
L_g wave	superposition of multiple S-wave reverberations and SV to P and/or P to SV conversions inside the whole crust
MUSIC	multiple signal classification
MVDR	minimum variance distortionless response
OBS	ocean bottom seismometer
P wave	compressional body wave
PCA	principal component analysis
PM	primary microseisms
PSAR	Pilbara Array
PSD	power spectral density
PSF	point spread function - equivalent to ARF in seismology
R	radial component
RL	Richardson-Lucy
R_g wave	short period Rayleigh wave
S wave	shear body wave
SASC	slowness-azimuth station correction

SM	secondary microseisms
SNR	signal to noise ratio
SPDF	short period double frequency
SS	signal subspace
T	transverse component
UTC	coordinated universal time
WRA	Warramunga Array
Z	vertical component

Mathematical nomenclature

η	noise term
λ	eigenvalues
Λ	Lagrangian parameter
$\mathcal{L}$	Lagrangian function
ω	angular frequency
ϕ	CLEAN control parameter
ψ	phase factor
θ	array look direction
ξ	polarization parameter
D	number of sources
f	frequency
H	conjugate transpose
K	number of stations
L	number of snapshots
M	number of CLEAN iterations
N	sensor output length
s_l	snapshot length
t	time
$\mathcal{A}$	amplitude
a	signal steering vector (signal model case, single source)
P	power spectrum
P_{ARF}	array response function
$\tilde{P}$	power spectrum derived from rotated components
P_B	Bartlett power spectrum
P_{Capon}	Capon power spectrum
P_{IAS}	incoherently averaged power spectrum
P_{CAS}	coherently averaged power spectrum
$P_{B,max}$	power of strongest source estimated with the Bartlett beamformer
P_{CLEAN}	CLEAN power spectrum
P_{PSF}	CLEAN + background spectrum
P_{3C}	3 component power spectrum
$P_{3C,Capon}$	3 component Capon power spectrum
$P_{3C,CLN}$	CLEAN 3 component power spectrum

P_{PSF-3C}	CLEAN + background 3 component power spectrum
S	Source term (signal model case, single source)
y	array trace
$\mathbf{a}$	steering vector
$\mathbf{A}$	signal steering vector (signal model case)
$\mathbf{c}$	polarization state
$\mathbf{e}$	steering matrix
$\mathbf{g}$	component-wise plane wave propagation
$\mathbf{k}$	wavenumber
$\tilde{\mathbf{k}}$	wavenumber of strongest source
$\tilde{\mathbf{M}}$	rotation matrix
$\mathbf{u}$	eigenvectors
$\mathbf{s}$	slowness vector
$\mathbf{S}$	source term (signal model case)
$\mathbf{T}$	transformation matrix
$\mathbf{w}$	weight vector
$\mathbf{w}_B$	weight vector of Bartlett beamformer
$\mathbf{w}_{Capon}$	Capon weight vector
$\mathbf{w}_{max}$	weight vector steered towards the strongest signal
$\mathbf{C}$	cross spectral matrix
$\hat{\mathbf{C}}$	sample cross spectral matrix
$\mathbf{C}_{PSF}$	modified cross spectral matrix
$\mathbf{C}_{syn}$	synthetic cross spectral matrix
$\mathbf{C}_{broadband}$	frequency averaged cross spectral matrix
$\mathbf{C}_{CAS}$	coherently averaged cross spectral matrix
$\mathbf{C}_{3C}$	3 component cross spectral matrix
$\mathbf{R}$	covariance matrix
$\hat{\mathbf{R}}$	sample covariance matrix
$\mathbf{r}$	distance to reference station
$\Delta\mathbf{r}$	distance to reference station
$\mathbf{x}$	sensor output
$\mathbf{X}$	Furier Transform of $\mathbf{x}$
$\mathbf{X}_{3C}$	frequency representation of the 3 component data vector
$\mathbf{Y}_{3C}$	array polarization matrix

Richardson-Lucy nomenclature:

x	pixel coordinate
$\bar{\alpha}(x)$	convolution of padded PSF with mask object, defined in eq. 3.12
σ	RL control parameter
b	background noise level
$I(x)$	observed image

J	pixel side-length of image
$\bar{M}_s(x)$	mask object used in RL deconvolution
$O(x)$	original noise-free image
$\hat{O}(x)$	deconvolved image by means of Richardson-Lucy algorithm
$P(x)$	point spread function
$\bar{w}(x)$	defined in eq. 3.11

Chapter 1

Introduction

1.1 Microseisms

The terms signal and noise are of ambiguous meaning in the field of seismology and solely depend on the definition of the observer. In general, the term seismic signal refers to the part of the seismic wavefield which is of importance to the observer while the term noise refers to the unwanted part of the wavefield. Hence a seismic signal for one observer can be noise for another and vice versa.

Originally, seismology concentrated on the study of earthquakes and the Earth's response to the release of seismic energy. From this definition, earthquakes are denoted as signals, while continuous background oscillation not linked to an earthquake source are referred to as ambient noise. Treated as unwanted signals, a considerable amount of effort went into removing the background oscillation from seismograms for the study of earthquakes.

Contrary to the conventional case, in this thesis the ambient noise with periods in the range of 0.5 to 20 seconds is treated as the signal while earthquake induced energy is considered noise. Microseisms can be found at any location on Earth and are present as low amplitude continuous background oscillations in seismic record.

1.1.1 Historical development

In the late 19^{th} early 20^{th} century, efforts have been made to understand the origin of microseisms and the causes of their generation. A potential source of microseisms was believed to be linked to ocean waves breaking on extended steep coasts (Wiechert, 1904). It was found that seismic stations close to coasts can exhibit displacements of around $\sim 10\mu m$, while inland stations show a decrease in displacement (Gutenberg, 1936). This power measurement alone pointed towards the oceans as a source of the oscillations. Additionally, a peak in the microseisms spectrum correlated with the ocean wave period recorded close to the seismic station. It was therefore likely, that ocean waves in shallow water were responsible for the generation of the microseisms with periods correlating with ocean waves. This mechanism however, could not explain the whole spectrum of observed microseisms especially in the period range of 4 to 10 seconds. Many potential causes for the excitation of microseisms were excluded, e.g. temperature, air pressure and windstorms or rain (Gutenberg, 1936). It was suspected that energy from the ocean waves could propagate to the bottom of the sea bed even in deep water and excite seismic waves. However, this was at the time not consistent with the underlying theory of ocean wave energy propagation. Miche (1944)

extended the underlying theory and found that under certain conditions, pressure can propagate unattenuated towards the sea bed. It was later shown, that these conditions can be met by two ocean wave trains propagating in opposite directions with almost the same wave number (Longuet-Higgins, 1950). The theory was later extended to incorporate random waves (Hasselmann, 1963). Hence, the theory could effectively explain the excitation of seismic waves on the sea bed in deep water, i.e. the presence of microseisms in the range of 4 to 10 seconds.

Analysis of microseisms soon confirmed the ocean gravity wave-wave interaction mechanism to be valid. Haubrich et al. (1963) analysed microseisms near San Diego, California and found two peaks in the frequency spectrum of the seismic time series. The first peak (primary microseisms peak - PM) was correlated with the ocean period and the second (secondary microseisms peak - SM) was at twice the frequency, hence confirming the mechanism of wave-wave interaction. Seismic array studies followed to contribute to the understanding of the microseism wavefield composition over a broad frequency range (e.g. Toksöz and Lacoss, 1968) and revealed the presence of diverse seismic phases, e.g. Rayleigh, Love and body waves.

1.1.2 Motivation for recent studies

In the last two decades, the analysis of microseisms has increased in popularity due to factors such as: digitalisation, storage and availability of seismic data, the increase in computing power and advances in theory and data processing. One of the most profound ambient noise discoveries in the last decades is the retrieval of the Green's function between two seismic stations extracted from the ambient noise wavefield via cross-correlation (Shapiro and Campillo, 2004) (given long enough temporal averaging of the cross-correlation function). Hence the coherent nature of the ambient noise field can be extracted over large distances and lead to increased research of Earth's structure with ambient noise (e.g. Shapiro and Campillo, 2004; Sabra et al., 2005; Campillo, 2006; Gerstoft et al., 2006; Bensen et al., 2008). Other contributions via the analysis of microseisms have aided amongst others in the understanding of climate variability (e.g. Bromirski et al., 1999; Grevemeyer et al., 2000; Aster et al., 2008; Grob et al., 2011; Ardhuin et al., 2012), monitoring of structural changes (e.g. monitoring of volcanos, structural changes due to earthquakes, seasonal changes) (e.g Snieder and Hagerty, 2004; Brenguier et al., 2008), localisation of generation regions of microseisms (e.g. Toksöz and Lacoss, 1968; Haubrich and McCamy, 1969; Cessaro, 1994; Friedrich et al., 1998; Essen, 2003; Schulte-Pelkum et al., 2004; Chevrot et al., 2007; Kedar et al., 2008; Gerstoft et al., 2008; Brooks et al., 2009; Koper et al., 2009; Landès et al., 2010; Zhang et al., 2010; Behr et al., 2013) and exploration studies (e.g. Riahi et al., 2013).

1.1.3 Microseismic spectrum

In this work, the microseism spectrum refers to the continuous background oscillation of the solid Earth in the period of 0.5 to 20 seconds. In general, the spectrum shows two characteristic peaks (Berger et al., 2004) when transformed into the frequency domain via the Fourier transformed. An example of the spectrum is shown by means of the power spectral density (PSD) in Fig. 1.1a for the

TAU station located in Tasmania, Australia. The smaller peak, also named 'primary' microseism (PM) peak or single frequency microseism peak displays its maximum close to 15 seconds for the TAU station. The origin of this peak is attributed to direct ocean wave interaction with a shallow sloping ocean seafloor topography (e.g. Hasselmann, 1963; Haubrich et al., 1963). Hence the frequency dependent energy distribution correlates with the period of the ocean waves close to the station and the maximum of the primary peak therefore differs with geographical locations. The second and stronger peak, can be found at roughly half the period of the primary peak and is named the secondary microseism (SM) or double frequency microseism peak. In this case, the SM peak shows its maximum at 7 seconds and is roughly 20 dB $[m^2/Hz]$ stronger than the PM peak.

Care needs to be taken when comparing different dB scales as the presentation of the spectrum can be based on displacement, velocity or acceleration units. For completeness, 3 possibilities are displayed (Fig. 1.1a-c) and show the influence the difference on the resulting spectrum. The difference in power between the PM and SM peak differs between displacement, velocity and acceleration. Further, the slope of the short period spectrum differs as well, hence care needs to be taken when comparing PSD's.

Generation of the SM peak is governed by ocean gravity wave-wave interaction (Longuet-Higgins, 1950; Hasselmann, 1963). In a simplified model, this can be explained as 2 ocean wave trains propagating in the opposite direction with roughly the same wave number. The superposition of the two wave trains invokes acoustic pressure waves which travel lossless vertically towards the ocean seafloor and excite seismic waves which propagate as surface waves along the ocean/seafloor boundary and body waves through the solid earth. Given the criterion of two interacting ocean wave trains, the generation of SM seismic waves is not as straightforward as the PM case, but requires a well defined ocean wave spectrum (Ardhuin et al., 2011).

Scenarios at which SM are generated given the needed ocean state were discussed by Ardhuin et al. (2011) and summarized in 3 classes:

- Ocean waves are reflected at a coastline to produce a wave train traveling in the opposite direction.

- An ocean storm at location A generates ocean waves radially outwards. When the storm travels faster than the ocean waves, the storm at location B will generate ocean waves that propagate in the opposite direction of a portion of the waves generated at location A. Hence creating an area with wave-wave interaction.

- Two swell systems generated by 2 different storms propagate in opposite directions.

The last case, where two storms produce swells traveling in opposite direction, was shown to produce the strongest microseisms excitation even at moderate sea heights (Obrebski et al., 2012).

The SM band can be further separated into two sub-bands, the long period and short period double frequency microseisms band (LPDF 0.085-0.2 Hz / SPDF 0.2 - 0.45 Hz) (Bromirski et al., 2005). Bromirski et al. (2005) investigated the correlation between ocean wave, wind and microseisms power at the H2O station in Hawaii. They found that in SPDF microseisms show correlations with wind speed and hence the local wind sea is responsible for the generation of

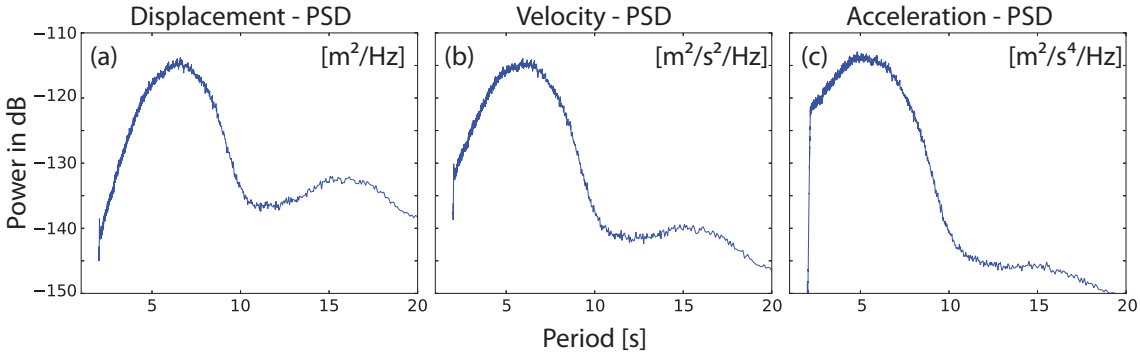

Figure 1.1: Power spectral densities (PSD) of the microseisms wavefield in the range of 2-20s. To generate these figures, the LHZ channel with a sampling period is used for July 2015. The time series is divided into 1 hour long subsets, the instrument response and mean of the trace is removed. For each hour, the PSDs are generated from (a) displacement, (b) velocity and (c) acceleration and the median of all data in July is taken to represent an average spectral representation of the microseisms spectrum. The data are prefiltered between 0.005-0.9 Hz to omit windowing effects, hence the short period end of the spectrum (at 2 seconds) shows a sharp decay in power. The power is given in decibel [dB] and the corresponding SI units are displayed in to top right of each subfigure.

SPDF microseisms in coastal areas. For LPDF microseisms the correlation was poor and it was concluded that swells generated in distant areas are reflected at the Hawaiian coastlines and produce LPDF microseisms. Hence LPDF microseisms are not generated by local wind conditions, while SPDF microseisms are increasingly affected by local winds with increasing frequency.

1.1.4 Spatial variability

The microseisms spectrum in Fig. 1.1 is representative of Tasmania only as microseismic energy in the PM band is generated at local coastlines (given the excitation mechanism in shallow waters) and in the SM band predominantly in the surrounding oceans (e.g. Bromirski and Duennebier, 2002; Schulte-Pelkum et al., 2004; Bromirski et al., 2005; Yang and Ritzwoller, 2008). The spatial variability around the globe is displayed at 6 stations in Fig. 1.2 as the median power of July 2015. Three stations are selected in the northern hemisphere, PFO in California, ESK in Scotland and ERM in Japan. For the southern hemisphere, apart from the TAU station, WRAB in Northern Territory Australia, NNA in Peru and HOPE at the South Georgia Island are selected.

For the northern hemisphere, the median power of the dominant SM peak shows similar values between -125 to -130 dB $[m^2/(s^2Hz)]$ and $\sim$ -147 dB $[m^2/(s^2Hz)]$ at the PM peak for all 3 stations. While the powers are similar, the shape of the PSD is not. The PFO station displays a broad SM peak, hence energy is present over a broad frequency range, while ESK and ERM display a narrower peak. The PSD of the ERM station in Japan displays two SM peaks, which suggest that two different microseisms sources are present (Koper and Hawley, 2010). The dominant peak is below 5s (SPDF), hence the local wind conditions are likely responsible for the generated microseisms, while the LPDF peak is generated by a different swell. At ESK in Scotland, the opposite scenario with 1 SM peak and 2 PM peaks is found. For the southern hemisphere, 2 SM peaks are clearly present in the PSD of WRAB and NNA, while HOPE displays a single strong SM peak

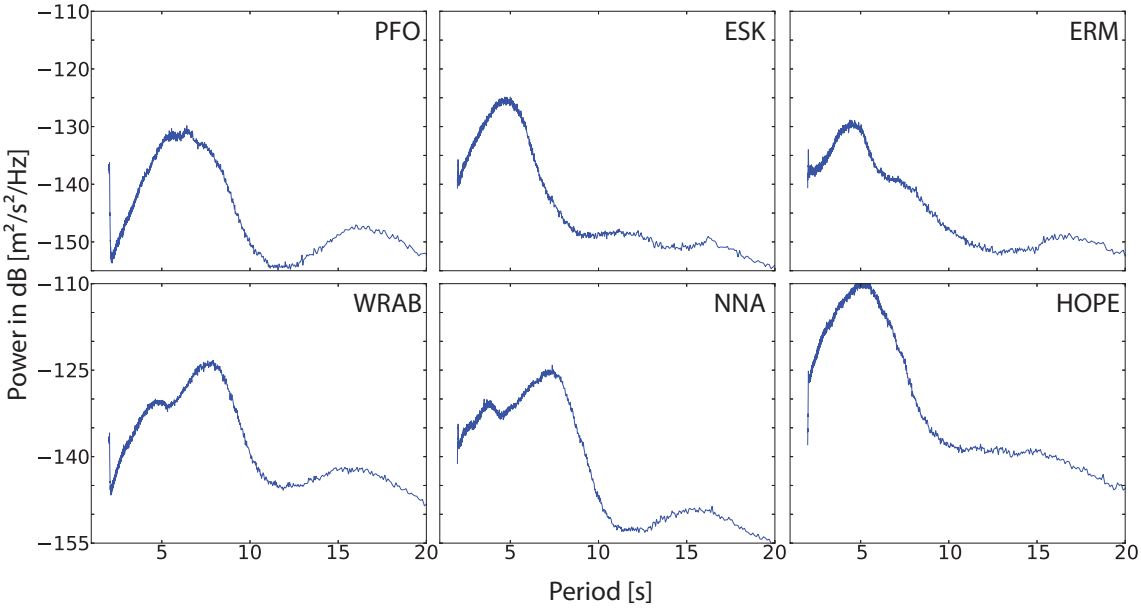

Figure 1.2: Analog to Fig. 1.1, the PSD's for 6 stations in dB $[m^2/(s^2Hz)]$ are displayed. PFO, ESK and ERM are located in the northern hemisphere (California North America, Scotland and Japan) and WRAB, NNA and Hope are located in the southern hemisphere (Northern Territory Australia, Peru and the South Georgia Island). The 6 graphs display the spatial variability for the median power in July 2015.

(-110 dB $[m^2/(s^2Hz)]$) and a less well defined PM peak.

There are multiple factors that contribute to the shape and power of the of the PSD at a given location. They can be categorised into three groups: generation, coupling and propagation effects. The generation is solely driven by the ocean state, i.e. the swell or wind sea. For PM, the generated energy is given by an interplay between ocean wave energy and the geometry of the incident coastline (Hasselmann, 1963), which is essentially the coupling that converts pressure to seismic waves. For the SM case, the condition of wave-wave interaction needs to occur and for the case of coastline reflections, the reflection coefficient of the coastline plays a key role (Ardhuin and Roland, 2012). The coupling effect for SM is given by an interplay between the ocean wave spectrum and the ocean depth (Longuet-Higgins, 1950) and was observed by e.g. Kedar et al. (2008); Hillers et al. (2012). Propagation effects include the transition between ocean and land, attenuation and scattering. Therefore seismic stations located further from the generation regions of microseisms show reduced power in their PSD's.

1.1.5 Temporal variability

Similar to the spatial variability, the microseismic signal shows variation in time (e.g. Stutzmann et al., 2000, 2012). The variability for the station TAU in Tasmania, Australia, is displayed in Fig. 1.3 for a 50 day period starting from 1^{st} of July 2015. The temporal spectrum shows multiple time periods with increased microseismic energy. Temporal variations in the spectrum are a direct result of the ocean state (e.g. Bromirski and Duennebier, 2002) and can be associated with swells interacting with Tasmania. The dependence on the frequency is given by the energy and period distribution of the swell that generates the microseismic waves. As most of the PM energy is

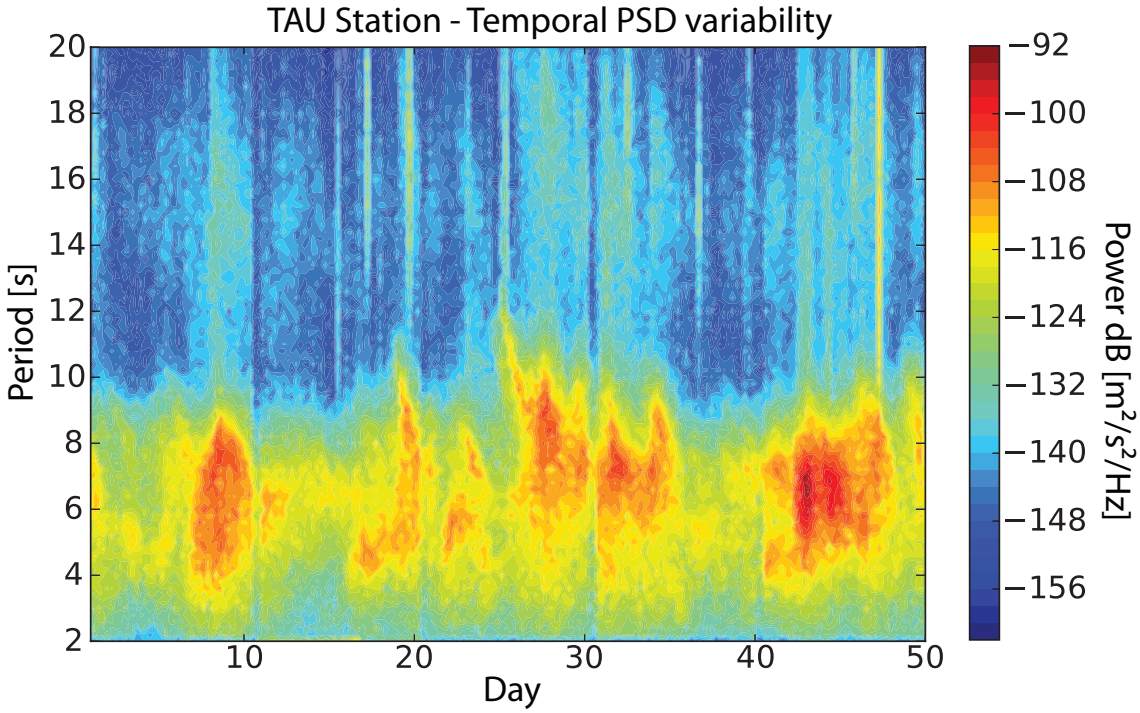

Figure 1.3: Temporal variability of the microseisms wavefield for the station TAU in Tasmania, Australia. Displayed is the time span of 50 days starting from July 2015 onwards and the figure shows for each hour, the median of 6 successive hours. The summary of those PSD's is the resulting figure.

present at times when SM energy is present, one can conclude that most of the SM energy is generated close to the Tasmanian coastlines, i.e. the SM process is driven by coastline reflection and the successive wave-wave interaction pressure excitation. The peak of the SM band can be variable, in this case between $\sim 4-10$s, and the power difference between days with a strong and weak microseisms presence can exceed 30 dB $[m^2/(s^2Hz)]$ within a few days (e.g. see Fig. 1.3 for days 35-45).

Given that the temporal variations of the microseismic wavefield are a result of the ocean state, the variations in power and frequency can be studied for multiple purposes such as: Sea height studies (e.g. Bromirski et al., 1999; Essen et al., 1999), increase in storm activity (e.g. Grevemeyer et al., 2000; Aster et al., 2010) and seasonal changes (e.g. Astiz and Creager, 1994; Stutzmann et al., 2000; Tanimoto et al., 2006; Aster et al., 2008; Stutzmann et al., 2012). Bernard (1990) observed a pattern in the microseisms power record which corresponded to the solar cycle. Since then, many studies have focused on the analysis of the temporal changes. Seasonal patterns clearly emerge (e.g. Astiz and Creager, 1994; Stutzmann et al., 2000; Tanimoto et al., 2006; Aster et al., 2008; Koper et al., 2009; Stutzmann et al., 2009; Grob et al., 2011; Stutzmann et al., 2012) and show elevated power levels in the winter months for each hemisphere. This process is driven by an increased storm activity in the winter months. It was shown, that the increase in power can be variable for the horizontal (H) and vertical (Z) component (Tanimoto et al., 2006) and could be related to higher mode surface waves generation. Further, Stutzmann et al. (2009) found that the seasonal variations are greater for stations further away from the equator and the power measurements of stations in the Antarctic region are affected by sea ice floe.

Analysis of multiple decades of microseismic data show a slight increase in power levels towards the present day (Grevemeyer et al., 2000; Aster et al., 2010), which suggest a change in the wave climate, potentially contributed by climate change.

1.1.6 Seismic wave types and their generation

Advances in analysing the composition of the microseismic wavefield have benefitted from the deployment of the Large Aperture Seismic Array (LASA) in Montana, North America in the early 60's. Utilising LASA and beamforming methods to separate the microseisms wavefield in slowness space (or frequency-wavenumber space) fundamental and higher-mode Rayleigh, Love and P waves were reported (Toksöz and Lacoss, 1968; Lacoss et al., 1969). In the PM band, Love waves with twice the amplitude of Rayleigh waves were identified, while in the SM band < 0.2Hz fundamental mode Rayleigh waves dominate. Between $0.2 - 0.3$ Hz a mix of Rayleigh and P waves were observed and at $0.3 - 0.6$ Hz the P waves dominate. However, as the authors point out, arrays closer to the coast will likely show a higher portion of fundamental mode Rayleigh waves at higher frequencies. These results are confirmed by an independent study on the same array (Haubrich and McCamy, 1969) and additionally show that P waves generation regions differ with frequency.

Rayleigh waves

The generation regions of Rayleigh waves are predominantly near coastlines (e.g. Friedrich et al., 1998; Bromirski and Duennebier, 2002; Bromirski et al., 2005; Chevrot et al., 2007; Bromirski et al., 2013) where SM excitation can occur (i.e. where swell/wind sea is present). Generation of Rayleigh waves occurs in the deep ocean far off coastlines (Cessaro, 1994; Stehly et al., 2006; Chevrot et al., 2007; Kedar et al., 2008; Obrebski et al., 2012), but is rarely observed on land. The generation locations of higher mode Rayleigh waves do not have to coincide with fundamental mode Rayleigh wave generation directions (Brooks et al., 2009) and a seasonal influence can occur (Tanimoto et al., 2006). Multiple locations, North America (Toksöz and Lacoss, 1968; Lacoss et al., 1969), New Zealand (Brooks et al., 2009) and the Netherlands (Kimman et al., 2012) find higher mode Rayleigh waves in the frequency range of $\sim 0.15 - 0.2$ Hz. This frequency range is also consistent with a study performed in the South Central Pacific with ocean bottom seismometers (OBS) (Harmon et al., 2007), where higher mode Rayleigh waves are observed between 3.5 - 7s, while the fundamental mode is observed between 2-16s. In general, the generation regions of Rayleigh waves are variable with time, depending on the swell / wind sea conditions, but generation regions that are dominant over the period of a full year have been observed as well (e.g. Tanimoto et al., 2006).

Love waves

The presence of Love waves in the microseisms spectrum, is now well established (e.g. Toksöz and Lacoss, 1968; Lacoss et al., 1969; Haubrich and McCamy, 1969; Capon, 1973; Friedrich et al., 1998; Campillo and Paul, 2003; Chevrot et al., 2007; Lin et al., 2008; Nishida et al., 2008a,b;

Hadziioannou et al., 2012; Matsuzawa et al., 2012; Behr et al., 2013), but is to date not fully understood. For the PM where direction interaction between the ocean bottom and the ocean gravity wave occurs, Saito (2010) derived that shear traction of ocean waves acting on the sea bottom can excite Love waves. For SM, a vertical point pressure force acting on the sea bottom, such as the one assumed for the wave-wave interaction (Longuet-Higgins, 1950; Hasselmann, 1963), should not excite Love waves. Hence, the mechanism has so far not been determined. Apart from fundamental mode Love waves, higher mode Love waves are also present in the microseisms wavefield (e.g. Nishida et al., 2008b).

The generation region for Love waves differs with frequency. For the PM band, the generation regions of Rayleigh and Love waves can be the same, but when observed from a single array, the generation region differ (e.g. Matsuzawa et al., 2012; Behr et al., 2013). The excitation mechanism in the PM band proposed by Saito (2010) is subject to a radiation pattern for Love waves, which are generated perpendicular to the propagation direction of the ocean gravity wave and no generation occurs inline with the propagation direction. This radiation is visible in observational analysis (e.g. Matsuzawa et al., 2012; Behr et al., 2013), although not explicitly stated in the latter work. For the SM band, the generation regions of Love waves seem to be closely related to Rayleigh waves (Toksöz and Lacoss, 1968; Lacoss et al., 1969; Haubrich and McCamy, 1969; Friedrich et al., 1998; Nishida et al., 2008a; Hadziioannou et al., 2012; Behr et al., 2013) and the H/Z component ration is < 1 (Friedrich et al., 1998; Nishida et al., 2008a) unlike in the PM band where it is > 1 (Toksöz and Lacoss, 1968; Lacoss et al., 1969; Nishida et al., 2008a).

L_g waves

Recently, the L_g phase was observed in the short period microseisms wavefield (Koper et al., 2009, 2010). The L_g phase is a supercritical S wave trapped in the crustal wave guide. Since the L_g phase does not propagate over ocean-continent margins (Zhang and Lay, 1995), the generation of this phase should be connected to near coastal generation or some sort of scattering process from a different wave type along its ray path towards the seismic array. Analysing 18 International Monitoring Stations (IMS) arrays, Koper et al. (2010) found the L_g phase to be the dominant part of the short period microseisms band (0.25-2.5s), with a contribution of about 50% to the vertical microseisms wavefield.

Compressional body waves

Apart from surface waves, P waves are present in the wavefield (e.g. Toksöz and Lacoss, 1968; Lacoss et al., 1969; Haubrich and McCamy, 1969; Capon, 1973; Gerstoft et al., 2008; Koper et al., 2009, 2010; Zhang et al., 2009; Landès et al., 2010; Zhang et al., 2010; Traer et al., 2012; Boue et al., 2013; Obrebski et al., 2013). A difference between surface and body waves is their localiziation. While surface waves propagate along great circle paths on of the Earth's surface, assuming no refraction due to anisotropic geology occurs, body waves travel through the Earth and their angle of incident carries information on the location of generation. The apparent velocity of the body wave or the angle of incident can be use to backproject the ray path to the location of origin with the help of traveltime tables such as ak135 (Kennett, 2005). Apart from the direct P

wave and P_n/P_g (e.g. Koper et al., 2010), PP and inner core phases PKP are present (e.g. Gerstoft et al., 2008; Koper and de Foy, 2008; Landès et al., 2010) and more exotic phases (Boue et al., 2013).

The generation regions of body waves are predominantly in deep oceans (e.g. Lacoss et al., 1969; Gerstoft et al., 2008; Zhang et al., 2010) and dependent on the frequency (e.g. Haubrich and McCamy, 1969; Zhang et al., 2009). In general, P wave generation regions are in agreement with the main storm paths in the northern and southern hemisphere, while little generation is found around the equatorial region. Similar to surface waves, P wave sources are subject to seasonal variation (e.g. Zhang et al., 2010) and show strongest excitation during the winter months of the particular hemisphere. In the short period microseisms range, strong P waves have been observed (Zhang et al., 2009) in close proximity to the array and correlate well with local wind conditions, i.e. are generated by wind swell in shallow locations.

Shear body waves

To date, no array analysis observed S body waves with beamforming to infer their generation location. The absence of S waves in three component (3C) beamforming studies suggests that the power of these waves is relatively weak.

1.1.7 Numerical modelling of microseisms

One of the aims of microseisms wavefield analysis, is to obtain supplementary results on the ocean state in times when satellite information is not present. In the case of big storms, the visible light that would offer insight into the ocean state is blocked by the storms clouds, or imagery is not available due to the static orbit path of satellites. Another reason is to study periods for which insufficient metrological data are present, yet seismic data are available. To obtain information that would help constrain the ocean state, the understanding of the wavefield needs to be refined. At present, many variables are yet to be constrained, limiting the ability to utilise seismic data as a reliable measurement tool.

PM microseisms are generated at the coastlines for incident ocean swells and are limited in their information content, given the information is restricted to the coastal region. Nevertheless, correlations between PM energy and ocean waves have shown that a prediction model, i.e. simulating ocean wave height from seismic waves, can be achieved (e.g. Bromirski and Duennebier, 2002). More potential can be attributed to SM energy, which is generated in deep water as surface and body waves (previous section 1.1.6) and in the case of body waves is predominantly generated at locations with increased storm activity.

Ideally, one wants to reconstruct the ocean state with the data recorded at a seismic station or network. To achieve this task, two models that attempt to mimic the processes in nature are needed. An accurate ocean model that has information on the frequency and directional energy distribution of ocean waves and a coupling and propagation model that accounts for the transfer of energy to the solid earth and attenuation effects along the path to the seismic receiver.

A state of the art model for the description of ocean wave properties on a global scale is

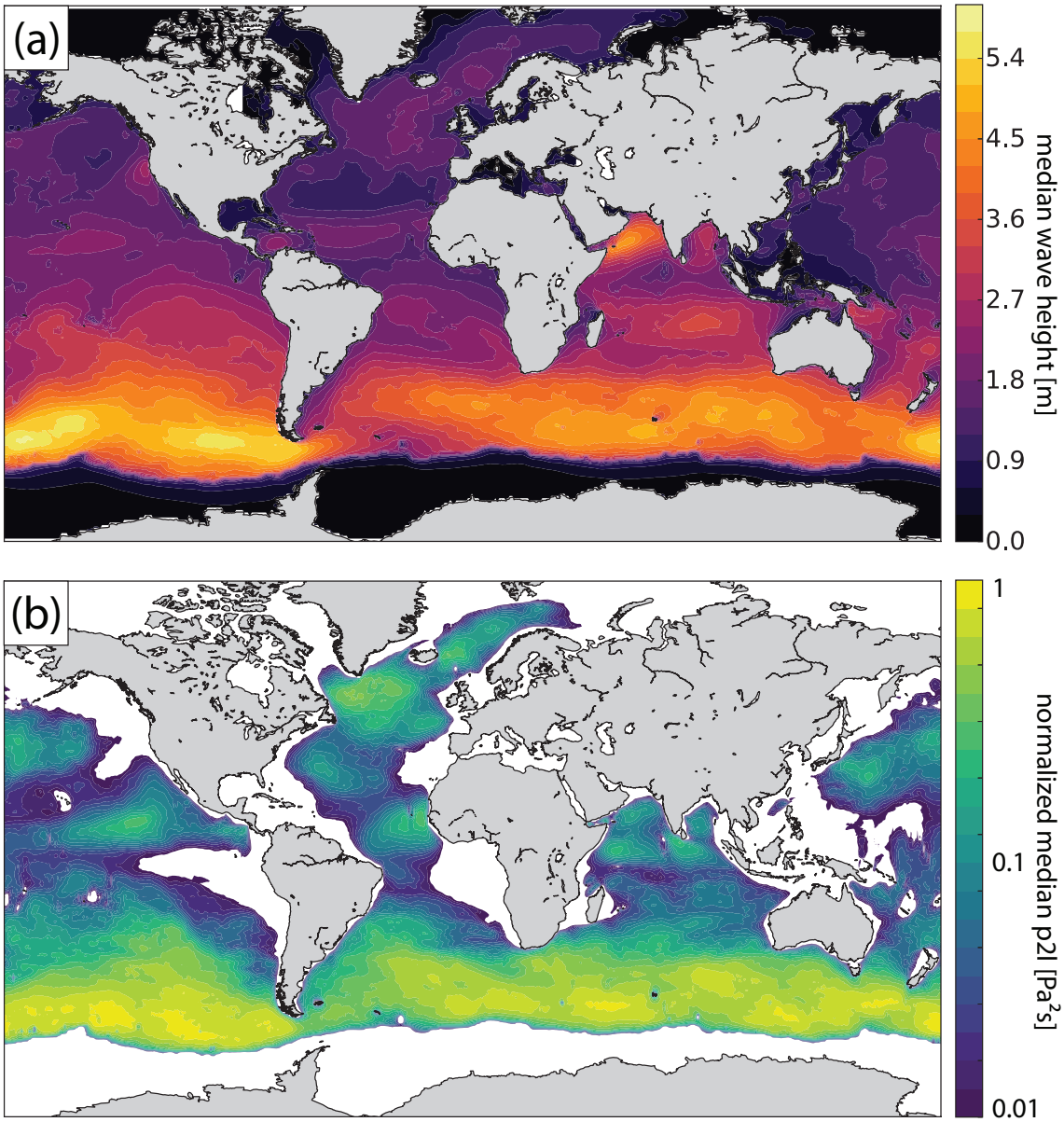

Figure 1.4: Displayed are (a) median wave height and (b) normalized median surface pressure density (p2l) for July 2015. These figures were generated from the IFREMER (French Research Institut for Expolration of the Sea) model (Ardhuin et al., 2011) build within the WAVEWATCH III model (Tolman, 2009). In (b), surfaces with white color represent p2l values smaller than 0.01.

WAVEWATCH III (Tolman, 2009). Combined with an improved parameterization for the dissipation of ocean wave spectra (Ardhuin et al., 2010), a prediction of microseism noise source generation derived from the ocean waves state can be modelled (Ardhuin et al., 2011; Ardhuin and Roland, 2012). The model is able to calculate the equivalent surface pressure density (p2l) acting on the sea floor, which excites seismic waves. An example of the p2l calculation generated by the WAVEWATCH III model, is displayed in Fig. 1.4 for the full month July 2015 alongside the median wave height. The strongest p2l values (here displayed as the median of the month) can be found along storm paths in the southern hemisphere (elevated wave height values in Fig. 1.4a), which is consistent with seasonal studies (e.g. Stutzmann et al., 2009). While the wave height somewhat correlates with the p2l map for the southern hemisphere, this is not the case for the equator and northern hemisphere regions. Hence wave height should not be used as a proxy for SM excitation, but the condition of interfering wavefields needs to be met (e.g. Obrebski et al., 2012).

This modelling approach is bound to certain limitations, mainly due to the predicted directional wave spectrum which is discretized into 31 discrete frequencies (0.04 - 0.17Hz) and 24 azimuths. The directional wave spectrum is generated by wind forcing in the numerical model, which in itself can deviate from true wind speeds and generate error affected wave spectra. The prediction of higher frequency microseismic excitation is strongly dependent on the accuracy of the directional wave spectrum (Ardhuin et al., 2011) which depends on reflected wave spectra (Ardhuin and Roland, 2012).

Aside from these limitations, the model has been shown to correlate well with observations (e.g. Stutzmann et al., 2012; Obrebski et al., 2013).

1.2 Array processing of microseisms

1.2.1 Overview of processing approaches

Unlike earthquake signals, microseisms do not have an impulsive onset and are relatively weak with displacements up to a few microns (e.g. Gutenberg, 1936). Hence the processing of such signals requires a particular set of techniques, which are capable of extracting coherent signals and their properties from a diffuse ambient wavefield. The most successful option is the use of seismic networks or seismic arrays to increase the signal to noise ratio (SNR) to extract the coherent part of the wavefield. A further advantage of multiple station seismology is the possible detection of weaker signals due to noise suppression. In this subsection, an overview of the commonly used processing techniques for single and multiple station analysis of ocean induced microseisms is given.

The processing methods of microseisms are bound by the type of available data and can differ for single/multiple stations and 1/3-component seismic data. In the case of a 1-component single station, the amount of information that can be extracted from the continuous signal is limited. Apart from the frequency and energy content present on the 1-component instrument, no other information can be extracted from a single station.

If 3-component data are available for a single station, access to polarization analysis becomes

possible. The comparison of the phase relation between all 3 components can yield the mode of propagation of the ambient noise wavefield and can distinguish between P, S, Rayleigh and Love waves given their unique polarization state. Many polarization methods have been developed and can operate either in the time (e.g. Flinn, 1965; Schimmel et al., 2011) or frequency domain (e.g. Vidale, 1986; Park et al., 1987; Jurkevics, 1988; de Franco and Musacchio, 2001; Koper and Hawley, 2010) and have been applied in the analysis of microsesims (e.g. Haubrich et al., 1963; Schulte-Pelkum et al., 2004; Tanimoto et al., 2006; Koper and Hawley, 2010; Schimmel et al., 2011; Sergeant et al., 2013). The use of polarization analysis on microseisms is favourable in regions with little seismic station coverage and heterogeneous geology where plane wave beamforming can not be applied. Another advantage of polarization analysis is its applicability to a board frequency range, i.e. there is no conceptual constraint apart from the limit of the recording seismograph.

By increasing the number of the stations, the capability of estimating wave speed velocity becomes accessible. In earthquake seismology, the velocity is measured by detecting a desired phase at each station and calculating the traveltime for the interstation distance. For the case of microseisms, which do not have a distinct phase arrival, the identification of the onset is not trivial. One way to estimate the velocities present in the wavefield is to use the cross-correlation method between station pairs. It can be shown, that for a diffused wavefield, the Green's function between two locations emerges from the cross-correlation when averaged over a long period of the time (e.g. Shapiro and Campillo, 2004). The underlying assumption is that waves present in the wavefield propagate in all directions, and hence sample the interstation distance from all directions. From the Green's function, with the consideration of some pre-processing steps (e.g. Bensen et al., 2007), the group and phase velocity dispersion curves can be extracted (e.g. Shapiro and Campillo, 2004). Additionally, the dispersion curves can be used to perform ambient noise tomography (e.g. Shapiro et al., 2005; Sabra et al., 2005; Gerstoft et al., 2006; Bensen et al., 2008) and study the propagation direction of surface waves (e.g. Bensen et al., 2008) with limited resolution.

Another method to analyse the ambient noise wavefield by means of multiple station analysis is plane waves beamforming. Beamforming makes use of all stations simultaneously and achieves higher resolution, in velocity and azimuth, than the cross-correlation of station pairs and polarization analysis (e.g. Harris, 1990). In contrast to the previously mentioned cross-correlation technique where sensor outputs are cross-correlated, beamforming cross-correlates the observed wavefield with a synthetic signal model. The most basic plane wave beamforming method, also known as frequency-wavenumber analysis or fk / Bartlett beamforming, is a natural extension of the Fourier analysis (Bartlett, 1948) and the signal model is defined as plane waves propagating over the array. The method is a grid search which yields the highest power for the azimuth-velocity pair where there is the greatest correlation between the synthetic and observed wavefield. Other seismic array methods are reviewed in Rost and Thomas (2002, 2009).

In this thesis, the basic concepts of data independent (e.g. fk) and data adaptive (e.g. Capon) beamforming are outlined (subspace based beamforming and its application with respect to microseisms is covered in chapter 6). For both of these beamforming techniques, the signal model is essential and is presented in the next section.

1.2.2 Signal model

The simultaneous use of all array stations requires a signal model, which lays out the propagation characteristics of seismic waves over the array. The predictions of the signal model are then compared with observed data to estimate coherent signal propagation over the array. Here, the model for plane wave propagation in the far field approximation (the source of the seismic waves is far from the array to ensure parallel raypaths), where the wavefield at a station is modelled as a stationary stochastic process as a sum of D complex sinusoids (i.e. sources) in a white noise environment is presented. For a single source at a given location, the time series recorded with a seismograph can be given as (bold symbols indicate vectors)

$$x(t) = \tilde{a}(\mathbf{s}, \omega)S(t) + \eta(t), \tag{1.1}$$

where $\tilde{a}(\mathbf{s}, \omega)$ denotes the signal steering vector for a single station

$$\tilde{a}(\mathbf{s}, \omega) = e^{-i\omega \mathbf{s}\Delta\mathbf{r}} \tag{1.2}$$

between source and station location $\Delta\mathbf{r}$ with a given slowness $\mathbf{s}$ and $S(t)$ describes the amplitude $\mathcal{A}$ and phase ψ of the source. The two dimensional slowness vector is denoted by $\mathbf{s}$, t is the time and ω the angular frequency. The noise is represented by the last term $\eta(t)$. For the case of D multiple sources and an array of K stations, the equation can be written in the elegant matrix form

$$\mathbf{x}(t) = \mathbf{A}(\mathbf{s}, \omega)\mathbf{S}(t) + \eta(t), \tag{1.3}$$

in detail

$$\begin{bmatrix} x_1(t) \\ x_2(t) \\ \vdots \\ x_K(t) \end{bmatrix} = \begin{bmatrix} e^{-i\mathbf{s}_1\omega_1\Delta r_{11}} & e^{-i\mathbf{s}_2\omega_2\Delta r_{12}} & \dots & e^{-i\mathbf{s}_P\omega_P\Delta r_{1D}} \\ e^{-i\mathbf{s}_1\omega_1\Delta r_{21}} & e^{-i\mathbf{s}_2\omega_2\Delta r_{22}} & \dots & e^{-i\mathbf{s}_P\omega_P\Delta r_{2D}} \\ \vdots & \vdots & \dots & \vdots \\ e^{-i\mathbf{s}_1\omega_1\Delta r_{K1}} & e^{-i\mathbf{s}_2\omega_2\Delta r_{D2}} & \dots & e^{-i\mathbf{s}_P\omega_P\Delta r_{MD}} \end{bmatrix} \begin{bmatrix} S_1(t) \\ S_2(t) \\ \vdots \\ S_D(t) \end{bmatrix} + \begin{bmatrix} \eta_1(t) \\ \eta_2(t) \\ \vdots \\ \eta_K(t) \end{bmatrix}, \tag{1.4}$$

where $\mathbf{A}$ denotes the steering matrix and r_{nm} is the distance between source n and station m. Hence the vector $x(t)$ represents the wavefield at K stations as a superposition of D complex sinusoids and additional white noise. The intrinsic plane wave constraint in the data model can be visualized with the example of a single source and 2 stations in which case one obtains (the noise term is left out for simplicity)

$$\begin{bmatrix} x_1(t) \\ x_2(t) \end{bmatrix} = \begin{bmatrix} S_1(t)e^{-i\mathbf{s}_1\omega_1\Delta r_{11}} \\ S_1(t)e^{-i\mathbf{s}_1\omega_1\Delta r_{21}} \end{bmatrix}. \tag{1.5}$$

The only difference is the distance between the station and the source in the exponent and it follows

$$x_1(t) = x_2(t)e^{i\psi}. \tag{1.6}$$

The two sensor outputs only differ by a phase shift which equates to $e^{i\Psi} = e^{-is\omega(r_2-r_1)}$, i.e. a plane wave propagating over both stations with the properties of the source signal.

The direction of arrival (DOA) of sources, can be extracted from the covariance matrix of the sensor outputs

$$\mathbf{R} = \mathrm{E}\{\mathbf{x}(t)\mathbf{x}^H(t)\} = \mathbf{A}\mathrm{E}\{\mathbf{s}\mathbf{s}^H\}\mathbf{A}^H + \mathrm{E}\{\mathbf{n}\mathbf{n}^H\}, \tag{1.7}$$

with $E\{\quad\}$ denoting the statistical expectation and the superscript ^{H} is the conjugate transpose. The term $\mathrm{E}\{\mathbf{s}\mathbf{s}^H\}$ denotes the source covariance matrix and $\mathrm{E}\{\mathbf{n}\mathbf{n}^H\}$ the noise covariance matrix.

$\mathbf{R}$ is a Hermitian matrix with real numbers in the diagonal and complex in the cross terms. The trace of $\mathbf{R}$ equals the sum of auto-correlations and represents the power contribution of all sources plus noise.

1.2.3 Frequency - wavenumber beamforming (fk)

In fk beamforming, the idea is to extract information from the covariance matrix to infer the DOA of the impinging signals. The underlying idea is to steer the array into a direction at a time, given the assumption of plane waves, and measure the output power. In seismology, where variable seismic wave speeds occur, the beamforming approach is a grid search over the slowness plane, i.e. in azimuth and velocity. The grid point at which the maximum output power is obtained, is considered the direction of arrival.

In the signal model, the covariance matrix $\mathbf{R}$ in eq. 1.7 is known due to the knowledge of the source parameters. For a wavefield where the DOA and slowness of the signal is of interest, the precise knowledge of the covariance matrix is unknown. In this case, the matrix is substituted with the sample covariance matrix

$$\hat{\mathbf{R}}(t) = \frac{1}{N}\sum_{t=1}^{N}\mathbf{x}(t)\mathbf{x}^H(t), \tag{1.8}$$

which is computed from the observed sensor output $\mathbf{x}(t)$. Given the Hermitian conjugate, this equation is only meaningful if the recorded time series $\mathbf{x}(t)$ is complex, which is not the case as the imaginary part is not an observable in the natural world. To correct for this ambiguity, one has the choice to either compute the analytical signal via the Hilbert transform and stay in the time domain, or perform a Fourier transform and switch to the frequency domain. The time domain is chosen here for simplicity, hence the analytical signal of $\mathbf{x}(t)$ needs to be computed.

The output power of the array is obtained by forming a linear combination of the weighted sensor outputs

$$y(t) = \sum_{l=1}^{K} w_l^* x_l(t) = \mathbf{w}^H\mathbf{x}(t), \tag{1.9}$$

where the choice of the weight vector $\mathbf{w}$ is dependent on the beamforming algorithm. The output power then follows to give

$$P(\mathbf{w}) = \frac{1}{N}\sum_{t=1}^{N}|y(t)|^2 = \frac{1}{N}\sum_{t=1}^{N}\mathbf{w}^H\mathbf{x}(t)\mathbf{x}^H(t)\mathbf{w} = \mathbf{w}^H\hat{\mathbf{R}}\mathbf{w}. \tag{1.10}$$

In Bartlett or fk beamforming, the beam power is maximized with

$$\max_{w} \mathrm{E}\{\mathbf{w}^H \mathbf{x}(t)\mathbf{x}^H(t)\mathbf{w}\} \tag{1.11}$$

under the constrain of $|\mathbf{w}| = 1$. The solution for the weight vector is then

$$\mathbf{w}_B = \frac{\mathbf{a}(\mathbf{s},\omega)}{\sqrt{\mathbf{a}^H(\mathbf{s},\omega)\mathbf{a}(\mathbf{s},\omega)}} = \frac{\mathbf{a}(\mathbf{s},\omega)}{|\mathbf{a}(\mathbf{s},\omega)|} = \frac{\mathbf{a}(\mathbf{s},\omega)}{\sqrt{K}}, \tag{1.12}$$

and $\mathbf{a}(\mathbf{s},\omega)$ is the array steering vector and defined as a complex sinusoid between a reference $\mathbf{r}_0$ and all other station $\mathbf{r}_n$

$$\mathbf{a}(\mathbf{s},\omega) = e^{-i\omega\mathbf{s}(\mathbf{r}_n - \mathbf{r}_0)}. \tag{1.13}$$

The fk power spectrum (Bartlett beamformer) follows to

$$P_B(\mathbf{s},\omega) = \mathbf{w}_B^H \hat{\mathbf{R}} \mathbf{w}_B = \frac{\mathbf{a}^H(\mathbf{s},\omega)\hat{\mathbf{R}}\mathbf{a}(\mathbf{s},\omega)}{\mathbf{a}^H(\mathbf{s},\omega)\mathbf{a}(\mathbf{s},\omega)} = \frac{\mathbf{a}^H(\mathbf{s},\omega)\hat{\mathbf{R}}\mathbf{a}(\mathbf{s},\omega)}{K}. \tag{1.14}$$

The power output of the beamformer is only dependent on the covariance matrix $\hat{\mathbf{R}}$. For a chosen slowness vector $\mathbf{s}$ and frequency ω, the array steering vector $\mathbf{a}$ yields phase delays between all stations pairs which are compared to the phase delays present in $\hat{\mathbf{R}}$. The better the fit between phase delays, the higher the power output of the beamformer.

It should be noted, that fk beamforming is a narrowband technique, i.e. the Hilbert transformed data vector $\mathbf{x}(t)$ needs to be narrowband filtered prior the computation of the covariance matrix. If the data vector is not pre-filtered, a mix of frequencies will be present in $\hat{\mathbf{R}}$ and the resulting comparison between a monochromatic steering vector and the covariance matrix will not be accurate. The effects of frequency mixing are discussed in section 2.4.

To avoid narrowband filtering, the alternative computation via the frequency domain can be computed with the sample cross spectral density matrix $\hat{\mathbf{C}}$

$$P_B(\mathbf{s},\omega) = \frac{\mathbf{a}^H(\mathbf{s},\omega)\hat{\mathbf{C}}(\omega)\mathbf{a}(\mathbf{s},\omega)}{K}, \tag{1.15}$$

with

$$\hat{\mathbf{C}}(\omega) = \frac{1}{2\pi}\sum_t \hat{\mathbf{R}}(t)e^{-i\omega t} = \mathbf{X}(\omega)\mathbf{X}^H(\omega), \tag{1.16}$$

where $\mathbf{X}(\omega)$ is the Fourier transform of $\mathbf{x}(t)$. These two matrices are interchangeable which can be shown for the example of a complex sinusoid

$$x(t) = e^{-i(\mathbf{kr}-\omega t+\psi)} \quad \longrightarrow \quad F(x(t)) \quad \longrightarrow \quad X(\omega) = \sqrt{2\pi}e^{-i(\mathbf{kr}+\psi)}\delta(\omega-\hat{\omega}). \tag{1.17}$$

Hence the $X(\omega)$ has only a value at frequency $\omega = \hat{\omega}$. The covariance and cross spectral matrix

are calculated for two sensor outputs $x(t)$ and $y(t)$

$$\begin{aligned}\mathbf{R} &= x(t)x^H(t) & \mathbf{C}(\omega) &= X(\omega)X^H(\omega)\\ &= e^{-i(\mathbf{k}\mathbf{r}_1-\omega t+\psi)-i(\mathbf{k}\mathbf{r}_2-\omega t+\psi)} & &= 2\pi e^{-i(\mathbf{k}\mathbf{r}_1+\psi)-i(\mathbf{k}\mathbf{r}_2+\psi)}\delta(\omega-\hat{\omega})^2\\ &= e^{-i\mathbf{k}(\mathbf{r}_1-\mathbf{r}_2)} & &= 2\pi e^{-i\mathbf{k}(\mathbf{r}_1-\mathbf{r}_2)}\delta(\omega-\hat{\omega})^2\\ &= e^{-i\omega\mathbf{s}(\mathbf{r}_1-\mathbf{r}_2)} & &= 2\pi e^{-i\omega\mathbf{s}(\mathbf{r}_1-\mathbf{r}_2)}\delta(\omega-\hat{\omega})^2.\end{aligned} \tag{1.18}$$

Only for $\omega=\hat{\omega}$ do the two representations display the same phase delay for the station distance of $\mathbf{r}_1-\mathbf{r}_2$ apart from the normalization factor of 2π. Given that $x(t)$ and $y(t)$ are subject to narrowband filtering one should add an identical delta function to the time domain case and hence the two representations are interchangeable.

Apart from these two representations, one can employ a sensor array normalization which yields a modified cross spectral density matrix (Capon, 1969; Haubrich and McCamy, 1969)

$$\hat{C}_{nm}(\omega)=\frac{X_n(\omega)X_m^H(\omega)}{\sqrt{|X_n(\omega)|\,|X_m(\omega)|}}, \tag{1.19}$$

also known as coherence. The advantage of such normalization is the removal of improper sensor equalization effects (Capon, 1969). Hence harmonic signals which are not recorded by the station pair *nm* are weakened. A disadvantage of this method is the removal of power from the diagonal elements, which means that the resulting power spectrum does not represent the true signal strength but a relative normalized power.

1.2.4 Imprint of the array

Ideally one wants to localise all signals arriving at the array and obtain accurate estimates of the power, velocity and azimuth. Given that the array is composed of a finite number of sensors, measurements of the wavefield are only available for a finite number of discrete locations. The resolution capabilities of an array can be illustrated through the array response to an impinging signal, also known as the array response function. In a synthetic test, all sensors are excited in phase, i.e. simulating a signal with a vertical raypath. The array response function (ARF) is given as

$$P_{ARF}(\mathbf{s},\omega)=\mathbf{w}_B^H(\mathbf{s},\omega)\mathbf{w}_B(0,\omega)\mathbf{w}_B^H(0,\omega)\mathbf{w}_B(\mathbf{s},\omega). \tag{1.20}$$

The term $\mathbf{w}_B(0,\omega)\mathbf{w}_B^H(0,\omega)$ excites all sensors simultaneously and gives a covariance matrix filled with 1's as there is no phase delay and all exponential functions result in the value 1. To illustrate the resolution capabilities of an array, 4 different arrays are displayed in Fig. 1.5(a-d) and their respective ARF's in Fig. 1.5(e-h). Each of the 4 arrays shows a different ARF due to the spatial station configuration. The maximum is located in the center of the figure at 0 slowness, hence an infinite apparent velocity as all sensors are excited simultaneously, and is called the beam main lobe. Apart from the main lobe, other local maxima are present in the ARF, which are called the beam side lobes. The side lobes of an array are a direct result of the finite wavefield sampling. The

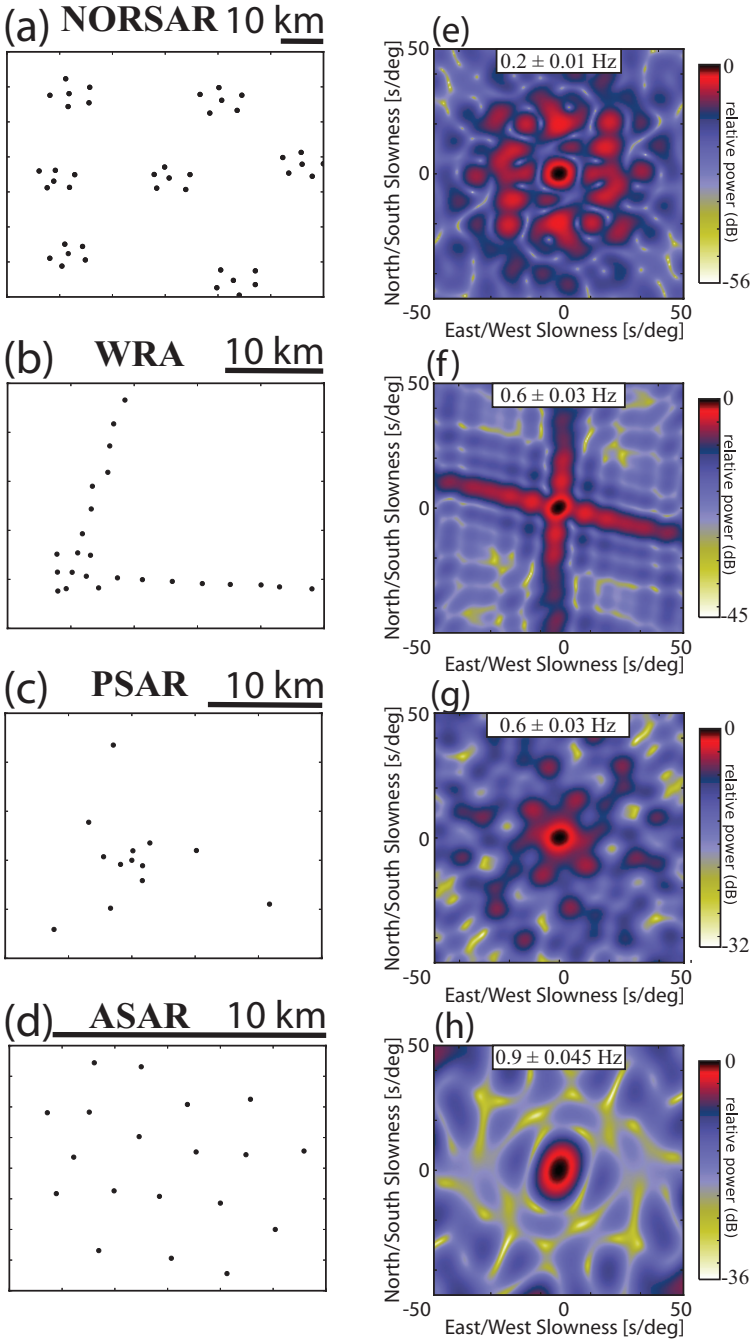

Figure 1.5: Display of 4 different seismic array configurations. NORSAR (a) located in Norway Europa, (b) Warramunga Array - WRA located in northern Australia, (c) Pilbara Array - PSAR located in north-west Australia and (d) Alice Springs Array - ASAR located in central Australia. Above each array configuration figure, a scale of 10 km distance is displayed. The corresponding ARF's are shown in the second column for each array on a 50 by 50 s/deg slowness grid with 0.5 s/deg resolution. The power is normalized to the maximal value and displayed in decibel, i.e. $10\log_{10}(P_{ARF})$. The frequency at which the ARF's are computed is displayed in each subfigure.

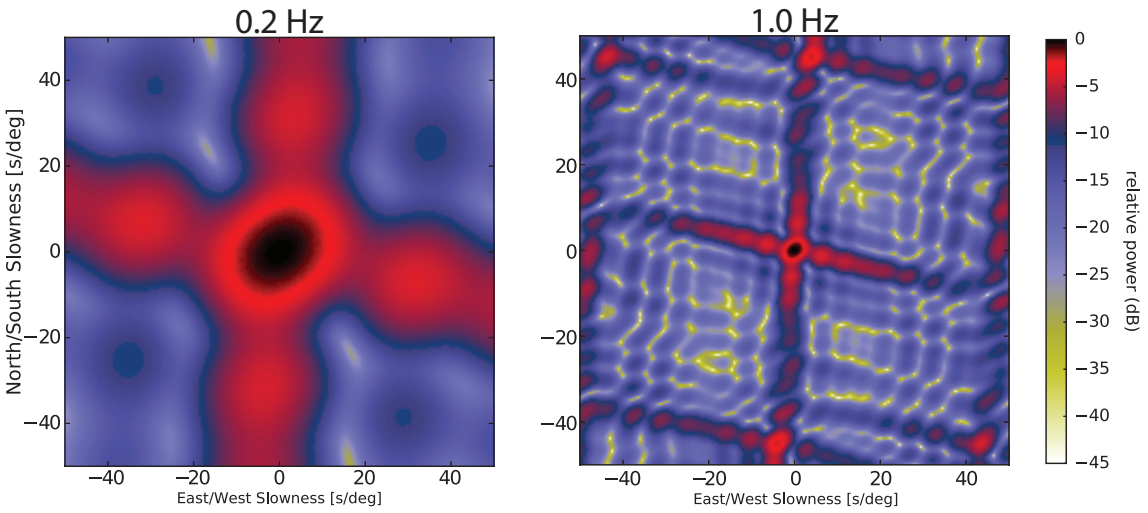

Figure 1.6: The ARF for the Warramunga Array for two frequencies, (a) 0.2 Hz and (b) 1.0 Hz. Resolution decreases for lower frequencies, while aliasing occurs for high frequencies.

beam power is computed as the cross-correlation between the phase delays of a synthetic plane wave and the phase delays of the real signal. The main lobe is positioned at the slowness position of highest correlation. Slowness vectors which show similar phase delays appear as side lobes in the power spectrum, i.e. the array assigns power to slowness vectors other than the real signal. Alternatively the array response function can be simplified to

$$P_{ARF}(\mathbf{s},\omega) = \left|\mathbf{w}_B^H(\mathbf{s},\omega)\mathbf{w}_B(0,\omega)\right|^2, \tag{1.21}$$

which is equivalent to the representations in Kelly (1967); Rost and Thomas (2002), and shows the cross-correlations of the array steering vector with the steering vector of the signal.

The width of the beam main lobe displays the resolution capabilities of the array at frequency ω. With decreasing frequency the width of the beam main lobe increases, i.e. the resolution of the array decreases. This can be understood by the fact that by decreasing the frequency the period of the signal increases. Ideally, the frequency of observation should allow multiple wave lengths of the signal to fit within the aperture of the array to obtain a good estimation of phase shifts. By decreasing the frequency, less periods of the signal fit within the array, hence the propagation characteristics is less constrained and resolution decreases. This property is illustrated in Fig. 1.6 for the Warramunga Array (WRA) for two differing frequencies. In fact, Fig. 1.6a is a magnified version of Fig. 1.6b and follows directly from the relationship of wavelength between velocity and frequency. In general, for higher frequencies the resolution of the array increases. However, if the frequency is too high, aliasing will occur and the presence of side lobes increases.

The ARF is unique for every array configuration and can be viewed as an elementary function of the array. One important property of the ARF is its shift invariance in slowness space. Hence a signal with an arbitrary slowness vector $\tilde{\mathbf{s}}$ will have the same ARF only shifted in slowness space so that the main lobe appears at $\tilde{\mathbf{s}}$. The fk power spectrum is essentially a superposition of ARF's

and can be written for P sources as

$$P_B(\mathbf{s},\omega) = \mathbf{w}_B^H(\mathbf{s},\omega)\hat{\mathbf{R}}_P\mathbf{w}_B(\mathbf{s},\omega) = \mathbf{w}_B^H(\mathbf{s},\omega)\left[\sum_{i=1}^{P}\mathbf{w}_B(\tilde{\mathbf{s}}_i,\omega)\mathbf{w}_B^H(\tilde{\mathbf{s}}_i,\omega)\right]\mathbf{w}_B(\mathbf{s},\omega). \tag{1.22}$$

The ARF becomes more important in the case of multiple sources, as the superposition of side lobes created by different sources can create large local maxima in the power spectrum. These local maxima, also called ghost or artefact sources, can appear at locations in the slowness plane where no 'true' source is present and discrimination between true and artefact signals is not trivial.

The 4 array configurations shown in Fig. 1.5 display different characteristics. NORSAR (Fig. 1.5a) is comprised of 42 stations that are divided into 7 sub arrays with 6 stations each. The distance between sub arrays is up to 50km, while within a sub array the interstation distance is small $\sim 3-10$km. This configuration enables the array to observe a broad range of frequencies, as the sub array perform well at high frequencies, while the aperture of the whole array gives good resolution at low frequencies. The drawback of this type of configuration are the relatively large side lobes.

For WRA (Fig. 1.5b), the array configuration is made of 2 station arms, which have a strong impact on the ARF and results in 4 side lobe arms. For PSAR and ASAR (Fig. 1.5c,d), the ARF shows relatively little side lobes, hence these arrays are better suited for an omni-directional wavefield estimation in the case of multiple sources.

1.2.5 Data adaptive beamforming (Capon)

In the case of fk beamforming, the power spectrum depends only on the interstation phase delay and the array configuration. Even in the case of a noise free data record, the beam side lobe contributions are not be mitigated. In order to incorporate the data information itself to enhance the power output of the array, new weights $\mathbf{w}$ are required. Capon (1969) designed a the minimum variance distortionless response (MVDR) beamformer to suppress noise contribution from all directions apart from the look direction which is set to maintain a constant gain. The weights for the Capon beamformer can be derived from the following minimization problem (for a normalized steering vector $\mathbf{a}$)

$$\begin{aligned} &\min \mathbf{w}^H\mathbf{R}\mathbf{w} \\ &\text{s.t.} \quad \mathbf{w}^H\mathbf{a}(\mathbf{s},\omega) = 1. \end{aligned} \tag{1.23}$$

Hence the output power is minimized under the constrained of loss less power contribution from $\mathbf{a}(\mathbf{s},\omega)$. The minimization can be solved using the Lagrangian multiplier method

$$\mathcal{L} = \mathbf{w}^H\mathbf{R}\mathbf{w} + \Lambda(\mathbf{w}^H\mathbf{a} - 1) = \mathbf{w}^H\mathbf{R}\mathbf{w} + \Lambda(\mathbf{a}^H\mathbf{w} - 1). \tag{1.24}$$

By solving

$$\frac{\partial\mathcal{L}}{\partial\mathbf{w}} = 0, \tag{1.25}$$

one obtains

$$\begin{aligned} \mathbf{w}^H\mathbf{R} &= -\Lambda\mathbf{a}^H \\ \mathbf{R}^H\mathbf{w} &= -\Lambda^*\mathbf{a} \\ \mathbf{w} &= -\mathbf{R}^{-1}\mathbf{a}\Lambda^*. \end{aligned} \tag{1.26}$$

By inserting the condition from eq. 1.23 and reordering, one obtains the expression for the Lagrangian parameter

$$\Lambda^* = -\frac{1}{\mathbf{a}^H\mathbf{R}^{-1}\mathbf{a}}, \tag{1.27}$$

which leads to the weight vector for the Capon beamformer

$$\mathbf{w}_{Capon} = \frac{\mathbf{R}^{-1}\mathbf{a}}{\mathbf{a}^H\mathbf{R}^{-1}\mathbf{a}}. \tag{1.28}$$

The Capon beamformer is then

$$P_{Capon} = \mathbf{w}_{Capon}^H\mathbf{R}\mathbf{w}_{Capon} = \frac{1}{\mathbf{a}^H\mathbf{R}^{-1}\mathbf{a}}, \tag{1.29}$$

and can be viewed as a sharp bandpass spatial filter (Krim and Viberg, 1996).

Given that the Capon beamformer accounts for the wavefield structure, its resolution outperforms the conventional fk beamformer as the sidelobe contributions are reduced. However, it was demonstrated that the performance of the Capon beamformer degrades in the case of low SNR and in the case where wavefront distortion occurs (Seligson, 1970), i.e. the violation of the plane wave assumption. In this case, the Capon beamformer can have worse performance than the conventional fk beamformer (Seligson, 1970).

Given that P_{Capon} is computed by means of the sample covariance matrix $\hat{\mathbf{R}}$, the existence of the inverse matrix needs to be ensured. Capon (1969) proposed the addition of a small noise term to the diagonal elements of the covariance matrix to ensure the existence of the inverse. Alternative approaches to solving this problem are smoothing procedures or diagonal loading. In the smoothing procedures, an average covariance matrix is computed by means of temporal or frequency averaging while diagonal loading adds a value to the diagonal elements of the covariance matrix. These techniques will be reviewed in more detail in chapter 2 along with examples from fk and Capon beamforming.

1.2.6 Extension from narrow to broadband

The beamforming techniques, as laid out in the previous sections, are narrowband techniques. The wavefield is examined at one frequency ω to yield the power spectrum $P(\mathbf{s},\omega)$. For signals which are distributed over a broad frequency range, as is the case for ocean induced microseisms, narrowband estimates reveal only a fraction of information present in the wavefield. The extension to broadband can be accomplished through a variety of different approaches (e.g. Wax et al., 1984; Wang and Kaveh, 1985; Kværna and Doornbos, 1986; Kværna and Ringdal, 1986; Westwood, 1992; Chiou and Bolt, 1993; Soares and Jesus, 2003) and can be divided into two groups. One

group focuses on some kind of averaging over multiple narrowband power spectra, while the second tries to modify the covariance matrix in some way to account for a broader frequency range. The optimal averaging technique was shown to be dependent on the SNR (e.g. Yoon et al., 2006). In this section, a small overview on how such extensions can be accomplished is presented.

One option is to average the cross spectral matrix over neighbouring frequencies (e.g. Koper et al., 2009)

$$\hat{\mathbf{C}}_{broadband} = \frac{1}{2n} \sum_{i=-n}^{n} \hat{\mathbf{C}}(\omega_i), \tag{1.30}$$

for some n neighbouring frequencies. The advantage of this procedure is the fast computational execution as there is little effort involved in order to obtain a broadband spectrum. Another advantage is the averaging of the cross spectral matrix, which gives a more robust estimate of the phase shifts between stations, and results in better performance of the beamformer. In the case of Capon beamforming, this averaging increases the likelyhood of the existence of the inverse matrix as the rank of the matrix is increased due to the averaging process. The disadvantages of this method are the decrease in the coherence of signals (Menon et al., 2014) and the presence of multiple frequencies in the cross spectral matrix, which can lead to an inaccurate slowness estimation. Hence this method should be only used for a small number of neighbouring frequencies.

Another option is to calculate multiple narrowband power spectra and compute the sum or average to obtain a broadband representation (e.g Kværna and Doornbos, 1986; Westwood, 1992). The extension is straight forward as (here the sum is used)

$$P_{IAS}(\mathbf{s}) = \sum_i P(\mathbf{s}, \omega_i). \tag{1.31}$$

The acronym IAS stand for incoherently averaged signal, as one computes multiple independent narrowband power spectra.

The advantage of this method is that it can be applied over a broad range of frequencies and in general the effects of the ARF can average out, given that the ARF for different frequencies is of different scale. Another advantage arises due to the nature of narrowband calculations. Lets assume two signals are present in the wavefield, one with ω_1 and the other with $\omega_2 = \omega_1 + \Delta\omega$. It is assumed that the Fourier transform can separate these signals in frequency domain, and their phase information is not mixed in the cross spectral density matrix. Hence the signals can be analysed without any interference between each other. While the fk beamformer does not benefit from this, as it is a superposition of ARF's, the spatial filter employed by Capon beamforming will show stronger suppression of sidelobes with less signals present and result in an increased resolution. A disadvantage of the IAS extension is the increased computational burden, as multiple narrowband spectra need to be computed. This method can suffer from robustness issues in case where the covariance / cross spectral density matrix is not well structured (low rank or poorly phase delays).

The last class of extensions introduced here, are the coherently averaged signal extensions (CAS). This class of extensions focuses on the modification of the covariance / cross spectral density matrix to account for a broad frequency range (e.g. Chiou and Bolt, 1993). In general, such a matrix can be found only as an approximation for a limited number of signals. For the analysis of microseisms, where such constrains are usually violated, another coherent approach

which uses coherent processing is presented.

For a frequency ω_k that differs from the projection frequency ω_0, one defines the matrix $\mathbf{T}$ as the transformation between the two array steering vectors at frequencies ω_0, ω_k

$$\mathbf{T}(\mathbf{s}, \omega_0, \omega_k)\mathbf{a}(\mathbf{s}, \omega_k) = \mathbf{a}(\mathbf{s}, \omega_0) \tag{1.32}$$

with

$$a_n(\mathbf{s}, \omega_0) = \exp[-i\mathbf{s}\mathbf{r}_n\omega_0], \tag{1.33}$$

where the subscript n denotes the n-th station of the seismic array and a_n denotes the steering vector. The transformation is then

$$\mathbf{T}(\mathbf{s}, \omega_0, \omega_k) = \begin{pmatrix} \exp[-i\mathbf{s}\mathbf{r}_1(\omega_k - \omega_0)] & 0 & \dots & 0 \\ 0 & \exp[-i\mathbf{s}\mathbf{r}_2(\omega_k - \omega_0)] & \dots & 0 \\ \vdots & \vdots & \ddots & \vdots \\ 0 & \dots & & \exp[-i\mathbf{s}\mathbf{r}_n(\omega_k - \omega_0)] \end{pmatrix} \tag{1.34}$$

The phase information in the cross-power spectral density $\mathbf{C}$ is focused onto a specific slowness $\mathbf{s}$ and frequency ω_k and can be used to obtain the slowness and frequency focused cross-powers spectral density

$$\mathbf{C}_{CAS}(\mathbf{s}, \omega_0) = \mathbf{T}(\mathbf{s}, \omega_0, \omega_k)\mathbf{C}(\omega_k)\mathbf{T}^H(\mathbf{s}, \omega_0, \omega_k). \tag{1.35}$$

In the case of $\omega_0 = \omega_k$ the matrix $\mathbf{T}$ will be the identity matrix and phase information is preserved. For $\omega_0 \neq \omega_k$ the cross-power spectral density is modified to coherently compute the phase delays at the frequency ω_0. The slowness spectrum for a conventional frequency-wavenumber approach is then given as

$$P_B(\mathbf{s}) = \mathbf{a}^H(\mathbf{s}, \omega_0)\mathbf{C}_{CAS}(\mathbf{s}, \omega_0)\mathbf{a}(\mathbf{s}, \omega_0) = \mathbf{a}^H(\mathbf{s}, \omega_k)\mathbf{C}(\omega_k)\mathbf{a}(\mathbf{s}, \omega_k). \tag{1.36}$$

Hence every contribution from a frequency other than ω_0 is modified by the appropriate phase delay. The focused cross-power spectral density matrix is now slowness dependent, and has to be recalculated for every slowness vector to achieve coherent phase summation.

This is an improved version of the frequency smoothing approach presented in eq. 1.30 as it can account for a wide range of frequencies, with the compromise that the computational time is greater. The coherent approach performs very well for low SNR while the incoherent approach is preferential for high SNR (Yoon et al., 2006). Care needs to be taken when phase velocities change with varying frequency. Here it is assumed that the velocity over the extended frequency range remains constant. In the case of a velocity change, the power spectrum will be smeared in slowness.

1.2.7 Three component beamforming

In three component plane wave beamforming, the same approximations and constrains are employed as in the one component case. The extension to three components can be implemented in

many ways, and in general the approaches can be classified into two groups. The first group rotates the coordinate system of the horizontal components into the look direction to separate radial and transverse signals (e.g. Haubrich and McCamy, 1969; Kværna and Doornbos, 1986; Nishida et al., 2008a; Poggi and Fäh, 2010; Gibbons et al., 2011; Behr et al., 2013) and applies single component beamforming on each component separately, while he second group makes uses of all three component simultaneously (e.g. Esmersoy et al., 1985; Wagner and Owens, 1996; Wagner, 1997; Miron et al., 2005; Riahi et al., 2013).

In this section, a brief overview into these two groups of extensions is given. The first group rotates the horizontal sensor outputs into the look direction θ

$$\begin{aligned} \mathbf{x}_R(t,\theta) &= \mathbf{x}_N(t)\cos\theta + \mathbf{x}_E(t)\sin\theta \\ \mathbf{x}_T(t,\theta) &= -\mathbf{x}_N(t)\sin\theta + \mathbf{x}_E(t)\cos\theta, \end{aligned} \tag{1.37}$$

where the subscripts N,E,R and T refer to the north, east, radial and transverse component. The rotated records are then Fourier transformed and used to calculate the radial and transverse cross spectral matrix

$$\begin{aligned} \hat{\mathbf{C}}_R(\omega,\theta) &= \mathbf{X}_R(\omega,\theta)\mathbf{X}_R^H(\omega,\theta) \\ \hat{\mathbf{C}}_T(\omega,\theta) &= \mathbf{X}_T(\omega,\theta)\mathbf{X}_T^H(\omega,\theta). \end{aligned} \tag{1.38}$$

The power spectrum for each component is then computed with the previously described single component plane wave beamforming methods, e.g.

$$\begin{aligned} P_{B,R}(\mathbf{s},\omega) &= \frac{\mathbf{a}^H(\mathbf{s},\omega)\hat{\mathbf{C}}_R(\omega,\theta)\mathbf{a}(\mathbf{s},\omega)}{K} \\ P_{B,T}(\mathbf{s},\omega) &= \frac{\mathbf{a}^H(\mathbf{s},\omega)\hat{\mathbf{C}}_T(\omega,\theta)\mathbf{a}(\mathbf{s},\omega)}{K}. \end{aligned} \tag{1.39}$$

The advantage of this method is its simplicity as single component methods and their extensions to broadband can be applied. A disadvantage is the intrinsic separation of the sensor data (eg. 1.37), which is easily biased by wavefront bending. Wavefront bending of only 5.7°, will result in a 10% signal leakage from the perpendicular polarized component, which will remain unnoticed as there is little power degradation in such case. Hence a mixing of radial and transverse energy occurs with little deviation from the assumed signal model.

The second group of extensions uses all three components simultaneously to obtain a power representation of the wavefield. The method of Esmersoy et al. (1985); Riahi et al. (2013) extends the Fourier transformed data vector to

$$\mathbf{X}_{3C}(\omega) = [X_{E,1}(\omega),\ldots,X_{E,K}(\omega),X_{N,1}(\omega),\ldots,X_{N,K}(\omega),X_{Z,1}(\omega),\ldots,X_{Z,K}(\omega)], \tag{1.40}$$

where X_{nm} denotes the amplitude and phase information of the n-th component and m-th station. The order of the components, here ENZ, is interchangeable, but is required to be consistent for the successive calculations. The cross spectral density matrix in 3C is defined as

$$\hat{\mathbf{C}}_{3C}(\omega) = \mathbf{X}_{3C}(\omega)\mathbf{X}_{3C}^H(\omega) \tag{1.41}$$

and is a $3K \times 3K$ matrix. In contrast to the single component case, the 3C cross spectral matrix is not a Hermitian matrix, which can be seen in the following representation (dependence on ω is omitted)

$$\hat{\mathbf{C}}_{3C} = \begin{bmatrix} \hat{\mathbf{C}}_{EE} & \hat{\mathbf{C}}_{EN} & \hat{\mathbf{C}}_{EZ} \\ \hat{\mathbf{C}}_{NE} & \hat{\mathbf{C}}_{NN} & \hat{\mathbf{C}}_{NZ} \\ \hat{\mathbf{C}}_{ZE} & \hat{\mathbf{C}}_{ZN} & \hat{\mathbf{C}}_{ZZ}, \end{bmatrix} \tag{1.42}$$

where the subscript denotes the components contributing to each sub-matrix. The 3 sub-matrices in the diagonal are Hermitian while the 6 off diagonal ones are not.

The idea behind the bemformer outlined by Esmersoy et al. (1985) is to project the 3C cross spectral matrix onto discrete polarization states $\mathbf{c}(\xi)$. The power of the 3C beamformer for a normalized steering vector $\mathbf{a}(\mathbf{s},\omega)$ is given as

$$P_{3C}(\mathbf{s},\omega,\xi) = \left(\mathbf{a}^H(\mathbf{s},\omega) \otimes \mathbf{c}^H(\xi)\right) \hat{\mathbf{C}}_{3C}(\omega) \left(\mathbf{c}(\xi) \otimes \mathbf{a}(\mathbf{s},\omega)\right), \tag{1.43}$$

where $\otimes$ denotes the Kronecker product and $\mathbf{c}(\xi) = [c_E(\xi), c_N(\xi), c_Z(\xi)]^T$ is the complex polarization state (Samson, 1983) with the polarization parameter ξ. It is easy to see, that by setting $\mathbf{c} = [0,0,1]^T$, the 3C beamformer collapses into its 1C form for the vertical component. This approach uses all stations and evaluates the power of a plane wave propagating with the polarization state $\mathbf{c}(\xi)$ over the array.

Another approach to treat the 3C cross spectral matrix and to obtain the power spectrum was given by Wagner and Owens (1996). In this case, a steering matrix is defined

$$\mathbf{e}(\mathbf{s},\omega) = [\mathbf{a}_E(\mathbf{s},\omega), \mathbf{a}_N(\mathbf{s},\omega), \mathbf{a}_Z(\mathbf{s},\omega)], \tag{1.44}$$

where the orthogonal $3K \times 3$ steering matrix $\mathbf{e}(\mathbf{k})$ is of the form

$$\mathbf{e}(\mathbf{s},\omega) = \begin{bmatrix} a_{E1} & \dots & a_{EK} & 0 & \dots & 0 & 0 & \dots & 0 \\ 0 & \dots & 0 & a_{N1} & \dots & a_{NK} & 0 & \dots & 0 \\ 0 & \dots & 0 & 0 & \dots & 0 & a_{Z1} & \dots & a_{ZK}. \end{bmatrix}^T \tag{1.45}$$

The steering matrix is then used to obtain the 3×3 polarization covariance matrix

$$\mathbf{Y}_{3C}(\mathbf{s},\omega) = \mathbf{e}^H(\mathbf{s},\omega)\hat{\mathbf{C}}(\omega)\mathbf{e}(\mathbf{s},\omega). \tag{1.46}$$

In contrast to the previous case, all polarization states are present in $\mathbf{Y}(\mathbf{s},\omega)$ under the assumption of plane wave propagation between all array stations. Hence the polarization covariance matrix can be viewed as the sum of all signals that propagate over the array as plane waves with a coherent polarization. To obtain the power spectrum, single station polarization techniques are used (e.g. Vidale, 1986). The polarization covariance matrix is decomposed into eigenvectors $\mathbf{u}$ and eigenvalues λ

$$\mathbf{Y}_{3C}(\mathbf{s},\omega) = \mathbf{u}(\mathbf{s},\omega)\lambda(\mathbf{s},\omega)\mathbf{u}^H(\mathbf{s},\omega), \tag{1.47}$$

which form the power spectrum

$$P_{3C}(\mathbf{s},\omega) = \sum_{i=0}^{2} \lambda_i(\mathbf{s},\omega). \tag{1.48}$$

The principal component analysis (PCA) estimates the polarization states of $\mathbf{Y}_{3C}$ (e.g. Samson, 1983; Wagner and Owens, 1996), where the eigenvalues estimate the power of each polarization state. In the case of $\lambda_0 \gg \lambda_{1,2}$, all polarized energy can be represented by a single polarized state, i.e. a pure state. The associated eigenvector $\mathbf{u}_0(\mathbf{s},\omega)$ carries the amplitude and phase information ψ of each component

$$\mathbf{u}_0(\mathbf{s},\omega) = [\psi_E, \psi_N, \psi_Z]^T \tag{1.49}$$

that fully describes the polarization state of the estimated signal. Note that the order of the components equals to the chosen order in the data vector, see eq. 1.40. The amplitude of each component (here shown for the case of a pure state) is

$$\begin{bmatrix} \mathcal{A}_E \\ \mathcal{A}_N \\ \mathcal{A}_Z \end{bmatrix} = |\mathbf{u}_0(\mathbf{s},\omega)| = \begin{bmatrix} |\psi_E| \\ |\psi_N| \\ |\psi_Z| \end{bmatrix} \tag{1.50}$$

and the power of each component is given as

$$\begin{bmatrix} P_E \\ P_N \\ P_Z \end{bmatrix} = \begin{bmatrix} \mathcal{A}_E^2 \\ \mathcal{A}_N^2 \\ \mathcal{A}_Z^2 \end{bmatrix} \lambda_0. \tag{1.51}$$

The power representation can be rotated into the radial and transverse component via a 2D rotation $\tilde{\mathbf{M}}$ of the phase informations $\psi_{R,T} = \tilde{\mathbf{M}}\psi_{N,E}$ with

$$\tilde{\mathbf{M}} = \begin{bmatrix} \cos\alpha & \sin\alpha \\ -\sin\alpha & \cos\alpha \end{bmatrix}, \tag{1.52}$$

where α denotes the angle between north and radial component. If mixed polarization states are present, the eigenvectors of λ_1 and λ_2 will parametrize these states.

Other promising extensions to 3 component array beamforming are for example the tensor formulation (e.g. Miron et al., 2005) and the quaternion algebra (e.g. Miron et al., 2006).

1.3 Thesis aims and structure

To date, the majority of microseisms studies carried out with beamforming analysis make use of the most basic algorithm, the frequency wavenumber beamforming. The robustness and simplicity of fk beamforming make it a appealing approach for estimating the ambient noise wavefield, but it is subject to limited resolution. Hence fk beamforming as implemented to date can be used to estimate only the strongest signals within the wavefield. When the interest is only the strongest

source in the wavefield, little benefit is gained by using higher resolution beamformers as the estimation of the strongest signal between fk and Capon beamforming is comparable (e.g. Koper et al., 2010). The true benefit of higher resolution beamforming approaches becomes evident when weaker or multiple sources are of interest, as the array response is more strongly suppressed. In the case of conventional fk beamforming, weak sources can be overshadowed by strong sources and remain undetected.

Ideally, one is interested in removing the effect of the ARF completely, which would allow accurate estimation of the directional energy present in the wavefield. A potential way of removing the ARF is to use deconvolution to remove the array pattern from the power spectrum. Such techniques have been popular in other fields of research, such as Astronomy (e.g. Richardson, 1972; Lucy, 1974; Högbom, 1974), and acoustic beamforming (e.g. Dougherty and Stoker, 1998; Wang et al., 2004; Brooks and Humphreys, 2006b,a; Sijtsma, 2007; Yardibi et al., 2008). To date, no use has been made of deconvolution to improve beamforming power spectra with the sole exception of Nishida et al. (2008a), who implemented the Richardson-Lucy deconvolution to reduce beam sidelobe contributions.

The aim of this thesis, is to design aand implement beamforming framework tailored to the optimal processing of the microseismic wavefield for the purpose of extracting novel information from the ambient noise wavefield.

The thesis is structured as follows:

- Chapter 1: Introduction
  The introduction chapter is divided into two parts. In the first part, the focus is to familiarize the reader with the properties of the microseismic wavefield and the conventional ways of observing/analyzing it. The microseisms spectrum and the processes that drive the generation of ambient noise vibration, the distribution of energy varying with frequency, seasonal patterns and regional and global differences in the observed wavefield are discussed. The commonly used methods to observe the wavefield are summarized. In the second part of this chapter, the focus is directed at array beamforming techniques which are utilised to study microseisms. The signal model, which is used to describe the wavefield, is introduced followed by the fk and Capon beamformer. Multiple ways to extend narrowband beamforming to broadband are discussed and an introduction to three component beamforming is given.

- Chapter 2: Optimal Beamforming Framework for the Analysis of Microseisms
  Given the existing beamforming methods, a framework is developed to for an optimal analysis of microseisms. The goal is to accurately estimate multiple arrivals from a variety of directions simultaneously. Procedures such as tapering, averaging over frequency and time, the use of the coherence matrix, diagonal loading for the Capon beamformer and how these procedures affect the beamforming result are discussed. The framework is tested on multiple arrays to display its performances under different conditions. As this paper was published (relatively) early in the PhD candidature, the notation used in this chapter follows the notation used by Capon (1969).

- Chapter 3: Implementation of Deconvolution Enhanced Beamforming

To analyse weak energy present in the microseisms wavefield, it is necessary to remove the beam sidelobe contribution from strong sources. One promising option is the process of deconvolution, where the the wavefield is decomposed into its most fundamental contributions. An overview of potential deconvolution techniques that can be used to remove the ARF from the power estimates and hence decompose the power spectrum into its most fundamental components is given. The specific focus is the CLEAN algorithm (Schmidt, 1986) developed in radio astronomy, which iteratively removes the ARF to reduce sidelobe contributions. The performance of this algorithm in combination with fk and Capon beamforming is analysed and an extension to three component array beamforming is presented. Capabilities of the novel algorithm are compared to the conventional beamformers on multiple arrays for single and three component arrays.

- Chapter 4: Long duration ambient study of the Southern Oceans
  In this chapter, the short-period microseisms wavefield over a two decade time span is investigated. Of interest is the temporal variability of the microseisms wavefield, which is directly linked to the ocean wave climate and storm patterns. With an array study over the course of 2 decades, the changes in the generation location of microseisms are studied. The study is performed with the single component Warramunga Array located in North Australia which was originally deployed for nuclear explosion monitoring. The IAS-Capon method introduced in chapter 2 is used, which extracts multiple arrivals estimated from each 1 hour beamforming result. The frequency dependence, temporal variability and locations of generations are studied over the course of 1991-2012.

- Chapter 5: Full Wavefield decomposition by means of deconvolution enhance beamforming
  The full short period microseismic wavefield is decomposed into its separable energy contributions by means of the CLEAN-3C (chapter 3). For this task, the Pilbara Array located in north west of Australia is used. The array is composed of 13 three component stations arranged in a spiral shape, which is ideal for a omnidirectional microseismic wavefield estimation. One year (2013) is analysed with CLEAN-3C and decomposed into its elementary energy contributions. The study focuses on surface waves, and estimates the mean power of Rayleigh, Love and L_g waves for the period of the full year. Generation locations, dependence on frequency and backazimuth of each surface phase and potential generation mechanisms of Love waves are discussed.

- Chapter 6: Presents an overall discussion and synthesis of main findings.

- Chapter 7: Summary.

Chapter 2

Improved implementation of the fk and Capon methods for array analysis of seismic noise

Published in Geophysical Journal International, year 2014, vol. 198, no. 2, pp 1045-1054 (This paper uses the original Capon notation (Capon, 1969) in contrast from prescending and subsequent chapters)

2.1 Abstract

The frequency-wavenumber (fk) and Capon methods are widely used in seismic array studies of background or ambient noise to infer the backazimuth and slowness of microseismic sources. We present an implementation of these techniques for the analysis of microseisms (0.05 - 2 Hz) which draws on array signal processing literature from a range of disciplines. The presented techniques avoid frequency mixing in the cross-power spectral density and therefore yield an accurate slowness vector estimation of the incoming seismic waves. Using synthetic data, we show explicitly how the frequency averaged broadband approach can result in a slowness-shifted spectrum. The presented implementation performs the slowness estimations individually for each frequency bin and sums the resulting slowness spectra over a specific frequency range. This may be termed an Incoherently Averaged Signal, or IAS, approach. We further modify the method through diagonal loading to ensure a robust solution. The synthetic data show good agreement between the analytically derived and inferred error in slowness. Results for real (observed) data are compared between the approximate and IAS methods for two different seismic arrays. The IAS method results in the improved resolution of features, particularly for the Capon spectrum, and enables, for instance, Rg and Lg arrivals from similar backazimuths to be separated in the case of real data.

2.2 Introduction

In recent years the study of the ambient seismic noise band from 0.05 to 2 Hz has attracted significant interest. Ambient noise provides a continuous record which may be used in both seismic source and Earth structure investigations (Cessaro, 1994; Friedrich et al., 1998; Shapiro and Campillo, 2004; Gerstoft et al., 2006; Chevrot et al., 2007; Bensen et al., 2008; Gerstoft et al.,

2008; Harmon et al., 2010; Landès et al., 2010; Köhler et al., 2011; Tkalčić et al., 2012). In addition, ambient noise generated by ocean storms can be used to infer their location and possible climate-related trends in storm severity (Bromirski et al., 1999; Essen et al., 1999; Grevemeyer et al., 2000; Bromirski and Duennebier, 2002; Essen, 2003; Stutzmann et al., 2009; Aster et al., 2010; Hillers et al., 2012).

The ambient seismic vibrations in the given frequency band are also known as microseisms. Their generation mechanism was first proposed to be linked with onshore swell (Wiechert, 1904). We now divide microseisms into two groups: primary and secondary. Primary microseisms have an amplitude peak at around 0.07 Hz and are caused by the interaction between ocean waves and coastal geometry (Haubrich et al., 1963). Secondary microseisms have an amplitude peak at around 0.14 Hz and are generated by the interaction of two opposing wave trains with approximately the same absolute value of the wave vector k (Longuet-Higgins, 1950). The microseism spectrum mainly consists of fundamental mode Rayleigh waves below a frequency of around 0.14 Hz, while body and surface waves are observed for higher frequencies (Lacoss et al., 1969).

Seismic array analysis has been driven throughout its history by both earthquake research and nuclear explosion detection (Schweitzer et al., 2002; Rost and Thomas, 2009). The lack of an impulsive onset for microseisms limits the capability of networks of single element stations in the determination of source backazimuth and slowness, hence, array analysis promises to contribute greatly to the study of the microseisms as it enables source backazimuth and slowness to be estimated. Initial studies located microseism sources via triangulation between several arrays, each having moderate spatial resolution (Cessaro, 1994; Friedrich et al., 1998; Essen, 2003). More recent studies have been able to improve the source localisation (Schulte-Pelkum et al., 2004; Chevrot et al., 2007; Koper et al., 2009; Behr et al., 2013) and show that secondary microseisms generated near coastal locations remain stable over longer periods. The stationarity of the signal was exploited to perform cross correlations between interarray stations in order to generate surface wave travel times and extract structural information at the array location (Gerstoft et al., 2006; Bensen et al., 2008; Li et al., 2010; Köhler et al., 2011; Young et al., 2011). Studies of body waves generated by deep ocean storms confirm the location of wave generation to be near observed active storms (Gerstoft et al., 2008; Kedar et al., 2008; Landès et al., 2010). A numerical perspective on their generation is given by Ardhuin et al. (2011).

Methods used to estimate the slowness and backazimuth of wave sources arriving at seismic arrays are reviewed by Rost and Thomas (2002). A popular method for the analysis of seismic ambient noise is the modified frequency-wavenumber algorithm proposed by Capon (1969) which has high resolution capability but is limited to the estimation of narrowband signals. Kværna and Doornbos (1986) proposed that the slowness spectra be averaged over a specific frequency range. It was further shown by Kværna and Ringdal (1986) that this broadband extension improves the stability of the estimated spectrum. This approach is well suited for the study of ambient noise as a broadband analysis is desirable.

In underwater sound processing, great detail has been devoted to the study of broadband signals with matched-field processing (Bucker, 1976; Baggeroer et al., 1993), which is a generalization of the conventional plane wave beamformer. The two main approaches for the extension of narrowband beamformers to broadband are the coherent and incoherent averaged signal methods.

While these extensions vary slightly between conventional beamforming, matched-field processing and subspace-based estimators, the central idea remains the same. The incoherently averaged signal (IAS) method in conventional beamforming (Kværna and Doornbos, 1986), matched-field processing (Baggeroer et al., 1993) and subspace-based estimators (Wax et al., 1984), averages over the narrowband direction of arrival spectra from each frequency bin to form a final result. For coherently averaged signal methods the spectrum is combined and focused on a single frequency prior to the slowness projection procedure. In the underwater sound literature, coherent averaging has been discussed in the context of matched-field processing (Westwood, 1992) and compared to the incoherent approach (Soares and Jesus, 2003). Coherent subspace-based methods (Wang and Kaveh, 1985; Chiou and Bolt, 1993) combine contributions from different frequencies. The application of standard narrowband techniques is then enabled by forming a modified cross-power spectral density matrix using a focusing matrix to project the narrowband estimates onto a single frequency (the focusing frequency). A disadvantage of this method emerges for multiple signals as an ideal focusing matrix does not always exist and approximations are needed. Other approaches for the estimation of broadband sources have been discussed by Krim and Viberg (1996).

The incoherent averaged signal method is well suited for the analysis of ambient noise as source locations are a function of frequency and a coherent averaging would be prone to smearing for closely spaced arrivals. In this work we re-examine the frequency averaged (approximate) approach for synthetic and observed ambient noise data and compare the performance to the incoherently averaged signal or IAS method which we present in an implementation tailored for the analysis of ambient noise. The IAS method uses a summation of narrowband spectra, which prevents the introduction of errors into the slowness estimation. We also implement diagonal loading for the IAS Capon method as it was found to increase robustness for narrowband solutions (Capon, 1969; Featherstone et al., 1997) by loading the diagonal elements of a singular or near singular cross-power spectral density with a constant factor to reduce the bias on the direction of arrival estimation.

In Section 2, we outline a definition of the frequency-wavenumber spectrum. In Section 3 we show why frequency smoothing will result in a shifted slowness estimation in the power spectrum and outline the IAS method which results in a correct representation. Further, we briefly review the concept of diagonal loading which promises to be a very useful approach in the stabilisation of the IAS Capon method. Synthetic and real (observed) ambient seismic data examples are given in Section 4 followed by a discussion of considerations that must be made in implementing the IAS method.

2.3 The frequency-wavenumber spectrum

The microseismic wavefield can be considered as a superposition of traveling waves generated by distant sources. At any spatial point of the field, a spectral representation can be calculated to construct the cross-power spectral density, which holds information on the mean-square values of the seismic wave amplitudes. Thus the cross-power spectral density can be used to estimate the backazimuths and slowness of these seismic waves.

Following the notation used by Capon (1969), the covariance matrix of the ambient noise for a station output at position j, with zero mean, is given by

$$\rho_{jl}(m-n) = E\left\{N_{jm}N_{ln}^{*}\right\}, \tag{2.1}$$

where E denotes the expectation value, (j,l) denote the station location and (m,n) correspond to the time element of a discrete-time parameter random process N. The cross-power spectral density is then

$$f_{jl}(\lambda) = \sum_{m=-\infty}^{\infty} \rho_{jl}(m)e^{im\lambda} \tag{2.2}$$

with $\lambda = 2\pi\tilde{f}T$ denoting the normalised frequency, $\tilde{f}$ is the frequency in Hz and T is the sampling period. For locally stationary arrays we can write

$$f(\lambda,\vec{r}) = f_{jl}(\lambda) \tag{2.3}$$

$$\rho(m,\vec{r}) = \rho_{jl}(m), \tag{2.4}$$

where $\vec{r} = \vec{x}_j - \vec{x}_l$ denotes the inter station spacings.
The frequency-wavenumber spectrum can then be defined as

$$P(\lambda,\vec{k}) = \sum_{m=-\infty}^{\infty} \int_{-\infty}^{\infty}\int_{-\infty}^{\infty} \rho(m,\vec{r})e^{i(m\lambda+\vec{k}\cdot\vec{r})}dr_x dr_y = \int_{-\infty}^{\infty}\int_{-\infty}^{\infty} f(\lambda,\vec{r})e^{i\vec{k}\cdot\vec{r}}dr_x dr_y. \tag{2.5}$$

For a monochromatic wave with unity amplitude we can write

$$f(\lambda,\vec{r}) = e^{-i\vec{k}_0\vec{r}}\delta(\lambda-\lambda_0), \tag{2.6}$$

where λ_0 denotes the normalised monochromatic frequency and substituting eq. (2.6) into eq. (2.5) yields

$$P(\lambda,\vec{k}) = \int_{-\infty}^{\infty}\int_{-\infty}^{\infty} e^{i(\vec{k}-\vec{k}_0)\cdot\vec{r}}\delta(\lambda-\lambda_0)dr_x dr_y = \delta(\lambda-\lambda_0,\vec{k}-\vec{k}_0), \tag{2.7}$$

which is a delta function for a specific frequency ω_0 and wave vector $\vec{k}_0$. It should be noted that the assumption of a monochromatic frequency constrains the position of the delta function in the spectrum.

2.4 Application to array noise

In some previous array-based studies of microseisms, researchers inferred slowness using an approximate method that averaged spectra over a narrow range of frequencies before projection on to the slowness grid (Koper et al., 2009). The cross-power spectral density of the frequency averaged method is then given as

$$\hat{f}(\vec{r}) = \int_{\lambda_1}^{\lambda_2} f(\vec{r},\lambda)d\lambda. \tag{2.8}$$

The matrix $\hat{f}(\vec{r})$ is therefore a spectral average of a specific frequency range between λ_1 and λ_2. While this process provides stability, as one includes phase information from additional frequency components, it induces scaling factors in the slowness $\vec{s}$ during the projection onto the array steering vector (Capon (1969), eq. 18). To illustrate the impact of a frequency averaged cross-power spectral density $\hat{f}(\vec{r})$, we substitute eq.(2.8) into eq. (2.5) for the example of a monochromatic wave and obtain

$$(2\pi)^{-1}P(\vec{k}) = \int_{-\infty}^{\infty}\int_{-\infty}^{\infty} e^{i(\vec{k}-\vec{k}_0)\cdot\vec{r}}dr_x dr_y = \delta(\vec{k}-\vec{k}_0). \tag{2.9}$$

Since $\vec{k} = \vec{s}\omega$, the equation $\vec{s}\omega = \vec{s}_0\omega_0$ must hold. It is therefore evident that we obtain the correct slowness $\vec{s}$ only if the frequency on which we project equals ω_0. In the case $\omega \neq \omega_0$ a scaling factor for the slowness is introduced into the slowness spectrum by the constraint of the delta function. Assuming we project on the frequency $\tilde{\omega} = \omega_0 + \Delta\omega$, an error is introduced to the observed slowness which scales linearly with the difference in frequency

$$\vec{s}_0 = \frac{\tilde{\omega}}{\omega_0}\vec{s}. \tag{2.10}$$

As a result, each frequency component of the cross-power spectral density which differs from the projection frequency will be shifted in the resulting slowness spectrum according to eq. (2.10). This approximate approach is significantly faster than other coherent (Wang and Kaveh, 1985; Westwood, 1992) or incoherent (Kværna and Doornbos, 1986; Baggeroer et al., 1988; Booth et al., 2000) broadband approaches and is therefore useful for processing very large datasets where the slowness shift is not significant.

With IAS, the slowness estimation is performed individually for each frequency bin and the resulting slowness spectra are summed over a specific frequency range. This prevents frequency mixing and therefore the incorrect estimation of slowness vectors. The cross-power spectral density of the IAS method is

$$P(\vec{s}) = \sum_{j=1}^{L}\int_{-\infty}^{\infty}\int_{-\infty}^{\infty} f(\lambda_j,\vec{r})e^{i\omega_j\vec{s}\cdot\vec{r}}dr_x dr_y = \sum_{j=1}^{L} P(\lambda_j,\vec{s}) \tag{2.11}$$

with

$$f(\lambda_j,\vec{r}) = f(\lambda,\vec{r})\delta(\lambda-\lambda_j) \quad \text{for} \quad j = 1,2,..,L \tag{2.12}$$

where L is the number of discrete frequencies. This restriction will ensure that only frequency components equal to the projection frequency are present in the cross-power spectral density. This broadband approach can be summarized as calculating the narrowband algorithms for many frequency bins in order to yield a representation of a broader frequency range.

For the Capon method we also use diagonal loading (Capon, 1969; Featherstone et al., 1997) in our implementation to obtain more robust estimates. The key concept of diagonal loading (DL) is to add a constant factor to the diagonal elements of the covariance or cross-power spectral density which can be seen as adding spatially white noise to the data prior processing. This process will ensure the existence of an inverse cross-power spectral density and decrease the bias

in slowness estimation. The 'loaded' cross-power spectral density matrix is given as

$$f(\lambda,\vec{r},\alpha)_L = f(\lambda,\vec{r}) + \alpha I \tag{2.13}$$

where I denotes the identity matrix and α is the DL parameter which was given (Featherstone et al., 1997) as

$$\alpha \approx \frac{\mathbf{tr}(f)}{N * 10^3} \tag{2.14}$$

with $\mathbf{tr}(f)$ denoting the trace of $f(\lambda,\vec{r})$ and N denotes the number of data points.
The high resolution spectrum (Capon, 1969) is given as

$$\hat{P}(\vec{s}) = \left[\sum_{n,m=1}^{K} \hat{q}_{nm}(\lambda) \exp\left(i\omega\vec{s}\cdot(\vec{x}_n - \vec{x}_m)\right) \right]^{-1}, \tag{2.15}$$

where K denotes the number of seismic stations and $\hat{q}_{nm}(\lambda_j)$ is the inverse of the cross-power spectral density $f_{nm}(\lambda)$. The broadband IAS Capon method with diagonal loading is summed over L discrete frequencies and we obtain

$$\hat{P}_{\mathrm{IAS}}(\vec{s},\alpha) = \sum_{j=1}^{L} \left[\sum_{n,m=1}^{K} \hat{q}_{nm}(\lambda_j,\alpha)_L \exp\left(i\omega_j\vec{s}\cdot(\vec{x}_n - \vec{x}_m)\right) \right]^{-1}, \tag{2.16}$$

where $\hat{q}_{nm}(\lambda_j,\alpha)_L$ is the inverse loaded cross-power spectral density from eq. (2.13) for a frequency bin λ_j and diagonal loading parameter α.

2.5 Data examples

To illustrate the slowness error introduced by the frequency averaging of the cross-power spectral density, we first consider synthetically generated data and then examine real (observed) data. We generate seismic waves to simulate multiple seismic background sources impinging on the array from different directions. The seismic wavefield is simulated with

$$\psi(\vec{r},t) = \sum_{i=1}^{N} \cos(\omega_i(\vec{s}_i\cdot\vec{r}_i - t) + \phi_i) \tag{2.17}$$

for N sources, random phase shift ϕ_i and amplitude of unity. We add white noise to each seismic trace for a more realistic simulation. For a realistic appraisal of the IAS method, we choose our array station configurations to match the real inter station spacings of WRA (Warramunga Array, Australia) and ASAR (Alice Springs Array, Australia) as the aperture and station configuration for these two arrays are contrasting cases. WRA has widely spaced stations along two distinct arms whereas ASAR has closer spaced stations in an irregular arrangement (Figure S2.1). We further apply IAS Capon to real ambient seismic data from these arrays to illustrate the resolution capabilities.

For the synthetic test case, 25 randomly generated sources in a frequency range of $0.4-1.1$ Hz and a velocity distribution between $2.5-5.5$ km/s are constructed. The discretised time step

is set to 0.025 seconds and the trace length is 144000 npts in the case of WRA spacing and 0.05 seconds and 72000 npts for the ASAR spacings which amounts to a 1 hour recording with the true station parameters. For the analysis we choose a frequency range of 0.575 ± 0.115 Hz, which yields reasonable resolution capabilities for the WRA configuration taking into account the array response function and the frequency content of the microseisms background. Out of 25 sources, 13 are located in the frequency range of interest (see Table *S*2.1 for list of parameters in the supplementary material). We perform approximate fk and Capon analysis by dividing the 1 hour long seismic signal into 23 non-overlapping time segments (temporal sub-windows) in order to obtain a reasonably accurate representation of the frequency spectrum. The cross-power spectral density is calculated as an average of the 23 temporal sub-windows to increase stability and the projection frequency is set to the middle of the frequency range of interest, namely $f_p = 0.575$ Hz. To reduce frequency leakage and side lobes, all sub-windows are tapered with the Hann window function. The results for the slowness spectra obtained by the approximate method are displayed, for the fk and Capon methods, together with the true source locations, in Fig. 2.1(a,c).

We repeat the fk and Capon analysis (eq. 2.11) with the same parameters using the IAS approach which sums over all possible frequencies in the computed frequency range and in the case of Capon we also implement diagonal loading with a constant factor of $\alpha_{synth} = 10^4 \alpha$ (eq. 2.14) to stabilise the results. The minimum frequency step size is the inverse of the sub-window time length and amounts to $\Delta\tilde{f} = 6.4 \cdot 10^{-3}$ Hz. This results in a slowness spectrum that is averaged over 37 discrete frequencies ($0.46 - 0.69$ Hz). The calculated spectra for the IAS methods are displayed in Fig. 2.1(b,d). For the approximate methods we find that the Capon algorithm shows an increased resolution compared to the fk method for all sources as found in previous studies, but owing to the slowness error introduced by the frequency averaging of the cross-power spectral density, the slowness recovered is not the true slowness of the sources. The IAS methods preserves the true slowness values and reduces spectral leakage owing to the implementation of diagonal loading.

As a further illustration, we show synthetic analysis for an array which matches the response of ASAR and obtain the results in shown Fig. 2.1(e,f). For the approximate Capon method we do not find isolated peaks but a smeared spectrum, which would make analysis of real data difficult. The smearing is a direct result of the frequency smoothing, as multiple sources enter the projection procedure on a single frequency. This is related to the smaller aperture of ASAR and is discussed in a later section. The ASAR array response function in the chosen spectrum prevents an accurate estimation of sources with the approximate method. The IAS method is able to resolve the spectrum well, because sources with different frequencies do not interfere during the projection procedure. The numerical results for backazimuth, slowness and relative power for these calculations, and the difference between inferred and true values for backazimuth and velocity for each maxima are given in the supplementary material. In all four synthetic slowness spectra Fig. 2.1(c-f), an additional source around $baz = 320$ degrees is estimated, which was not generated in the frequency range of interest. This is due to frequency leakage and will be discussed in Section 5 in more detail.

We now apply the approximate and IAS methods to real data for the case of WRA (Fig. 2.2) and ASAR (Fig. 2.3) showing the results for the Capon method only. We average over 37 discrete frequency bins for all real data WRA calculations and use a diagonal loading parameter

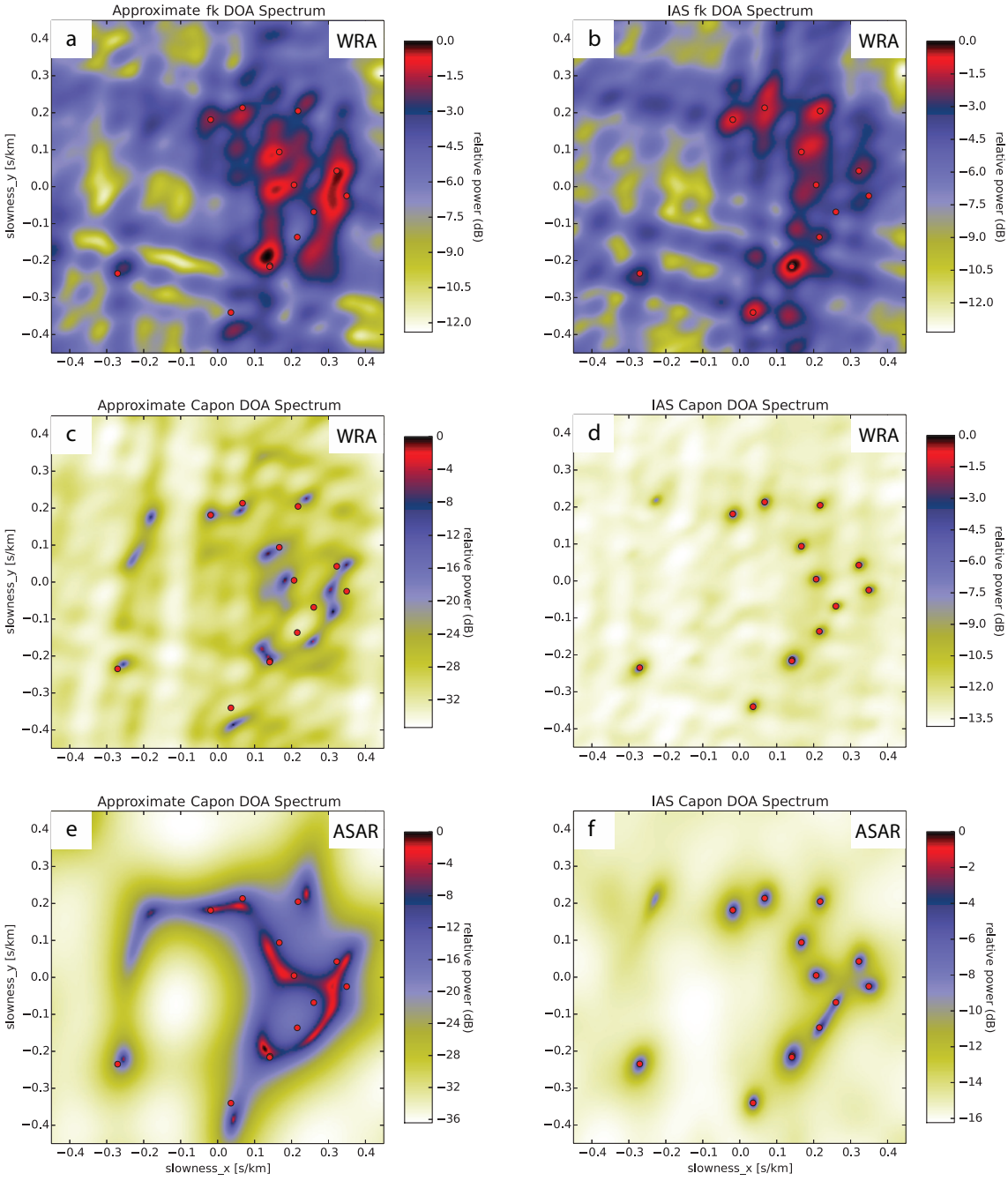

Figure 2.1: a)b) Synthetic data fk analysis with WRA inter array spacings for the approximate and IAS algorithm: c)d) Synthetic data Capon analysis for WRA and (e,f) for ASAR inter array spacings. The red circles denote the true position of the synthetic sources. In both cases the IAS method accurately corrects the slowness vector to the true values. We use the same colour scheme to highlight the estimated sources although the relative power levels are different.

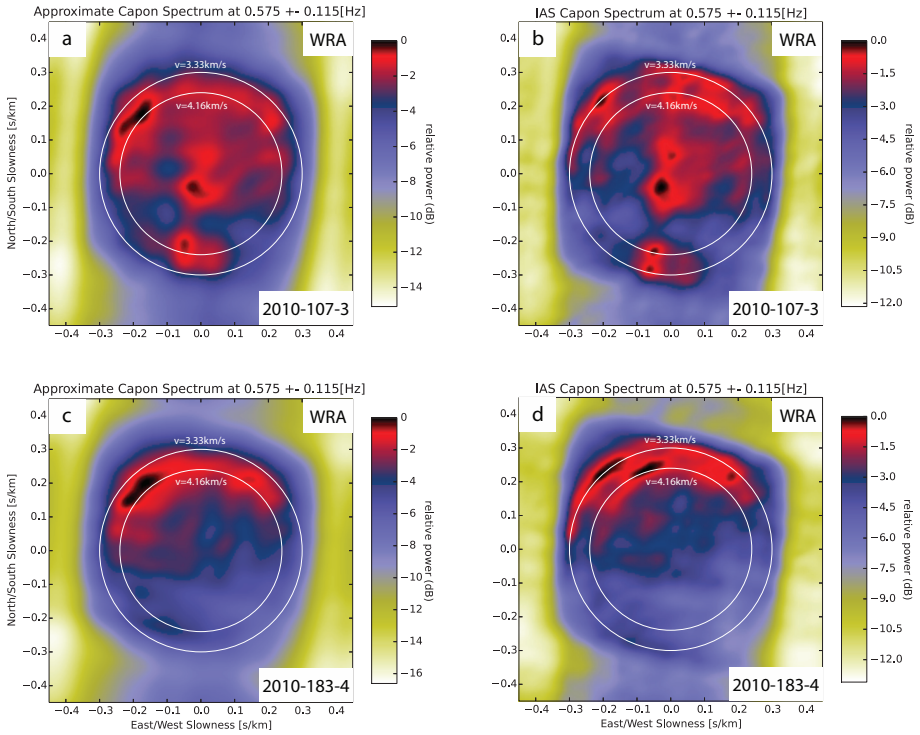

Figure 2.2: a)b) Real (observed) data comparison between the approximate Capon analysis and the IAS Capon analysis with diagonal loading for WRA. The bottom right label in each subfigure indicates the date and time of the one hour long data sample (year - Julian day - start hour , UTC); c)d) Comparison between methods for a different day and time. We observe an increase in the resolution of seismic wave arrivals which we associate with R_g and L_g waves.

of $\alpha_{real} = 10^3\alpha$. For real data, this value is an order of magnitude smaller than is required for the synthetic data owing to the greater signal content in the frequency range of interest. We display spectra from two different days to illustrate the improvement in performance using the IAS method, Fig. 2.2(a-d). In both cases we refine the observed peak showing multiple wave arrivals. The loaded IAS method finds main arrivals around $v = 3.33$ km/s and $v = 4.16$ km/s which can be associated with R_g and L_g phases [Koper et al. (2010)]. Further we observe a second body wave arrival which was not detected by the approximate approach, Fig. 2.2(b). For the second WRA example we observe another peak split into R_g and L_g phases, Fig. 2.2(d). We compute the seismic data with the same parameters for ASAR and obtain Fig. 2.3(a,b). The resolution of the approximate and loaded IAS estimates is similar in this case, except that the slowness vector associated with the R_g wave is correctly recovered by the loaded IAS method at 3.41 km/s (the approximate method gives 3.76 km/s). ASAR's resolution capabilities in the analysed frequency range are limited by the array response function due to the small inter array spacings, therefore we evaluate the data at a frequency range suitable for the ASAR configuration, Fig. 2.3(c,d). We select 34 temporal sub-windows which amounts to a window length of 105.9 seconds and average over 49 discrete frequency bins in order to extract more information from the data. The approximate method detects a body wave arrival with $v = 12.33$ km/s and a backazimuth $baz = 340.56$ degrees. The loaded IAS Capon method estimates the velocity $v = 10.9$ km/s with a backazimuth of $baz = 348.69$ degrees. It further detects R_g arrivals at a velocity $v = 3.03$ km/s that were not detected with the approximate approach.

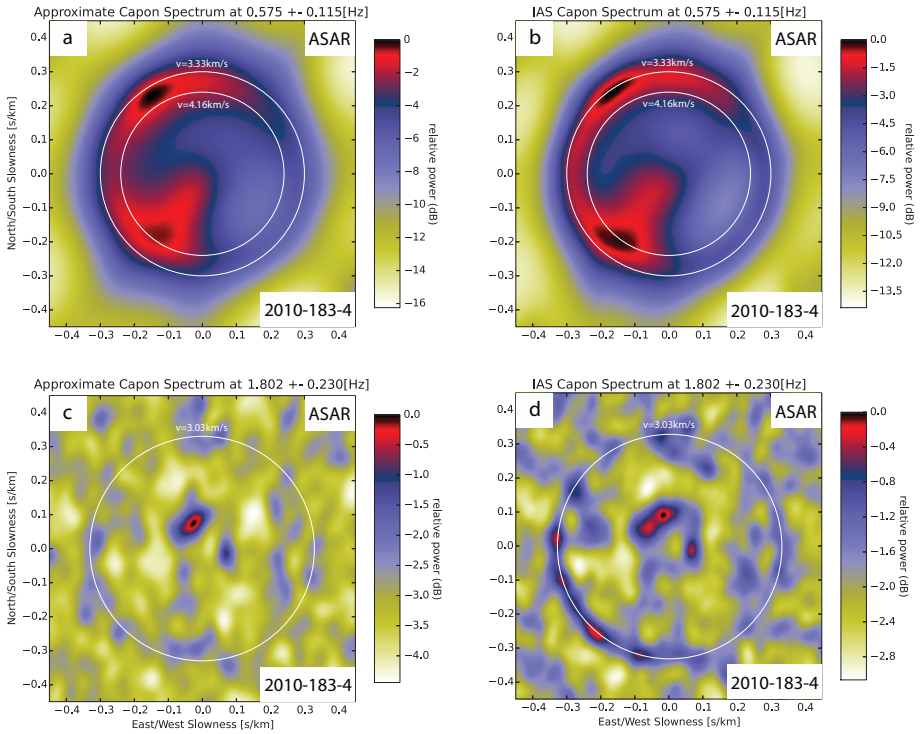

Figure 2.3: a)b) Real (observed) data comparison between methods for ASAR using the same parameters as in Fig. 2.2. c)d) Estimation for a different frequency range that is more suitable for the detection capabilities of ASAR.

In improving the understanding of ambient seismic noise (microseisms) it is desirable to determine a slowness spectrum that provides information on simultaneous sources from multiple directions. This is usually not required for earthquake or nuclear event analysis. We therefore compare the IAS Capon estimation without temporal averaging, hence a rank-1 cross-power spectral density (Kværna and Doornbos, 1986), and a temporal averaged full-rank matrix, as we propose in this implementation, Fig. 2.4(a,b). We suggest that a well structured full rank matrix reveals a more detailed slowness spectrum, and therefore highlights the main arrivals and reveals further ambient seismic phases previously undetected. Temporal averaging is therefore a useful improvement, used in the IAS implementation, with particular benefit in the analysis of seismic noise.

2.6 Discussion

The synthetic data results displayed in Fig. 2.1 and in supplementary material (Tables *S*2.2 and *S*2.3) suggest that the IAS implementation of the fk and Capon methods will be of considerable utility. In the following section we first outline the limitations of the IAS method under various parameters, then re-evaluate where the approximate approach is favourable and discuss the results obtained by the IAS method for synthetic and real data.

For the case of synthetic data, we find an increase in the background power level for IAS fk and IAS Capon compared to the approximate approaches. This can be explained by the fact that the approximate methods project on a single frequency and therefore a single array response function. For the IAS methods, we average over multiple array response functions with different frequencies

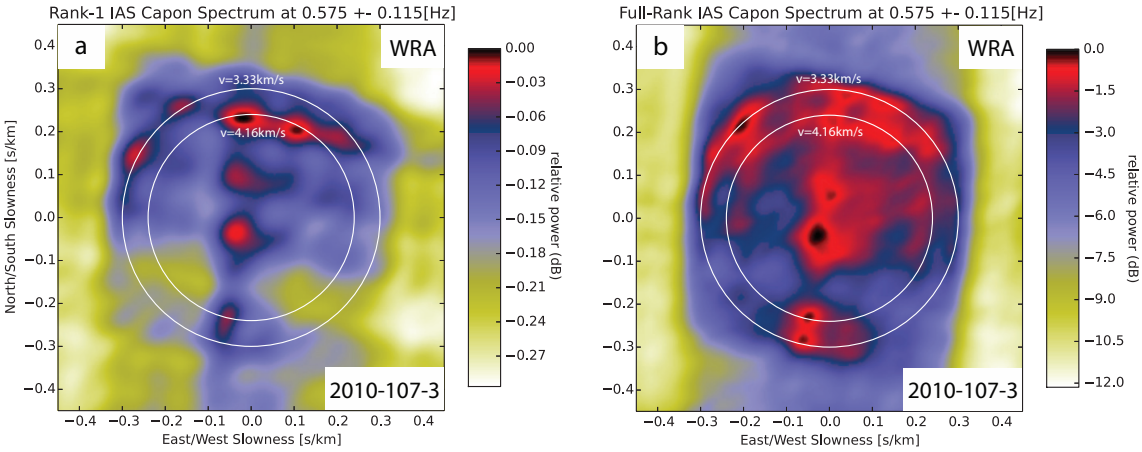

Figure 2.4: a) Real (observed) data slowness spectrum without temporal averaging (rank-1 cross-power spectral density) compared to a temporal averaged slowness spectrum b) (full-rank cross-power spectral density). The full rank approach increases the resolution of the IAS method and estimates wave arrivals in more detail. All IAS Capon spectra shown throughout this contribution (except Fig. 4a) are estimated using a full-rank matrix.

which leads, in the case of synthetic data, to a higher power spectrum background level. We find that the length of the temporal sub-windows and diagonal loading parameter in the case of IAS Capon strongly influence the accuracy of the method. For smaller temporal sub-windows the Fourier transform is less accurate and we observe frequency leakage (Fig. 2.5a, 138 temporal sub-windows), which can be seen as multiple sources with a constant backazimuth. Sources from neighbouring frequencies 'leak' into the cross-power spectral density and are estimated with an incorrect slowness vector according to eq. (2.10), which is equivalent to frequency smoothing and results in radial smearing (Woods and Lintz, 1973). It should be noted that frequency leakage is present in the approximate methods as well, but owing to the averaging over frequencies and projection onto a single frequency, the effect is suppressed. It is unclear which frequencies in the averaged frequency range contribute most to the resulting approximate power spectrum as it has been shown that strongest signals do not necessarily dominate (Gibbons et al., 2010). For this reason setting the projection frequency to the peak of the frequency range of interest might not yield the correct slowness for the main microseism sources. On the other hand, selecting short temporal sub-windows will ensure a robust backazimuth estimation of the sources as phase information are divided into small portions (amount of temporal sub-windows) and added to the cross-power spectral density. This averaging procedure of the cross-power spectral density matrix is desirable as the robustness of the Capon algorithm increases with more phase information stored in the matrix. An increase in temporal sub-window length is therefore desirable to minimise the effect of frequency leakage but will result in a less averaged cross-power spectral density and therefore less stable estimates (Fig. 2.5b, 23 temporal sub-windows). The figure displays an estimate that is corrupted by the array response pattern. The estimate is corrupted because we sum over frequency bins with low information content which falsifies the resulting averaged slowness spectrum (Wang and Kaveh, 1985). Fortunately, the microseismic background is continuous and does not display any spectral gaps, which minimises the risk of noise dominated spectra falsifying the final result.

The increase of temporal sub-window length is therefore a trade-off between spectral leakage

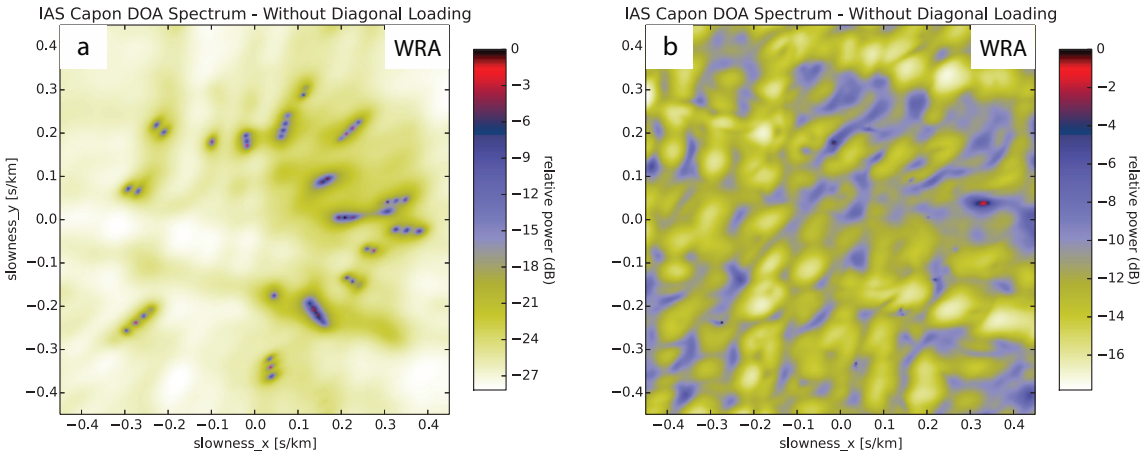

Figure 2.5: a) An example of synthetic data analysis using the IAS method with an insufficiently accurate Fourier spectrum and no diagonal loading correction. We observe frequency leakage which can be seen as source locations on constant backazimuth paths. b) Spectrum generated by frequency bins with a sufficiently accurate Fourier spectrum. In this synthetic case some bins are devoid of information which results in a noise dominated estimate. The noise influence can be reduced by diagonal loading as shown in Fig 2.1(d).

and noise contributing to the final averaged spectrum.

In our analysis we found that diagonal loading will decrease spectral leakage and reduce the error introduced by frequency bins with low SNR as can be seen in Fig. 2.5(b) where IAS Capon is displayed without diagonal loading and Fig. 2.1(d) with diagonal loading where all sources are identified with great accuracy and the noise influence is suppressed. The diagonal loading constant has to be chosen by the user in this simple model although methods that operate in the spatial domain have been developed to automate this calculation (Du et al., 2010). We have found that the influence of the DL parameter is dependent on the number of temporal sub-windows and its application is therefore important for lower frequencies as their accurate spectral representation demands longer temporal sub-windows.

The Capon method demands the existence of the inverse cross-power spectral density matrix. This criterion would not be fulfilled in the IAS Capon approach if the number of windows is less than the number of sensors as the matrix is not full rank. Diagonal loading adds a constant parameter to all diagonal elements (this can be seen as adding spatially white noise to the data prior processing) and therefore ensures the existence of the inverse even in the case of less windows than sensors. We select 22 temporal sub-windows for WRA which has 23 stations and find a strongly biased slowness spectrum (Fig. 2.6a-d, for different DL parameters). For a diagonal loading parameter of $10^1\alpha$, Fig. 2.6(a), we observe a highly localised spectrum. The arrival maxima of these highly localised spectra match well the backazimuth and slowness vector of the robust estimates. This behaviour is also observed for a smaller number of temporal sub windows, but slowness estimates coincide more with the robust estimates in the near full rank matrix case. Averaging over fewer temporal sub-windows than array sensors can therefore be used to better estimate the location of body waves although artefact arrivals may also be produced. Increasing the DL parameter will reduce the bias and we obtain a good agreement with previous calculations (Fig. 2.2b) although multiple peaks are no longer observed. We observe a performance decrease of the IAS method if the window length is further increased. This can be explained as less phase

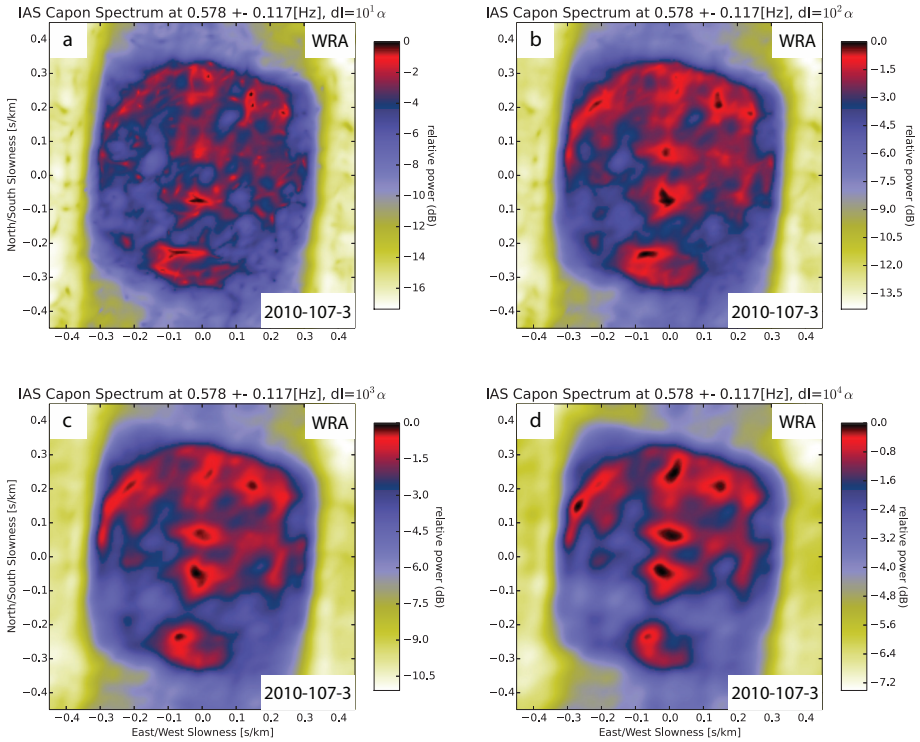

Figure 2.6: a) IAS spectra, where the number of temporal sub-windows is lower by 1 than the number of array sensors, for the case of WRA. With this setting the estimated spectrum becomes highly dependent on the diagonal loading parameter and displays highly resolved arrivals. For (b-d) the parameter is increased to induce stability into the estimations.

information being stored in the cross-power spectral density (lower rank). IAS therefore shows best performance when the number of temporal windows is equal or greater then the number of sensors.

The approximate approach remains favourable in situations with low SNR as frequency smoothing increases the robustness of the Capon method. Signals with low signal to noise ratio can still be used to calculate slowness and backazimuth, but error introduction according to eq. (2.10) should be considered. Computationally, the approximate approach outperforms IAS as the cross-power spectral density is projected only on a single frequency, while for IAS this step is performed for each frequency bin.

As an additional advantage of using IAS, we find that averaging over narrowband calculations minimises the smearing effect which is connected to the array response function (Fig. 2.1e). This results in a better resolved, more accurate estimation of the arrival maxima. In studies that were previously limited by the array response function owing to smearing effects between closely spaced sources, the frequency bounds may be extended. We have further attempted to implement leakage free frequency estimations with multi taper coherency measurements between the inter array seismic traces (Thomson, 1982; Park et al., 1987; Vernon et al., 1991; Prieto et al., 2007). These narrowband measurements may be combined in future research to yield an alternate, accurate direction of arrival estimation in a broader frequency range.

In the case of real ambient noise data we observe better resolved slownesses to the equivalent of either R_g or L_g wavespeeds, which gives us confidence that the IAS method is working as intended. This effect can be seen very well in Fig. 2.3(d) where multiple sources are detected with

a velocity equivalent to R_g waves. We have produced an open source code that implements this technique (see acknowledgments).

2.7 Conclusion

We advocate the use of an IAS implementation of the fk and Capon methods for detecting the backazimuth and slowness of seismic noise arrivals using array data. The method preserves the correct slowness by averaging over multiple narrowband spectra, instead of the frequency averaged cross-power spectral density, and minimises the effect of the array response function for closely spaced sources. In the case of the Capon method, diagonal loading is helpful in obtaining stable estimates with IAS. The analysis of real data from WRA yields a slowness spectrum which shows an improved recovery of slowness values and resolves two different wave phase arrivals (corresponding to R_g and L_g surface waves) in the short-period microseism band. For the ASAR case, the method is able to identify previously undetected surface waves and further displays increased resolution capabilities. Synthetic tests and real data examples show that the IAS method improves the accuracy of slowness estimation compared to approximate methods.

2.8 Acknowledgements

We acknowledge data access through the IRIS DMC archive. Our thanks are due to D. B. Harris, an anonymous reviewer and the editor for constructive reviews which have improved both content and readability. The research was funded by the Australian Research Council (DP110103677) and MG supported through a Tasmanian Government Research Scholarship. [Computer programs which implement the techniques are freely available and may be obtained by contacting the University of Tasmania authors].

2.9 Supplementary material

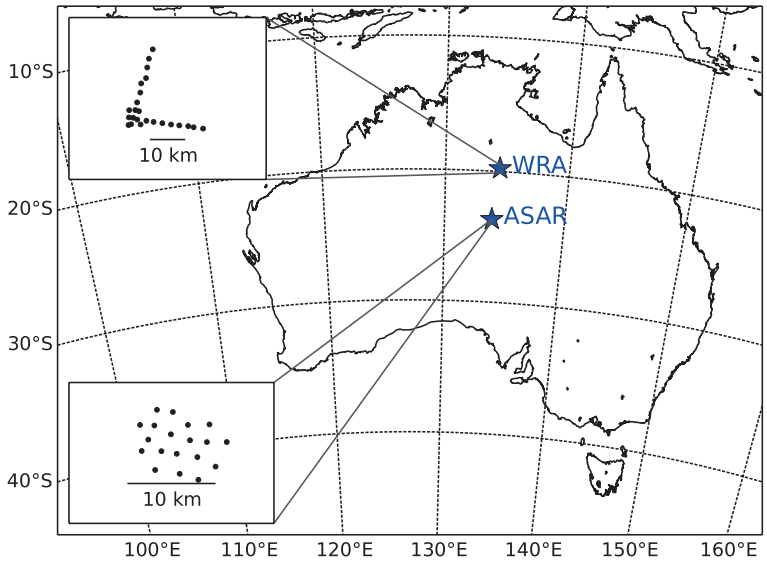

Figure S2.1: Location and shape of the Warramunga Array (WRA) and Alice Springs Array (ASAR).

Table S2.1: Synthetic sources used in testing. From 25 synthetic generated (random) sources that are distributed over a spectral range of $0.4 - 1.1$ Hz, 13 sources are in the frequency band used for the analysis ($0.46 - 0.69$ Hz). A: amplitude, Baz: backazimuth, f: frequency, v: velocity.

Synthetic Sources

Source	A	Baz[deg]	f[Hz]	v[km/s]
2	1	104.71	0.69	3.72
4	1	173.96	0.65	2.92
5	1	229.06	0.55	2.79
6	1	46.74	0.63	3.35
8	1	60.65	0.46	5.22
9	1	94.08	0.50	2.86
13	1	88.70	0.50	4.83
15	1	17.53	0.52	4.47
16	1	146.44	0.55	3.91
19	1	354.07	0.58	5.49
20	1	146.95	0.48	3.87
21	1	122.36	0.68	3.92
23	1	82.46	0.62	3.08

Table S2.2: Maxima detected using frequency-wavenumber analysis. ΔBaz and Δv denote the absolute value difference between the true and inferred source parameter of synthetic data. The proposed IAS method shows a more accurate slowness estimation and a slight increase in detection as the relative power is higher. Sources for which no maxima was found are denoted with no values '-'.

	Conventional fk					IAS fk				
Source	P_{rel} [dB]	Baz [deg]	v [km/s]	Δ Baz [deg]	Δ v [km/s]	P_{rel} [dB]	Baz [deg]	v [km/s]	Δ Baz [deg]	Δ v [km/s]
2	-	-	-	-	-	-	-	-	-	-
4	-1.93	174.09	2.54	0.13	0.38	-0.93	173.91	2.95	0.05	0.02
5	-2.34	229.32	2.96	0.26	0.17	-2.45	228.95	2.71	0.11	0.09
6	-1.88	46.67	3.05	0.07	0.30	-0.87	46.25	3.42	0.50	0.07
8	-0.56	59.30	5.98	1.35	0.75	-1.12	60.26	4.60	0.39	0.63
9	-0.42	93.27	6.34	0.81	3.49	-2.84	97.91	3.06	3.83	0.20
13	-0.24	85.24	3.08	3.46	1.76	-1.92	96.01	5.82	7.31	0.99
15	-1.31	17.20	5.06	0.33	0.59	-1.28	17.18	3.86	0.36	0.61
16	0.00	145.38	4.36	1.06	0.45	0.00	145.75	3.91	0.69	0.00
19	-1.87	353.05	5.38	1.02	0.10	-1.00	352.88	5.52	1.19	0.03
20	-3.95	146.31	1.87	0.64	2.00	-	-	-	-	-
21	-1.33	124.38	3.22	2.02	0.70	-2.44	122.01	3.93	0.36	0.01
23	-0.24	85.24	3.08	2.78	0.003	-2.07	81.43	3.01	1.03	0.06

Table S2.3: Maxima detected using loaded IAS Capon analysis of synthetic data. We observe an increased resolution compared to the fk analysis (Table S2.2) for backazimuth and slowness estimation. The proposed IAS method decreases deviations in estimated slowness values.

Source	Conventional Capon					Loaded IAS Capon				
	P_{rel} [dB]	Baz [deg]	v [km/s]	Δ Baz [deg]	Δ v [km/s]	P_{rel} [dB]	Baz [deg]	v [km/s]	Δ Baz [deg]	Δ v [km/s]
WRA inter array spacings										
2	0.00	104.62	3.12	0.09	0.60	-3.39	104.50	3.71	0.21	0.01
4	-0.23	174.03	2.57	0.06	0.35	-1.62	173.99	2.91	0.03	0.01
5	-8.50	228.74	2.93	0.31	0.14	-1.55	229.01	2.75	0.04	0.04
6	-0.74	46.67	3.05	0.07	0.30	-1.68	46.85	3.38	0.11	0.03
8	-0.86	60.46	6.45	0.19	1.23	-1.88	60.42	5.23	0.23	0.004
9	-4.08	94.27	3.31	0.19	0.45	-3.88	94.40	2.84	0.32	0.01
13	-0.78	88.57	5.56	0.13	0.72	-2.06	88.76	4.83	0.06	0.001
15	-4.70	18.03	4.92	0.50	0.45	-0.68	17.70	4.51	0.17	0.04
16	-2.94	146.31	4.11	0.13	0.21	-	-	-	-	-
19	-5.29	354.29	5.53	0.22	0.04	-0.08	354.29	5.53	0.22	0.04
20	-3.05	146.98	4.66	0.03	0.79	0.00	147.14	3.89	0.20	0.02
21	-2.93	122.28	3.30	0.09	0.62	-3.08	122.86	3.89	0.49	0.03
23	-0.73	82.60	2.86	0.14	0.21	-3.73	82.09	3.06	0.37	0.02
ASAR inter array spacings										
2	-2.03	105.61	3.15	0.90	0.57	-4.10	105.68	3.76	0.97	0.04
4	-2.53	174.03	2.57	0.06	0.35	-1.45	173.99	2.91	0.03	0.01
5	-3.82	228.74	2.93	0.31	0.14	-2.61	229.01	2.75	0.04	0.04
6	-2.33	46.67	3.05	0.07	0.30	-2.49	46.85	3.38	0.11	0.03
8	-2.38	64.18	6.46	3.53	1.23	-3.73	60.42	5.23	0.23	0.004
9	-1.64	94.15	3.21	0.06	0.36	-3.79	94.40	2.84	0.32	0.01
13	-1.98	87.06	5.70	1.63	0.86	-4.18	88.76	4.83	0.06	0.001
15	-2.32	16.82	4.95	0.71	0.48	-1.69	17.70	4.51	0.17	0.04
16	0.00	146.93	4.33	0.49	0.43	-	-	-	-	-
19	-2.80	354.29	5.53	0.22	0.04	-0.86	354.29	5.53	0.22	0.04
20	-	-	-	-	-	0.00	147.14	3.89	0.20	0.02
21	-2.40	121.11	3.28	1.26	0.64	-2.50	122.86	3.89	0.49	0.03
23	-2.11	83.25	2.91	0.79	0.17	-2.75	82.09	3.06	0.37	0.02

H

Chapter 3

Deconvolution enhanced direction of arrival estimation using one- and three-component seismic arrays applied to ocean induced microseisms

Published in Geophysical Journal International, year 2016, vol. 206, no. 1, pp 345-359

3.1 Abstract

Microseisms in the period of $2-10$ seconds are generated in deep oceans and near coastal regions. It is common for microseisms from multiple sources to arrive at the same time at a given seismometer. It is therefore desirable to be able to measure multiple slowness vectors accurately. Popular ways to estimate the direction of arrival of ocean induced microseisms are the conventional (fk) or adaptive (Capon) beamformer. These techniques give robust estimates, but are limited in their resolution capabilities and hence do not always detect all arrivals. One of the limiting factors in determining direction of arrival with seismic arrays is the array response, which can strongly influence the estimation of weaker sources. In this work, we aim to improve the resolution for weaker sources and evaluate the performance of two deconvolution algorithms, Richardson-Lucy deconvolution and a new implementation of CLEAN-PSF. The algorithms are tested with 3 arrays of different aperture (ASAR, WRA and NORSAR) using 1 month of real data each and compared with the conventional approaches. We find an improvement over conventional methods from both algorithms and the best performance with CLEAN-PSF. We then extend the CLEAN-PSF framework to 3 components and evaluate 1 year of data from the Pilbara Seismic Array (PSAR) in north-west Australia. The 3 component CLEAN-PSF analysis is capable in resolving a previously undetected *Sn* phase.

3.2 Introduction

Two processes are responsible for the generation of ocean induced microseisms in the frequency range $0.05-2$ Hz. Primary microseisms are generated by the interaction between ocean waves and

the sloping ocean floor close to the coastline (Hasselmann, 1963; Ardhuin et al., 2015). Secondary microseisms are generated by opposing ocean wave trains with slightly different wavenumber $\vec{k}$ (Longuet-Higgins, 1950). Seismic waves induced by the secondary process are observed from the deep ocean (Gerstoft et al., 2008; Euler et al., 2014; Beucler et al., 2015) as well as coastal areas (Cessaro, 1994; Essen, 2003; Schulte-Pelkum et al., 2004; Bromirski et al., 2005; Chevrot et al., 2007; Behr et al., 2013; Reading et al., 2014).

In array based microseisms studies, it is common to observe multiple wave arrivals from different backazimuths owing to the complex nature of the frequency dependent ambient noise field (Brooks et al., 2009; Koper and Hawley, 2010; Traer et al., 2012; Gal et al., 2015). This poses increased requirements on the detection techniques compared to a single source. The analysis of the wavefield may be carried out with the conventional or adaptive beamformer (Kelly, 1967; Capon, 1969) that show robust estimates but also suffer from limited resolution capabilities (Krim and Viberg, 1996; Shumway et al., 2008).

In the presence of a strong source, weaker arrivals can remain undetected or are overshadowed by the beam pattern of the strong source. A further difficulty arises if the array has a wide mainlobe or strong sidelobe, which results in a blurred power spectrum in the case of multiple wave arrivals from different backazimuths. To mitigate the effect of a blurred power spectrum, Nishida et al. (2008a) applied Richardson-Lucy (RL) deconvolution (Richardson, 1972; Lucy, 1974), which deconvolves the array response function from an image in a maximum likelihood fashion to reduce blurring. A similar approach named CLEAN (Högbom, 1974), was designed in the field of radio astronomy to remove bright objects from the measured sky brightness distribution to improve the sensitivity to weaker emission. CLEAN iteratively removes the power and beam pattern of the strongest source and replaces it with a 'clean' beam to give a sidelobe-free representation of the sky. The algorithm was adapted to acoustic beamforming as CLEAN-PSF (Sijtsma, 2007), by iteratively removing fractions of plane wave energy from the cross spectral density associated with the strongest source in the acoustic record. Hence this techniques can be applied directly to seismic array data.

The increase of publicly available 3-component (one vertical and two horizontals) single station and array data allows for the study of the full seismic wavefield. For the single station case, polarisation analysis methods are commonly used to infer the particle motion and arrival direction (Vidale, 1986; Park et al., 1987; Jurkevics, 1988; Schimmel and Gallart, 2003, 2004). In the case of ocean induced microseisms, the use of single station analysis provides a great alternative for regions with no seismic arrays (Schimmel et al., 2011; Sergeant et al., 2013; Davy et al., 2015). For 3 component array data, beamforming can be performed separately for each component by rotation of the horizontal components (Poggi and Fäh, 2010; Gibbons et al., 2011; Behr et al., 2013) or using all components simultaneously (Wagner, 1996, 1997).

The aim of this work is to increase the resolution of the power spectrum to allow detection of weaker ocean induced microseisms and enable robust direction of arrival estimation. We evaluate the performance of RL deconvolution (Richardson, 1972; Lucy, 1974) and CLEAN-PSF (Sijtsma, 2007) for 3 arrays (ASAR, WRA and NORSAR) with different apertures and compare the results with IAS Capon (Gal et al., 2014). We further extend the CLEAN-PSF algorithm to 3 component seismic data. The performance of the 3 component extension is assessed by evaluating 1 year of

data from the Pilbara Seismic Array (PSAR).

3.3 Methods

3.3.1 Conventional Beamforming

For the conventional Bartlett beamformer (Bartlett, 1948) the sample cross spectral matrix (also known as cross power spectral density) is given as

$$\mathbf{C}(f) = \frac{1}{L}\sum_{l=1}^{L} \mathbf{X}_l(f)\mathbf{X}_l^H(f) \tag{3.1}$$

where $\mathbf{X}_l(f)$ denotes the Fourier transform of the l-th snapshot (temporal subwindow) $\mathbf{x}_l(t)$, ^{H} is the conjugate transpose, f is the frequency, and L the number of snapshots. Hence the phase information for the wavefield at each seismic sensor, for a frequency f, is present in the cross spectral matrix $\mathbf{C}(f)$. The power output of the beamformer is then

$$P(\mathbf{w}) = \mathbf{w}^H\mathbf{C}(f)\mathbf{w} \tag{3.2}$$

where $\mathbf{w}$ denotes a weight vector. For the conventional Bartlett beamformer the weight vector is obtained by maximising the output power of the beamformer and it follows that

$$\mathbf{w}_B = \frac{\mathbf{a}(\mathbf{k})}{\sqrt{\mathbf{a}^H(\mathbf{k})\mathbf{a}(\mathbf{k})}} \tag{3.3}$$

with $\mathbf{a}(\mathbf{k})$ denoting the steering vector and $\mathbf{k}$ is the wave number. Inserting Eq. 3.3 into Eq. 3.2, leads to the power spectrum

$$P_B(\mathbf{k}) = \mathbf{w}_B^H(\mathbf{k})\mathbf{C}(f)\mathbf{w}_B(\mathbf{k}). \tag{3.4}$$

3.3.2 CLEAN and CLEAN-PSF Algorithms

The CLEAN algorithm in its basic form, introduced in radio astronomy by Högbom (1974), is based on the assumption that the brightness distribution of the radio sky can be represented by spatially separated point sources. The idea is to find the position and strength of point sources and iteratively deconvolve their contribution to the image, i.e. their point spread function (PSF). This iterative approach reduces the power of the 'dirty' image. Because the position and strength of the deconvolved source is known, point sources with the appropriate strength are placed into the 'clean' image. After a user specific threshold of source power was deconvolved (cleaning is stopped when the peak in the residual image reaches a level comparable with the theoretical noise), the "cleaned" image is then constructed by convolving the clean components with an ideal beam (one with the same resolution as the array PSF, but no sidelobes) and adding the residual image. This approach is very successful in removing bright point objects that overshadow sources with a

low signal to noise ratio.

Following the idea of CLEAN, the same principle of source power reduction can be introduced for conventional fk beamforming by removing the PSF (the point spread function is equivalent to array response function) from the power spectrum in a least squares optimisation (Dougherty and Stoker, 1998; Wang et al., 2004). CLEAN-PSF is an improved implementation of the conventional CLEAN that removes phase information associated with the strongest source directly from the cross spectral matrix (Sijtsma, 2007), hence mitigating edge effects for PSF's that suffer from strong sidelobes. This extension allows the use of CLEAN-PSF with adaptive beamforming, i.e. for slowness dependent PSF's. CLEAN-PSF can be formulated by removing a fraction of the dominant source power $P_{B,max}$ from the cross spectral matrix

$$\mathbf{C}_{PSF}^{i+1} = \mathbf{C}^{i} - \phi P_{B,max}^{i} \mathbf{w}_{max} \mathbf{w}_{max}^{H} \tag{3.5}$$

where ϕ is the control parameter that determines the fraction of removed power and $\mathbf{w}_{max}(\tilde{\mathbf{k}})$ is the normalised steering vector for a plane wave with a wave number $\tilde{\mathbf{k}}$ that is associated with the maximum value in the power spectrum $P_{B,max}^{i}(\tilde{\mathbf{k}})$. The idea behind removing a fraction of power is to iteratively remove sidelobe contributions associated with the strongest sources on the rest of the power spectrum. This process can be viewed as the introduction of a synthetic point source of negative power at the position of the dominant source. The choice of ϕ is in general data dependent and will be discussed on synthetic and observed data. Since the amount of removed power is known (e.g. $\phi = 0.05$ removes 5% of power from the strongest source), we can construct the CLEAN power spectrum P_{CLEAN} as

$$P_{CLEAN}(\mathbf{k}) = \sum_{i}^{M} \phi P_{B,max}^{i} \tag{3.6}$$

with M denoting the number of iterations and $\phi P_{B,max}^{i}$ is the amount of reduced power for the dominant sources at iteration i. The final spectrum P_{PSF} is then obtained by summing the CLEAN and background spectrum

$$P_{PSF}(\mathbf{k}) = \mathbf{w}_{B}^{H}(\mathbf{k}) \mathbf{C}_{PSF}^{M}(f) \mathbf{w}_{B}(\mathbf{k}) + P_{CLEAN}(\mathbf{k}), \tag{3.7}$$

where $\mathbf{C}_{PSF}^{M}(f)$ is the cross spectral matrix after M iterations. The reason for adding the background spectrum is to obtain the correct power levels as phase information may be difficult to remove for high iterations once a low signal to noise ratio is present. The extension of CLEAN-PSF to the Capon beamformer follows a similar logic and is given in appendix 3.10.1. For our calculation, we use a nested grid search to refine the position of the maximum in the slowness plane to an accuracy of $10^{-3} s/deg$. This procedure is implemented to reduce error accumulation with increasing iteration number.

3.3.3 Richardson-Lucy Algorithm

In astronomy and medical microscopy, a widely used method for the deblurring of images is the Richardson-Lucy deconvolution (Richardson, 1972; Lucy, 1974). The data model of an observed

image $I(x)$ is defined as

$$I(x) = P(x) * O(x) \tag{3.8}$$

where $P(x)$ denotes the PSF of the system, $O(x)$ is the original noise-free image, $*$ is the convolution operator and x denotes the image coordinates. Ideally one wants to obtain the original noise-free image from the observed image and a known point spread function. Richardson (1972) and Lucy (1974) adressed the reconstruction within a Bayesian framework that leads to the iterative equation

$$\hat{O}_{i+1}(x) = \hat{O}_i(x) \left[P(x)^T * \frac{I(x)}{P(x) * \hat{O}_i(x)} \right], \tag{3.9}$$

where i denotes the iteration number and $\hat{O}_0$ is the first guess for the solution. This equation was later rederived as the maximum likelihood solution under Poisson statistics (Shepp and Vardi, 1982). The equation therefore iteratively deconvolves the PSF under a maximum likelihood constraint. In this analysis, we use an implementation of RL deconvolution (Bertero and Boccacci, 2005), previously successfully applied to beamforming (Nishida et al., 2008a; Picozzi et al., 2010), that reduces Gibbs oscillations created by edge effects, allows the use of non symmetric PSF's and improves overall performance.

The implementation is given as

$$\bar{O}_{i+1}(x) = \bar{w}(x)\bar{O}_i(x) \left[\bar{P}(x)^T * \frac{\bar{I}(x)}{\bar{P}(x) * \bar{O}_i(x) + b} \right], \tag{3.10}$$

where the bar denotes objects that have been extended by zero padding. The observed image $I(x)$ with a pixel length of $J \times J$ is extended by zero padding to the dimensions $2J \times 2J$ and placed into the centre of the extended area (an example of $\bar{I}(x)$ can be found in Fig. S3.1a). The same procedure is applied to $P(x)$, see Fig. S3.1b, and $O_i(x)$. The PSF placed into the centre of $\bar{P}(x)$ can have a larger extent than J and/or a non symmetric form and is normalised to unity volume. The regularisation parameter b is the background noise level. When set, it will enforce the constrain of non-negativity upon the image. $\bar{w}(x)$ is defined as

$$\bar{w}(x) = \begin{cases} \frac{1}{\bar{\alpha}(x)} & \text{if } \bar{\alpha}(x) > \sigma \\ 0 & \text{otherwise} \end{cases} \tag{3.11}$$

with

$$\bar{\alpha}(x) = \bar{P}(x) * \bar{M}_s(x), \tag{3.12}$$

where $M_s(x)$ is a mask object of dimensions $J \times J$ filled with values equal to 1 and $\bar{M}_s(x)$ is the zero padded version. Hence, $\bar{\alpha}(x)$ is the convolution of the zero padded PSF with the mask object and describes the reach and influence of the PSF upon an image with dimensions $J \times J$. An example of both $\bar{\alpha}(x)$ and $\bar{w}(x)$ are shown in Fig. S3.1c,d. The threshold parameter σ is introduced to avoid any divisions by zero during the iterative process and was suggested to be 0.01 or smaller for astronomical applications (Bertero and Boccacci, 2005).

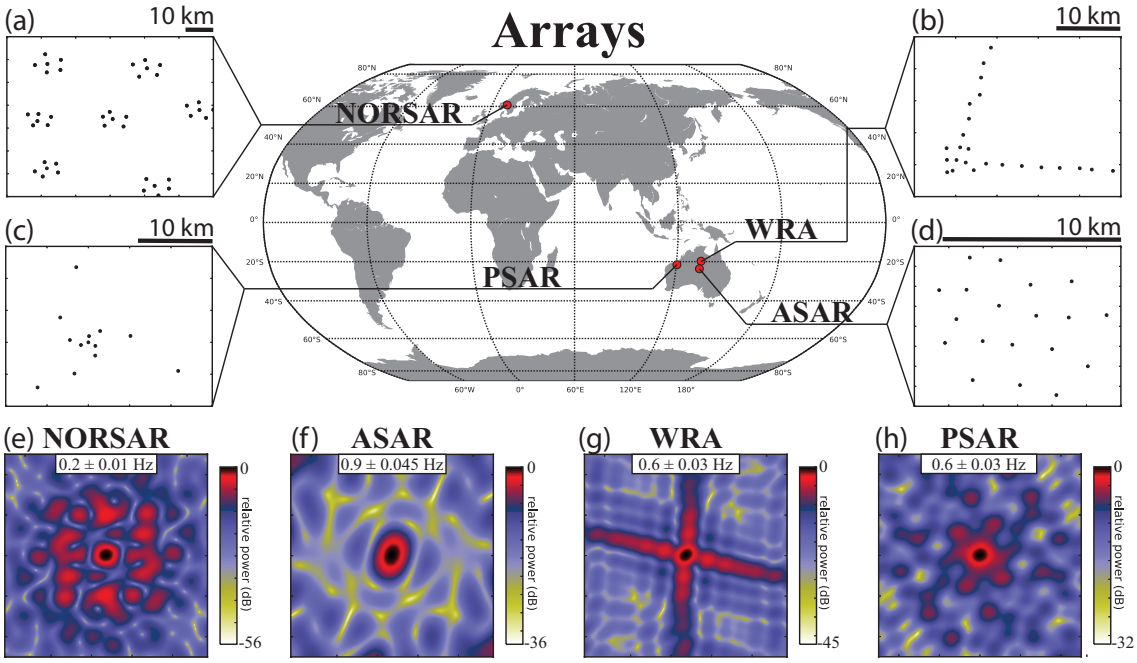

Figure 3.1: Geographical location of the arrays with their station configurations (a-d) and array response functions (e-h). A scale of 10 km above each station configuration map is displayed as reference. The array response functions are displayed on a $\pm 50 \times \pm 50\ s/deg$ slowness grid. The displayed frequencies are used during beamforming analysis of each array.

3.4 Synthetic Data

3.4.1 Point Sources

We evaluate the performance of the two deconvolution approaches using synthetic data with the array element configurations of ASAR (aperture of 10 km), WRA (26 km) and NORSAR (77 km). Array locations, shapes, array response functions and relevant frequency bands are displayed in Fig. 3.1. We generate 10 synthetic sources with a phase velocity of 3.3 km/s (simulating R_g waves) and 3 synthetic sources with a phase velocity of 4.1 km/s (L_g waves), as shown in Fig. 3.2. The slowness distribution of the synthetic sources is chosen to cover a variety of scenarios, e.g. multiple backazimuths, closely spaced sources and similar directions for R_g and L_g waves. Instead of creating synthetic seismograms and calculating the Fourier transform for each station to generate the cross spectral matrix (eq. 3.1), we introduce phase shifts with equal power directly into the synthetic cross spectral matrix

$$\mathbf{C}_{syn} = \sum_n \mathbf{w}_B(\mathbf{k}_n)\mathbf{w}_B^H(\mathbf{k}_n), \tag{3.13}$$

where n iterates over the number of sources and $\mathbf{w}_B(\mathbf{k}_n)$ denotes the normalised steering vector of the n-th source. For conventional (Bartlett) fk analysis in combination with CLEAN and RL the cross spectral matrix does not require additional processing prior to the beamforming procedure. In the case of the Capon method, we apply diagonal loading to ensure the existence of the inverse matrix (Featherstone et al., 1997). In astronomy the removed power is replaced by the main

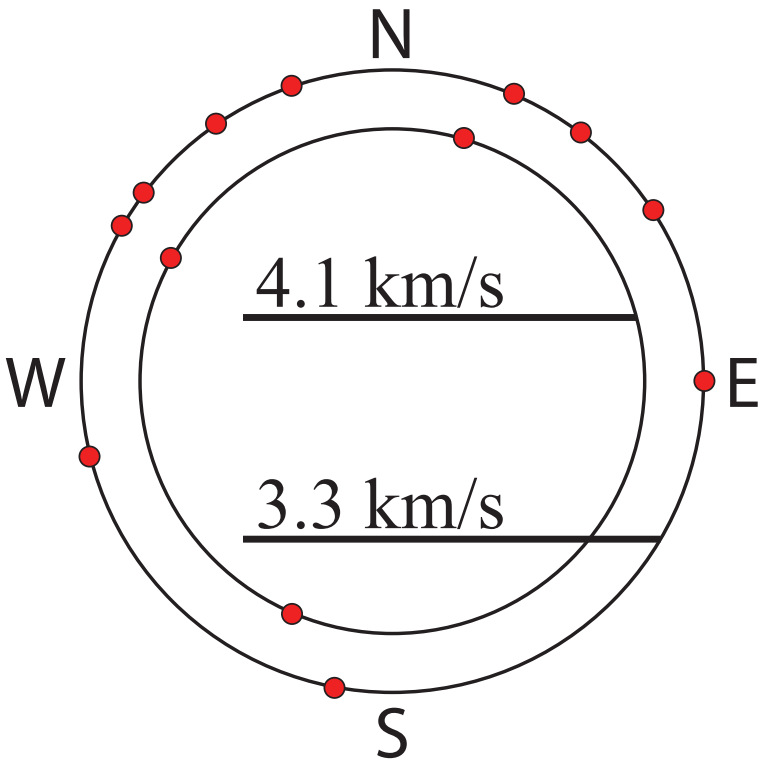

Figure 3.2: Representation of 10 synthetic sources with a velocity of 3.3 km/s and 3 synthetic sources with a velocity of 4.1 km/s in the slowness plane. All sources are generated with equal power.

lobe only. This could be done for the fk algorithm for which a main lobe is data independent. For the Capon algorithm, the main lobe is data dependent and varies in the slowness plane. We chose an arbitrary configuration, which is solely chosen for visualisation purposes and replace the removed power of sources in the CLEAN-PSF algorithm by a Gaussian kernel which occupies 7×7 grid points in the slowness plane and has no impact on the results. All other parameters used for the calculation are displayed in Table 3.1. The choice of the control parameter ϕ is selected in an accuracy vs computational cost compromise and will be discussed alongside the synthetic results. The iterations are stopped after a user defined value M, although other stopping criteria are discussed in section 3.7. For the RL control parameter σ, we have tried a variety of threshold values and found robust estimates between $0.05 < \sigma < 0.11$.

The results of the synthetic analysis are displayed in Fig. 3.3. In the case of the conventional fk analysis, we find a blurred spectrum for each of the 3 arrays. Depending on the array station geometry, and frequency band, each array shows unique resolution capabilities and shortcomings. The dense station configuration of ASAR shows good power suppression for faster arrivals (i.e. body waves), but strong blurring of surface waves due to the large beam mainlobe in the chosen frequency range (Fig. 3.1b). WRA shows strong aliasing due to its L-shaped geometry. NORSAR shows the best resolution of the 3 arrays for the surface waves. However, NORSAR with its 7 dense subarrays (Fig. 3.1a) is prone to aliasing of body waves for the selected frequency range.

In the case of CLEAN-PSF, we find a strong improvement in source localisation for all 3 arrays and the recovery of previously overshadowed sources in the original power spectrum. In

	Array	$s_l[s]$	n_w	ϕ	σ	M	stop
Synthetic Data							
Point Sources	ASAR,WRA,NORSAR	∞	1	0.1	0.09	$100_C/200_{RL}$	user defined
Extended Sources	ASAR,WRA,NORSAR	∞	1	0.1	0.09	$180_C/200_{RL}$	user defined
Observed Data							
1 Component	ASAR	100	71	0.05	0.09	$120_C/200_{RL}$	user defined
	WRA	200	35	0.05	0.09	$120_C/200_{RL}$	user defined
	NORSAR	400	17	0.05	0.09	$120_C/200_{RL}$	user defined
Earthquake excluded	ASAR	100	69	0.025	0.09	200_C200_{RL}	user defined
Earthquake included	ASAR	100	71	0.025	0.09	$250_C/200_{RL}$	user defined
3 Component	PSAR	200	35	0.1	-	60	user defined

Table 3.1: Parameters used for the analysis of synthetic and observed data. The following symbols denote: s_l snapshot length in seconds, n_w number of snapshots (windows), ϕ CLEAN control parameter, σ RL control parameter, M number of iterations where subscript $_C$ and $_{RL}$ are to be associated with the 2 deconvolution approaches and 'stop' denotes the stopping criterion for both algorithms.

general, we see a suppression of artefacts generated by beam sidelobes, especially for the case of WRA and NORSAR. For the CLEAN-PSF with conventional fk, closely spaced sources are identified as a single source due to the overlapping array response. CLEAN-PSF in combination with Capon shows very good reconstruction of the true synthetic source parameters. Only minimal errors are visible for the case of ASAR, while WRA and NORSAR show an error free spectrum. We have tested a range of ϕ values and their influence on the recovery of weaker sources. In general, a small value of $\phi < 10^{-3}$ will converge towards a unique solution but suffers from high computational cost, i.e. a high iteration number M. The optimal ϕ is dependent on the array design (number of stations and configuration), the frequency range chosen and the SNR. Arrays with a small station count and low SNR are likely to converge only for small ϕ values. For completeness, we display the convergence behaviour of CLEAN-PSF-fk for the ASAR case for different ϕ and iteration values and display which $\tilde{k}$ is removed per iteration in Fig. S3.2.

The RL deconvolution shows strong reduction of blurring and a good recovery of synthetic sources for the case of ASAR and NORSAR. For WRA, we see only minimal improvement in comparison with conventional fk. The reason for the low improvement is the PSF of WRA, which has relatively large sidelobes (Fig. 3.1g). In this specific case, better recovery can be obtained with a reflective boundary condition (Ng et al., 1999). In the conventional case periodic boundary conditions are used, while the reflective boundary acts as a mirror on the boundaries. To preserve consistency, we use the extension of Bertero and Boccacci (2005) for all further RL deconvolution calculations. It has to be noted that the RL deconvolution is strongly dependent on the number of iterations (Picozzi et al., 2010) and the optimal number to achieve the best resolution/bias compromise requires an empirical approach. In this case, where the true source location of the synthetics is known, we chose the best match between the RL and the true power spectrum (200 iterations). We do not attempt to combine Capon beamforming with the RL approach, as the Capon power spectrum is not a superposition of PSF's, hence bias of weaker sources is to be expected.

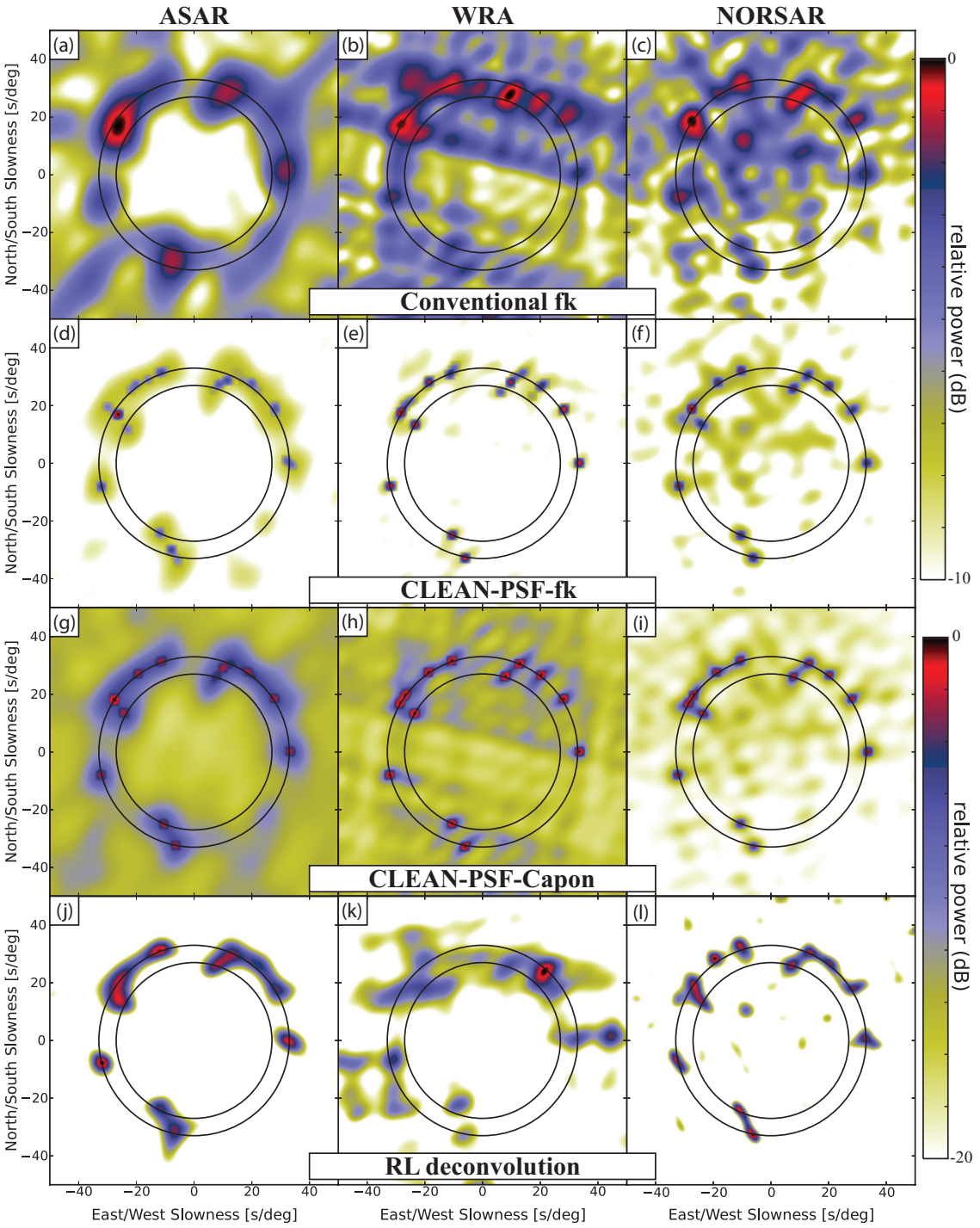

Figure 3.3: Comparison between different beamforming algorithms in the case of synthetic sources. Algorithms are displayed in rows, (a-c) Conventional fk, (d-f) CLEAN-PSF with fk, (g-i) CLEAN-PSF with Capon and (j-l) RL deconvolution. Each column shows results from a specific array. Black circles of constant velocity are displayed at the true synthetic source velocities of 3.3 and 4.1 km/s.

The above results are presented with the idealisations of noise free data and an infinite observation window. To account for noise and finite window effects, each source is constructed in the time domain with a SNR of -20 dB, a snapshot length of 200 s and the Hann window function is applied. The results are shown in Fig. S3.3 and display comparable results to the idealised case with minimal performance degradation for CLEAN-fk and RL while CLEAN-Capon suffers from the low SNR and shows worse source recovery than with the fk beamformer. Essentially, the deconvolution approaches are dependent on the performance of the underlying beamformer and are robust to noise in the study of ocean induced microseisms.

3.4.2 Extended Sources

We simulate the performance of the deconvolution methods for the case of extended sources, see Fig. 3.4a for the synthetic configuration. The results are presented for ASAR in Fig. 3.4b-d, while the results for WRA and NORSAR can be found in the supplementary material, Fig. S3.4. Both CLEAN variations tend to cluster energy from extended backazimuths to a finite group of backzimuths for ASAR. The effect of clustering varies for all 3 arrays in this study and is less pronounced for WRA and NORSAR (Fig. S3.4a,b,d,e). The clustering is dependent on the width of the mainlobe and the amount of recovered sources increases with a decreasing mainlobe width (e.g. WRA and NORSAR). The RL deconvolution shows a strong suppression of sidelobes and retains the structure of extended sources well for ASAR although little clustering is present as well. For NORSAR and WRA, Fig. S3.4c,f, the RL deconvolution is not capable of resolving the extended sources. For NORSAR, we see strong artefacts in the centre of the slowness plane, which could not be removed due to the extended area of the PSF, while WRA shows a complete incompatibility for extended sources with RL deconvolution.

In conclusion, clustering can occur for the CLEAN approaches dependent on the PSF of the array, while the RL deconvolution retains a relatively smooth power output for arrays with a gaussian PSF and shows strong performance degradation for extended (non gaussian type) PSF's. CLEAN further shows stronger resolution in the separation of closely spaced sources in the case of WRA and NORSAR, where the arrivals from the south are successfully resolved as waves with 2 distinct velocities.

3.5 Observed data

In the following section, we evaluate the performance of the two algorithms on observed ambient noise data. The difference in aperture of the 3 arrays enables observations of different frequency bands within the microseism wavefield. The frequency bands of interest are 0.2 ± 0.01 Hz (NORSAR), 0.6 ± 0.03 Hz (WRA) and 0.9 ± 0.045 Hz (ASAR). We evaluate 1 month of observed data for ASAR (January, 2010), WRA (January, 2010) and NORSAR (December, 2012).

Beamforming is performed on 1 hour data samples with conventional fk and Capon algorithms. Each one hour time series is divided into smaller 50% overlapping time windows (also known as snapshots) and tapered with the Hann window function to reduce spectral leakage. Each

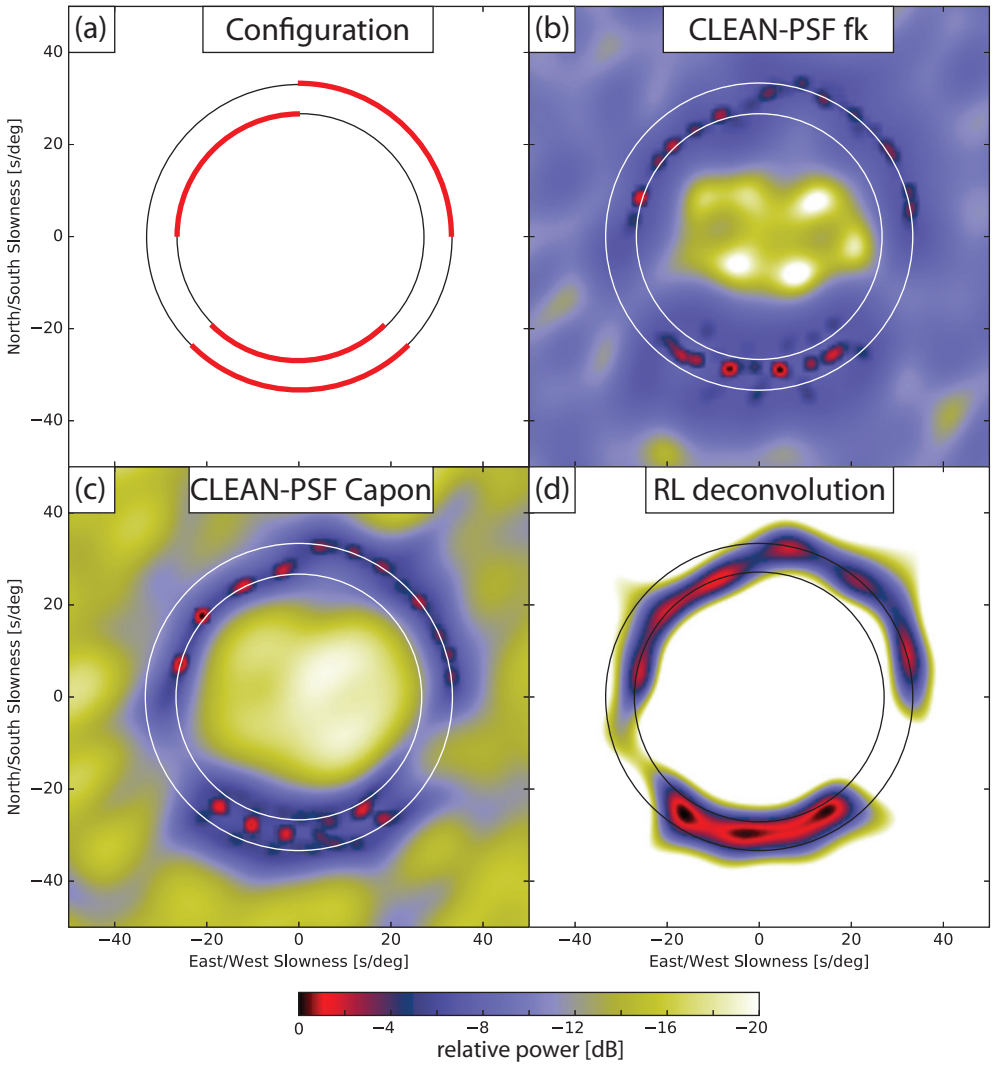

Figure 3.4: (a) Display of the synthetic configuration of extended sources. The red arcs symbolise incoming energy from extended backazimuths. The 2 black circles are placed at 3.3 and 4.1 km/s. Results for ASAR for the 3 approaches are shown in (b-d).

of these snapshots is Fourier transformed and used to construct a cross spectral matrix that is an average of the 1 hour sample. The averaging over time increases the rank of the cross spectral matrix and the robustness of the power spectrum. We additionally average over neighbouring frequencies with up to 5% width of the projection (centre) frequency. The averaging over frequency further stabilises the power spectrum and allows us to evaluate a broader frequency range. It is important to keep the width over which frequency is averaged to a small percentage of the projection frequency as increasing the width leads to incorrect phase summation in the cross spectral matrix (Menon et al., 2014; Gal et al., 2014). The main reason to apply averaging over frequency is that it gives rise to a well structured cross spectral matrix as phase information is extracted with the CLEAN algorithm. All other related parameters can be found in Table 3.1. For CLEAN we chose $\phi = 0.05$ and $M = 120$ for all arrays which removes the following amount of relative power on average: ASAR = -3.5 dB, WRA = -4 db and NORSAR = -6 dB. These values are chosen in order to be confident that the underlying beamformer is not degenerated by the SNR in the residual cross spectral matrix. For the RL deconvolution we choose the same parameters as in the synthetic case, as they seem to produce the best results for the observed data.

We compare the deconvolution approaches to IAS Capon (Gal et al., 2014) which has shown strong capabilities in estimating multiple wave arrivals from a variety of backazimuths. IAS Capon calculates multiple narrowband spectra supported by diagonal loading to increase robustness of the solution. The narrowband power spectra are combined to give a broadband representation of the wavefield. For RL deconvolution, we use 200 iterations as this seems to yield the most reliable results in this case. The results are shown in Fig. 3.5. The summary plots are a combination of 1 hour evaluations for the whole month and are constructed by only considering local maxima above a certain relative power threshold (ASAR -3.5 dB, WRA -4 dB and NORSAR -6 dB), which is free of sidelobes due to CLEAN.

For ASAR (Fig. 3.5, left column), all 4 algorithms find multiple sources with a velocity of 3.3 km/s and 1-2 sources with a velocity of 4.1 km/s with identical backazimuths. IAS Capon shows the strongest contribution of artefact arrivals, which are caused by beam sidelobes of strong sources. This is to be expected as IAS Capon was not designed to recover weaker sources accurately (Fig. 3.5a, ~ 11.2 sources per hour). CLEAN-PSF removes these artefacts in both cases of fk and Capon, while Capon shows superior suppression capabilities, consistent with the synthetic tests. The RL algorithm shows a clean spectrum, but has the downside of recovering the least sources. We observe that the RL deconvolution does not preserve the power relations between sources and weaker sources are strongly suppressed. Lowering the power threshold for ASAR below -3 dB shows an increase in weaker arrivals, but it is accompanied by an increase in artefacts with velocities < 3 km/s.

For WRA (Fig. 3.5, middle column), we find most surface waves originate from the northern directions. IAS Capon shows signal concentrations along straight lines due to the array response. CLEAN-PSF-fk shows an improvement by reducing the presence of the array pattern although many scattered arrivals are visible. CLEAN-PSF-Capon displays the best performance in the suppression of the array pattern in both body and surface waves arrivals. With the RL deconvolution, we obtain a similarly bad resolution as in the synthetic case. The body wave arrivals do not match the results of the other three algorithms and very few sources are recovered overall. In the case of

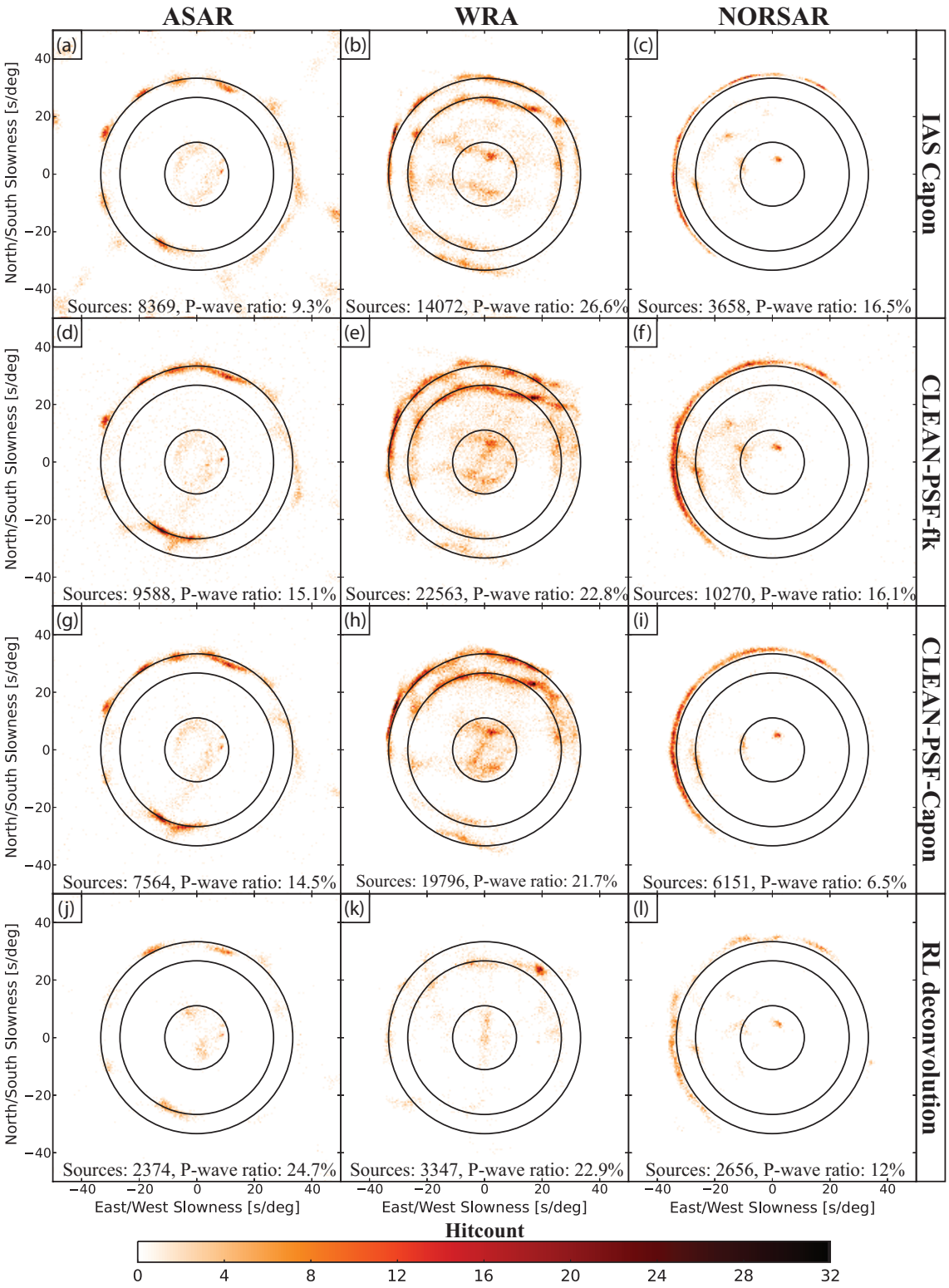

Figure 3.5: Beamforming summary (histograms) plots in the same layout as Fig. 3.3, but for observed array data. Instead of conventional fk, the first row shows beamforming results with IAS Capon. Circles of constant velocity are drawn at 3.3 and 4.1 km/s.

a reflective boundary condition, we observe an increase in source and artefact arrivals, hence little improvement.

NORSAR (Fig. 3.5, right column) shows arrivals from the Atlantic Ocean, in accordance with previous studies e.g., (Friedrich et al., 1998). IAS Capon shows exceptional slowness vector recovery, as Rayleigh waves are estimated with a very sharp velocity profile Fig. 3.5c. CLEAN-PSF-fk shows poorer performance, potentially due to the low sidelobe suppression of conventional fk. CLEAN-PSF-Capon shows a result similar to the IAS method with the exception of a body wave region (north west), which is a likely artefact (we see a similar scenario for the synthetic case, where CLEAN-PSF-Capon suppresses an artificial body wave arrival, Fig. 3.3i). The RL deconvolution shows a result similar to CLEAN-PSF-Capon in suppression of artefacts, but recovers only half of the sources in comparison.

Overall, both CLEAN-PSF and RL deconvolution show an improvement in beam sidelobe reduction on ASAR and NORSAR, while CLEAN-PSF outperforms the RL devoncolution on WRA which has large sidelobes. CLEAN-PSF further shows a superior performance in weak source recovery on all 3 arrays.

3.5.1 Presence of an earthquake

Earthquakes are unwanted signals in the analysis of microseisms. Discarding earthquake perturbed data or performing a frequency normalisation to retain phase information only (e.g. Gerstoft et al., 2008), thus reducing the earthquake signal, are the common approaches. In the case of a strong earthquake, weaker microseism signals can remain undetected or their true slowness vector can be concealed due to the influence of strong beam sidelobes. We tested CLEAN-PSF and RL deconvolution on a 1 hour record of ASAR (2nd January 2010, 00:00:00 - 01:00:00 UTC, magnitude: 5.1 mb, origin: Tonga Islands) to determine if the algorithms can accurately resolve weaker microseism sources in the presence of an earthquake. At first, we remove 2 snapshots that contain the earthquake signal and evaluate the noise wavefield. In the second step we include the 2 snapshots containing the earthquake to study the influence of the strong arrival on the underlying noise wavefield. The results for the earthquake perturbed dataset are displayed in Fig. 3.6.

The noise wavefield shows similar results for the 2 CLEAN variations and the RL deconvolution (Fig. 3.6a-c). Slight differences are visible for body waves and the southern direction where the CLEAN approaches indicate multiple arrivals while RL deconvolution estimates these arrivals as one source. With the included earthquake signal (Fig. 3.6d-f), both algorithms are capable of removing the array pattern from the earthquake source and show the same noise wavefield. For visualisation purposes, we clip the earthquake signal and show the same power levels as in the earthquake free case, for an easy comparison of the noise wavefield. The results show that earthquake induced signals, including their sidelobe contributions, can be successfully removed from the power spectrum by both algorithms, while CLEAN-PSF shows higher resolution.

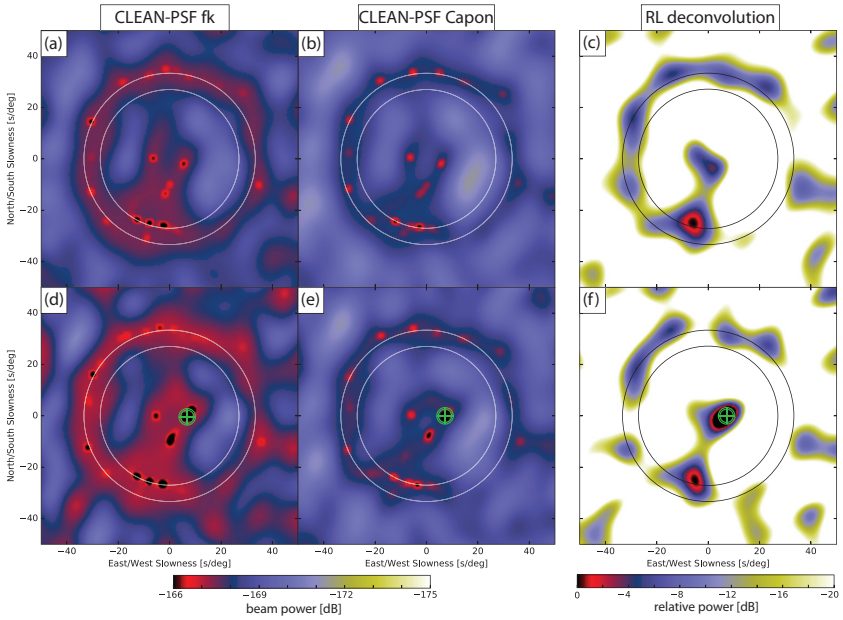

Figure 3.6: Beamforming results on a 1 hour long record of ASAR during an earthquake arrival. The top row shows the results which contain noise only. This was achieved by removing 2 snapshots from the cross spectral matrix which contain the earthquake signal. The bottom row includes the earthquake signal which is marked with a green crosshair in the slowness plane. The algorithms are organised in columns, (a,d) CLEAN-PSF-fk, (b,e) CLEAN-PSF-Capon and (c,f) Richardson Lucy deconvolution. Circles of constant velocity are set at 3.3 and 4.1 km/s. For the CLEAN approaches, we show the true beam power and clip the power of the earthquake arrival to show the background arrivals within the same limits. For the RL deconvolution, the results are shown with relative power, as RL does not accurately retain power information.

3.6 Three component case

With the increasing deployment of seismic three component (3C) arrays, better processing of 3C ground motion data is desirable. For 3C arrays, a popular way of performing the direction of arrival analysis is to rotate the horizontal north-south and east-west components into radial and transverse directions, e.g. (Fäh et al., 2008; Poggi and Fäh, 2010; Behr et al., 2013). Radial and transverse components are then processed separately, exploiting the fact that Rayleigh and Love waves have orthogonal particle motions. A disadvantage of this approach is that the cross spectral matrix needs to be recalculated for each direction, and phase information between the 3 orthogonal directions are not recovered by this analysis.

3.6.1 Extension of CLEAN-PSF to three components

We make use of an approach that evaluates all 3 components simultaneously and allows access to polarisation information. The technique was developed by Wagner (1996) and can be used with multiple flavours of beamformers (fk, Capon, MUSIC, EMV). We briefly summarize the 3C approach followed by the extension of CLEAN for this framework. The 3C cross spectral matrix is given as

$$\mathbf{C}_{3C}(f) = \frac{1}{L}\sum_{l=1}^{L}\mathbf{X}_{3C,l}(f)\mathbf{X}_{3C,l}^{H}(f) \tag{3.14}$$

with

$$\mathbf{X}_{3C}(f) = [\mathbf{X}_{z1}, ..., \mathbf{X}_{zK}, \mathbf{X}_{n1}, ..., \mathbf{X}_{nK}, \mathbf{X}_{e1}, ..., \mathbf{X}_{eK}]^T, \tag{3.15}$$

where $\mathbf{X}_{ab}$ on the right hand side denotes the Fourier transform of component a (vertical, north-south, east-west) and station b. Hence $\mathbf{X}_{3C}(f)$ is a vector of length $3K$ and $\mathbf{C}_{3C}(f)$ is a $3K \times 3K$ matrix that governs the phase information between all 3 components. The cross spectral matrix is then projected onto the steering matrix composed of 3 orthogonal steering vectors

$$\mathbf{Y}_{3C}(\mathbf{k}) = \mathbf{e}^{\mathbf{H}}(\mathbf{k})\mathbf{C}_{3C}(f)\mathbf{e}(\mathbf{k}) \tag{3.16}$$

with

$$\mathbf{e}(\mathbf{k}) = [\mathbf{a}_z(\mathbf{k}), \mathbf{a}_n(\mathbf{k}), \mathbf{a}_e(\mathbf{k})], \tag{3.17}$$

where the orthogonal $3K \times 3$ steering matrix $\mathbf{e}(\mathbf{k})$ is of the form

$$\mathbf{e}(\mathbf{k}) = \begin{bmatrix} a_{z1} & \dots & a_{zK} & 0 & \dots & 0 & 0 & \dots & 0 \\ 0 & \dots & 0 & a_{n1} & \dots & a_{nK} & 0 & \dots & 0 \\ 0 & \dots & 0 & 0 & \dots & 0 & a_{e1} & \dots & a_{eK} \end{bmatrix}^T \tag{3.18}$$

and $a_{zi} = a_{ni} = a_{ei}$ is the normalised steering vector from eq. 3.3. The resulting 3×3 polarisation covariance matrix $\mathbf{Y}_{3C}(\mathbf{k})$ is processed analogously to the single station case (Vidale, 1986; Wagner and Owens, 1996). An eigenvalue decomposition of $\mathbf{Y}_{3C}(\mathbf{k})$ transforms the polarisation characteristics into an orthogonal basis

$$\mathbf{Y}_{3C}(\mathbf{k}) = \mathbf{u}(\mathbf{k})\lambda(\mathbf{k})\mathbf{u}^{\mathbf{H}}(\mathbf{k}), \tag{3.19}$$

where the eigenvalues λ denote the strength for a certain polarisation direction that is given by the associated complex eigenvectors $\mathbf{u}(\mathbf{k})$. Each eigenvector parametrises the amplitude and phase relations of the 3 components (z,n,e) for the given polarisation direction. The power estimate of the 3C conventional beamformer is the sum of the eigenvalues

$$P_{3C}(\mathbf{k}) = \lambda_0(\mathbf{k}) + \lambda_1(\mathbf{k}) + \lambda_2(\mathbf{k}). \tag{3.20}$$

The total power spectrum can be written as the sum of the three components

$$\begin{aligned} P_{3C}(\mathbf{k}) &= \sum_{j=z,n,e} P_j(\mathbf{k}) = \sum_{j=z,n,e} \sum_{i=0}^{2} \lambda_i(\mathbf{k}) |u_{i,j}(\mathbf{k})|^2 \\ &= \sum_{j=z,r,t} \tilde{P}_j(\mathbf{k}) = \sum_{j=z,r,t} \sum_{i=0}^{2} \lambda_i(\mathbf{k}) |\tilde{u}_{i,j}(\mathbf{k})|^2, \end{aligned} \tag{3.21}$$

where tilde (e.g. $\tilde{P}_j(\mathbf{k})$) denotes rotated components from north-south, east-west to radial and transverse. For each wave number $\mathbf{k}$, i.e. velocity, direction and frequency, the 3C beamformer yields an estimate of the amplitude and phase information of each component. The Capon 3C beamformer can be obtained by replacing the 3C cross spectral matrix in eq. (3.16) by its inverse

and inverting the eigenvalues

$$P_{3C,Capon}(\mathbf{k}) = \frac{1}{\lambda_0(\mathbf{k})} + \frac{1}{\lambda_1(\mathbf{k})} + \frac{1}{\lambda_2(\mathbf{k})}. \tag{3.22}$$

For strong transients and the case of conventional 3-component beamforming, the largest eigenvalue λ_0 and eigenvector $\mathbf{u_0}(\mathbf{k})$ (assuming the eigenvalues and eigenvectors are sorted, $\lambda_0 > \lambda_1 > \lambda_2$) are used for the power estimate (e.g. Wagner, 1997). This is a useful approach for signals whose polarisation characteristics can be described by a single eigenvalue/eigenvector pair, hence $\lambda_0 \gg \lambda_{1,2} \approx 0$. The remaining two eigenvalues are close to 0 and are dominated by noise. This approach is invalid for superimposed signals which are likely to occur in the study of ocean induced microseisms. We therefore outline the CLEAN approach in 3C in its general form for all 3 eigenvalues/eigenvectors.

The above framework allows us to implement the cleaning procedure in multiple ways. Signal removal can be performed on the maximum of the total power output, eq. 3.20, on each component (z,r,t) separately, or any other way appropriate for the user's application. We present the equations for CLEAN-PSF in 3C, where cleaning is subject to the maximal energy of the spectrum $\mathbf{P}_{3C}(\mathbf{k})$. In analogy to section 3.3.2, the first step is to identify the dominant contribution in the power spectrum, i.e. $P_{3C,max}(\tilde{\mathbf{k}})$ along with its eigenvalues $\lambda_i(\tilde{\mathbf{k}})$ and eigenvectors $\mathbf{u}_i(\tilde{\mathbf{k}})$. We remove the power in 3 components

$$\mathbf{C}_{3C}^{i+1} = \mathbf{C}_{3C}^{i} - \phi \sum_{j=0}^{2} \lambda_j(\tilde{\mathbf{k}}) \mathbf{g}_j(\tilde{\mathbf{k}}) \mathbf{g}_j^H(\tilde{\mathbf{k}}), \tag{3.23}$$

where

$$\mathbf{g}_j(\tilde{\mathbf{k}}) = \sum_{m=z,n,e} |u_{j,m}(\tilde{\mathbf{k}})| \mathbf{a}_m(\tilde{\mathbf{k}}) e^{i\psi_m(\tilde{\mathbf{k}})} \tag{3.24}$$

is a 1 dimensional vector of length $3K$ constructed from the 3 orthogonal steering vectors $\mathbf{a}_m(\tilde{\mathbf{k}})$, see eq. 3.17 and 3.18. The vector $\mathbf{g}_j(\tilde{\mathbf{k}})$ essentially describes the component-wise plane wave propagation of all 3 components associated with the strongest source in the power spectrum with the wave vector $\tilde{\mathbf{k}}$. The eigenvector $\mathbf{u}_0(\tilde{\mathbf{k}})$ assigns the contributions of each component, e.g. for a Love wave $|u_{0z}(\tilde{\mathbf{k}})|$ will be close to 0, hence minimal power will be removed from the vertical z component. While the phase information is initially arbitrary (Vidale, 1986), it is important to retain the phase information between the components, which we account for with $e^{i\psi_m(\tilde{\mathbf{k}})}$ for the m-th component. This will ensure that polarisation properties are taken into account during the cleaning procedure (for instance Rayleigh waves with a phase difference of 90° between the vertical and radial components).

Further calculations follow the same principals as CLEAN-PSF and the clean power spectrum is

$$P_{3C,CLN}(\mathbf{k}) = \sum_{i}^{M} \phi P_{3C,max}^{i}. \tag{3.25}$$

Combined with the background the full spectrum is of the form

$$P_{PSF-3C}(\mathbf{k}) = \mathbf{e}^H(\mathbf{k})\mathbf{C}^{i_M}_{PSF}(f)\mathbf{e}(\mathbf{k}) + P_{3C,CLN}(\mathbf{k}). \tag{3.26}$$

The CLEAN-PSF-3C approach can be combined with Capon beamforming following the same logic as in the 1 dimensional case (see appendix 3.10.1).

In this work, we implemented CLEAN-PSF to clean each component separately, hence we computed 3 cross spectral matrices (eq. 3.14) that are identical before CLEAN's first iteration. For the matrix $\mathbf{C}_{3C,i}$, we remove the energy associated with the local maxima from the i-th component only. This approach will prevent the corruption of each component's power information. We illustrate the introduction of bias through the following example. Let there be 3 wave arrivals with equal strength (0 dB) and backazimuth, but different velocities (3.7 km/s, 4.4 km/s and 5.6 km/s) and each wave is recorded by a separate component only. An illustration of the 3 component fk beamformer output is displayed in the supplementary material, Fig. S3.5 and the estimated parameters are given in, Table S3.1. Even though the signals do not interfere with each other on any component, the polarisation analysis estimates power from the sidelobe contributions of the sources present on the other two components. This can be seen in the source present on the Z component, which has power accurately estimated with 0 dB, while the other two components show a power of -2.22 dB, which is a result of sidelobes. Therefore, if a fraction of the power is removed from the Z component, the other two components lose power proportional to their sidelobes power levels. This will bias the two other components and will inevitably lead to an incorrect decomposition of the spectrum. Hence, the easiest way to clean the components is to compute 3 cross spectral matrices and clean each separately to obtain 3 unbiased components.

3.6.2 CLEAN-PSF-3C with observed data

For the three component case, we use the Pilbara seismic array (PSAR) which is comprised of 13 three component stations arranged in a spiral geometry (Kennett et al., 2015), located in north-west Australia. PSAR was deployed by Geoscience Australia and data access is available through the IRIS Data Management centre. The location, array configuration, array response and frequency band can be found in Fig. 3.1.

In the following section we show the capabilities of CLEAN-PSF-3C by evaluating 1 year of PSAR data (2013). Instead of conventional fk, we use the Capon beamformer in combination with the above framework. We average over time and frequency analogous to the vertical component case in section 3.5. Since we are interested in the ambient noise field, and the main wave phases are R_g, L_g, P and Love waves (Nishida et al., 2008a; Koper et al., 2010), we implement the CLEAN-PSF-3C algorithm to remove power separately from the strongest vertical, radial and transverse source per iteration (see appendix 3.10.2). We remove signals associated with the 2 smallest eigenvalues only (in the case of Capon the smallest eigenvalues represent the signals with strongest polarization, see eq. 3.22), as the largest eigenvalue is, in general dominated by noise. All other parameters are stated in Table 3.1

The results are presented in equivalent fashion to the single component case as summary plots of the full year, for both 3 component Capon beamforming and the CLEAN-PSF implementation

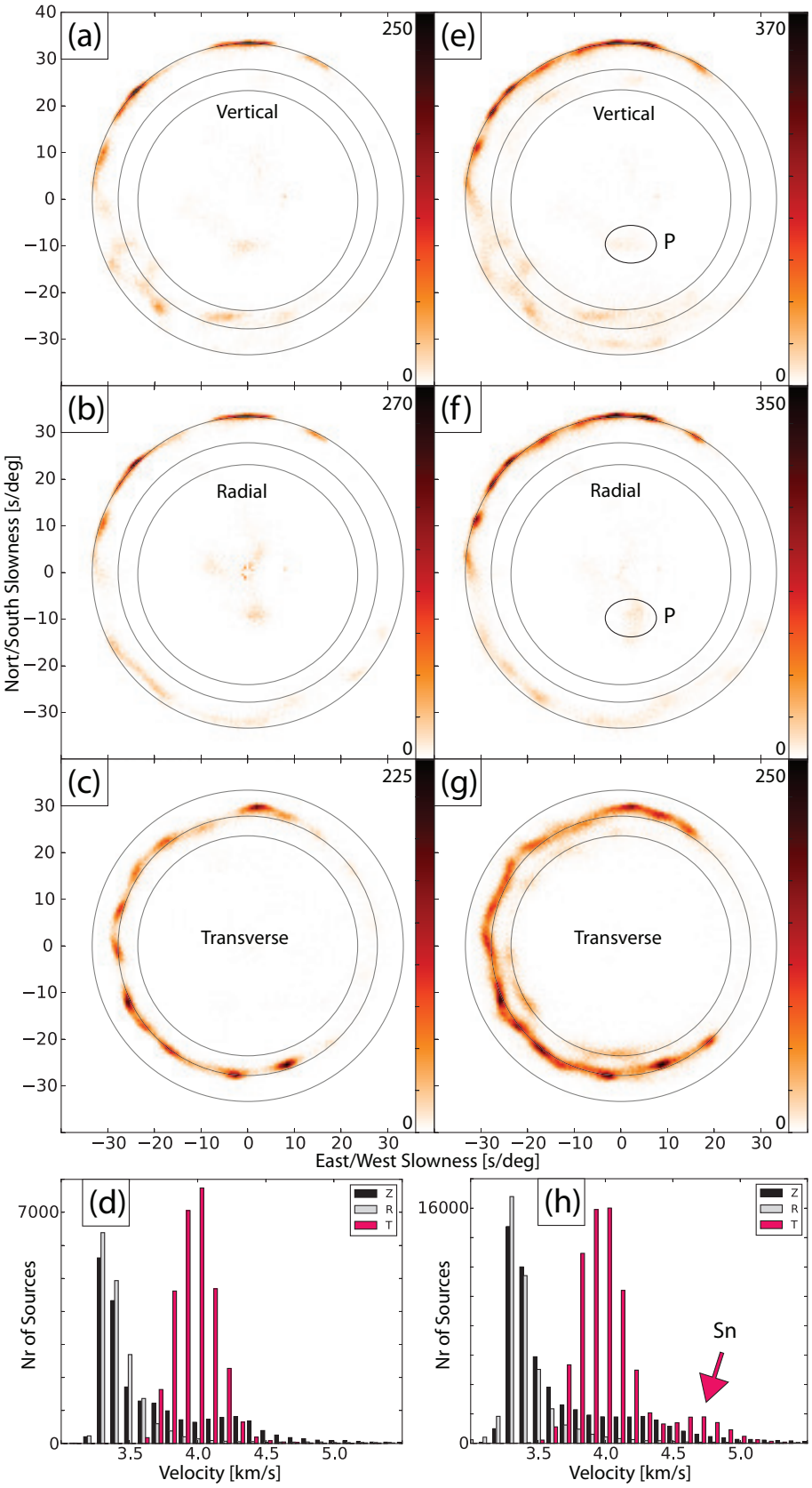

Figure 3.7: Beamforming summary plots (histograms) for (a-c) 3 component Capon and (e-g) it's CLEAN-PSF extention for each component. Circles of constant velocity are displayed at 3.3, 4.0 and 4.7 km/s. The velocity histograms (d,h) were created from the arrival data in the corresponding column and display vertical, radial and transverse in black,white and red. For (e,f) we explicitly mark a region of P wave arrivals that correlate in the slowness plane.

(Fig. 3.7). We display local maxima up to a relative power threshold of -5 dB for each component, which is the amount that is cleaned on average by the CLEAN procedure. The first column shows the 3 component Capon summary of arrivals for (a) vertical, (b) radial and (c) transverse component respectively. A velocity histogram of the components is shown in Fig. 3.7d. The second column (e-h) shows the corresponding CLEAN power spectra which were computed with 60 iterations. Increasing the number of iterations, hence removing less power in one step, leads to the same result.

The vertical and radial component plots (Fig. 3.7a,b) are dominated by arrivals with a velocity of 3.3 km/s from the north to the west. For both components these arrivals are found at identical positions in the slowness plane, hence show typical R_g behaviour. For arrivals from the south to the west, the positions in the slowness plane are not identical between the two components. This suggests an additional phase is present. A potential candidate is the Lg phase, as the vertical component shows arrivals with an increased velocity, in contrast to the radial component. The majority of body waves do not have correlated vertical and radial components and are hence likely to be artefacts. For the transverse component (Fig. 3.7c), we find a multitude of sources around a velocity of $3.9 - 4.0$ km/s present in the wavefield, which are likely Love waves.

Similarly, the CLEAN algorithm shows arrivals from the same directions on all 3 components. For the cleaned vertical and radial components (Fig. 3.7e,f), we find again identical positions in the slowness plane. In contrast to the conventional results, the cleaned spectrum shows significantly better resolution and is able to distinguish greater detail in arrivals from the main arrival directions in the north and west. Further, the previously scattered body waves are reduced and the remaining energy on the vertical and the radial component correlates well in the slowness plane. For the energy from the south to the west, little improvement is visible compared with the conventional approach. The cleaned transverse component shows additional sources from the north-east and south-east and reveals a previously undetected shear phase with a velocity around $4.6 - 4.7$ km/s, Fig. 3.7g. Comparing the 2 velocity histograms, Fig. 3.7d,h illustrates the detection of this phase. A likely candidate is the *Sn* phase, which matches the observed velocity in Australia (Huestis et al., 1973; Stephens and Isacks, 1977).

3.7 Discussion

For the single component case, CLEAN-PSF shows significant resolution improvements in identifying weaker sources. The algorithm allows a specified amount of power to be cleaned from the spectrum and hence removes the associated sidelobe bias. Assuming the control parameter ϕ is not large, the algorithm converges to a solution. The extracted phases can be used to validate the accuracy of the solution by replacing the cross spectral density matrix with the matrix that includes all removed phases (last term in eq. 3.5). This can be seen as a variation of the covariance fitting algorithm (Yardibi et al., 2008).

A limiting factor of CLEAN is its dependence on the dominant source. If the original beamformer result is biased in the dominant source, by a closely spaced source or multiple wave phases which generate an artificial local maximum due to sidelobe superposition, CLEAN will remove

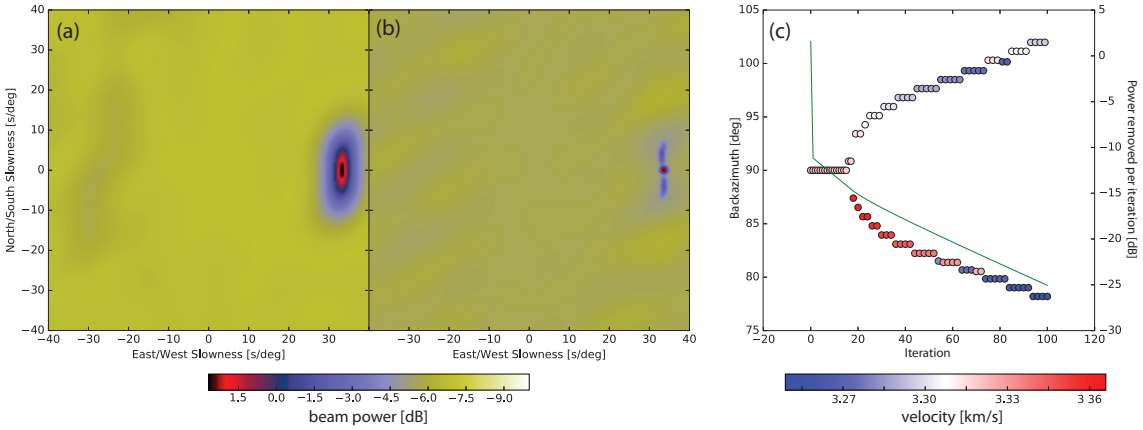

Figure 3.8: (a) Synthetic example of 2 closely spaced sources (baz = 85°, 95°), which cannot be separated by the Capon beamformer. (b) Displays the results after the CLEAN procedure. (c) Shows from which backazimuth power is removed as a function of the iteration and the green line marks the fraction of power removed as a function of iteration.

plane wave energy associated with the incorrect slowness vector and lead to an incorrect solution. A possible solution is to use a hybrid algorithm that combines CLEAN and RL deconvolution. Later iterations of CLEAN will benefit from a hybrid approach, as multiple peaks with the same power levels are likely to occur. Applying the RL algorithm in this scenario will give CLEAN a better estimate of the strongest source present in the spectrum and therefore enhance the correct recovery of weaker sources.

In contrast to CLEAN-PSF, the RL deconvolution does not depend on the position of the strongest source in the slowness plane and can in some cases correct the bias of the initial beamformer result. It shows strong deblurring capabilities but cannot resolve as many sources as CLEAN-PSF. A difficulty of the RL algorithm is the non-converging behaviour, hence it is strongly dependent on the number of iterations (Picozzi et al., 2010). It is not possible to find the optimal solution and a compromise between resolution and bias has to be selected by the user which limits the resolution capabilities of this approach.

In the conventional CLEAN in astronomy, the cleaning procedure is stopped once the maximum of the residual image reaches the level of the background noise. For beamforming, we have investigated two stopping criteria, apart from the trivial case in which the user sets the iteration number M to clean a specific amount of power. The first is to stop iteration after 1 eigenvalue of the covariance matrix becomes negative, i.e. violates the positivity constrain embedded in the conventional beamformer. We found this approach to give unreliable results, owing to higher iterations lowering the SNR. This can strongly influence the performance of the underlying beamformer and CLEAN will remove random energy until the stop criterion is fulfilled. A more robust option is to monitor the parameters of the removed energy. In an iteration vs backazimuth plot, the removed energy tends to cluster around certain backazimuths (Fig. S3.2). Once the energy starts to scatter from these backazimuths, it is likely that the underlying beamformer is biased by noise and CLEAN should be stopped. An illustrative figure is presented in the supplementary material, Fig. S3.6.

The RL deconvolution faces the issue of a missing stop criterion in order to obtain the optimal solution. During our analysis we find that the optimal number of iterations selected from synthetic

tests, fits well with results from observed data for ASAR and NORSAR.

In the case of CLEAN, we examine the possibility of introducing errors by removing energy from the power spectrum that differs from the true source location. We study the behaviour for two closely spaced sources which cannot be separated by the underlying beamformer. Two noise free synthetic sources are generated at backazimuth 85° and 95° and analysed with the ASAR configuration with CLEAN-Capon. In this case, we have set diagonal loading to a level where the two sources are observed as a single source by the Capon beamformer. Therefore, CLEAN will start to remove power between the two sources. The results shown in Fig. 3.8 display from which backazimuth power is removed, with each iteration. During the first iterations, power is removed from backazimuth 90° until enough power is removed to separate the two sources. The following iterations show that the removal of energy overshoots the true backazimuth values to compensate for the removal between the sources. The CLEAN approach cannot correctly separate the sources, but succeeds in the correct estimation of the combined power.

For completeness, we estimate the amplitude and slowness errors of the cleaned spectrum in the synthetic case presented in section 3.4.1. The results are displayed in a backazimuth histogram for ASAR, WRA and NORSAR (Fig. S3.7,S3.8,S3.9). The estimated error in slowness depends on the wavefield and is greater when sources are closely spaced and cannot be separated by the beamformer and hence is dependent on the mainlobe of the array. For the case of ASAR, we find backazimuth errors of up to 5° and this decreases for the other arrays. The amplitudes are well estimated and show strong improvement over the conventional case (Fig. 3.3). For WRA and NORSAR the error in backazimuth is ($< 3°$) due to the increase in the number of stations and the smaller beam mainlobe.

The main source of error for the RL deconvolution is connected to the control/threshold parameter σ. In astronomy the PSF's have a finite extent and can be easily normalised to unity volume. In array seismology this is not the case as PSF's are not finite and can have complicated shapes. This poses a problem as the volume of the PSF and σ are essentially dependent on the grid size of the PSF. The fact that the PSF is not finite is directly responsible that power levels of each source are not accurately estimated. We have tried a variety of threshold values and found robust estimates between $0.05 < \sigma < 0.11$ for ASAR and NORSAR. Between these two values, the RL deconvolution shows robust results when applied to synthetic data.

3.8 Conclusion

We have tested the performance of two deconvolution algorithms, CLEAN-PSF and Richardson-Lucy deconvolution, in the context of a single component array microseism (ambient noise) analysis. We used a range of arrays with different apertures and shapes (ASAR, WRA and NORSAR). In all 3 cases (synthetic, real and earthquake perturbed data), both approaches show improvement over the conventional methods in removing artefacts and identifying weaker sources. CLEAN-PSF shows better suppression capabilities mainly due to the fact that it can be used with the Capon beamformer. A further advantage was shown through an earthquake example, where CLEAN-PSF is capable of removing the earthquake imprint and revealing the underlying ambient noise sources.

We have extended the CLEAN approach to 3 components and analysed its performance on 1 year of 3 component ambient noise data from PSAR. The extension demonstrates improved resolution on all three components and reveals the previously undetected *Sn* phase. We therefore conclude that CLEAN-PSF is of strong utility in the study of the ambient noise field for the accurate identification of weaker arrivals for single and three component arrays.

3.9 Acknowledgements

We acknowledge data access through the IRIS DMC archive. Our thanks is due to two anonymous referees and the editor for constructive reviews which have improved both content and reproducibility. We further thank Hrvoje Tkalčić and Gregory Wagner for constructive discussions. The research was funded by the Australian Research Council (DP15101005) and MG supported through a Tasmanian Government Research Scholarship. Computer programs which implement the techniques are freely available and may be obtained by contacting the University of Tasmania authors.

3.10 Appendix

3.10.1 CLEAN-PSF-Capon

The Capon beamformer can be formulated as the following minimisation

$$min \quad \mathbf{w^H C}(f)\mathbf{w} \tag{3.27}$$

under the constrain that the gain in the look direction $\mathbf{k}$ is constant

$$\mathbf{w^H a}(\mathbf{k}) = 1. \tag{3.28}$$

The minimisation can be solved with the Lagrangian multiplier method and yields the weight vector

$$\mathbf{w} = \frac{\mathbf{C}^{-1}(\mathrm{f})\mathbf{a}(\mathbf{k})}{\mathbf{a^H}(\mathbf{k})\mathbf{C}^{-1}(\mathrm{f})\mathbf{a}(\mathbf{k})}. \tag{3.29}$$

Inserting into eq. 3.2 leads to the Capon beamformer (Capon, 1969)

$$\mathbf{P}(\mathbf{k}) = \frac{1}{\mathbf{a^H}(\mathbf{k})\mathbf{C}^{-1}(\mathrm{f})\mathbf{a}(\mathbf{k})}. \tag{3.30}$$

CLEAN-PSF can be implemented by removing phase information from the cross spectral matrix $\mathbf{C}$ prior to its inversion. The algorithm can be summarised with the following steps (for a normalised steering vector $\mathbf{a}(\mathbf{k})$):

1. Calculate cross spectral matrix $\mathbf{C}$, eq. (3.1)

2. Compute the inverse $\mathbf{C}^{-1}$

Component	BAZ[°]	v[km/s]	Power of Peak λ_0 [dB] (Z,R,T)		
Z	90.0	4.4	0.00	-2.22	-2.22
R	90.0	5.6	-2.25	0.02	-5.14
T	90.0	3.7	-2.25	-5.09	0.00

Table S3.1: Parameter of sources evaluated with the 3 component beamformer.

3. Compute Capon beamformer, eq. (3.30), and locate maximum in slowness plane
4. Remove fraction of power from cross spectral matrix, $\mathbf{C}^{i+1}_{PSF} = \mathbf{C}^{i} - \phi P^{i}_{Capon,max}\mathbf{a}_{max}\mathbf{a}^{H}_{max}$
5. Place removed power into clean spectrum, eq. (3.6)
6. Iterate steps (ii-v)
7. Combine clean and background spectrum

3.10.2 Cleaning each component separately with Capon CLEAN-PSF-3C

The Capon beamformer in three components is obtained by projecting the 3 orthogonal steering vectors onto the inverse cross spectral matrix

$$\mathbf{Y}_{3C,Capon} = \mathbf{e}^{\mathbf{H}}(\mathbf{k})\mathbf{C}^{-1}_{3C}(f)\mathbf{e}(\mathbf{k}). \tag{3.31}$$

Contrary to the conventional beamformer case, the power is given as

$$P_{3C,Capon}(\mathbf{k}) = \frac{1}{\lambda_0(\mathbf{k})} + \frac{1}{\lambda_1(\mathbf{k})} + \frac{1}{\lambda_2(\mathbf{k})}, \tag{3.32}$$

with $\lambda_0 > \lambda_1 > \lambda_2$. In this case, λ_2 is connected to the strongest polarization. To clean each component separately we use the following steps:

1. Calculate cross spectral matrix $\mathbf{C}_{3C}$, eq. (3.14), and create 2 additional duplicates
2. Compute the 3 inverse matrices $\mathbf{C}^{-1}_{3C,i}$
3. Calculate 3 polarisation covariance matrices $\mathbf{Y}_{3C,i}(\mathbf{k}) = \mathbf{e}^{\mathbf{H}}(\mathbf{k})\mathbf{C}^{-1}_{3C,i}(f)\mathbf{e}(\mathbf{k})$
4. Compute power for the two lowest eigenvalues and each component, $i = z,r,t$, $P_{3C,i} = \sum_{n=1,2} \frac{1}{\lambda_{n,i}(\mathbf{k})}|\tilde{u}_{n,i}(\mathbf{k})|^2$ and find maximum in each component
5. Remove fraction of power from 3C cross spectral matrices, $m = z,r,t$, $\mathbf{C}^{i+1}_{3C,m} = \mathbf{C}^{i}_{3C,m} - \phi \sum_{j=1,2} \frac{1}{\lambda_{j,m}(\tilde{\mathbf{k}})}\mathbf{g}_j(\tilde{\mathbf{k}})\mathbf{g}^{H}_j(\tilde{\mathbf{k}})$
6. Place removed power into clean spectra, $P_{3C,CLN,m}(\mathbf{k}) = \sum^{M}_{i} \phi P^{i}_{3C,max,m}$
7. Iterate steps (ii-vi)
8. Combine clean and background spectra

3.11 Supplementary material

	ASAR			
Nr	pow [dB]	baz [°]	pow fk [dB]	pow Capon [dB]
1	0	22.95	-0.11	0.94
2	0	37.17	-0.46	0.45
3	0	56.76	-0.28	-0.16
4	0	89.96	0	-0.03
5	0	190.68	1.07	0.01
6	0	256.03	-0.18	-0.04
7	0	299.87	3	2.44
8	0	307.16	3	2.44
9	0	325.60	0.54	0.11
10	0	341.16	-0.34	0.16
11	0	16.40	-0.76	-1.75
12	0	203.32	-1.41	-0.05
13	0	299.09	-3.17	-0.33

Table S3.2: Beam power for the synthetic test with the two CLEAN variations on ASAR. These values are derived from Fig. S3.7, by summing over a small backazimuth range for each source. Source 8 and 9 could not be separated and their power is displayed as the combined power over both backazimuth ranges. Iteration stopped after $\sim 98\%$ of power was removed by CLEAN.

WRA		NORSAR	
pow fk [dB]	pow Capon [dB]	pow fk [dB]	pow Capon [dB]
-0.61	0.81	0.23	-0.08
-0.49	0.08	-0.05	-0.08
-0.21	-0.03	0	-0.08
-0.14	-0.04	-0.13	-0.08
-0.19	-0.04	-0.10	-0.08
-0.04	-0.04	-0.02	-0.09
0.92	0.15	-3.76	-0.19
-1.28	-0.65	1.19	-0.10
-0.26	-0.03	-0.14	-0.09
0.02	0.15	-0.13	-0.08
-0.44	-0.09	-0.13	-0.07
-0.15	-0.04	-0.10	-0.09
-0.17	-0.03	0.20	-0.09

Table S3.3: Same as Table S3.2, but for WRA and NORSAR. The results are generated from Fig. S3.8 and Fig. S3.9. Iteration stopped after $\sim 98\%$ of power was removed by CLEAN.

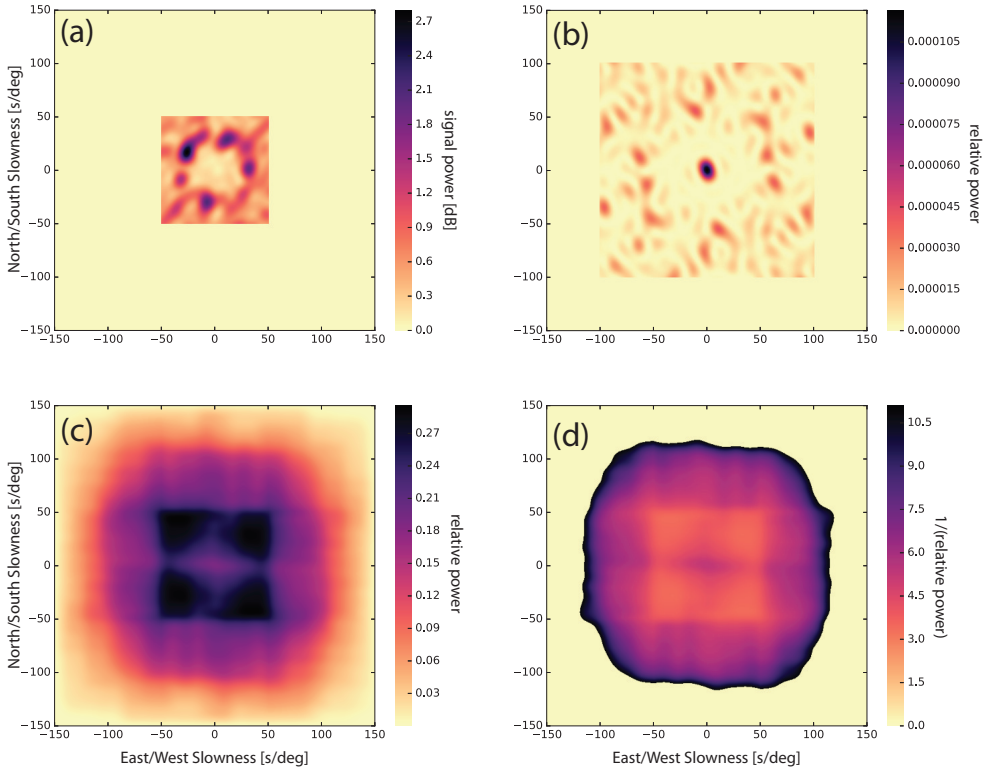

Figure S3.1: (a) Illustration of zero padding of the original power spectrum (for ASAR). In this case we extend the image plane to $3J$ to account for the large extent of the used PSF. (b) Zero padded PSF of ASAR with an extent of $2J-1$ pixels and normalised to unity volume. (c) Display of α where (b) is convolved with a mask object M_s to generate a field where the PSF mostly contributes to. (d) Shows w with a threshold parameter $\sigma = 0.09$.

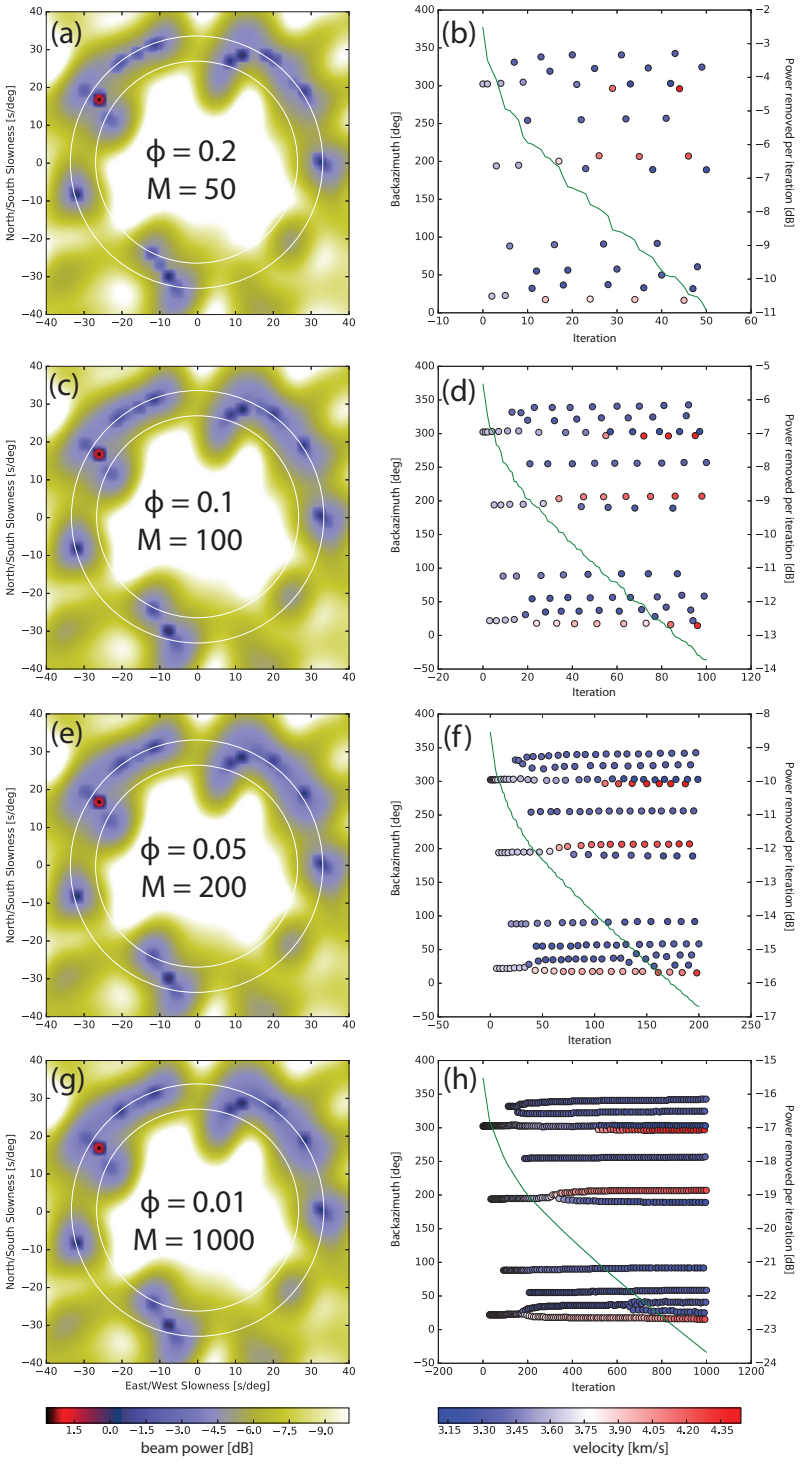

Figure S3.2: Examples of different control parameters ϕ and their effect on the iteration process. The rings of constant velocity are set to 3.3 and 4.1 km/s

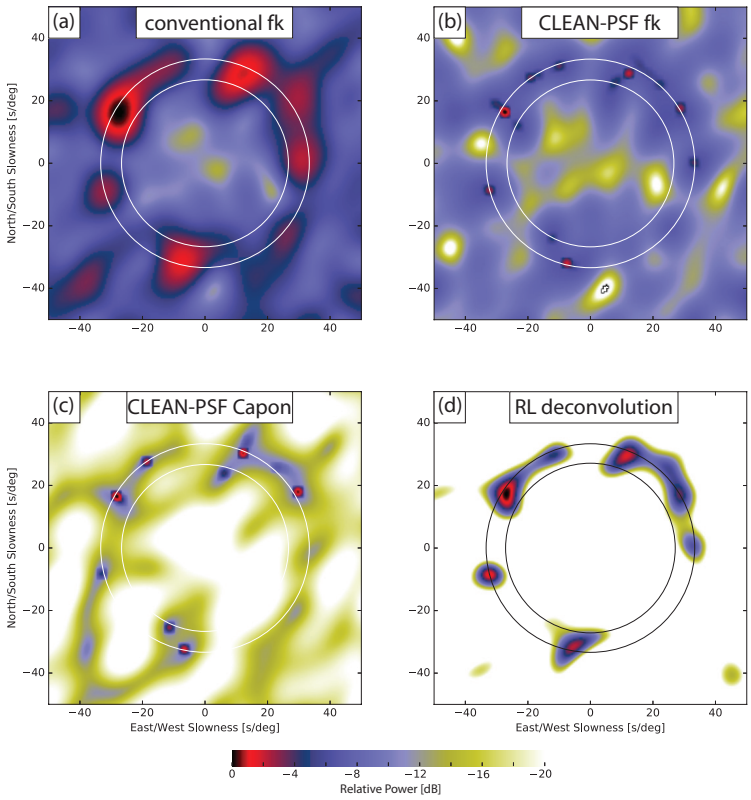

Figure S3.3: Same as Fig. 3 but with a SNR of −20 dB and Hann window applied for ASAR only. The rings of constant velocity are set to 3.3 and 4.1 km/s

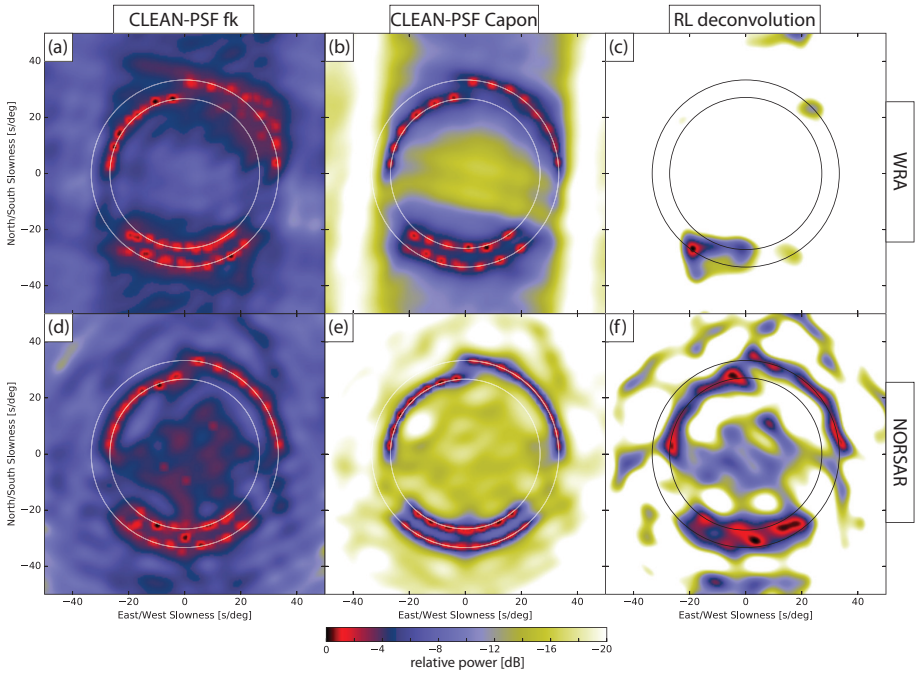

Figure S3.4: Synthetic results for he case of extended sources. The columns show the 3 deconvolution algorithms and rows the 2 arrays. The rings of constant velocity are set to 3.3 and 4.1 km/s

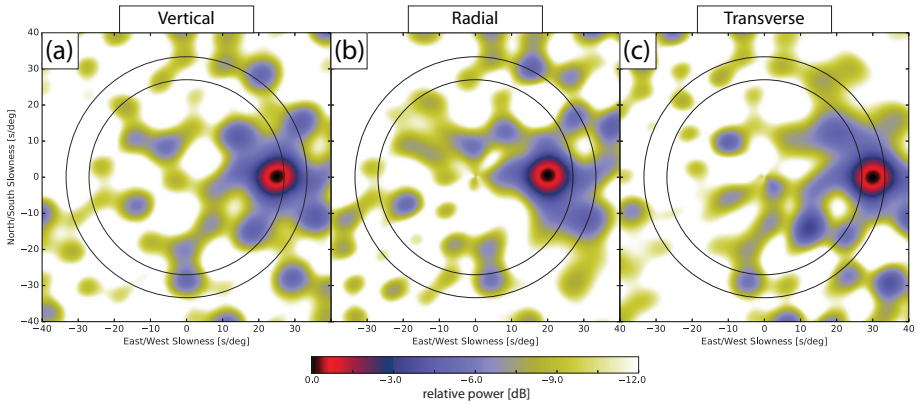

Figure S3.5: Illustrative figure for the case of 3 point sources, where each source is recorded by a single component only. The rings of constant velocity are set to 3.3 and 4.1 km/s

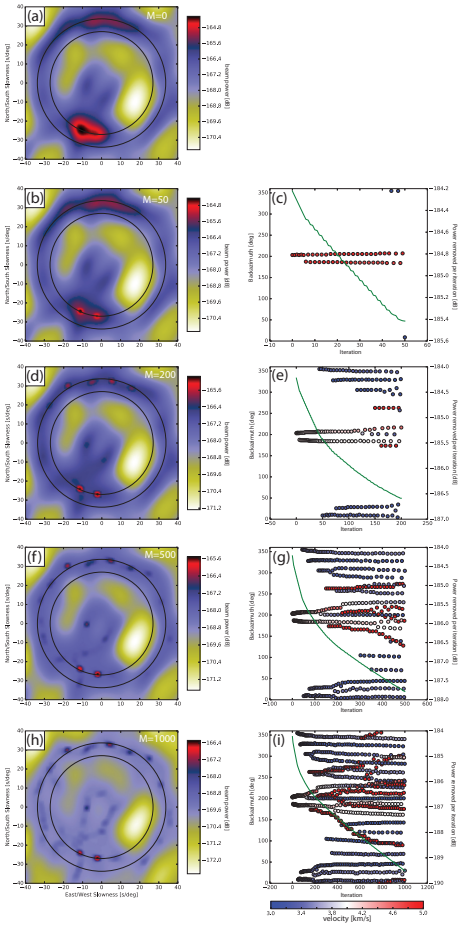

Figure S3.6: Observed data results for ASAR for different iterations numbers and their power removal history. The power of the main peak is gradually reduced with increasing M as sidelobe contributions which overestimate the source power are removed. After iteration 600 scattering in (i) is visible which suggest that removed power may not be accurate. The rings of constant velocity are set to 3.3 and 4.1 km/s

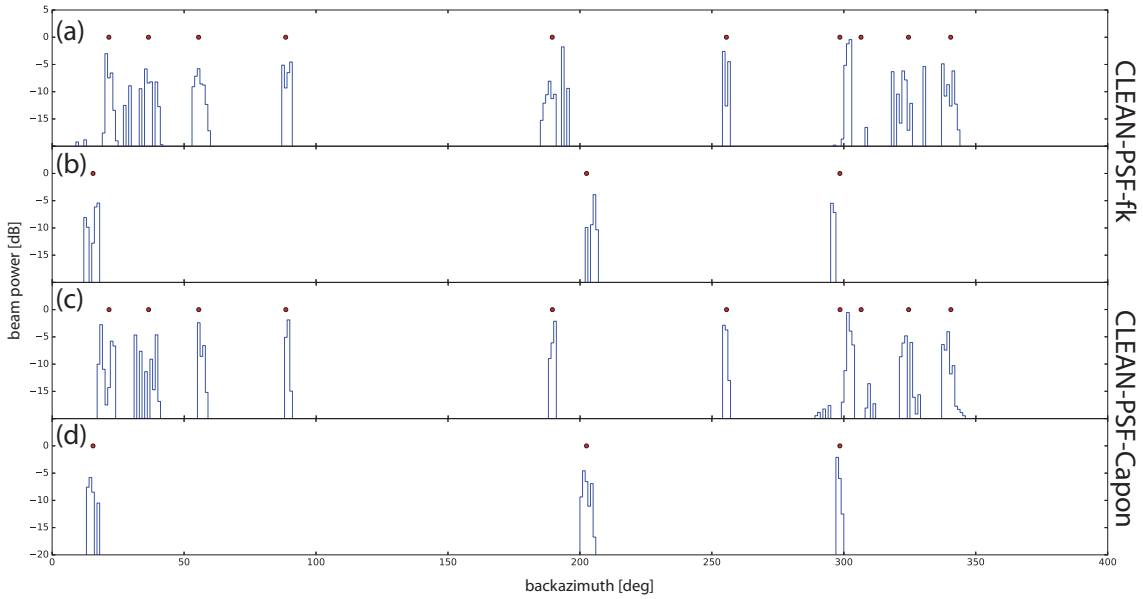

Figure S3.7: We show a Backazimuth histogram of removed power by the CLEAN algorithm. The synthetic configuration is identical to the case in Fig. 3. For the control parameter we select $\phi = 0.1$ and CLEAN iteration is stopped once 98% of the synthetic power is removed. The red dots symbolise the true backazimuth and the true source power in decibel. (a) Shows 10 synthetic sources with a velocity < 3.715 km/s and (b) shows the remaining 3 sources with velocities > 3.715. (c,d) Show the the same parameters but for CLEAN-PSF-Capon. The combined power for each source derived from the CLEAN approaches can be found in Table S3.2.

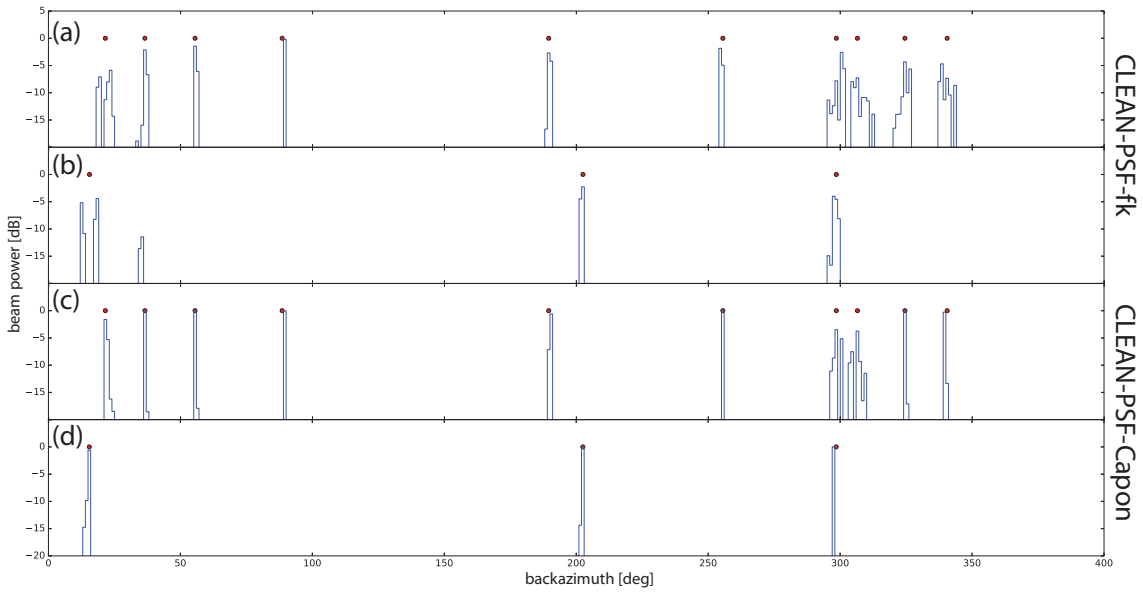

Figure S3.8: Same as Fig. S3.7, but for WRA. Beam power results for each source are shown in Table S3.3.

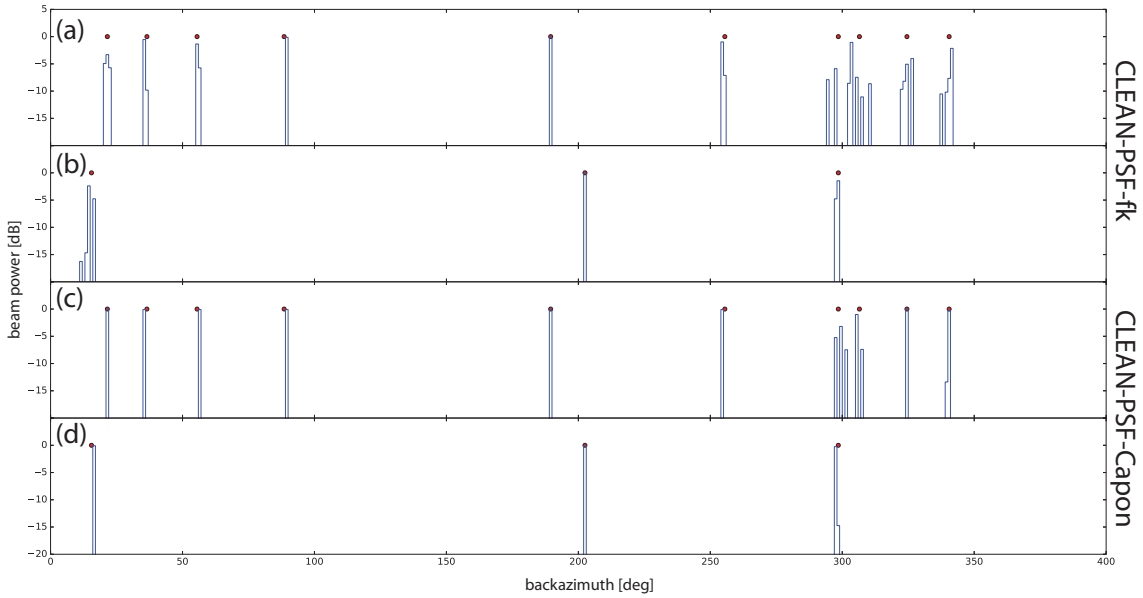

Figure S3.9: Same as Fig. S3.7, but for NORSAR. Beam power results for each source are shown in Table S3.3.

Chapter 4

The frequency dependence and locations of short-period microseisms generated in the Southern Ocean and West Pacific

Published in Journal of Geophysical Research: Solid Earth, year 2015, vol. 120, no. 8, pp 5764-5781

4.1 Abstract

The origin of the microseismic wavefield is associated with deep ocean and coastal regions where, under certain conditions, ocean waves can excite seismic waves that propagate as surface and body waves. Given that the characteristics of seismic signals generally vary with frequency, here we explore the frequency and azimuth dependent properties of microseisms recorded at a medium aperture (25 km) array in Australia. We examine the frequency dependent properties of the wavefield, and its temporal variation, over two decades (1991-2012), with a focus on relatively high-frequency microseisms (0.325-0.725 Hz) recorded at the Warramunga Array (WRA), which has good slowness resolution capabilities in this frequency range. The analysis is carried out using the Incoherently Averaged Signal (IAS) Capon beamforming, which gives robust estimates of slowness and backazimuth, and is able to resolve multiple wave arrivals within a single time window. For surface waves, we find that fundamental mode Rayleigh waves (R_g) dominate for lower frequencies (<0.55 Hz) while higher frequencies (>0.55 Hz) show a transition to higher mode surface waves (L_g). For body waves, source locations are identified in deep ocean regions for lower frequencies and in shallow waters for higher frequencies. We further examine the association between surface wave arrivals and a WAVEWATCH III ocean wave hindcast. Correlations with the ocean wave hindcast show that secondary microseisms in the lower frequency band are generated mainly by ocean swell, while higher frequency bands are generated by the wind sea, i.e. local wind conditions.

4.2 Introduction

Ambient seismic noise is the continuous background energy that is present in seismometer recordings. In the frequency range of 0.05-2 Hz, these microseisms have long been linked to ocean wave processes (e.g. Wiechert, 1904; Gutenberg, 1936; Deacon, 1947; Traer et al., 2012). The frequency spectrum of microseisms displays two peaks, around 0.07 Hz and 0.14 Hz, named the primary and secondary microseisms, respectively (Friedrich et al., 1998; Stutzmann et al., 2000; Berger et al., 2004). The primary microseisms are generated where pressure fluctuations from ocean waves interact with the ocean floor (Hasselmann, 1963; Ardhuin et al., 2015). For secondary microseisms, the underlying theory was first proposed by Longuet-Higgins (1950) and later extended by Hasselmann (1963). The interaction of two opposing ocean wave trains with approximately the same wavenumber can generate pressure fluctuations that propagate unattenuated to the ocean bottom to excite seismic waves. Microseisms therefore carry information on the ocean state and the Earth structure between source and receiver.

The primary microseisms (PMs) are composed of Love and Rayleigh waves that are generated close to coastal areas (Nishida et al., 2008). The frequency of the PM ambient noise field is similar to the frequency of the ocean waves; hence it carries information on near shoreline ocean wave dynamics (Aster et al., 2010). For secondary microseisms (SMs), most of the energy is present in the form of Rayleigh waves (Lacoss et al., 1969) and has been observed to have an origin close to coastal areas (Bromirski et al., 2013), although SM energy generated in the deep ocean might also be observed on land (e.g. Beucler et al., 2015).

A number of studies have focused on locating the source regions of SM Rayleigh wave energy with seismic arrays (Cessaro, 1994; Friedrich et al., 1998; Essen, 2003; Chevrot et al., 2007; Kedar et al., 2008; Koper et al., 2009; Behr et al., 2013; Reading et al., 2014). It was found that SM generation regions remain relatively constant over the period of a few days (Schulte-Pelkum et al., 2004; Chevrot et al., 2007) and show correlations with storm activity (Schulte-Pelkum et al., 2004). Coastal reflections (Ardhuin and Roland, 2012) and bathymetry effects (Longuet-Higgins, 1950; Kedar et al., 2008) were shown to be important factors for an improved understanding of microseisms recorded by on-land seismic stations.

The excitation of SM body waves is mainly driven by strong ocean storms and primarily observed in deep ocean regions (Gerstoft et al., 2008). Slowness estimation with a seismic array enables the inference of body wave source location through backprojection. Such teleseismic raypaths also elicit information on the interior structure of the Earth (Boué et al., 2013). In our earlier study (Reading et al., 2014), over a decade of continuous data (2000-2012) from the Warramunga Array (WRA) in central Australia were analyzed. The work was carried out in a single frequency band of 0.4-0.6 Hz and identified multiple surface wave arrivals surrounding Australia and three dominant P wave sources in the Southern Ocean and West Pacific for which the seasonal patterns were studied.

Here we analyze the frequency dependence of the microseismic wavefield in the frequency range of 0.325-0.725 Hz observed at WRA. We estimate its properties in eight distinct frequency bands, with a width of 0.05 Hz for each band, and include a detailed slowness-azimuth station correction (SASC) calibration. Although the frequency bands are narrow in the context of ocean induced seismic ambient noise analysis in general, the frequency range corresponds to ocean swells

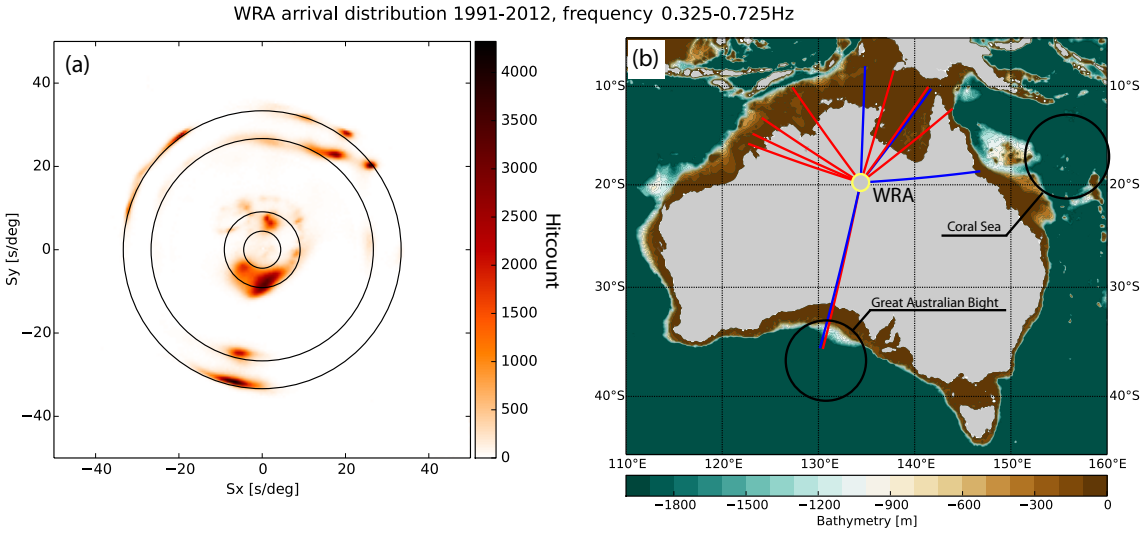

Figure 4.1: (a) 2D hit count histogram on a North-South (Sy) and East-West (Sx) slowness grid. This was derived using every one-hour segment of WRA data for the whole frequency range and time period of study using the IAS Capon algorithm. The outer circles are drawn at values of 30 s/deg and 26.5 s/deg corresponding to R_g and L_g slownesses. The inner circles are drawn at 9.1 s/deg and 4.5 s/deg and represent the boundaries for unbiased P wave backprojection (25° - 98°). (b) The backazimuth of regional surface wave maxima extracted from (a) and displayed on the continent of Australia centered on WRA (red: R_g Rayleigh waves, blue: L_g guided shear waves). The length of the displayed raypaths is not significant and the exact source location is discussed in the text.

or wind seas with periods between 2.75 and 6.15 s. This allows the investigation of variations in SM generation for each frequency band. The analysis is further extended from that of Reading et al. (2014) by including an additional decade of data (1991-2000) and, importantly, interpreting multiple distinct microseism arrivals within a particular time window, as opposed to only the largest. We relate our seismic results to ocean site effects, ocean and wind properties, and include a brief analysis of seasonal variations.

4.3 Data and methods

4.3.1 Overview of data used

We use data from the Warramunga Array (WRA), located in central Australia (Fig. 4.1), from 1991 to 2012. The array is operated by the Australian National University as part of the International Monitoring System (IMS) network and was originally deployed for the long-range detection of nuclear explosions. The multidecadal record from WRA has significant gaps of 4-5 months in the years 1997, 2006, and 2007, 8 months in the year 2009, and no data are available in the years 1998 and 1999. For all other years the data are complete.

4.3.2 Array properties

WRA initially consisted of 20 short period, vertical component stations deployed in an "L" shape with irregular interstation spacing of 2-3 km. In 1999, four three-component stations were added

to the existing network (Fig. S4.1a in the supplement material, figures are denoted with an 'S') and all stations were upgraded to broadband. The interstation spacing of WRA allows the accurate study of regional surface waves (0.3-1 Hz) and body waves (0.5-2 Hz) with respect to the array response (Fig. S4.1c-e). WRA provides a multidecade set of continuous seismic data in a central position in Australia, and is thus appropriate for the synoptic study of short period microseism properties. In this study, we focus exclusively on the vertical component of the WRA sensors.

4.3.3 Array calibration

It is well known that many small-to-middle aperture seismic arrays exhibit a systematic bias in slowness and backazimuth estimates (e.g. Manchee and Weichert, 1968). This bias can be mainly explained by bending/refraction of seismic waves at the boundary of geological structures beneath the array, for instance Moho topography (Jacobeit et al., 2013). With independent knowledge of the origin of the seismic signal, the bias can be accounted for by calculating mislocation vectors for the given array and the application of the resulting slowness-azimuth station corrections (SASCs). Here we perform mislocation vector analysis (Bokelmann, 1995; Bondár et al., 1999; Schweitzer, 2001) for WRA to ensure accurate slowness estimates for observed microseisms. For this purpose we consider earthquakes with a magnitude of 3.5 mb or higher from the International Seismological Centre (ISC) catalog (International Seismological Centre, 2012) for the two full years of 2010-2011. To obtain suitable coverage for the southern Indian Ocean, which has lower seismicity than areas to the north, we analyze all earthquakes below the latitude of 30° S for the additional years 2001-2009. We consider only earthquakes located at distances farther than 25°. Body waves that are generated closer than 25° turn in the upper mantle and may lead to biased results owing to triplicated arrivals. We therefore make use of epicentral distances greater than 25° in the study of body wave microseisms, with an upper limit of 98°. From this list, all earthquakes with overlapping P arrivals from different backazimuths are excluded, leaving a total of 22175 earthquakes.

The earthquake waveforms are extracted in 100 s lengths, where the P wave onset is positioned 50 s into the window. Each segment is tapered with a Hann window and an implementation of the IAS Capon beamforming (Gal et al., 2014) is used to estimate slowness and backazimuth. The recovered backazimuths are compared to those expected for the ISC locations, while slowness values are compared to theoretically predicted values from the 'ak135' model (Kennett et al., 1995). The mislocation vectors are presented in Fig. S4.1b, where a 0.5 s/deg grid spacing was used. To reduce statistical errors, we follow the methodology of Bondár et al. (1999) and compute the median for each slowness cell. Correction vectors are displayed if at least five earthquakes enter into the estimation, with the corresponding standard deviations of slowness below 1 s/deg and backazimuth below 0.3°. The slowness spectrum shows a good agreement with the results of Bondár et al. (1999) and highlights two potential backazimuths (170° and 330°) where corrections are significant. We do not see a systematic bias that would potentially point to a dipping geological layer (Jacobeit et al., 2013) below the array. The generated mislocation vectors are used to compute an interpolated vector field that extends corrections systematically to other slowness vectors. We take these corrections into account during backprojections of P waves.

4.3.4 Analysis methods

For the years 1991-1999 we evaluate a 1 h segment every 3 h owing to limitations in data availability, while for the years 2000-2012 all available hours of data are analyzed. For the continuous data recorded prior to 2000 (short period vertical, SHZ), we remove the instrument response. For data recorded after 31 December, 2000 (broadband vertical, BHZ), the instrument response is flat over the analyzed frequency bands and response deconvolution is not needed. The beamforming algorithm averages over multiple narrowband slowness spectra and its stability is ensured via diagonal loading of the cross power spectral density. It has been shown that IAS Capon recovers slowness vectors accurately and is able to resolve multiple arrivals (Gal et al., 2014) in a given time window. The analysis is performed in eight frequency bands with widths of 0.05 Hz in the range of 0.325 to 0.725 Hz. A 1 h record is divided into 35 time slices, with an overlap of 50%, and the Hann windowing function is applied to reduce spectral leakage. For each estimated slowness spectrum, up to 10 local maxima of surface and body waves within a $\pm$ 50 s/deg slowness grid are extracted. For the arrivals associated with local maxima, we require the estimated power to be greater than 80% of the global maximum to avoid spurious or sidelobe effects. An example of a beamforming analysis combined with the extraction of maxima from the slowness domain is presented in Fig. S4.2.

4.4 Results

4.4.1 Dominant microseism arrivals

Using the IAS Capon method, we identified $\sim 6.9 \times 10^6$ arrivals over the period of 1991-2012. In the following section we focus on the strongest arrivals, i.e. those corresponding to the absolute maximum of beam power in a particular time window. We find an approximately equal number of surface (52%) and body waves (48%) for the dominant arrivals. We observe a slight resolution increase in surface and body wave slowness peaks after 1999, which we attribute to the upgrade of instruments and the deployment of four additional stations; however, the results before and after the station upgrades are very similar and can therefore be evaluated together.

Surface waves

For surface waves, we find multiple spatially concentrated source regions and present the corresponding hit count plot in Fig. 4.1a. The analysis reveals two separate phases with velocities around 3.3 km/s and 4.1 km/s, which can be associated with fundamental mode Rayleigh waves (R_g) and supercritical S waves trapped in the crustal waveguide (L_g). We have validated both phase velocities, R_g 3.3$\pm$0.1 km/s and L_g 4.1$\pm$0.2 km/s, by performing IAS Capon analysis on R_g and L_g coda from a local earthquake. By extracting the slownesses from the maxima of the hit count plot (Fig. 4.1a), we generate raypaths oriented toward R_g and L_g source regions (Fig. 4.1b). The

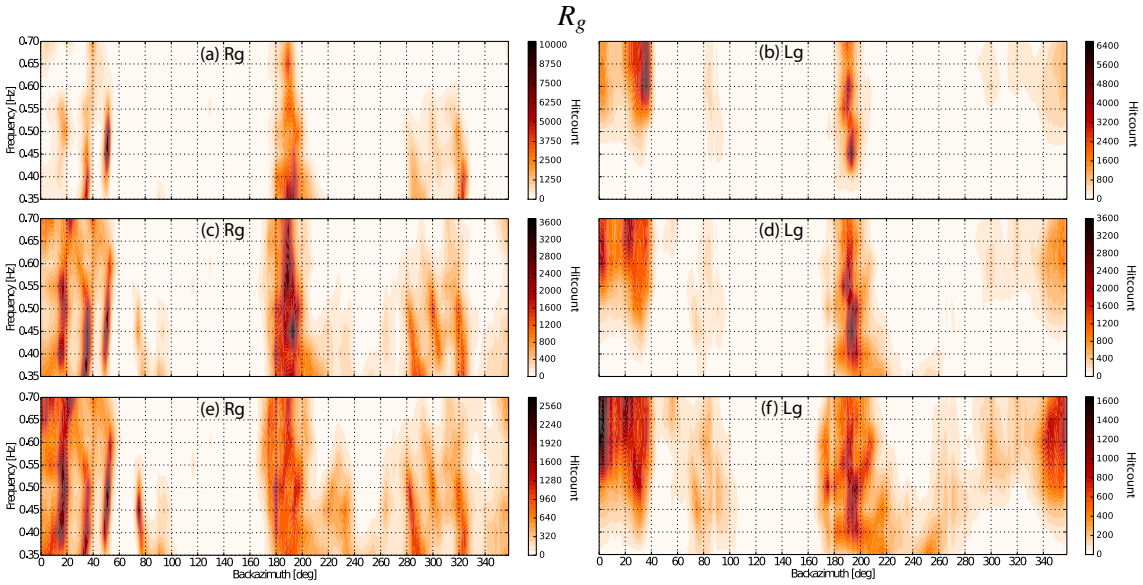

Figure 4.2: Representation of dominant (a) R_g and (b) L_g arrivals with respect to frequency. Weaker phases, namely second and third strongest surface wave arrivals, for R_g (c,e) and L_g (d,f) with respect to frequency.

result suggests the presence of favorable coastline conditions for the generation of short period microseisms, i.e. reflectors of swell and wind sea. This can either be small islands, close to coastal regions, as supported by the three arrivals from the northeast (Fig. 4.1b) or bays where a more coherent reflection of the ocean wave train over a larger area is likely. A summary of all eight frequency bands can be seen for R_g (Fig. 4.2a) and L_g waves (Fig. 4.2b). For lower frequencies (0.325-0.425 Hz) we find R_g waves only, while higher frequency bands (>0.5 Hz) show a transition to L_g waves. The figure further shows a frequency dependent signal strength, i.e. different sources dominate for different frequency bands. Only minor changes in backazimuth occur that might be connected to bathymetry effects (Kedar et al., 2008; Gualtieri et al., 2013). The only exception is an extended area of generation between the backazimuths of 180-220° in the low frequency bands (0.375-0.525 Hz), which gradually shifts towards a lower backazimuth as frequency increases. We analyzed the azimuthal sensitivity of WRA due to its station geometry (Fig. S4.3ab) and did not find any bias towards the arrival directions of R_g and L_g waves.

Body waves

Combining all eight frequency bands together, we obtain the P wave arrival hit count plot for the period of our study (Fig. S4.4a). Only arrivals that are between the two circles, which correspond to slownesses (distances) of 9.1 s/deg (25°) and 4.45 s/deg (98°), are used for backprojection. We assume P wave propagation for the purpose of body wave backprojection as this has been used successfully for microseisms in higher frequency range (Zhang et al., 2009) as in our study. A potential difficulty in the frequency dependent analysis is created by earthquakes. While lower frequencies show a relatively earthquake-free hit count summary, higher frequencies are affected by earthquake arrivals. This is due to the spectral properties of the ambient wavefield, as lower frequencies show greater amplitudes than higher frequencies (for our range 0.325-0.725 Hz), while

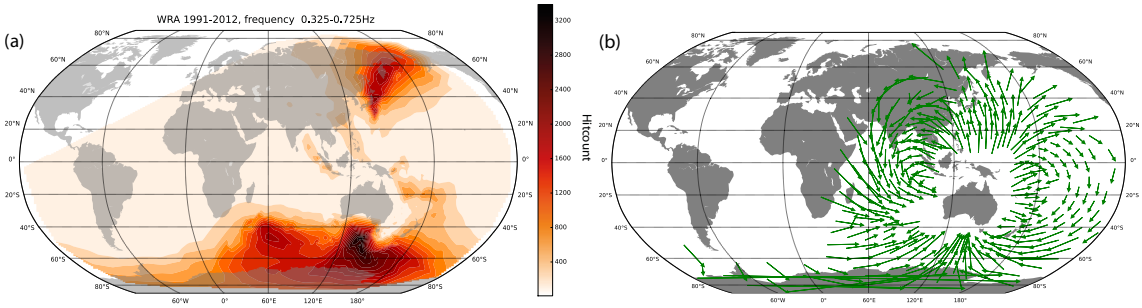

Figure 4.3: (a) Backprojection of dominant P wave arrivals for all eight frequency bands and the full study period with SASCs applied. Maxima are found in the southern Indian Ocean (south of Australia), the Kerguelen Plateau and the east coast of Japan. b) Backprojection of the mislocation vectors onto the world map to visualize their impact on the interpretation.

P arrivals from earthquakes tend to have larger SNR in the higher frequency range. We do not attempt to discard time intervals that are affected by earthquakes, as these still provide information on weaker ambient noise signals.

To visualize areas with high earthquake potential, we analyzed over 10000 earthquakes through a full year of the ISC bulletin (International Seismological Centre, 2012) (Fig. S4.4b). After accounting for these, three distinct noise sources remain that match our earlier study (Reading et al., 2014). We overlay the information on the figure with the mislocation vector results to indicate biased arrivals (Fig. S4.4a). We backproject body wave arrivals as P arrivals with the mislocation vectors plotted to stress the importance of the array calibration (Fig. 4.3). The P wave arrivals from the north correlate well with the east coast of Japan, arrivals from the south with the southern Indian Ocean (south of Australia), and arrivals from southwest with the Kerguelen Plateau. Although the east coast of Japan is a region of strong seismicity, we are confident that the observed body waves are generated by ocean waves (see also section 4.4.2). Without the SASCs, the Indian Ocean source would map more strongly on to the continent of Antarctica (assuming P and not PP propagation). This emphasizes the importance of applying the SASCs, which can be as large as 25°, i.e. 2780 km. We also analyzed the azimuthal sensitivity of WRA for P waves (Fig. S4.3c) averaged over all eight frequency bands and found our results to be robust.

The frequency dependent analysis reveals that the maximum number of arrivals for the lowest frequency band originate in the southern Indian Ocean (Fig 4a). The position of the peak shifts to the west for the second lowest frequency band and then continues to shift, with increasing frequency, toward the Great Australian Bight (Fig. 4.4a). For the P waves from the northern hemisphere, we find the source location in the lowest frequency band to be in the area of the Kamchatka Peninsula, namely north of the Sea of Okhotsk, shifting toward the east coast of Japan for the highest frequencies (Fig. 4.4b). The shifting locations of the dominant P wave arrivals for different bands in the southern Indian Ocean and Japan region will be examined in the context of ocean site effects in section 4.5.1. The arrivals from the Kerguelen Plateau do not show significant shifts in location with frequency for bands 3-8 (bands 1 and 2 do not have local maxima in P wave arrivals at this location). The corresponding slowness spectra that were used for the backprojection are presented in Fig. 4.4c. An increase in the hit count in earthquake arrivals with increasing frequency is observed, as described previously.

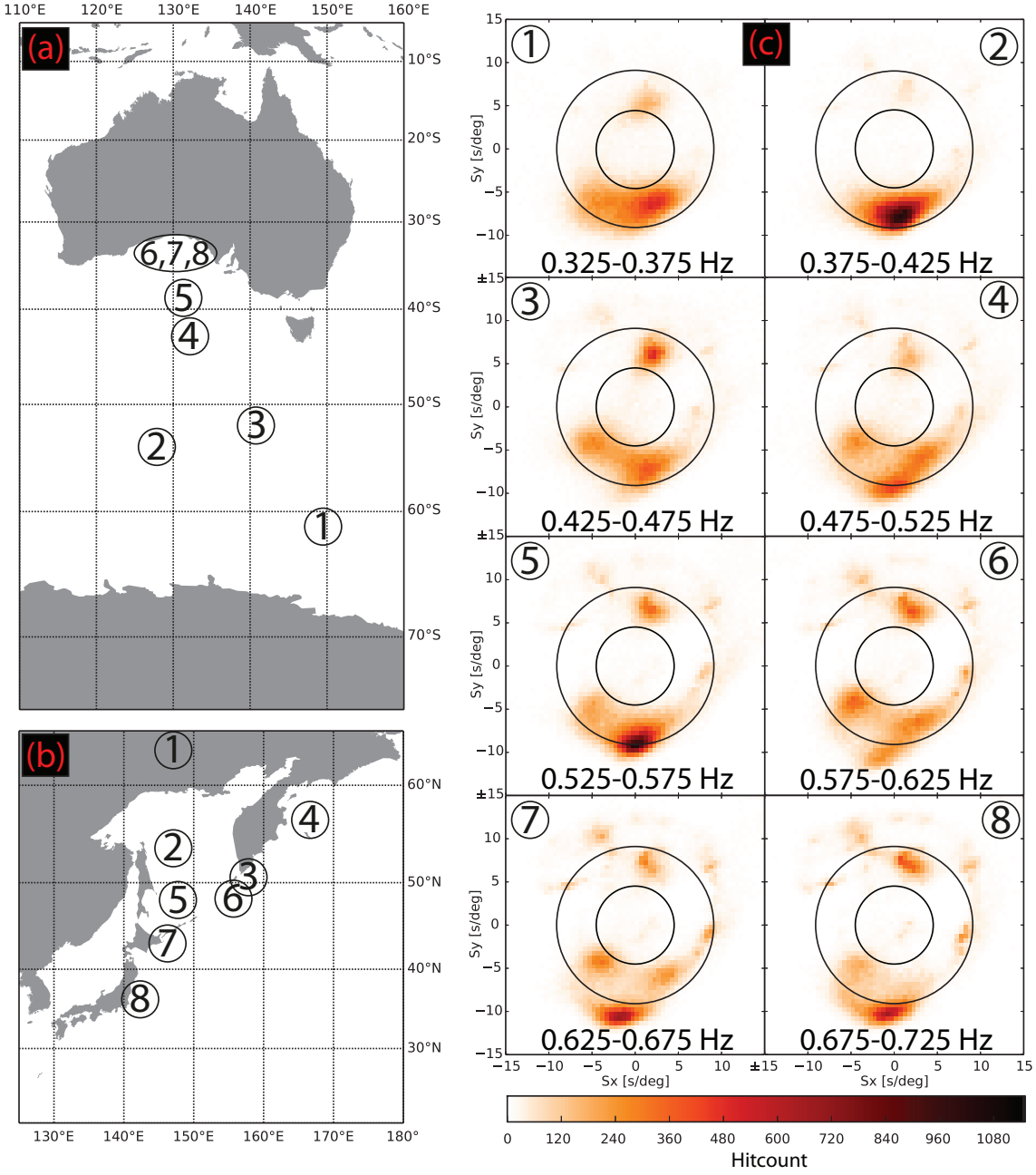

Figure 4.4: Maxima of dominant P wave arrivals for each frequency band with SASC applied. Arrivals for each frequency band from (a) south of Australia and (b) Sea of Okhotsk and Japan area. (c) Corresponding slowness plots for each frequency band. Analog to Fig. 1a, the area between the two circles is used for P wave backprojection.

4.4.2 Weaker microseism arrivals

Surface waves

We now focus on the analysis of weaker microseism arrivals that correspond to local (but not global) beam power maxima in slowness space. For every hour of processed data, we extract lower strength arrivals above a predefined threshold (those within 20% of absolute maxima). We then follow the procedure of section 4.4.1 and generate hit count plots in frequency-backazimuth space (Fig. 4.2c-f). The frequency dependent analysis for the weaker arrivals is in good agreement with the main arrival analysis and shows new regions that generate surface waves. For low frequencies, we observe weak L_g arrivals from the south and west, which were not previously identified. For frequency bands 2-5 (0.375-0.575 Hz) we observe surface wave arrivals from all directions except the southeastern region, which remains arrival-free for all periods and frequencies of our study. For higher frequencies, R_g and L_g wave arrivals are primarily from the south and north.

The analysis of weaker signals reveals that spatially concentrated surface waves are active in a broader frequency range. Sources appear to slightly change backazimuth with frequency. Arrivals between 280-330° shift toward a lower backazimuth with increasing frequency, while sources between 30-55° shift towards a higher backazimuth with increasing frequency. Possible reasons for the shift in frequency will be covered in the Discussion section. For dominant L_g arrivals, we observe a slight variability from the source region at 180-220° and multiple arrivals do not reveal variations in source location. We find good agreement between R_g and L_g source locations, which favors the idea of an R_g-to-L_g conversion mechanism (He et al., 2008), except for the source region at backazimuths near 50° which displays weak L_g arrivals. R_g waves dominate the lower frequencies and a possible conversion example can be seen around 35° where R_g arrivals are converted to L_g above 0.55 Hz.

Body waves

For body waves associated with secondary beam power maxima, we find results similar to those from global slowness maxima, where most of the arrivals correspond to the Kamchatka region, Kerguelen Plateau, and southern Pacific Ocean (Fig. S4.5). Earthquakes do not interfere in this analysis, as only weaker arrivals are plotted. This can be seen from the comparison between Fig. S4.5a and Fig. S4.5b-c, as areas with sharp contrasts that symbolize earthquake arrivals (Fig. S4.4b) are eliminated or minimally present for secondary beam power maxima. New arrival patterns appear that correspond well with the east coasts of Japan, Taiwan, and the Philippines. The weaker arrivals, which show no bias due to earthquakes, give us confidence that the observed body waves are generated by ocean wave interactions. For the northeast region, the Coral Sea correlates well with an increased arrival hit count region. An overview of backprojected P waves, combining dominant and weaker arrivals for all eight frequency bands, is shown in Fig. 4.5.

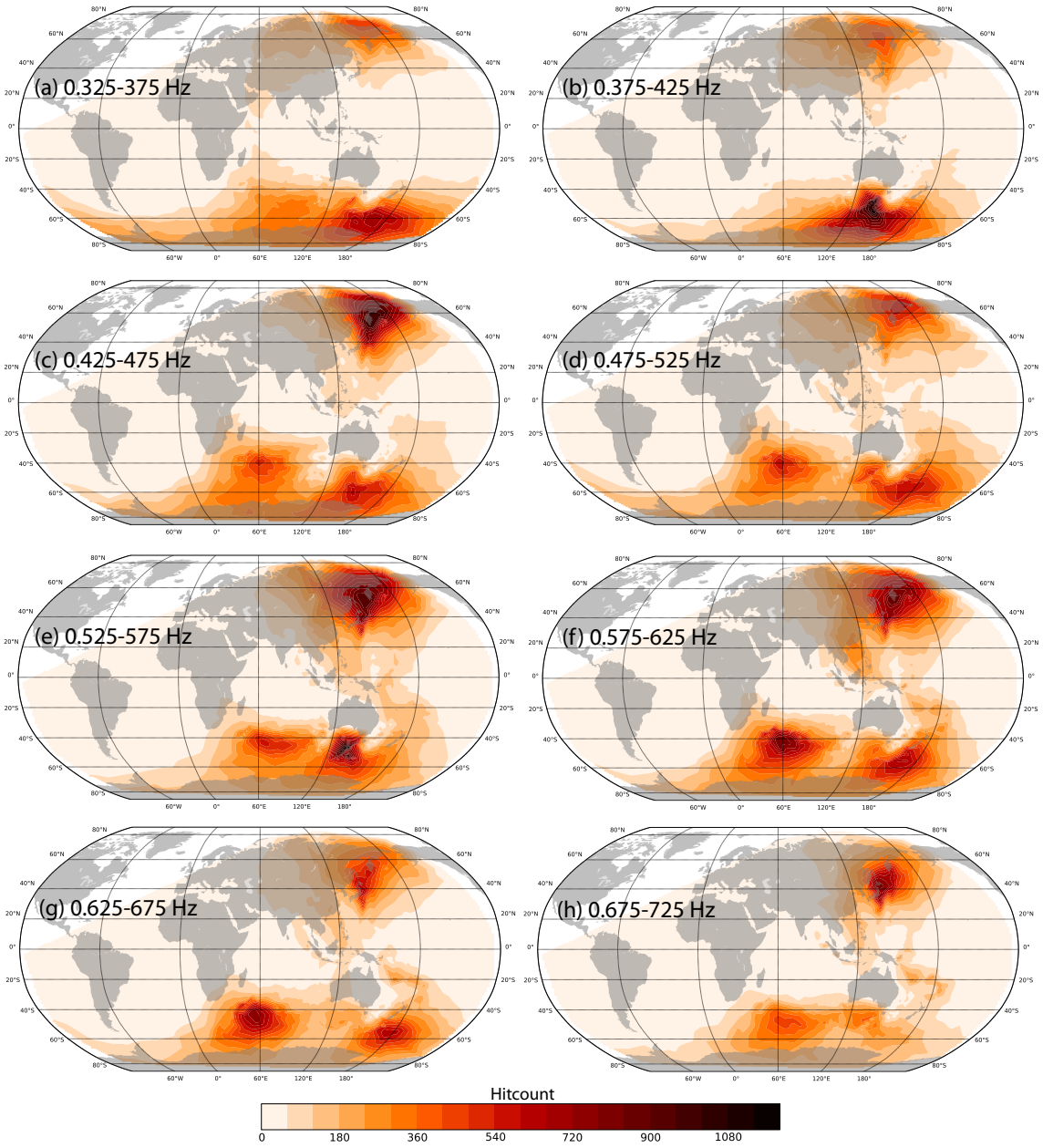

Figure 4.5: A summary of dominant and weaker P wave arrivals combined for each frequency band (a-h) and period of the study with SASCs applied. The addition of weaker arrivals allows for a more complete representation of P wave generation regions in each band.

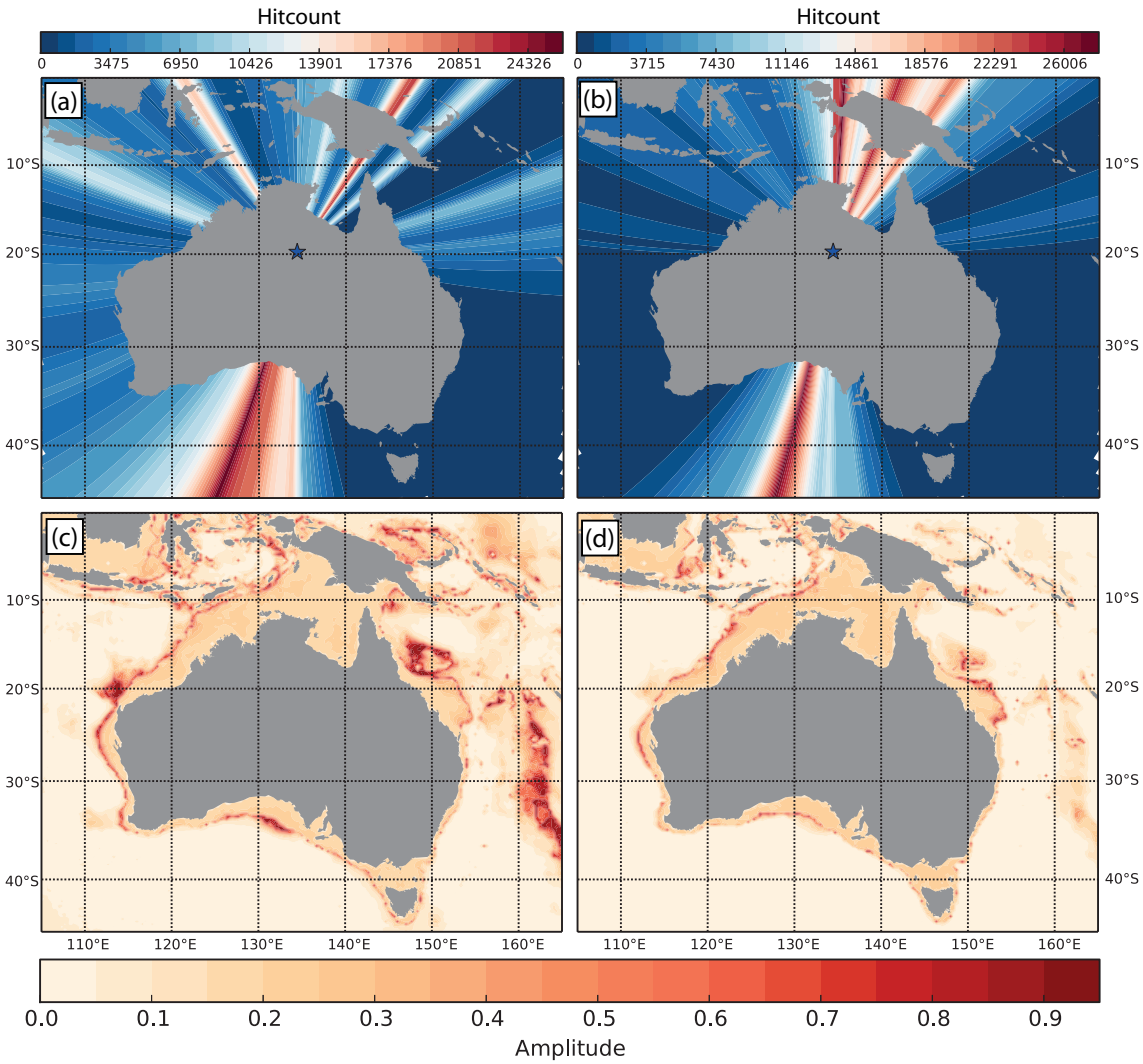

Figure 4.6: (a) Surface wave arrivals, R_g and L_g, for frequency band 1. The estimated arrivals are discretized into 2° bins and displayed on their respective raypaths. We have used up to five arrivals per hour for the whole period of the study. (b) R_g and L_g arrivals for frequency band 8. The fundamental amplitude coefficient derived from (Longuet-Higgins, 1950) is displayed for the appropriate frequency: (c) band 1 and (d) band 8.

4.5 Interpretation

4.5.1 Effect of bathymetry

We relate our results to the bathymetry and frequency dependent amplitude coefficients for a half space over a flat-Earth model (Longuet-Higgins, 1950) for the analysis of surface waves. The coefficients can be seen as an energy transfer function between the liquid and solid layers and are dependent on the depth of the ocean layer and the seismic wave frequency. The maximum of energy transfer occurs at depth and frequency combinations that can be associated with resonant behavior and differs between seismic wave phases (R_g, P, S...). For the analysis of P waves, we use the approach of Gualtieri et al. (2014) in which the amplitude coefficients are described by a plane wave decomposition and are in addition dependent on the distance between source and receiver. We compute amplitude coefficient maps for the case of surface and body arrivals and compare them with observations (sediment layers are not accounted for in both cases).

For surface waves, we display the frequency bands 1 (Fig. 4.6a) and 8 (Fig. 4.6b) as a sum of all years for combined R_g and L_g arrivals and their corresponding fundamental coefficient maps for 0.35 Hz and 0.7 Hz, (Fig. 4.6c,d). At 0.35 Hz, the regions with high amplitude coefficients show some surface wave arrivals but cannot explain all arrivals. For spatially concentrated sources in the north, the amplitude map does not explain the strong directional behavior found in the data. For higher frequencies, we find a reduction of high amplitude regions that is well correlated with the observed seismic arrivals for these backazimuths. Owing to the higher frequency, areas with favorable amplitude coefficients move into shallower water yet they still cannot explain the sources from the north and south. We see a reduction in the number of arrivals from distant coastlines. The spatial concentration of surface arrivals cannot be explained by bathymetry effects alone in either case, and possible reasons for this will be discussed in section 4.6.

For P waves, we generate amplitude coefficient maps following the work of Gualtieri et al. (2014) for the region south of Australia (Fig. 4.7a) and the Kamchatka/Japan region (Fig. 4.7b), for all eight frequency bands. For the region south of Australia we find the maxima of P wave arrivals in the first four bands to be in close vicinity to favorable amplitude coefficient regions. For higher frequency bands, the maxima of arrivals are found in more shallow water and are less correlated than for lower frequencies. For the northern hemisphere, we see good correlations in bands 2, 4, 5 and 6. Bands 7 and 8 are again associated with shallow water/coastlines and do not show strong correlations with amplitude coefficients. Band 1 shows the maximum of P arrivals to be located on land north of the Sea of Okhotsk. A possible explanation is that these are actually PP arrivals from one of the well-known microseism source regions in the North Atlantic (Kedar et al., 2008). For the Kerguelen Plateau, the source locations are found within a few degrees of the Kerguelen Islands for bands 3-8 (Fig. 4.5d-h).

The maximal P wave arrivals in the low frequency bands are located in areas with favorable amplitude coefficients, but not all areas with high amplitude coefficients show P wave arrivals, hence ocean site effects alone cannot explain the observed distribution of P wave arrivals. We expect the inhomogeneous swell distribution and spatial reflector distribution to be the main causes. The majority of storms follow a certain spatial pattern and generate similar swells that can be reflected by coastlines. Ocean regions close to coastlines that lie in the main storm tracks therefore generate better conditions for SM generation (Ardhuin and Roland, 2012). For higher frequency bands, we observe a decrease in the influence of ocean site effects on the P wave generation regions and coastline reflection seems to play a more important role. It should be further mentioned that coastline reflection is not the only contribution for favorable SM generation regions, we detect P wave arrivals east from the Kerguelen Islands, which suggests that ocean swells bend around the islands to form areas with opposing wave trains.

4.5.2 Correlation with ocean and wind dynamics

Our multidecadal short period microseism analysis allows us to search for general correlations between the seismic arrivals and an ocean wave hindcast. The hindcast was performed using the WAVEWATCH III, v4.08 software, and was forced hourly with Climate Forecast System Reanalysis surface winds and sea ice variations (Durrant et al., 2013a,b). The wave spectra are discretized

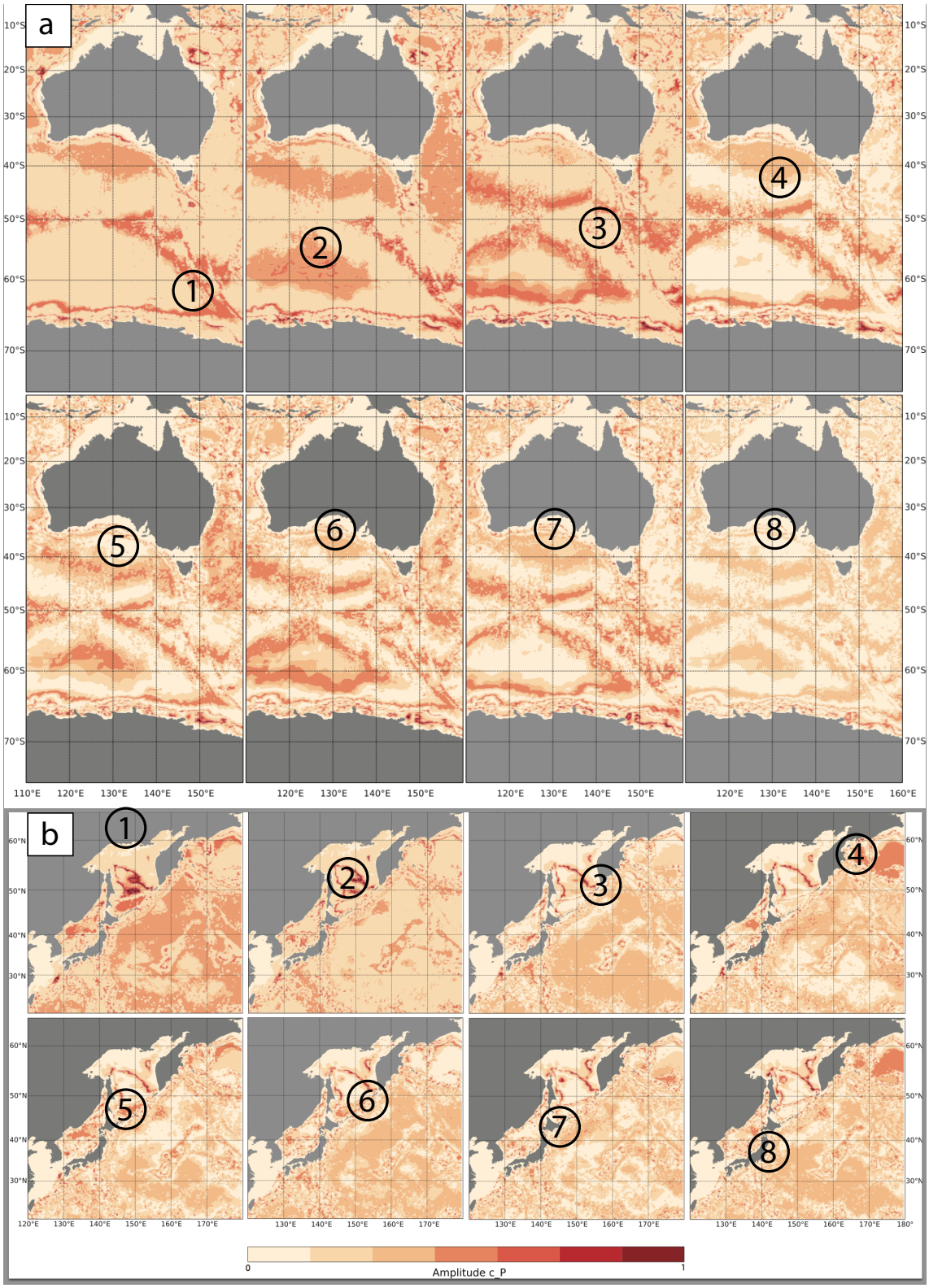

Figure 4.7: Amplitude coefficients for all eight frequency bands for (a) south of Australia and (b) Kamchatka/Sea of Okhotsk/Japan region. The maximum of P wave arrivals is marked with a black circle for each band (SASC applied). The amplitude coefficient maps are generated by averaging over the whole width of the frequency band.

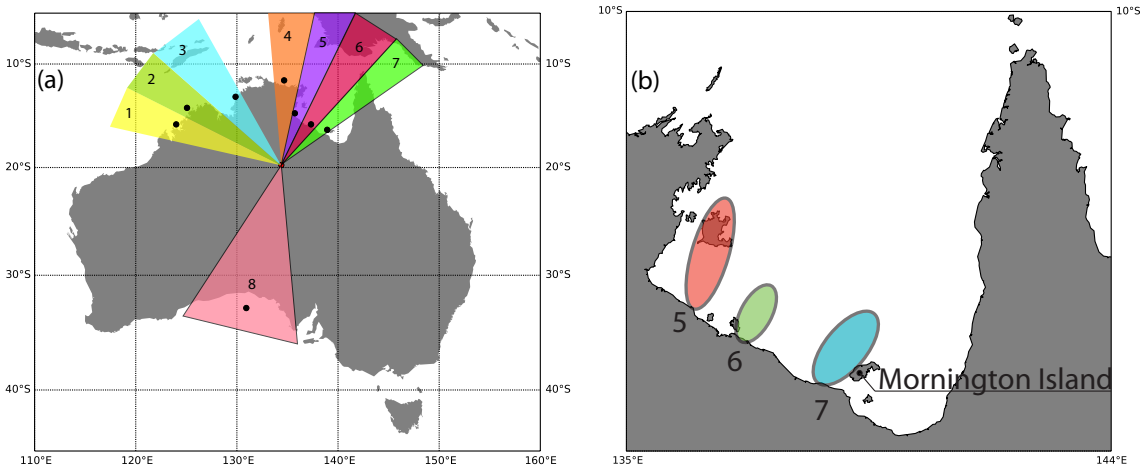

Figure 4.8: (a) Discretization of backazimuths for the comparison with ocean and wind dynamics. A grid location that coincides with the maximum of surface wave arrivals is selected in each sector to represent the local ocean and wind properties. (b) Possible generation locations for R_g waves in the northeast basin of Australia.

over 29 exponentially spaced frequencies between 0.038-0.5 Hz and 24 equally spaced directions (Δ=15°). Coastal reflections are not taken into account in this model.

We discretize the seismic arrivals into sectors (Fig. 4.8a) that coincide with spatially concentrated surface wave backazimuths extracted from a histogram over the full period of the study. For each sector, we select a grid point of the ocean wave hindcast to represent the local wave and wind state. The location of the grid point is selected to be closest to the maximal arrival count of each sector and close to the coastline. For each surface wave arrival from a sector n, we record the ocean and wind state at grid point n during the same time period to investigate correlations between seismic arrivals and the ocean and wind state. We acknowledge that wave height is not, in general, the dominant factor for the generation of microseisms (Obrebski et al., 2012), which arise due to the interaction of opposing wave trains; however, within the areas shown in section 4.4, where surface waves are consistently generated, the scenario of opposing wave trains is realized and wave height is a good additional correlation parameter.

The results for sector 8 and band 1 are summarized in Fig. 4.9. We find a strong correlation between seismic arrivals and ocean wave height and wind speed, and a slightly preferred mean wave and wind direction. For a complete picture, we extend this analysis to all eight frequency bands and show wave height and wind speed correlations for sectors 6, 7, and 8 (Fig. 4.10). These three sectors show unique correlation patterns with varying frequency. Sector 6 (north) shows the highest correlation for band 8 and reduced correlation toward band 1, sector 8 (south) shows the inverse effect with frequency and sector 7 shows the highest correlation in band 3. The important information in these graphs is that for location 6, which is sheltered from long period ocean swells (>6 s), higher frequency Rayleigh waves are more likely to be excited by smaller ocean waves or less strong wind speed in comparison to band 1. In order to generate Rayleigh waves from sector 6 and band 1, the wind speed and wave height have to be greater on average. The hindcast also shows the dominant wind and wave direction to be around 270°. As the northern ocean basin is sheltered from remote swells and dominated by east winds, the local wind sea is the driving mechanism for the generation of Rayleigh waves. For the exposed southern sector 8, long period swell mostly

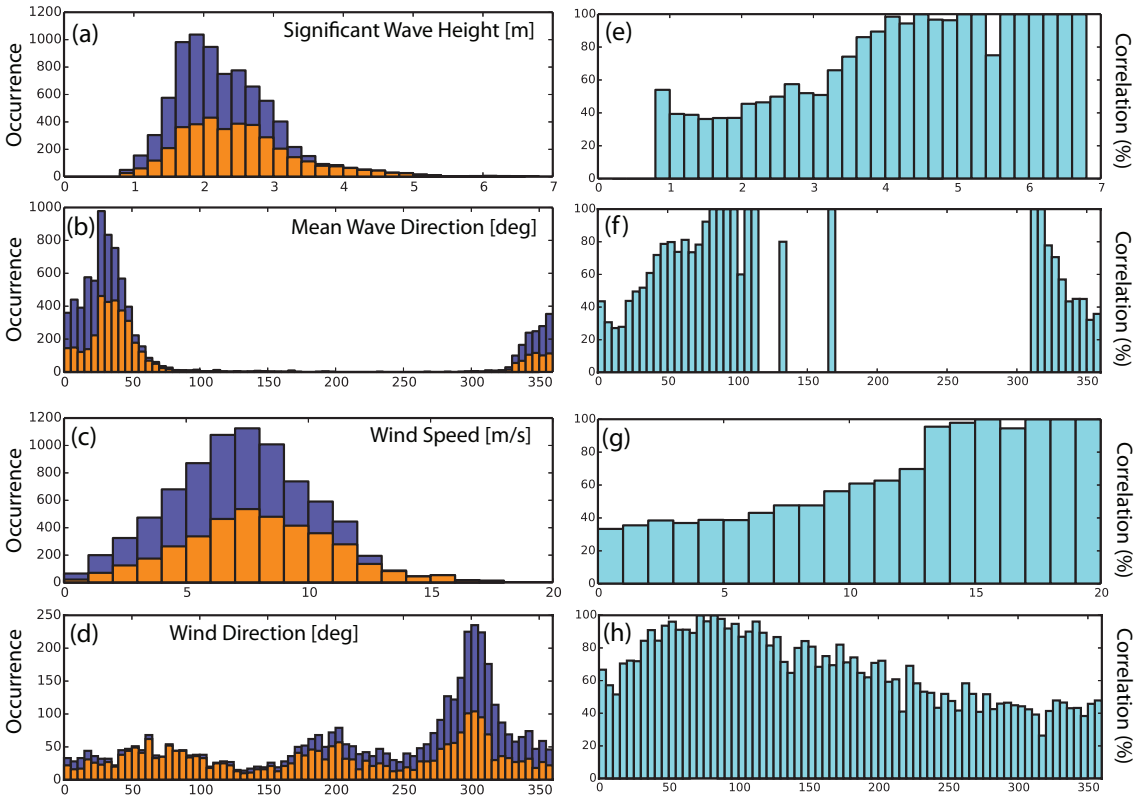

Figure 4.9: Parameters extracted from the ocean hindcast model for sector 8 (Great Australian Bight) and frequency band 1, for the full year of 2011: (a) wave height, (b) mean wave direction, (c) wind strength and (d) mean wind direction. Parameters are shown as a histogram for the complete year (violet) and for time intervals when corresponding dominant surface wave arrivals were observed (orange). The correlation between the two histograms (violet and orange) is given in the right hand column (e-h). Correlation for mean wave height is only plotted if at least 10 measurements for a given direction occur during the year. Results for wind direction are constrained to wind speeds higher than 7 m/s as lower wind speeds are unlikely to have any effect on the generation of surface waves in frequency band 1.

originates from remote parts of the southern Indian Ocean and seismic arrivals are only observed during times of strong winds and increased wave heights for band 8. The strong source at sector 7 in band 3 cannot be explained by the hindcast data alone. WRA is recording Rayleigh waves from sector 7 mainly for wind and swell directions between 250-330°. The generation of Rayleigh waves is likely to be connected with the location of Mornington Island (Fig. 4.8b) and resonance effects between the coastline and Mornington Island may be the cause of the strong source in band 3.

The above results represent a yearly average for the seismic and ocean hindcast data. To highlight the diversity of the secondary microseism wavefield, we display the arrival direction of the dominant surface wave in each frequency band for a single hour (Fig. 4.11a). We find the two lowest frequency bands pointing southwards, while higher frequency bands show arrivals from the northeast. We further present the ocean wave height (Fig. 4.11b) and dominant wave period (Fig. 4.11c) for the same time frame (1 January, 2010, 3:00 UTC). For the Great Australian Bight, we find a swell height around 3 m and period of 7-8 s. This fits well with the seismic observations for the lower frequency bands. To the northeast, we find a swell height below 1 m and periods below 4 s, which fits well with the observations in the higher frequency bands and supports our

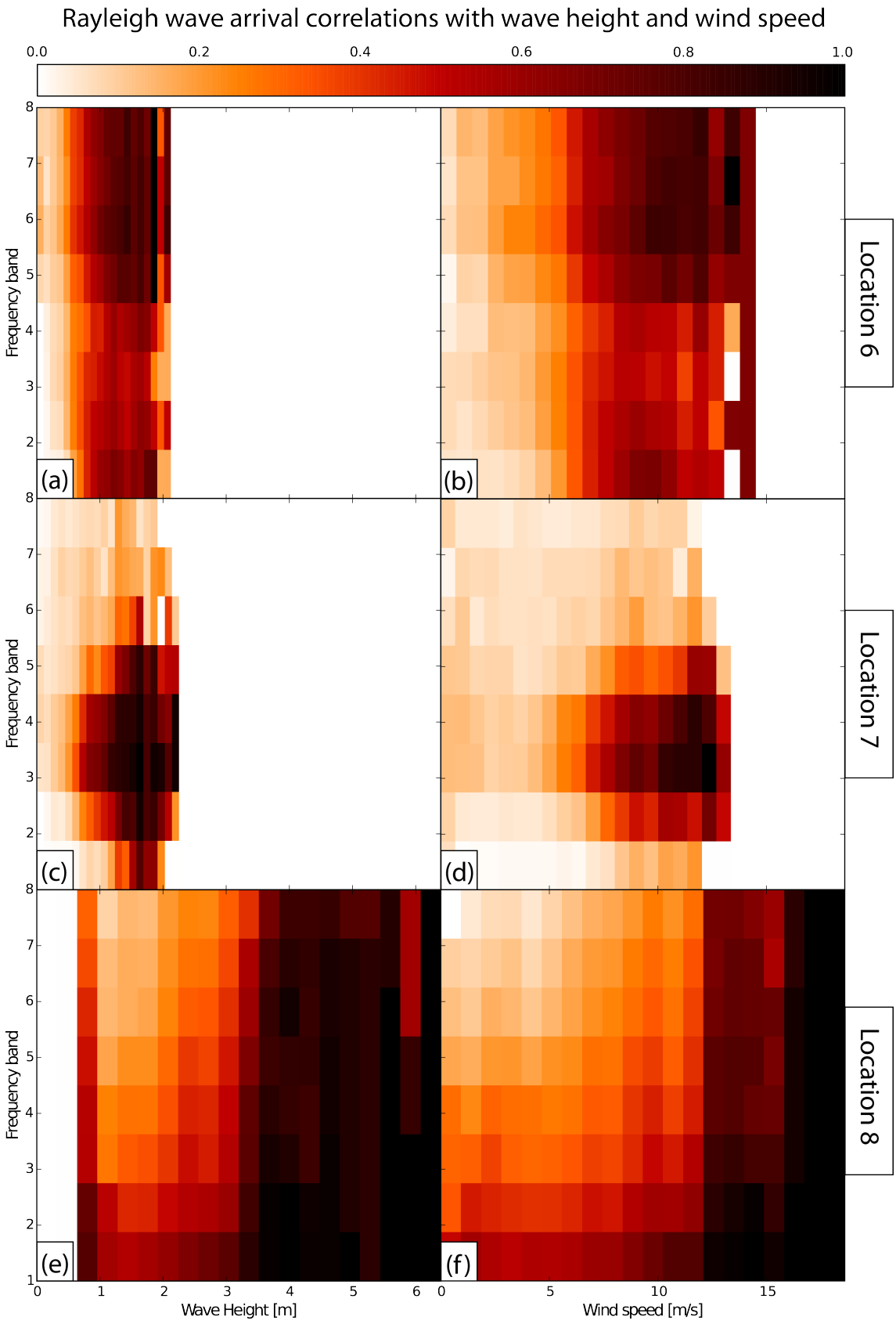

Figure 4.10: Frequency dependent correlations between arrivals of Rayleigh waves and wave height (left side) and wind speed (right side) for location 6 (a,b), 7 (c,d) and 8 (e,f).

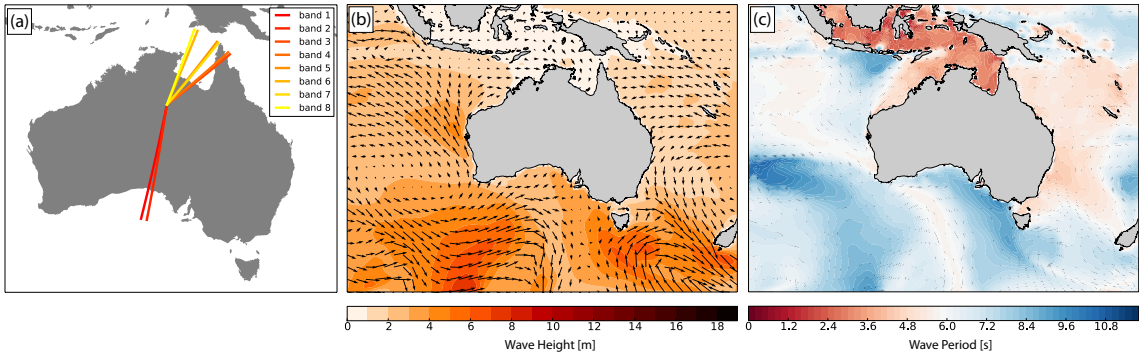

Figure 4.11: (a) Dominant surface wave arrivals for 8 different frequency bands observed in the same 1 hour record at WRA for the date 2010-01-01, 03:00:00 UTC. The estimated backazimuth is strongly dependent on the frequency band. The length of the raypath is arbitrary. (b) Wave height and (c) wave period for the same date as predicted by the ocean hindcast. Arrows in (b) display the wind direction and length of the arrow corresponds to wind speed.

previous conclusion that the wind sea is the main contributor to the generation of higher frequency secondary microseisms. The average depth for the northeast sources is around 50-60 m and shows that Rayleigh waves are excited in shallow waters.

4.5.3 Seasonal variations

To examine the seasonal patterns of surface waves at WRA, we sum all arrivals in all frequency bands for the whole time period of the study (Fig. 4.12). The figure is normalized and shows a monthly average of each of the sources. We find the Great Australian Bight (sector 8, Fig. 4.8a) to be the main contributor to microseism arrivals over the whole year, with a minimum of activity in February and a maximum in September. This can be explained by the fact that the Great Australian Bight is the closest southern coastline to WRA that receives major swells and the main swell direction has a frontal incident angle on the coastline, which would allow wave reflections over a large area. Sectors 4, 5, and 6 display similar activity with a maximum in June, while sectors 1, 2, and 3 display the inverse pattern with a maximum in January. Sector 7 remains relatively constant over the whole year, on average.

To examine the long-term stability of the seismic arrivals, we next evaluate each year separately. The data do not reveal any changing trend except for marginal variations, which can be explained by strong storm events. The seasonally dependent seismic arrival count also remains the same for each year and each frequency bin, which suggests that global swell and wind patterns remain approximately the same. The seasonality of body waves recorded at WRA has been discussed previously by Reading et al. (2014) and is in agreement with our present results for the Kerguelen Plateau and Sea of Okhotsk/east Japan region (Fig. 4.12b). The Kerguelen Plateau shows its minimum in January and displays a slow rise in P wave generation that peaks in October. For the Sea of Okhotsk and east Japan we find a similar pattern, which peaks in December and displays its P wave minimum in July. The number of estimated P waves from the Great Australian Bight correlates well with the surface wave pattern from this location and peaks in the southern

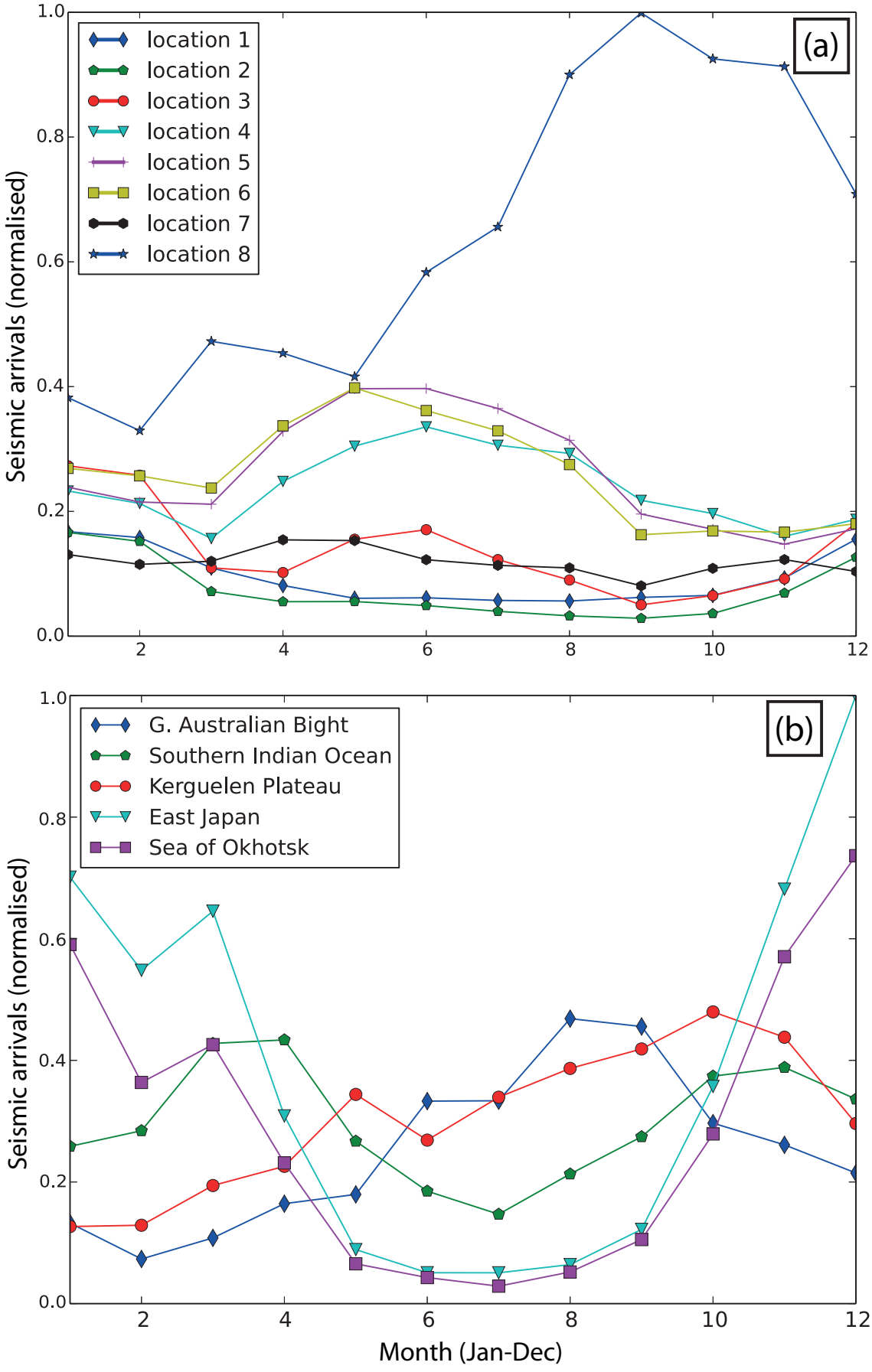

Figure 4.12: Seasonality shown as seismic arrival hit count (normalized) per month for (a) surface waves and (b) P waves. See Fig. 4.8a for the match to geographic location for surface waves. P wave arrivals for the southern Indian Ocean are mostly those in the region south of Australia. The 5 strongest arrivals per evaluated hour were used for the computation of monthly averages.

hemisphere winter months. This suggests that P waves are probably generated by coastal reflections as well, by the same swell systems that excite surface waves. The source in the southern Indian Ocean shows two peaks, in April and November, which are consistent with peaks in wind strength data in this region.

4.6 Discussion

In this section we discuss the possible mechanisms for the conversion of R_g-to-L_g waves, followed by the generation region of surface waves. Further, we discuss the correlations with an ocean wave hindcast, and swell and wind parameters, in more detail. The results in section 4.4.1 show an increase in the relative abundance of L_g with respect to R_g, with increasing frequency. Although most of the microseism energy is present in the form of Rayleigh waves (Lacoss et al., 1969), a previous study on IMS arrays and short period microseisms has shown Lg waves to be the dominant contributor in the frequency range of 0.5-4 Hz (Koper et al., 2010). As Lg waves are unlikely to propagate in the oceanic crust (Zhang and Lay, 1995; Koper et al., 2010) argued that irregular morphology of coastlines is a possible cause for L_g excitation.

For explosive seismic sources it has been suggested that L_g waves are generated by near-source scattering of R_g waves (Patton and Taylor, 1995; Gupta et al., 1997). The conversion mechanism/transfer function was found to be frequency and source-depth dependent (Myers et al., 1999). Additionally, a numerical study was performed to investigate the influence of a rugged free surface on seismic phase conversion in the frequency range of 1-4 Hz (He et al., 2008). It was found that a considerable amount of R_g energy is scattered into L_g waves for low frequencies (1 Hz). In our study, we find the backazimuth of impinging R_g and L_g arrivals to be similar (Fig. 4.2), which favors an R_g-to-L_g conversion for which irregular morphology of coastlines or rugged surface scattering are potential candidates.

The analysis of surface wave microseism locations shows a stationary behavior with respect to frequency over the full duration of the study. This supports our assumption that coastline reflections are the main contributors to the generation of surface waves around Australia, as coastline geometry, bathymetry, and storm tracks remain constant over two decades. We find small variations between the results estimated before and after 2000. Since all post-2000 results show a similar behavior, the small differences in the arrival patterns are likely to be connected to different seismic instruments and the absence of four stations in WRA prior to 1999. Although we find concentrated source regions for surface waves, their actual generation distance from the coasts is unknown. Observing the arrivals from the north (Fig. 4.6a,b) and relating them to the amplitude maps (Fig. 4.6c,d), we do not find any relation that can explain the strong geographical concentration of source regions. The main factor for this spatial concentration should therefore be the coastline geometry, which supports the idea of nearshore generation regions.

It is possible in surface wave microseism analysis to use multiple arrays to infer the distance to the source region via triangulation (Cessaro and Chan, 1989; Cessaro, 1994; Friedrich et al., 1998). We explored this possibility by analyzing 6 years of data from the Alice Springs Array (ASAR, for station configuration see Fig. S4.1a), which is located about 410 km south of WRA.

Figure 4.13: Triangulation of surface waves from ASAR and WRA. The red raypaths denote R_g waves while blue denote L_g waves.

ASAR has smaller interstation spacing and aperture compared to WRA, and so its array response is optimal at slightly higher frequencies. However, we can compare the backazimuths of surface wave arrivals for these two arrays because our results have shown that the backazimuth of surface waves remains relatively constant with frequency. The ASAR results confirm some locations seen by WRA (Fig. 4.13). For arrivals from the north and south, for which ASAR and WRA are aligned with the source direction, triangulation does not yield meaningful information on the source distance from the shorelines; however, for arrivals from the northwest we find the source location via triangulation to be immediately offshore. We conclude that the generation of surface wave microseisms is mainly driven by coastal reflections, aided by bathymetry effects. The slope-coastline configuration does not seem to play an important role in the generation of short period surface waves. The figure also shows that R_g and L_g waves are observed for the same source region by the two arrays. This finding strengthens the idea of an R_g-to-L_g conversion.

For weaker surface wave arrivals we observe a small shift in backazimuth with varying frequency (Fig. 4.2). A possible explanation is a frequency dependent coastal reflection coefficient, hence a varying dominant frequency for different spatial points. For the sources in the north west, 280-330°, the mean swell direction is from the southern Indian Ocean and with increasing frequency we see these sources shifting toward a lower backazimuth (south). We see the same effect for the surface wave sources in the north east, 10-55°. The mean swell direction for the north

east basin is from the east to west and for increasing frequency the generation location is shifting toward a higher backazimuth, i.e. east towards the swell direction.

We find both R_g and L_g arrivals from each source region with the exception of the region around a backazimuth of 50°. The L_g signal is absent from the dominant summary plot (Fig. 4.2b) and starts showing a weak presence for tertiary L_g arrivals (Fig. 4.2f). We performed a correlation analysis between the ocean hindcast and the recorded seismic arrivals to investigate the Coral Sea as a possible source generation location, as the re-entry of the L_g phase might be attenuated due to the crossing of the oceanic lithosphere. The results show correlation coefficients below 0.20 and a random distribution with wave height and wind speed between seismic arrivals and the Coral Sea hindcast parameters. Because all other sources show a strong correlation, we conclude that the seismic signal does not originate from the Coral Sea, but from a closer location. Therefore, the correlation of Rayleigh waves with the ocean hindcast shows great utility for the identification of the generation region in the case of a raypath crossing multiple coastlines.

Further insight can be gained by observing the distribution and correlation between Rayleigh wave arrivals, mean wave direction (Fig. 4.9b,f), and wind direction (Fig. 4.9d,h) for sector 8 and band 1. The majority of the swell is generated in the southern Indian Ocean and reaches sector 8 around 25°. As can be seen from the mean wave direction correlation, certain wave directions are more likely to generate Rayleigh waves that can be measured at WRA. We observe a local minimum for the correlation coefficient around 10°-15° and increasing toward 290° or 110°. A possible explanation is that the reflection coefficient of coastlines is swell direction dependent and can promote suitable conditions for the generation of secondary microseisms. For swell directions that face away from the coastlines, it is likely that two swell/wind sea trains are responsible, which would explain the high correlation and the rarity of the event at the southern Australian coast. The wind direction correlation shows a smoother distribution and a trend toward onshore wind. The trend toward onshore wind becomes stronger with increasing frequency and other wind directions show a less correlated behavior. This is in agreement with the conclusion that higher frequency arrivals are generated by local wind sea (Zhang et al., 2009).

4.7 Conclusion

We have evaluated two decades of ambient seismic noise in a frequency dependent analysis of vertical component data from the Warramunga Array in central Australia. For an accurate interpretation of the incoming signals, we made use of the IAS Capon algorithm followed by a mislocation vector analysis to reduce the slowness and backazimuth bias in P waves attributed to 3D variations in geology near the array.

For surface waves, we find preferred backazimuthal directions except from the southeastern region, which remains arrival-free for the entire time period and frequency band of our study. Lower frequency bands (<0.55 Hz) are dominated by R_g arrivals from a range of distances, while higher frequency bands (>0.55 Hz) show a transition to L_g arrivals and a preference for nearby coastlines, except for the Great Australian Bight. Weaker arrivals show new spatially concentrated generation regions and extend the frequency range of previously observed microseism sources at

WRA (Reading et al., 2014). R_g and L_g waves display similar backazimuths, which suggest an R_g-to-L_g conversion mechanism, possibly similar to the generation of L_g from nuclear explosions (Patton and Taylor, 1995; Gupta et al., 1997). Irregular coastline morphology and the scattering on a free rugged surface were identified as possible conversion mechanisms. Surface waves can show a backazimuth drift with respect to frequency, which is most likely connected to bathymetry effects. Triangulation with the Alice Springs Array (ASAR) and the strong spatial concentration of the arrivals suggest the generation regions of surface waves to be close to coastlines.

P wave microseism locations are found to be frequency dependent. For the lower frequency bands (0.325-0.475 Hz), we find the dominant arrivals to originate from deep waters in the southern Indian Ocean and north of Japan (Sea of Okhotsk), showing good correlation with regions with strong amplitude coefficients. For higher frequency bands (0.525-0.725 Hz), we see a migration of body wave arrivals towards shallower regions: the Great Australian Bight, the Kerguelen Plateau, in the South Pacific Ocean south of New Zealand, and the east coast of Japan. In higher frequency bands, these regions are less correlated with regions with strong amplitude coefficients and the presence of coastal boundaries outweighs the importance of bathymetry effects. We further show that weaker body wave arrivals are not contaminated by earthquake arrivals and, in fact, reveal new P wave source regions. In our study, weaker arrivals revealed increased P wave activity from the northeast Coral Sea, the eastern coastlines of the Philippines and Taiwan.

We compared our microseism observations to a WAVEWATCH III hindcast and observed strong correlations between microseismic activity and ocean wave height and wind speed for regions with consistent surface wave sources. We further observed a preferred, onshore, wind direction for the generation of surface waves. The wind direction is found to be increasingly important for higher frequencies, as the local wind sea is the main generator of surface waves observed at WRA. The hindcast can be used to distinguish between surface wave generation regions in the case of a raypath crossing two or more coastlines.

4.8 Acknowledgements

We acknowledge data access through the IRIS DMC archive, the Australian National University, and the ISC. We thank the Tasmanian Partnership for Advanced Computing (TPAC), which enabled the access to its HPC Facilities. The research was funded by the Australian Research Council (DP150101005). MG is supported through a Tasmanian Government Research Scholarship. L.G. acknowledges support from a Lamont-Doherty Earth Observatory Postdoctoral Fellowship and the Brinson Foundation. KDK and RB acknowledge support from NSF-Earthscope under award EAR-091558. IAS Capon code and beamforming results for the whole span of two decades are freely available in the NetCDF4 file format and may be obtained by contacting the University of Tasmania authors.

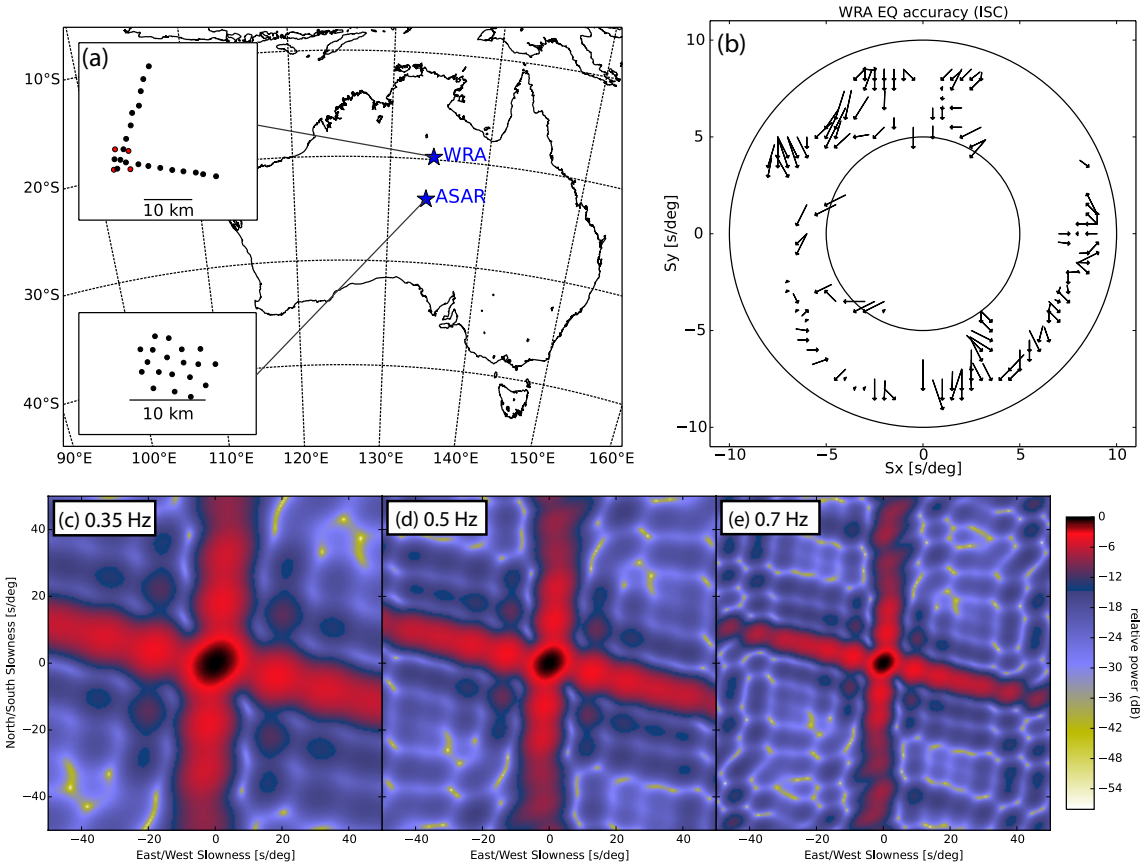

Figure S4.1: (a) The Warramunga Array (WRA) is located in the center of Australia, Northern Territory. In 1999 the station configuration was upgraded from 20 stations (black) with 4 additional stations (red). (b) Mislocation vectors calculated from over 20000 earthquakes displayed on a 11 $\times$ 11 s/deg slowness grid with a resolution of 0.5 $\times$ 0.5 s/deg. The arrowhead points towards the 'true' slowness vector derived from locations in the ISC Bulletin and the spherically symmetric Earth model ak135. Circles are drawn at values of 5 and 10 s/deg. (c-e) Array response function for WRA across the frequency band considered in this study.

4.9 Supplementary material

This material contains 5 additional figures to support the main article. Figure S4.1 displays the location of the Warramunga and Alice Springs array and their shape. Further the mislocation vector analysis is visualized for WRA and the array response function is plotted for 3 different frequencies relevant to our study. Figure S4.2 shows an example of a beamforming result combined with the procedure of picking arrival maxima. Figure S4.3 displays the azimuthal sensitivity of WRA for R_g, L_g and P waves. Figure S4.4 shows P waves overlaid with the mislocation vector analysis to show potentially biased body waves arrivals. We also supply a plot of earthquake arrivals to show regions with strong seismicity. In Figure S4.5, we visualize dominant, second strongest, third strongest and weaker body wave arrivals. For weaker arrivals the bias due to earthquakes disappears and new generation locations are observed.

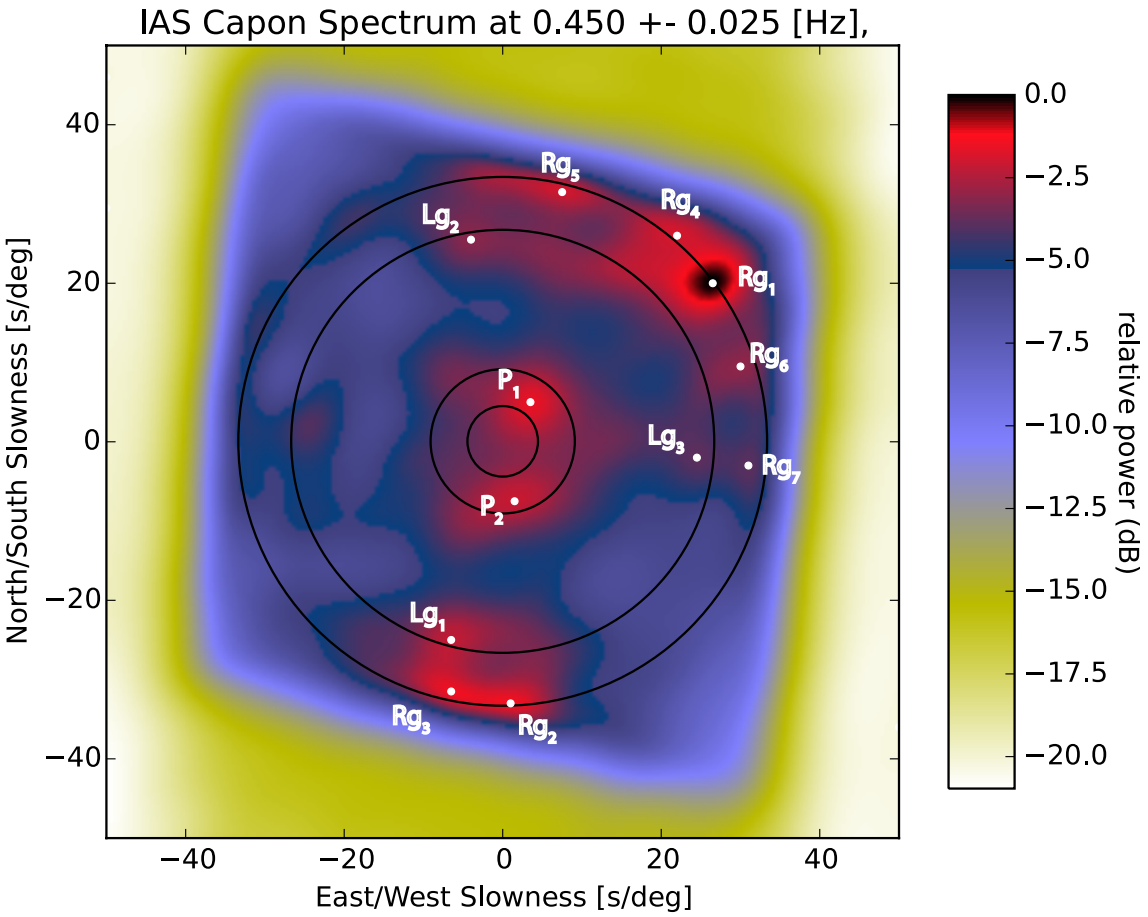

Figure S4.2: IAS Capon beamformer result for the date 2010, 1st January 10-11am, UTC. Local maxima are shown with the corresponding wave type if their power level is in the top 20% of the relative power. The subscript next to the wave arrival symbolizes the order according to the extracted relative power, hence 1 is the dominant phase, 2 is the second strongest, 3 is the third strongest, etc. Circles are displayed as in Fig. 4.1.

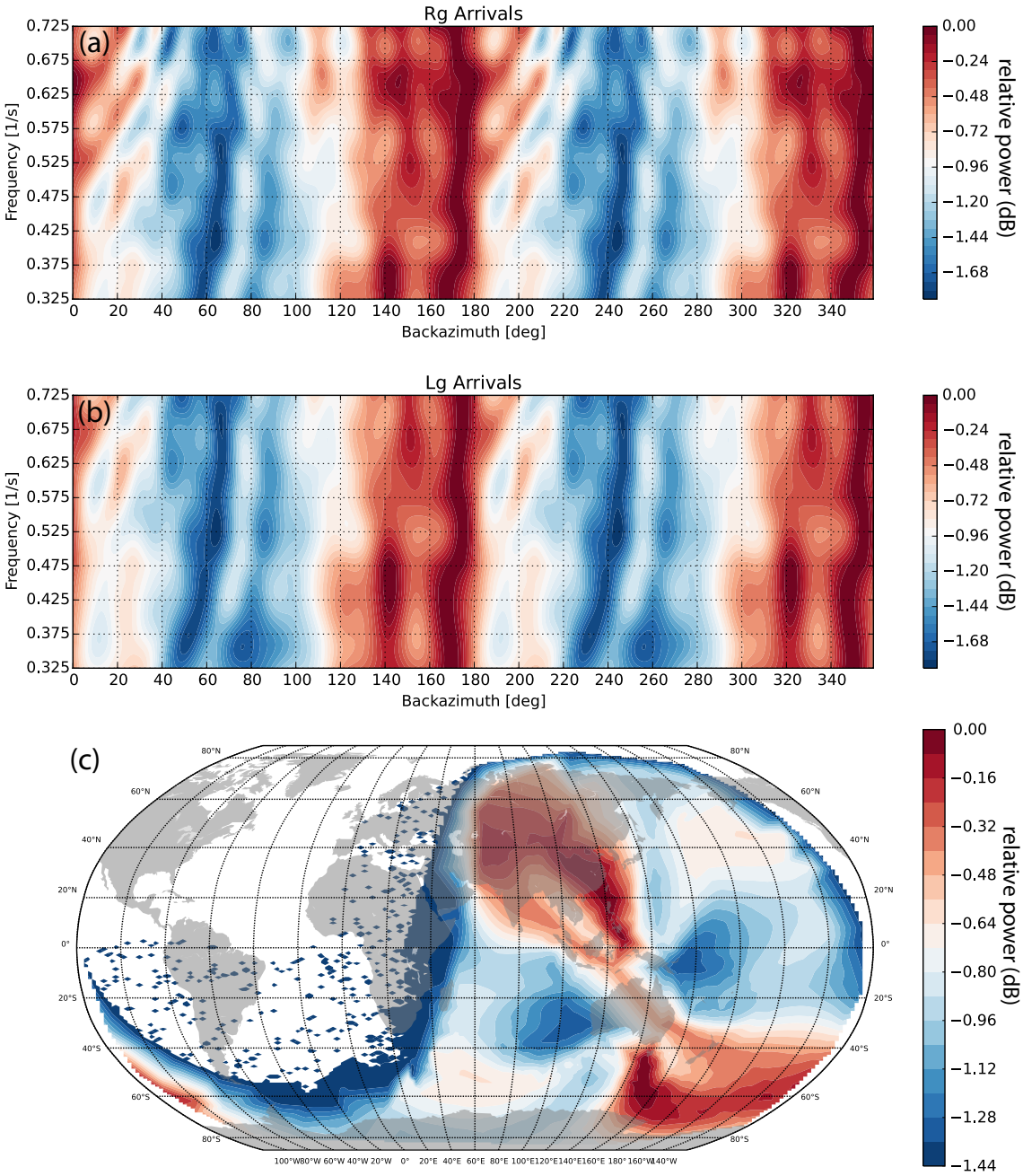

Figure S4.3: Sensitivity map for special velocity and frequency configurations. Azimuths at which WRA over and underestimates the source power are shown. The sensitivity test is obtained by generating synthetic sources from all directions with a specific velocity and frequency. The synthetics are then evaluated with IAS Capon to yield the sensitivity maps. (a) Sensitivity map for R_g waves for comparison to Fig. 4.2(a,c,e). (b) Sensitivity map for L_g waves. (c) Sensitivity map for P waves averaged over all 8 frequency bands.

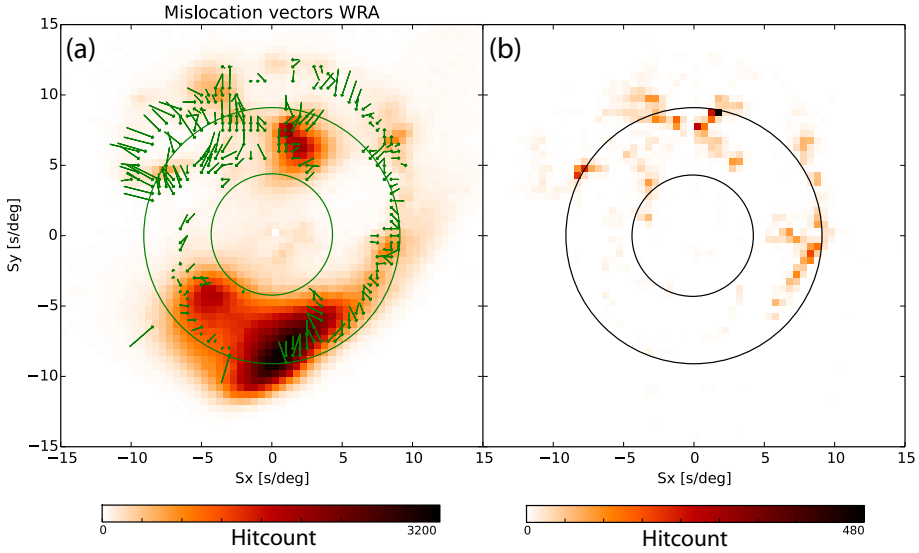

Figure S4.4: a) Dominant P wave arrivals for the whole frequency range and time period of the study, including earthquake arrivals and mislocation vectors. The green arrow heads point towards the theoretically calculated slowness vector. b) Earthquake arrivals for one year of WRA data. The outer black circle corresponds to an epicentral distance of 25° (slowness of 9.1 s/deg) for a P wave and hence shows the limit for unbiased backprojection with ak135. The inner circle shows a slowness of 4.45 s/deg, i.e. the most distant unbiased P waves arrivals (98°).

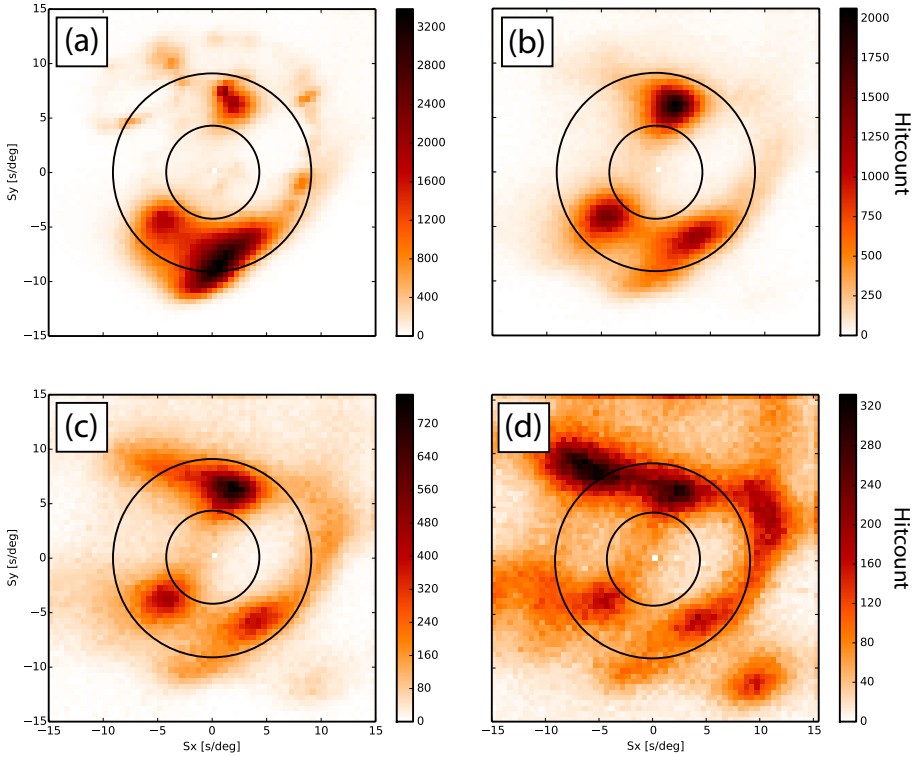

Figure S4.5: (a) Dominant, (b) second strongest, (c) third strongest and (d) weaker P arrivals from all frequency bands during the whole study period visualized as hit count plots.

Chapter 5

Microseism wavefield decomposition using deconvolution enhanced three-component beamforming

Submitted to Geophysical Research Letters, 1^{st} *August 2016*

5.1 Abstract

In the secondary microseism band (0.1-1.0 Hz) the theoretical excitation of Rayleigh waves (R_g), through oceanic wave-wave interaction, is well understood. For Love waves (LQ), the excitation mechanism in the secondary microseism band is less clear. We explore secondary microseism excitation by analyzing a full year (2013) of records from a three-component seismic array in Pilbara, Australia (PSAR). Our recently developed three-component waveform decomposition algorithm (CLEAN-3C) fully decomposes the beam power in slowness space into multiple point sources. This method allows for a directionally dependent power estimation for all separable wave phases, and enables us to quantitatively compare microseismic energy recorded on vertical and transverse components. We find the total power of R_g waves to dominate at 0.35-0.6 Hz, but the transverse component to be stronger at 1 Hz. The Rayleigh/Love wave ratio strongly varies with direction and frequency, and the azimuth of Love waves indicates correlations with sedimentary basins.

5.2 Introduction

Ambient noise studies in the range of 0.05-1 Hz have predominantly focused on the analysis of Rayleigh (R_g) (e.g. Friedrich et al., 1998; Shapiro, 2004; Chevrot et al., 2007; Kedar et al., 2008; Schimmel et al., 2011; Reading et al., 2014) and P waves (e.g. Gerstoft et al., 2008; Zhang et al., 2009; Landès et al., 2010; Traer et al., 2012; Euler et al., 2014; Gal et al., 2015). The excitation mechanism of Rayleigh (R_g) and P waves is well understood in primary microseisms (direct coupling of gravity waves in sloping shallow bathymetry (Haubrich et al., 1963)) and in secondary microseisms (wave-wave interaction (Longuet-Higgins, 1950; Hasselmann, 1963)). Numerical models (Kedar et al., 2008; Ardhuin et al., 2011; Ardhuin and Roland, 2012) correlate well with observations (e.g. Stutzmann et al., 2012; Obrebski et al., 2013; Koper and Burlacu, 2015).

Transversely polarized energy in the form of Love waves (*LQ*) (Toksöz and Lacoss, 1968; Haubrich and McCamy, 1969), L_g (Koper et al., 2009, 2010) and SH body waves (Liu et al., 2016) is also present in microseisms. The generation mechanisms of these phases in the secondary microseism band (defined here as 0.1-1.0 Hz) are not fully understood. The L_g phase, predominantly observed in short-period microseisms (Koper et al., 2010), is thought to be generated by topographic or bathymetric scattering of other wave types (e.g. He et al., 2008; Gal et al., 2015). While *LQ* generation in the primary microseism band (0.05-0.1 Hz) is related to shear traction of ocean waves on the sea-bottom topography (Saito, 2010), in the secondary band the excitation mechanism is less clear. Recent observations show that the backazimuth of the strongest R_g and *LQ* waves is approximately the same (Nishida et al., 2008; Hadziioannou et al., 2012; Behr et al., 2013). The power ratio between secondary microseism R_g and *LQ* waves show differing results between three component array beamforming studies (Friedrich et al., 1998; Nishida et al., 2008), which suggest that R_g dominates over *LQ*, and ring laser studies (Tanimoto et al., 2015, 2016), which suggest the opposite.

In this work, we utilize the capabilities of deconvolution enhanced three-component beamforming (Gal et al., 2016) to decompose the short-period secondary microseismic wavefield as a function of polarization, backazimuth, velocity, and frequency. The analysis is carried out with a spiral shaped array composed of broadband three-component sensors that is ideal for an omnidirectional study of the seismic wavefield. Our analysis allows for a bias free assessment of beam power, which we use to estimate the mean power distribution of R_g, *LQ*, and L_g waves for the full year 2013. We then compare ratios of vertical and transverse energy as a function of velocity, backazimuth, and frequency to gain insight on the generation mechanisms of R_g, *LQ*, and L_g.

5.3 Data and Processing

The wavefield decomposition is carried out with the Pilbara Array (PSAR) in northwest Australia (Fig. 5.1a). This analysis requires a horizontally isotropic velocity field within the array footprint to ensure plane wave propagation over a broad frequency range and high signal coherence for all stations. PSAR fulfils these conditions over the frequency range of 0.35-1 Hz. The array is composed of 13 broadband three-component (3C) stations in a spiral configuration with an aperture of 22.6 km. The spiral shape leads to a delta-like function array response (Fig. 5.1b) with strong sidelobe suppression (Kennett et al., 2015). The instrument response of the seismometers (type: KS2000, 120 s) is flat over the range of 0.02-10 Hz and all time series are divided by the instrument gain to transform the raw data to ground velocity (m/s).

We process the full year 2013 of 3C PSAR data in 3 separate frequency bands: $f_1 = 0.35 \pm 0.0175$ Hz, $f_2 = 0.6 \pm 0.03$ Hz, and $f_3 = 1 \pm 0.05$ Hz. The continuous data are divided into 1-hour time windows and evaluated via deconvolution enhanced CLEAN-3C Capon beamforming (Gal et al., 2016). Using this new algorithm, each component (i.e., vertical (Z), radial (R), and transverse (T)) is evaluated and decomposed into separate point sources. The decomposition into point sources has the advantage that no sidelobe beam power is present, and a simple summation

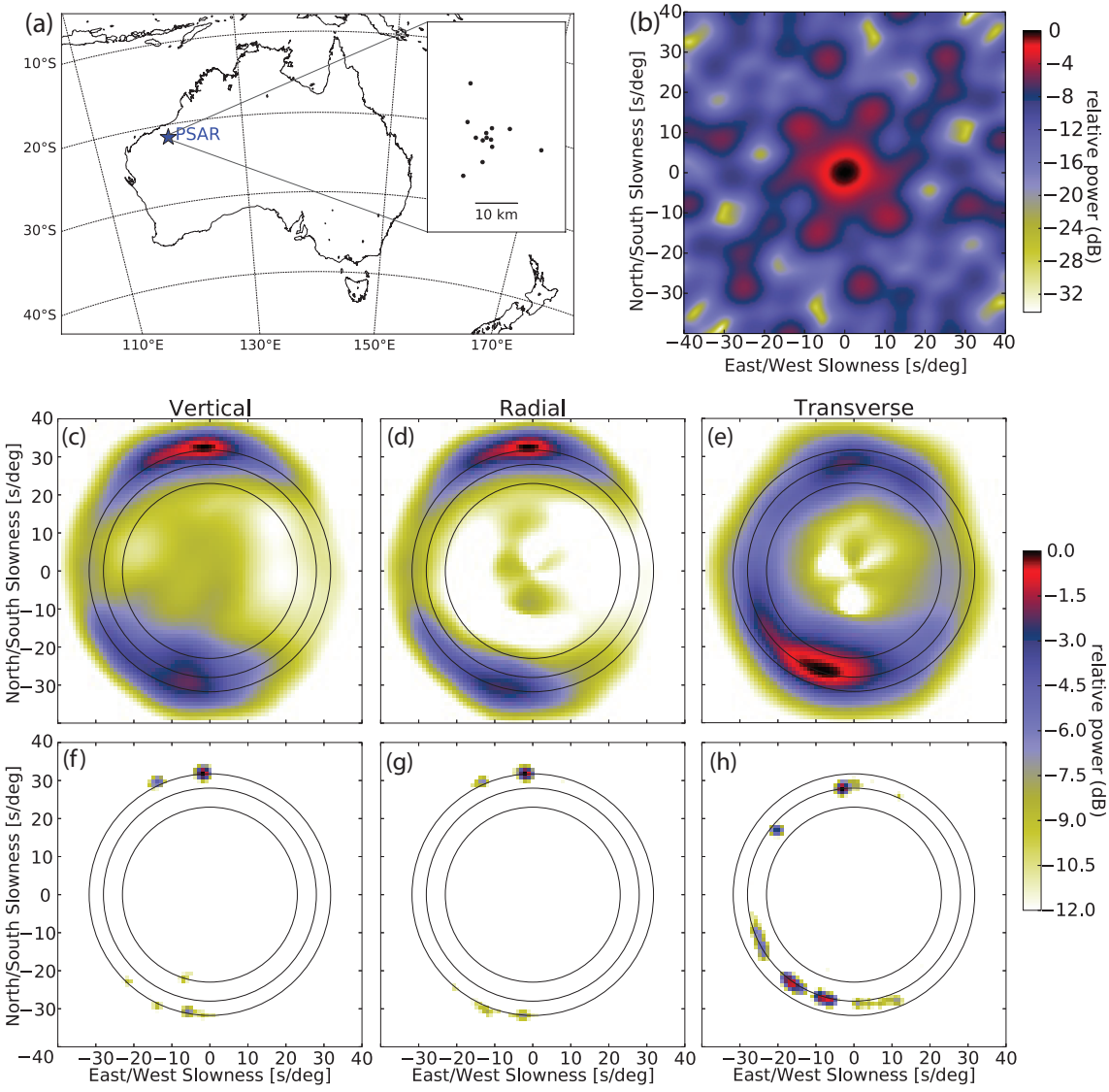

Figure 5.1: Geographical location and array geometry are shown in (a) with the corresponding array response function (b) at 0.6 Hz. Beamforming power spectra for a one-hour long record, beginning on Jan. 2, 2013 at 00:00:00 UTC, evaluated with 3C Capon beamforming at frequencies (f_1) of 0.35 ± 0.0175 Hz are shown in the bottom two rows. The power spectra are displayed for (c) Z-, (d) R- and (e) T-component data. The black circles of constant velocity are set at 3.4, 4.0, and 4.7 km/s. The bottom row (f,g,h) shows the decomposition of the power spectra into point sources (convolved with a small Gaussian kernel to aid visibility). The decomposition of Z- and R-component shows identical results with the exception of the southern L_g arrival which is only visible on the Z-component. Both the strong capability of the array and the robustness of CLEAN-3C are evident. The power of cleaned sources is lower as the beam sidelobe bias is removed.

over all 'cleaned' sources results in the total power of the given component. Alternatively, summation can be performed with bounds on azimuth and velocity to obtain directional power estimates for different phases. CLEAN-3C results for a typical one-hour long sample are displayed in Fig. 5.1(c-h).

A user-defined stopping criterion must be implemented in CLEAN-3C so that the results are not biased by spurious features contributed by the low signal-to-to noise ratio and all power from the cross spectral matrix is decomposed. The automatic stopping criterion is as follows: in an initial frequency dependent analysis, we estimate the phase velocities for R_g, L_g and LQ waves with conventional 3C Capon beamforming (Wagner and Owens, 1996) using a month of data (January 2013). We find velocities of R_g 3.4 km/s, L_g 4.0-5.0 km/s on the Z-component, and LQ 3.8-4.0 km/s on the T-component. Acceptable velocity bounds are then set to $3 < v < 5.5$ km/s, and, in case body waves are present, $v > 8.2$ km/s. Iterations of the CLEAN-3C procedure for the Z-component are stopped once the beam power estimated from the residual phase information lies outside of the acceptable velocity bounds. The stopping criterion for the R-component is identical to the Z-component while $3.3 < v < 5.5$ km/s applies for the T-component. As we are interested in accurate power estimation of microseismic energy, we remove all earthquake related signals. This is achieved by analyzing the strongest 'cleaned' source for each hour. In general, the power of the strongest source shows little change for adjacent hours and generates a smooth curve as a function of time. Strong earthquakes appear as outliers in this curve and the 'cleaned' sources associated with such behavior are removed from our results. Additionally, only results which passed at least 50 CLEAN-3C iterations are retained to avoid biased estimates.

5.4 Observations

The recovered arrivals are summarized in a histogram in Fig. 5.2 and demonstrate which parts of the slowness plane, i.e. backazimuth and velocity, are most active during the year 2013. A drawback of this representation is that the power of each arrival is not taken into account, hence the figure does not reflect the true mean power distribution of the microseism wavefield. Since CLEAN-3C decomposes the field into point sources, and the power contribution of each source is known, a mean beam power representation can be constructed. We present the mean beam power per hour in Fig. 5.3, for all three frequency bands, as outgoing rays from the array location. For this operation the backazimuth is discretized into 5 degree bins. Fig. 5.3(a-c) shows R_g waves in the three frequency bands derived from the Z-component for velocities $3.0 < v < 3.6$ km/s. We observe high beam power from the north, south, and west for the lowest frequency, f_1 (Fig. 5.3a). The directions with high mean beam power to the south are associated with convex coastline morphology (i.e., coastline bulges). With increasing frequency, f_2 and f_3, we see a strong reduction (by a factor of 10) in the average beam power from the south and west (Fig. 5.3b,c). The reduction in power with increasing frequency matches well the increased attenuation expected for R_g waves traveling from distant coastlines (Mitchell, 1995).

Beam power from the T-component for $3.4 < v < 5$ km/s is shown in Fig. 5.3(d-f) for the three frequency bands. This result highlights transverse energy from LQ, L_g, and Sn phases. The

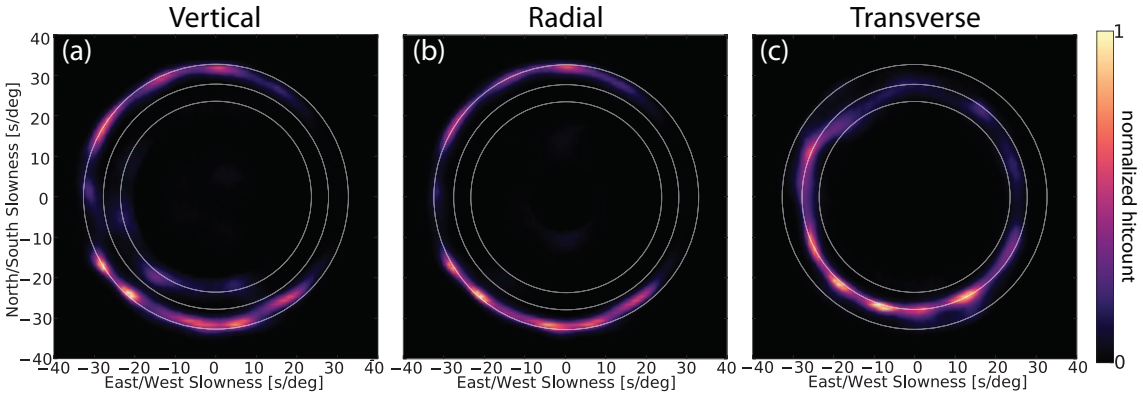

Figure 5.2: Summary plots for the full year 2013 for (a,b,c) Z-,R- and T-component at f_1 = 0.35 $\pm$ 0.0175 Hz. These summaries are generated as a histogram of all evaluated arrivals and represent the slowness-backazimuth pairs with the most arrivals estimated with CLEAN-3C over the course of 2013 (this is power independent). Circles of constant velocity are identical to Fig. 5.1. The Z- and R-component show again an identical result for R_g waves and the Z-component shows clear higher velocity L_g arrivals from the south to west.

T-component results show some correlation with R_g for the case of f_1 (compare Fig. 5.3a,d). The arrivals to the south do not fully align with the convex coastlines, but the power distribution to the west correlates well for the strongest directions. In general, we see smaller variation of mean power with respect to direction than for R_g, which shows stronger preference for certain backazimuths. For f_2 (Fig. 5.3e), almost all directions (apart from the north-east to south-east where little to no signals are recorded) are within a mean beam power of 7 dB/hr. We further observe a slight shift in the strongest beam directions on all coastlines. The strongest southern direction fits better with previously observed R_g directions at f_1 (Fig. 5.3a). For f_3 (Fig. 5.3f), the beam power from the south is reduced compared to directions for which the coastlines are closer. It should be noted that for the three frequency bands the strongest mean power direction of the T-component is weaker than the estimated mean power of the strongest R_g direction (see differences in power between first and second row in Fig. 5.3).

For higher velocity (3.8 < v < 5 km/s) arrivals on the Z-component (Fig. 5.3g-i), we observe predominantly L_g waves, which likely include some contribution from higher mode R_g. As L_g is prominent on the vertical and transverse components, the results correlate to some degree with the results shown in Fig. 5.3d-f. The strongest mean power direction for f_1 is to the west and shifts to the north for f_2 and f_3. For f_3 and partially f_2, the L_g phase shows higher mean power to the south compared to the R_g phase, consistent with the lower attenuation of L_g.

We show the azimuthal variability in the ratio between Z- and T- component energy, for all three frequency bands, in Fig. 5.3(j-l). The Z/T ratio in Fig. 5.3 is displayed as the difference in dB/hr to make the scale linear and to readily show the large differences in power. Here we allow only surface waves with velocities <5.0 km/s. (Subdivision into R_g, LQ, and L_g is not feasible owing to the limited resolution of PSAR and the similarity in velocities.) The Z/T ratio at f_1 (Fig. 5.3j) is in general positive for directions where R_g waves show strong beam power, and negative for directions with low R_g beam power. At f_2 (Fig. 5.3k) the effect of R_g attenuation/scattering is clearly visible as all directions from the south to west are dominated by T-component energy. Only the coastlines north of PSAR, that are in close proximity to the array, display stronger mean

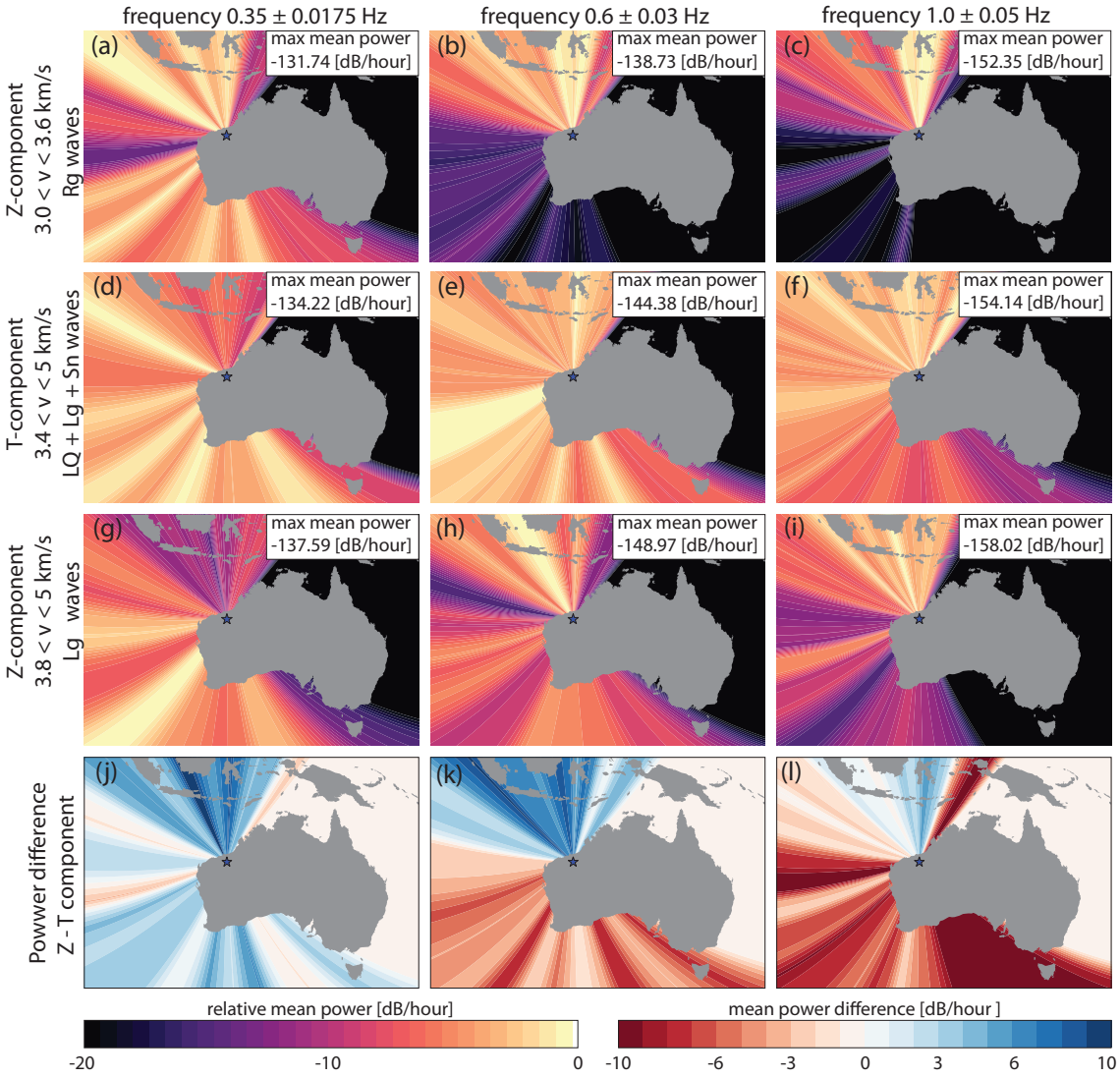

Figure 5.3: Projections of mean beam power towards the estimated direction of arrival for all of 2013. The top 3 rows (a-i) are generated by taking all evaluated arrivals with CLEAN-3C, dividing the backazimuth into 5 degree wide bins, and dividing the sum of all power in all bins by the number of hours processed, assuming the raypaths follow great circle paths. Owing to the lack of arrivals at backazimuths of 40-125°, the directions are masked as they would not produce meaningful results. Each column represents one of the three frequency bands, and the first three rows show the estimated mean beam power for different wave types. Wave type, velocity and component information are stated at the beginning of each row. The label 'max mean power', represents the mean power of the strongest direction in each case. The lowest row (j-l) shows the difference in power between the Z- and T-component (for the Z-component here we refer to R_g + L_g). The colormap levels are set from -10/hr to 10 dB/hr, hence values smaller or larger than these bounds are clipped with the maximal color. Clipping only occurs for the case (f) where the T-component exceeds a difference of 10 dB/hr (the arrivals from the SSE direction are up to -20 dB/hr difference).

vertical (R_g) beam power. For f_3 (Fig. 5.3l), the dominance of the T-component energy (L_g) increases further, and only a narrow swath of backazimuths to the north-northeast show a stronger vertical component. The Z/T power ratio integrated over all directions shows a notable decrease with increasing frequency: 1.95 for f_1, 1.86 for f_2, and 0.83 for f_3.

5.5 Discussion

The results presented in this work show that vertical (R_g, L_g) and transverse (LQ, L_g) component surface waves are generated along all the coastlines of Australia except for the east coast, which is sheltered from Southern Ocean swells and very distant from PSAR. R_g waves recorded on the Z-component show a stronger azimuthal dependence compared to the LQ/L_g energy recorded on the T-component. Previously reported directional similarities between R_g and LQ energy in the secondary microseism band (Nishida et al., 2008; Hadziioannou et al., 2012; Behr et al., 2013) are partially present in our results, but deviations occur, especially for directions where R_g is weak. At the lowest frequency (f_1 = 0.35 Hz), we observe the Z-component energy to be almost twice the strength of the T-component, however it is likely that Z/T ratios are regionally dependent especially for seismometers sited in sedimentary basins (Koper and Burlacu, 2015).

Attenuation and scattering of R_g play a key role for higher frequencies (f_2 = 0.6 Hz and f_3 = 1.0 Hz) and is consistent with observations that arrays located farther inland in central Australia (Warramunga and especially Alice Springs) are dominated by L_g from all directions (Koper et al., 2010; Gal et al. 2015). The R_g/L_g ratios obtained for the three frequency bands, calculated from the Z-component only, are 8.34, 9.00, 2.76 for f_1, f_2, f_3 respectively. The first two bands show a similar ratio, but strong reduction in the southern R_g energy is observed for f_2 when compared with f_1 (see Fig. 5.3a,b), therefore attenuation seems to be the main contributor for this reduction. The further decrease in directional R_g energy at f_3 suggests scattering from R_g-to-L_g (e.g. He et al., 2008; Gal et al., 2015) owing to the strong decrease in the R_g/L_g ratio at f_3. Given the characteristics of the higher attenuation/scattering of R_g waves for f_2 and f_3, it is safe to assume that this ratio is strongly dependent on the location of the array with respect to the closest coastline.

In Fig. 5.4, we investigate the azimuthal variations in beam power in more detail and compare R_g waves from the Z-component with mean power on the T-component. For this analysis we focus on f_1, where the attenuation and scattering effects have the least impact, and source excitation should be most important. The north-facing coastline shows three directions with elevated R_g mean power levels (Fig. 5.4a), which correspond well with convex portions of the coastline. The T-component (Fig. 5.4b) shows a different picture as LQ waves are not generated by the same three convex coastlines. This result implies that typical oceanic wave-wave interaction alone is not enough to generate LQ waves, as might be expected from the theory. In this case, the location of LQ waves correlates with the Dampier Archipelago Islands, north of the coast.

For the west-facing coast (Fig. 5.4c,d), the strongest azimuth for R_g and T component is identical and correlates with a large (almost straight) coastline section. These directions also correlate with strong L_g directions (see Fig. 5.3g). The ratio between the T-component and L_g from the Z-component is close to 1 for these directions. Most of the transverse component power

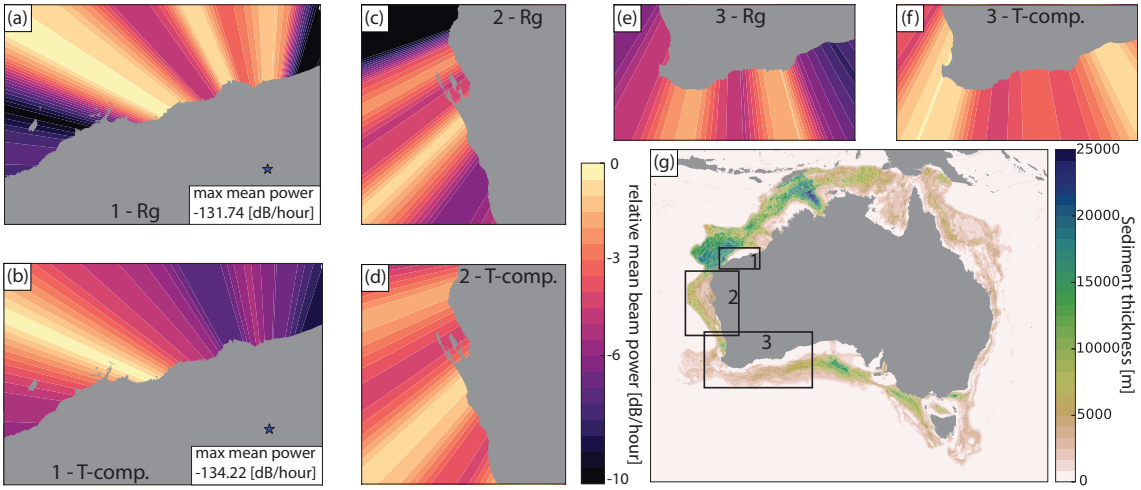

Figure 5.4: Enlarged regions from Fig. 5.3a,d. The northern (a,b), the western (c,d), and the southern coastlines (e,f) for R_g waves and the T-component are shown in the lowest frequency band, f_1. The colormap levels are identical to the values in Fig. 5.3a,d for the R_g and T-component case and shown here only for the case of the northern coastline. The corresponding sediment thickness map (g) 'OZ SEEBASE' - product of FROGTECH (2006) displays which geographical locations are enlarged. Directions of strong *LQ* waves (b,f) correlate well with thick sediment locations, while strong directions in (d) are expected to be mainly L_g waves.

is therefore part of L_g and not *LQ*. To the south (Fig. 5.4e,f), the *LQ* waves are generated at different coastline locations than R_g. The eastern direction correlates again to a large and almost straight coastline section with no islands close by. Due to an absence of islands, we can exclude any excitation via such process in this case. The potential shear traction of ocean waves, which is assumed to excite *LQ* in the primary microseism band (e.g. Nishida et al., 2008), can also be excluded as the observed mean power is too high for these frequencies. In this case, very little R_g energy is measured for this direction. If we assume that the oceanic wave-wave interaction, in combination with sloping sea bottom topography (seamounts), or a scattering process is capable of *LQ* wave excitation, the large power difference could be explained by the neglected transfer function between ocean and land.

The fact that we find a more homogenized directional *LQ* distribution suggests that the oceanic wave-wave interaction, in combination with seamounts, is unlikely to be the only process responsible for the excitation of *LQ* waves, otherwise R_g waves would be observed from these directions as well. When the *LQ* wave directions are compared to a sediment thickness map (Fig. 5.4g), partial correlations are observed. *LQ* waves are known to be excited by S-waves incident on sedimentary basin boundaries (e.g. Kinoshita et al., 1992; Hatayama and Fujiwara, 1998) and hence could contribute to the observed *LQ* wavefield. It is yet to be determined if another mechanism contributes to the generation of *LQ* waves when interacting with a sediment layer. A potential candidate could be a R_g-to-*LQ* conversion, as Hatayama and Fujiwara (1998) showed that the SV body waves can excite *LQ* waves at the sediment layer boundary. In a similar fashion, the SV component of R_g waves could potentially excite *LQ* waves. Such a process could also explain the more homogenized directional *LQ* distribution as R_g waves excited in the ocean propagate in all directions (Ardhuin et al., 2015) and conversion from R_g-to-*LQ* could occur at distant sedimentary basin boundaries, which are not directly exposed to wave-wave microseism excitation.

5.6 Conclusion

We have presented the first 3C array study that decomposes the microseismic wavefield in slowness space on each component and removes power contributions from beam sidelobes. The analysis accounts for the full power on each component and gives unprecedented azimuthal resolution on the excitation and propagation of short-period microseisms in Australia. It enables an accurate assessment of the power of R_g and L_g waves on the Z-component and the surface wave portion of the T-component (LQ, L_g), which is used to investigate the directional mean power differences of these phases.

R_g waves are predominantly generated close to convex portions of the coastlines at 0.35 Hz and experience increased attenuation/scattering with increasing frequency. LQ waves show little correlation with R_g waves at 0.35 Hz and increased correlation for higher frequencies, which is likely due to an increased proportion of the L_g phase on the T-component. Partial correlation with sedimentary thickness measurements around Australia is also observed. While the mean beam power of the Z-component is roughly twice as large as the T-component for 0.35 and 0.6 Hz, a strong directional difference between these two components can be observed.

5.7 Acknowledgements

We acknowledge data access through the IRIS DMC. We thank the Tasmanian Partnership for Advanced Computing (TPAC), which enabled the access to its HPC Facilities. Funded by the Australian Research Council under project DP150101005. MG is supported through a Tasmanian Government Research Scholarship. KDK and RB acknowledge support from NSF-EarthScope under award EAR-091558. CLEAN-3C code is freely available may be obtained by contacting the University of Tasmania authors.

Chapter 6

Discussion of synthesis

In chapters 2 and 3, new implementations of improved beamforming approaches were presented and their applicability demonstrated in chapters 5 and 6. The aims of the thesis are now revisited to give an overview of insights drawn. A discussion of the applicability and limitations of the newly implemented techniques is also provided.

6.1 Beamforming for seismic array analysis

For the purpose of designing the optimal beamforming framework for the analysis of microseisms, different beamforming algorithms have been considered in this thesis. The approaches can be categorized into three groups: The data independent (fk), data adaptive (Capon) and subspace based (multiple signal classification - MUSIC) algorithms. The first group does not exploit the data structure and results in a low resolution. The data adaptive approaches exploit the data structure via spatial filtering and obtain higher resolution. The subspace-based algorithms are based on the statistical analysis of the cross spectral matrix, which is decomposed via a principal component analysis (in the case of MUSIC) and the resulting eigenvectors parametrize the signal and noise properties. Each eigenvector forms an orthogonal subspace system which can be exploited to infer the direction of arrival. Of the three types of algorithms, the subspace approaches are considered to have the highest resolution capabilities (Krim and Viberg, 1996).

During the review and performance evaluation of these methods, I have often found strong resolution degradation of the so called 'optimal beamformers' when evaluating the ambient noise wavefield. There appear to be a variety of reasons for the degradation, however, they are most often the result of a mismatch between signal model and true signal propagation. Some of the reasons for this include, violation of the plane wave assumption, anisotropy of the geology resulting in wave front deformations, extended sources, loss of coherence, scattering and limited number of sensors. The conventional fk method is the most robust approach in the presence of model errors, and hence very popular when evaluating the ambient noise. The Capon algorithm shows improved resolution capabilities, but is less robust than the fk analysis, and hence is more sensitive to model errors. Robustness can be improved by applying diagonal loading, as is the case in the IAS Capon approach described in chapter 2, which extends the algorithm's range of applicability.

The MUSIC algorithm, in other fields recognized as the superior approach in terms of resolution (Krim and Viberg, 1996), shows inconsistent results for the analysis of ambient noise. Apart from model errors, which have a significant impact on the performance of MUSIC, the reason for

the low resolution lies in the methodology of the algorithm. An underlying constraint is that MUSIC can estimate only $K-1$ signals (K is the number of sensors) and the parametrization has to be divided into a signal and noise subspace. Given the weak and diffuse nature of the ambient noise wavefield, the partition between to two subspaces is not trivial. Techniques which deduce the optimal subspace partition from the data structure have been proposed (e.g. Wax and Kailath, 1984), but did not show reliable results in my performance analysis. Another approach is to compare the magnitude of the eigenvalues (EV) in descending order, and choose the division between signal and noise subspace once a large gap between EV's appears (e.g. Schisselé et al., 2004). However, in the analysis of microseismic wavefield such gap may not be present, and even in the case of its presence, the partition might not give robust results. This can be visualized with a simple example, where I chose all possible signal subspace dimensions (denoted as SS), in Fig. 6.1. Gaps in the EV distribution occur between EV's $8-9$ and $12-13$, i.e. at SS 8 and 12 for which no robust result is present. It is not possible to be sure which signal subspace yields the most accurate power spectrum in this case.

It is likely, that the robustness of MUSIC increases with a larger number of seismic sensors as the principal component analysis better parametrises the internal structure of the cross spectral matrix. Indications of such improvement are obtained by extending the previous example into three components (Fig. 6.2), which effectively increases the subspace dimensions by a factor of three. Even though it is still not clear which subspace correctly partitions between signal and noise, the improved parametrization results in a more robust MUSIC power spectrum. This example suggests, that there might be seismic arrays with a larger number of sensors where it is possible to obtain accurate parameterization by means of principal component analysis and MUSIC can be applied with superior results.

Apart from MUSIC, other high resolution approaches have been proposed, e.g. ESPRIT (Paulraj et al., 1985) and root-MUSIC (Barabell, 1983). These beamformers show excellent estimation capabilities, but are designed for uniform linear arrays, i.e. arrays with a symmetric geometry. Exploiting the symmetry allows the algorithms to achieve higher performance than an arbitrary array configuration and also evaluate correlated signals (e.g. Goldstein and Archuleta, 1991). Seismic arrays are generally not deployed in a uniform linear configuration, hence given the very small number of uniform linear arrays with an aperture suited to study the microseism wavefield, such techniques have not been considered in this thesis.

I have found the best compromise between resolution and reproducibility/robustness to be achieved with the Capon beamformer especially when aided by diagonal loading and the IAS extension to improve robustness (chapter 2). For the optimal use of the beamformer, the use of the coherence (eq. 1.19) matrix instead of the cross spectral density is preferred if the power of the source is not of interest. The coherence matrix will suppress incoherent energy and retain the coherent part, hence increasing the resolution. As for temporal averaging, the optimal time is dependent on the task at hand and the wavefield observed. If the wavefield is of stationary nature (or approximately stationary), averaging over longer time periods will achieve a better result as the phase information in the cross spectral / coherence matrix is better estimated. For the case of non-stationary wavefield, averaging over long periods of time will lead to smearing of feature in

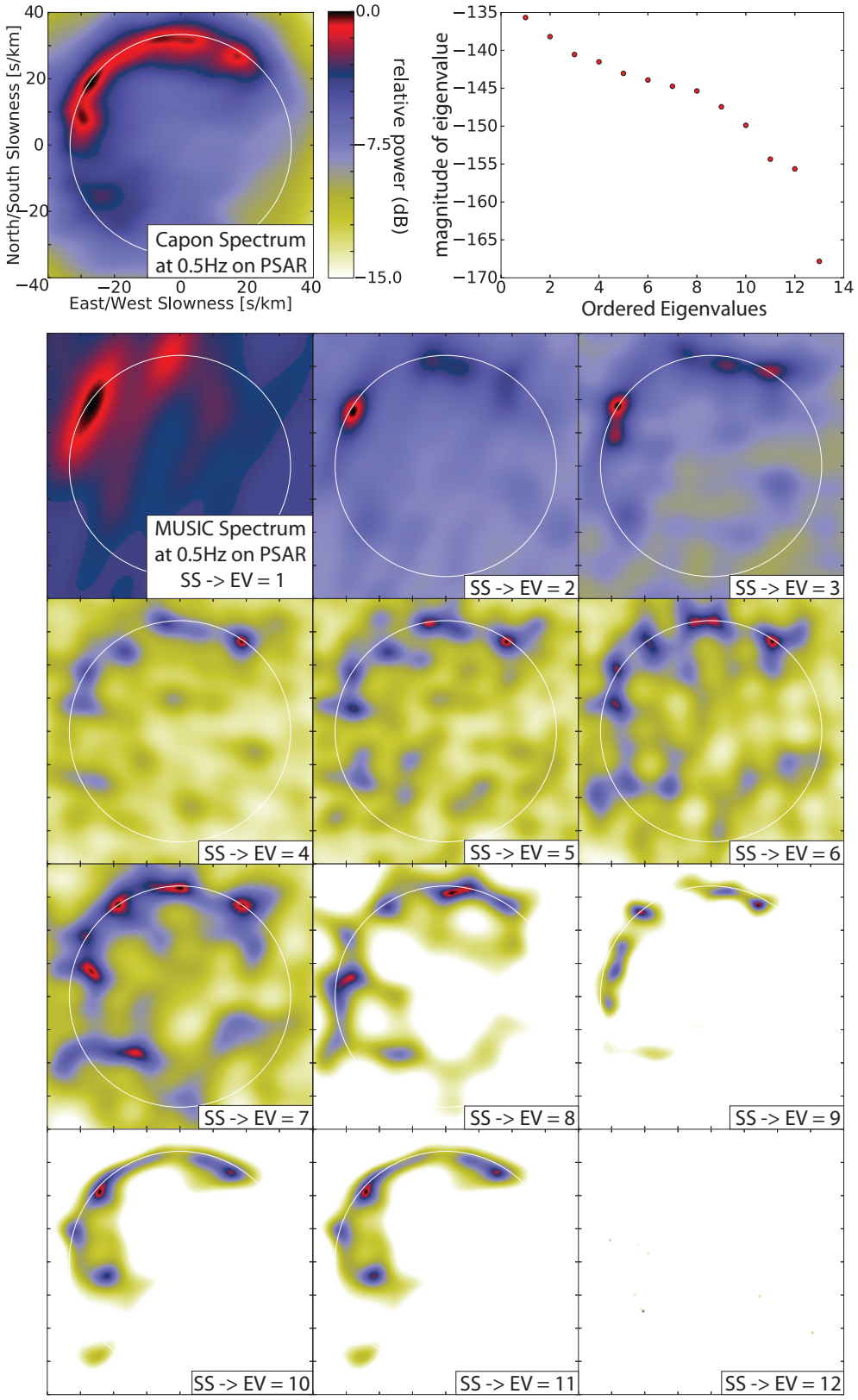

Figure 6.1: One hour of ambient noise processed with Capon (top left) and MUSIC (bottom figure). The example shows the power spectrum for the 1st January 2013 from 0:00:00 to 1:00:00 UTC (h:mm:ss). The top right figure shows the magnitude of the ordered eigenvalues derived from the cross spectral matrix. The MUSIC power spectra are generated by increasing the number of signal subspaces (SS). The circle of constant velocity is set to 3.3 km/s

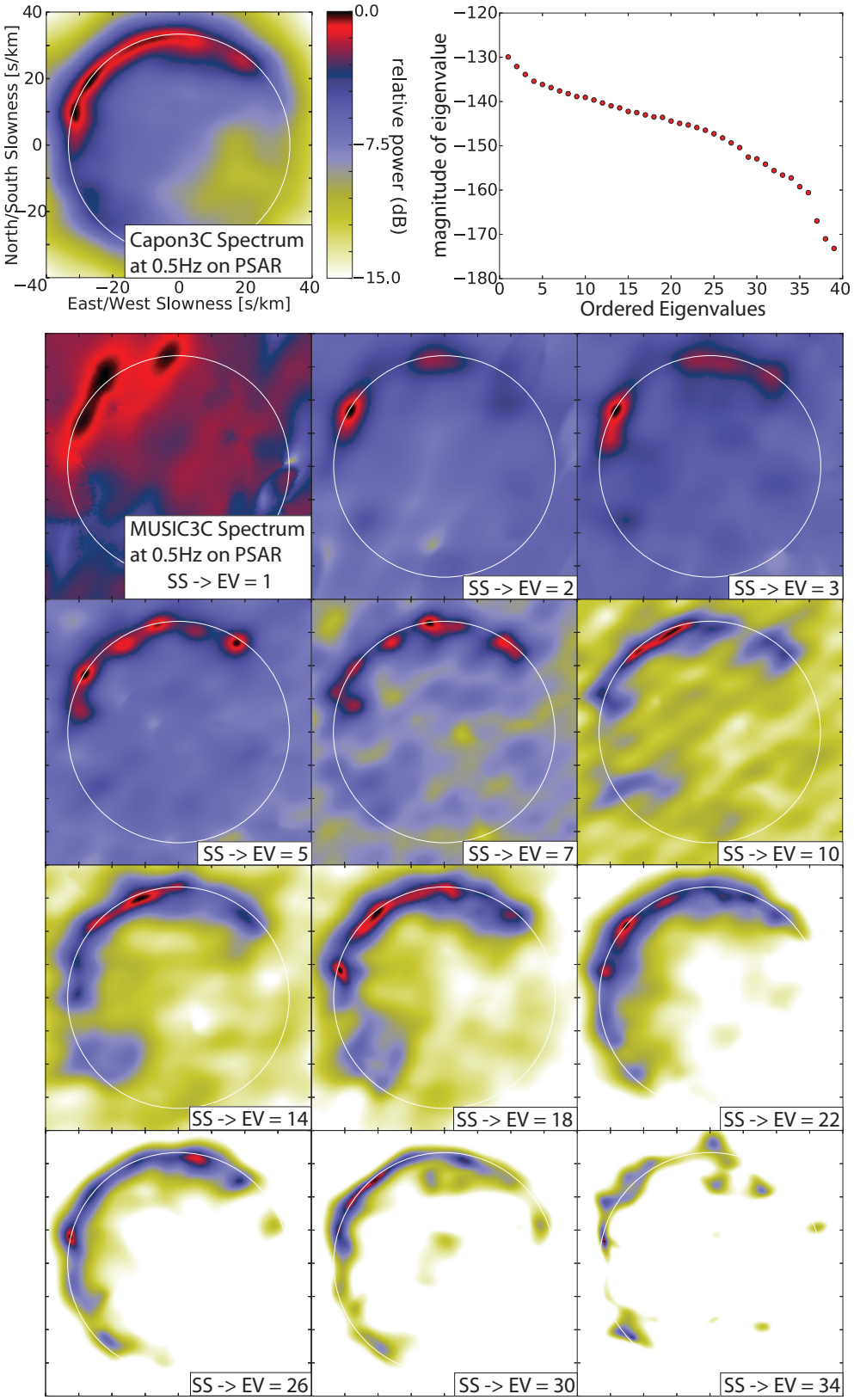

Figure 6.2: Same as Fig. 6.1 but for the 3C case. Only the vertical component of the power spectrum is displayed.

the power spectrum and can lead to resolution degradation. In the case of fk, one would experience a stronger bias due to the ARF, while in the case of Capon, the spatial filter would decrease in performance, hence resolution would decrease. The optimal parameter for the observed wavefield and frequency range, needs to be adjusted by the user independently for each array.

Once the optimal beamforming framework for the processing of ocean induced array data was developed, I have explored deconvolution techniques which can be viewed as a type of post processing for further resolution refinement. In chapter 3, I analysed 3 promising deconvolution methods that could improve the beamforming power spectrum to detect weaker sources which are overshadowed by the strongest energy contributions in the power spectrum. These approaches are CLEAN (Högbom, 1974), the RL deconvolution (Richardson, 1972; Lucy, 1974) and DAMAS (Brooks and Humphreys, 2006b,a). The initial results with DAMAS and DAMAS2 did not produce robust results, and hence DAMAS was not included in chapter 3.

The true power of the CLEAN technique is achieved by implementing the deconvolution as part of the beamforming process Sijtsma (2007), with deconvolution performed on the cross spectral matrix instead of an image. This allows CLEAN to be accurately combined with any type of beamformer, which improves resolution as all beam sidelobe contributions are removed. I have shown, that the CLEAN approach is capable to accurately decompose the observed microseism wavefield while maintaining robustness and reproducibility.

The applicability of these new implementations will depend on the specific task and the array specifications. IAS Capon, can readily be used as a substitute for the conventional fk approach and will yield a better resolved spectrum due to a stronger sidelobe suppression. This allows the approach to be used at lower frequencies than the fk analysis and still produce useful direction of arrival estimations. The CLEAN implementation is most beneficial for small arrays which struggle with resolution capabilities in the microseisms range or arrays which have a problem with strong sidelobes. Strong smearing in the power spectrum can be eliminated and potential new signals are revealed. CLEAN has the capability to increase confidence in beamforming results for weaker signals as it can remove the contribution from the strongest sources in the spectrum (i.e. a partial CLEAN) and hence estimate if local maxima in the power spectrum are the result of sidelobe contributions from the strong source. For arrays which obey the signal model, a high resolution wavefield decomposition can be achieved as demonstrated in chapter 3. The decomposition can then be used to accurately represent the mean power of the ambient noise wavefield over a long period of time, Fig. 6.3.

6.2 Limitations of improved techniques and future priorities

While in general the improved techniques presented in this thesis improve the array analysis of ocean induce microseisms, their applicability has limits. The IAS approach is designed to be used in the range of 0.5 - 20 seconds, where the SNR is relatively high. Degradation of the resolution is to be expected for low SNR and a small amount of snapshots (temporal subwindows). In such

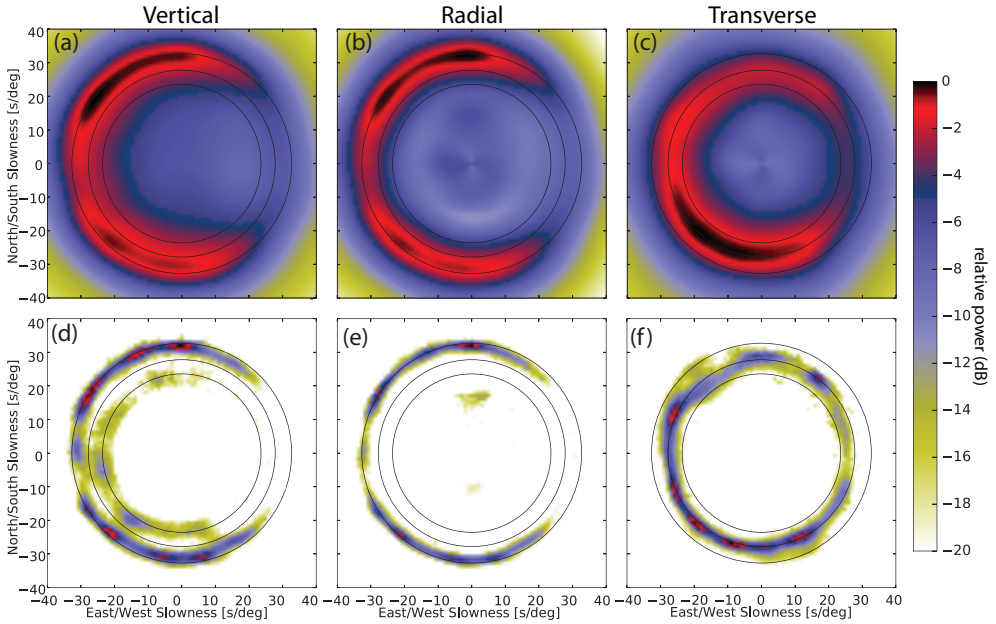

Figure 6.3: Example of a mean power representation for the full calendar year 2013 with PSAR for Z-,R- and T-component at f1 = 0.35 $\pm$ 0.0175 Hz. The top row (a,b,c) displays the average power distribution estimated with the 3C-Capon beamformer (Wagner and Owens, 1996). The bottom row displays the mean power distribution derived with CLEAN (Gal et al., 2016). The figures are generated by summing over all 1 hour power spectra divided by the amount of hours in a full year. The wavefield decomposition results in a sidelobe free energy representation.

cases, the cross spectral matrix is dominated by noise and will not lead to an optimal solution. The diagonal loading approach in IAS Capon is capable of increasing the robustness by applying a larger loading factor to the cross spectral matrix, but by doing so will eventually converge towards the resolution of the conventional fk analysis.

The CLEAN approach, requires a match between the signal model and the true signal propagation characteristics. If the array slightly deviates from the signal model, errors will accumulate over the iteration process and lead to a biased wavefield decomposition, where the bias depends on the degree of mismatch between model and true signal propagation. Such mismatch is to be expected for arrays with an aperture larger than 50 km, but can occur for smaller arrays as well.

In the future, further improving the plane wave beamforming approach is likely to yield diminishing returns. The reason is that optimal resolution is only rarely achieved due to a deviation from the plane wave signal model, given that seismic waves do not travel with constant velocities in the solid Earth but are geology dependent. Hence the biggest benefit will be to incorporate geological variations below the array into the array approaches to have a more accurate signal model. Ideally, one is interested in an array calibration framework, which derives the true wave propagation characteristics via an analysis of the ambient noise wavefield, i.e. can estimate the true steering vectors automatically. The results of such analysis could be used as standard calibration templates, as is the case with SASC derived from earthquakes (e.g. Bokelmann, 1995; Bondár et al., 1999; Schweitzer, 2001), to allow optimal array processing. Once such templates exist for a given array, CLEAN can be applied to achieve optimal beamforming performance and its capabilities can be extended to remove near field sources.

6.3 Insight into microseism sources

The novel techniques developed in this thesis allow for a better observation of the ambient noise field. The benefit of analysing multiple sources with IAS Capon is that it allows the observer to estimate multiple generation regions of microseisms simultaneously. This is demonstrated by means of a multi decadal study presented in chapter 4, on an array which is impacted by large beam sidelobes, hence benefits strongly from the suppression of such by IAS Capon. Combined with the frequency dependent analysis, the true complexity of the microseism wavefield is shown and can be observed in more detail (Fig. S4.2). Multiple surface and body wave generation regions are simultaneously active, and the strongest signals change location depending on frequency.

Rayleigh waves are confirmed to be the dominant surface wave type at 3 seconds and display a strong reduction in power for decreasing periods. The decrease in Rayleigh wave energy is connected to attenuation and scattering effects as observed and is clearly observable in western Australia with PSAR (chapter 5). With WRA, scattering is observed from R_g-to-L_g which leads to a dominance of the L_g phase for lower periods. A similar transition from R_g-to-L_g is also observed with PSAR. It is yet to be verified if R_g scatters into L_g only at the ocean-land transition or if this process is also common on the path towards the array. With PSAR, the R_g energy is found stronger for generation regions close to the array while L_g dominates for azimuths with a larger distance towards the generation region. If scattering is the dominant process, then the above results would suggest conversion from R_g-to-L_g along the raypath.

Love waves are found at slightly different backazimuths than Rayleigh waves and display smaller attenuation at short periods than Rayleigh waves. Given the lower attenuation, the Z/T ratio decreased for shorter periods and the T component is found to be the most energetic part of the wavefield. Their generation is observed to originate from a larger azimuthal range. A potential generation via an interaction between R_g waves and sedimentary basin boundaries is suggested in chapter 5 as Love waves seem to originate from regions close to large sedimentary basins.

For body waves observed with WRA, multiple deep ocean regions are found to be generating microseisms simultaneously and seasonal variations are observed that match with the occurrence of deep ocean storms. Deep ocean microseisms are predominantly generated at periods of 3 s while the generation regions move towards the shallower waters for shorter periods (chapter 4, Fig. 4.5,4.7). Most body wave energy recorded at PSAR is masked by the strong presence of surface waves. However, during strong storm events in the southern ocean, where large wave heights reach the south-western Australian coast, P waves are visible. P waves are also observed from the north during large storms close to the coastline. The majority of these P waves are estimated with a very shallow ray path, i.e. a slowness between $10-15$ s/deg hence generated relatively close to the array. At 0.35 Hz, P waves are observed predominantly from the south while for 0.6 and 1 Hz, P waves are only observed from the north, i.e. the closest coastline. Their presence is mainly observed on the radial component and only very little detections are observed on the vertical component. This is not surprising given the angle of incidence of shallow P waves. The lack of shallow P wave energy on the vertical component is in agreement with the short period microseisms survey performed on multiple arrays by Koper et al. (2010). This raises the question,

if shallow P wave energy is truly present in the short period microseisms wavefield. Zhang et al. (2009) reported on strong shallow P wave energy with a velocity of ~ 5 km/s at the Parkfield array in California. Given the low velocity and strong signal on the vertical component, it is more likely that this energy belongs to the L_g phase, which is observed at PSAR with slightly slower velocities between $4.0 - 5.0$ km/s and is also in agreement with the multi array study of Koper et al. (2010).

The presence of S wave energy is a recent discovery (Liu et al., 2016) and was aided by the 3C beamforming implementation presented in this thesis (Gal et al., 2016). S waves are found to be generated in the northern Atlantic and northern Pacific, where SV wave generation locations coincide with the one of P waves and are in agreement with their current excitation model (Gualtieri et al., 2014), while SH waves are observed to originate from a close proximity of P and SV generation locations. The SH wave generation is less clear, but a scattering process of the P-SV wavefield via seamounts or sedimentary basins seems likely.

Chapter 7

Summary

In this thesis, beamforming techniques are evaluated and developed to create an optimal framework for the analysis of the microseism wavefield in the range of $0.5-20$ seconds with a particular emphasis on multiple source detection and accurate estimation of the slowness vector. Additionally, multiple deconvolution approaches are tested to improve the beamforming power spectrum even further and reduce bias of weak sources. These novel implementations are then applied to seismic arrays in Australia to characterise the properties of the microseism wavefield, which are predominantly controlled by the ocean wave response to atmospheric processes in the Southern Ocean.

The Capon beamformer is found to achieve the best resolution and robustness of all tested beamformers for the case of microseisms. The improved beamforming framework makes use of the Hann window function to reduce frequency leakage, which can induce inaccurate slowness estimates. Robustness is achieved by applying diagonal loading to stabilize the inversion of the cross spectral matrix. Combined with the incoherently averaged signal broadband extension, the optimal framework is achieved. The IAS Capon framework shows considerable improvement over the conventional fk approach, especially when multiple signals and accurate slowness estimation are of interest.

For the estimation of weak sources, which are commonly masked by the sidelobes of strong sources, a removal of the beam pattern was studied with the most prominent deconvolution candidates. Deconvolution enhanced beamforming shows best performance when combined with the CLEAN algorithm. Owing to its implementation into the beamforming process, i.e. modification of the cross spectral matrix and not a post processing procedure on an image, CLEAN is the only deconvolution algorithm which can be used with high resolution beamformers that do not have a static array response. This allows the combined use of the Capon beamformer with CLEAN for optimal performance. The resulting power spectrum decomposition removes all contributions form beam sidelobes, hence CLEAN decomposes the spectrum into its fundamental energy contributions.

The application of IAS Capon, to over two decades of microseism data recorded at WRA, reveals that multiple surface and body waves sources are simultaneously active. Surface wave energy is mainly present in form of Rayleigh waves and transitions towards L_g waves for increasing

frequency due to R_g-to-L_g scattering. Body waves are predominantly present as P waves and generated in the southern oceans along storm tracks in the southern hemisphere winter. In the southern hemisphere summer, P waves from the northern pacific close to Japan and the Kamchatka Peninsula are found, while PP energy is observed from the northern Atlantic. It is further found, that lower frequency (0.35 Hz) body waves are generated in deeper oceans while at higher frequencies their generation regions move to shallower areas. Comparison with a ocean hindcast, strengthens the array observations and correlations between wave height, windspeed and wind direction are found for multiple generation locations.

The full wavefield decomposition for a full calendar year by means of deconvolution enhanced beamforming combined with CLEAN, is the first study of its kind. Owing to the decomposition into the fundamental energy contributions, a frequency, directional and slowness dependent mean power representation of the microseism wavefield is obtained. Energy ratios between different types of surface waves show R_g waves to be dominant at 0.35 and 0.6 Hz while LQ waves show higher energy contribution at 1 Hz. The increase in the L_g energy also supports scattering from R_g waves to be their main generation mechanism. LQ waves are found to be generated in slightly different regions than R_g waves and there are indications for a R_g-to-LQ transition at sedimentary basin boundaries.

With the array beamforming techniques developed during the course of this thesis, novel information can be derived from the analysis of the microseism wavefield as has been demonstrated with the long duration study and the decomposition of the full wavefield. The IAS Capon approach is comparable in terms of computational time with the conventional fk analysis, and offers a resolution increase of the power spectrum. For seismic arrays, where the observed wavefield is in agreement with the signal model, CLEAN beamforming results in the most accurate estimation of the microseism wavefield. It is hoped that these new implementations, optimized for the analysis of ambient noise, will help the research community to obtain further insight from microseism wavefield observations.

Bibliography

Ardhuin, F., Balanche, A., Stutzmann, E., and Obrebski, M. (2012). From seismic noise to ocean wave parameters: General methods and validation. *Journal of Geophysical Research*, 117(C5):C05002.

Ardhuin, F., Gualtieri, L., and Stutzmann, E. (2015). How ocean waves rock the Earth: Two mechanisms explain microseisms with periods 3 to 300 s. *Geophysical Research Letters*, 42:765–772.

Ardhuin, F., Rogers, E., Babanin, A. V., Filipot, J.-F., Magne, R., Roland, A., van der Westhuysen, A., Queffeulou, P., Lefevre, J.-M., Aouf, L., and Collard, F. (2010). Semiempirical Dissipation Source Functions for Ocean Waves. Part I: Definition, Calibration, and Validation. *Journal of Physical Oceanography*, 40(9):1917–1941.

Ardhuin, F. and Roland, A. (2012). Coastal wave reflection, directional spread, and seismoacoustic noise sources. *Journal of Geophysical Research*, 117(May):C00J20.

Ardhuin, F., Stutzmann, E., Schimmel, M., and Mangeney, A. (2011). Ocean wave sources of seismic noise. *Journal of Geophysical Research*, 116(C9):C09004.

Aster, R. C., McNamara, D. E., and Bromirski, P. D. (2008). Multidecadal Climate-induced Variability in Microseisms. *Seismological Research Letters*, 79(2):194–202.

Aster, R. C., McNamara, D. E., and Bromirski, P. D. (2010). Global trends in extremal microseism intensity. *Geophysical Research Letters*, 37.

Astiz, L. and Creager, K. C. (1994). Geographic and seasonal variations of microseismic noise. *EOS, Transactions, American Geophysical Union*, 75(419):1–2.

Baggeroer, A., Kuperman, W., and Mikhalevsky, P. (1993). An overview of matched field methods in ocean acoustics. *IEEE Journal of Oceanic Engineering*, 18(4):401–424.

Baggeroer, A., Kuperman, W. A., and Schmidt, H. (1988). Matched field processing: Source localization in correlated noise as an optimum parameter estimation problem. *Journal of the Acoustic Society of America*, 83(May):571–587.

Barabell, A. (1983). Improving the resolution performance of eigenstructure-based direction-finding algorithms. *Acoustics, Speech, and Signal Processing, IEEE ...*, pages 336–339.

Bartlett, M. S. (1948). Smoothing periodograms from time-series with continuous spectra. *Nature*, 161:686–687.

Behr, Y., Townend, J., Bowen, M., Carter, L., Gorman, R., Brooks, L., and Bannister, S. (2013). Source directionality of ambient seismic noise inferred from three-component beamforming. *Journal of Geophysical Research*, 118:240–248.

Bensen, G. D., Ritzwoller, M. H., Barmin, M. P., Levshin, A. L., Lin, F., Moschetti, M. P., Shapiro, N. M., and Yang, Y. (2007). Processing seismic ambient noise data to obtain reliable broad-band surface wave dispersion measurements. *Geophysical Journal International*, 169(3):1239–1260.

Bensen, G. D., Ritzwoller, M. H., and Shapiro, N. M. (2008). Broadband ambient noise surface wave tomography across the United States. *Journal of Geophysical Research*, 113(B5):B05306.

Berger, J., Davis, P., and Ekström, G. (2004). Ambient Earth noise: a survey of the global seismographic network. *Journal of Geophysical Research*, 109(B11307).

Bernard, P. (1990). Historical sketch of microseisms from past to future. *Physics of the Earth and Planetary Interiors*, 63(3-4):145–150.

Bertero, M. and Boccacci, P. (2005). A simple method for the reduction of boundary effects in the Richardson-Lucy approach to image deconvolution. *Astronomy and Astrophysics*, 437(1):369–374.

Beucler, E., Mocquet, A., Schimmel, M., Chevrot, S., Quillard, O., Vergne, J., and Sylvander, M. (2015). Observation of deep water microseisms in the North Atlantic Ocean using tide modulations. *Geophysical Research Letters*, 42(2):316–322.

Bokelmann, G. (1995). Azimuth and slowness deviations from the GERESS regional array. *Bulletin of the Seismological Society of America*, 85(5):1456–1463.

Bondár, I., North, R., and Beall, G. (1999). Teleseismic slowness-azimuth station corrections for the International Monitoring System seismic network. *Bulletin of the Seismological Society of America*, 89(4):989–1003.

Booth, N., a.T. Abawi, Schey, P., and Hodgkiss, W. (2000). Detectability of low-level broad-band signals using adaptive matched-field processing with vertical aperture arrays. *IEEE Journal of Oceanic Engineering*, 25(3):296–313.

Boue, P., Poli, P., Campillo, M., Pedersen, H., Briand, X., and Roux, P. (2013). Teleseismic correlations of ambient seismic noise for deep global imaging of the Earth. *Geophysical Journal International*, 194(2):844–848.

Brenguier, F., Shapiro, N. M., Campillo, M., Ferrazzini, V., Duputel, Z., Coutant, O., and Nercessian, A. (2008). Towards forecasting volcanic eruptions using seismic noise. *Nature Geoscience*, 1(2):126–130.

Bromirski, P. and Duennebier, F. (2002). The near-coastal microseism spectrum: Spatial and temporal wave climate relationships. *Journal of Geophysical Research*, 107(B8):1–20.

Bromirski, P. D., Duennebier, F. K., and Stephen, R. a. (2005). Mid-ocean microseisms. *Geochemistry, Geophysics, Geosystems*, 6(4).

Bromirski, P. D., Flick, R. E., and Graham, N. (1999). Ocean wave height determined from inland seismometer data: Implications for investigating wave climate changes in the NE Pacific. *Journal of Geophysical Research*, 104(C9):20753.

Bromirski, P. D., Stephen, R. a., and Gerstoft, P. (2013). Are deep-ocean-generated surface-wave microseisms observed on land? *Journal of Geophysical Research: Solid Earth*, 118(7):3610–3629.

Brooks, L., Townend, J., Gerstoft, P., Bannister, S., and Carter, L. (2009). Fundamental and higher-mode Rayleigh wave characteristics of ambient seismic noise in New Zealand. *Geophysical Research Letters*, 36(23):L23303.

Brooks, T. F. and Humphreys, W. M. (2006a). A deconvolution approach for the mapping of acoustic sources (DAMAS) determined from phased microphone arrays. *Journal of Sound and Vibration*, 294(4):856–879.

Brooks, T. F. and Humphreys, W. M. (2006b). Extension of DAMAS Phased Array Processing for Spatial Coherence Determination (DAMAS-C). *12th AIAA/CEAS Aeroacoustics Conference*, Paper 2006:1–18.

Bucker, H. (1976). Use of calculated sound fields and matched-field detection to locate sound sources in shallow-water. *The Journal of the Acoustical Society of America*, 59(2):368–373.

Campillo, M. (2006). Phase and correlation in 'random' seismic fields and the reconstruction of the green function. *Pure and Applied Geophysics*, 163(2-3):475–502.

Campillo, M. and Paul, A. (2003). Long-range correlations in the diffuse seismic coda. *Science (New York, N.Y.)*, 299(5606):547–9.

Capon, J. (1969). High-resolution frequency-wavenumber spectrum analysis. *Proceedings of the IEEE*, 57(8):1408–1418.

Capon, J. (1973). Analysis of microseismic noise at LASA , NORSAR and ALPA. *Geophysical Journal of the Royal Astronomical Society*, 35:39–54.

Cessaro, R. K. (1994). Sources of primary and secondary microseisms. *Bulletin of the Seismological Society of America*, 84(1):142–148.

Cessaro, R. K. and Chan, W. W. (1989). Wide-angle triangulation array study of simultaneous primary microseism sources. *Journal of Geophysical Research*, 94:15555–15563.

Chevrot, S., Sylvander, M., Benahmed, S., Ponsolles, C., Lefèvre, J. M., and Paradis, D. (2007). Source locations of secondary microseisms in western Europe: Evidence for both coastal and pelagic sources. *Journal of Geophysical Research*, 112(B11).

Chiou, S.-J. and Bolt, B. (1993). Seismic wave slowness-vector estimation from broad-band array data. *Geophysical Journal International*, 114(2):234–248.

Davy, C., Stutzmann, E., Barruol, G., Fontaine, F., and Schimmel, M. (2015). Sources of secondary microseisms in the Indian Ocean. *Geophysical Journal International*, 202(2):1180–1189.

de Franco, R. and Musacchio, G. (2001). Polarization filter with singular value decomposition. *Geophysics*, 66(3):932.

Deacon, G. E. R. (1947). Relations between sea waves and microseisms. *Nature*, 160:419–421.

Dougherty, R. P. and Stoker, R. W. (1998). Sidelobe suppression for phased array aeroacoustic measurements. In *Proceedings of the 9th AIAA/CEAS Aeroacoustics Conference*, pages 235–245.

Du, L., Li, J., and Stoica, P. (2010). Fully automatic computation of diagonal loading levels for robust adaptive beamforming. *IEEE Transactions on Aerospace and Electronic Systems*, 46(1):449–458.

Durrant, T., Hemer, M., Trenham, C., and Greenslade, D. (2013a). CAWCR wave hindcast 1979-2010, v5. *CSIRO. Data Collection.*

Durrant, T., Hemer, M., Trenham, C., and Greenslade, D. (2013b). CAWCR wave hindcast extension Jan 2011-May 2013, v2. *CSIRO. Data Collection.*

Esmersoy, C., Cormier, V. F., and Toksöz, M. N. (1985). Three-Component Array Processing. *The VELA Program: A Twenty-five Year Review of Basic Research*, pages 565–578.

Essen, H.-H. (2003). On the generation of secondary microseisms observed in northern and central Europe. *Journal of Geophysical Research*, 108(B10).

Essen, H. H., Klussmann, J., Herber, R., and Grevemeyer, I. (1999). Does microseisms in Hamburg (Germany) reflect the wave climate in the North Atlantic? *Deutsche Hydrographische Zeitschrift*, 51(1):33–45.

Euler, G. G., Wiens, D., and Nyblade, A. A. (2014). Evidence for bathymetric control on the distribution of body wave microseism sources from temporary seismic arrays in Africa. *Geophysical Journal International*, 197(3):1869–1883.

Fäh, D., Stamm, G., and Havenith, H. B. (2008). Analysis of three-component ambient vibration array measurements. *Geophysical Journal International*, 172(1):199–213.

Featherstone, W., Strangeways, H. J., Zatman, M. A., and Mewes, H. (1997). A novel method to improve the performance of Capon's minimum variance estimator. *Antennas and Propagation, Tenth International Conference on (Conf. Publ. No. 436)*, 1:332–335.

Flinn, E. (1965). Signal analysis using rectilinearity and direction of particle motion. *Proceedings of the IEEE*, 53(12):1874–1876.

Friedrich, A., Klinge, K., and Krüger, F. (1998). Ocean-generated microseismic noise located with the Graefenberg array. *Journal of Seismology*, 2(1):47–64.

FROGTECH (2006). OZ SEEBASE Proterozoic Basins Study. *Report to Geoscience Australia by Frog Tech Pty Ltd., http://www.frogtech.com.au/australia.html*.

Gal, M., Reading, A. M., Ellingsen, S., Koper, K. D., Burlacu, R., and Gibbons, S. J. (2016). Deconvolution enhanced direction of arrival estimation using one- and three-component seismic arrays applied to ocean induced microseisms. *Geophysical Journal International*, 206(1):10.1093/gji/ggw150.

Gal, M., Reading, A. M., Ellingsen, S. P., Gualtieri, L., Koper, K. D., Burlacu, R., and Tkalčić, H. (2015). The frequency dependence and locations of short-period microseisms generated in the Southern Ocean and West Pacific. *Journal of Geophysical Research: Solid Earth*, 120(8):5764–5781.

Gal, M., Reading, A. M., Ellingsen, S. P., Koper, K. D., Gibbons, S. J., and Näsholm, S. P. (2014). Improved implementation of the fk and Capon methods for array analysis of seismic noise. *Geophysical Journal International*, 198(2):1045–1054.

Gerstoft, P., Sabra, K. G., Roux, P., Kuperman, W. A., and Fehler, M. C. (2006). Green's functions extraction and surface-wave tomography from microseisms in southern California. *Geophysics*, 71(4, S):SI23–SI31.

Gerstoft, P., Shearer, P. M., Harmon, N., and Zhang, J. (2008). Global P, PP, and PKP wave microseisms observed from distant storms. *Geophysical Research Letters*, 35(23):1–6.

Gibbons, S. J., Kværna, T., and Ringdal, F. (2010). Considerations in phase estimation and event location using small-aperture regional seismic arrays. *Pure and Applied Geophysics*, 167(4-5):381–399.

Gibbons, S. J., Schweitzer, J., Ringdal, F., Kværna, T., Mykkeltveit, S., and Paulsen, B. (2011). Improvements to seismic monitoring of the European Arctic using three-component array processing at SPITS. *Bulletin of the Seismological Society of America*, 101(6):2737–2754.

Goldstein, P. and Archuleta, R. (1991). Deterministic Frequency-Wavenumber Methods and Direct Measurements of Rupture Propagation During Earthquakes Using a Dense Array : Theory and Methods. *Journal of Geophysical Research*, 96(90):6173–6185.

Grevemeyer, I., Herber, R., and Essen, H. H. (2000). Microseismological evidence for a changing wave climate in the northeast Atlantic Ocean. *Nature*, 408(6810):349–352.

Grob, M., Maggi, a., and Stutzmann, E. (2011). Observations of the seasonality of the Antarctic microseismic signal, and its association to sea ice variability. *Geophysical Research Letters*, 38(11).

Gualtieri, L., Stutzmann, E., Capdeville, Y., Ardhuin, F., Schimmel, M., Mangeney, A., and Morelli, A. (2013). Modelling secondary microseismic noise by normal mode summation. *Geophysical Journal International*, 193(3):1732–1745.

Gualtieri, L., Stutzmann, E., Farra, V., Capdeville, Y., Schimmel, M., Ardhuin, F., and Morelli, A. (2014). Modelling the ocean site effect on seismic noise body waves. *Geophysical Journal International*, 197(2):1096–1106.

Gupta, I., Zhang, T., and Wagner, R. (1997). Low-Frequency Lg from NTS and Kazakh nuclear explosions– Observations and interpretation. *Bulletin of the Seismological Society of America*, 87(5):1115–1125.

Gutenberg, B. (1936). On microseisms. *Bulletin of the Seismological Society of America*, 26(2):111–117.

Hadziioannou, C., Gaebler, P., Schreiber, U., Wassermann, J., and Igel, H. (2012). Examining ambient noise using colocated measurements of rotational and translational motion. *Journal of Seismology*, 16:787–796.

Harmon, N., Forsyth, D., and Webb, S. (2007). Using ambient seismic noise to determine short-period phase velocities and shallow shear velocities in young oceanic lithosphere. *Bulletin of the Seismological Society of America*, 97(6):2009–2023.

Harmon, N., Rychert, C., and Gerstoft, P. (2010). Distribution of noise sources for seismic interferometry. *Geophysical Journal International*, 183(3):1470–1484.

Harris, D. B. (1990). Comparison of the direction estimation performance of high-frequency seismic arrays and three-component stations. *Bulletin of the Seismological Society of America*, 80(6B):1951–1968.

Hasselmann, K. (1963). A statistical analysis of the generation of microseisms. *Reviews of Geophysics*, 1(2):177–210.

Hatayama, K. and Fujiwara, H. (1998). Excitation of secondary Love and Rayleigh waves in a three-dimensional sedimentary basin evaluated by the direct boundary element method with normal modes. *Geophysical Journal International*, 133:260–278.

Haubrich, R., Munk, W., and Snodgrass, F. (1963). Comparative spectra of microseisms and swell. *Bulletin of the Seismological Society of America*, 53(1):27–37.

Haubrich, R. A. and McCamy, K. (1969). Microseisms: Coastal and pelagic sources. *Reviews of Geophysics*, 7(3):539–571.

He, Y., Xie, X.-B., and Lay, T. (2008). Explosion-Source Energy Partitioning and Lg-Wave Excitation: Contributions of Free-Surface Scattering. *Bulletin of the Seismological Society of America*, 98(2):778–792.

Hillers, G., Graham, N., Campillo, M., Kedar, S., Landès, M., and Shapiro, N. (2012). Global oceanic microseism sources as seen by seismic arrays and predicted by wave action models. *Geochemistry, Geophysics, Geosystems*, 13(1):doi:10.1029/2011GC003875.

Högbom, J. (1974). Aperture synthesis with a non-regular distribution of interferometer baselines. *Astronomy and Astrophysics Supplement Series*, 15:417–426.

Huestis, S., Molnar, P., and Oliver, J. (1973). Regional Sn velocities and shear velocity in the upper mantle. *Bulletin of the Seismological Society of America*, 63(2):469–475.

Jacobeit, E., Thomas, C., and Vernon, F. (2013). Influence of station topography and Moho depth on the mislocation vectors for the Kyrgyz Broadband Seismic Network (KNET). *Geophysical Journal International*, 193(2):949–959.

Jurkevics, A. (1988). Polarization analysis of three-component array data. *Bulletin of the Seismological Society of America*, 78(5):1725–1743.

Kedar, S., Longuet-Higgins, M., Webb, F., Graham, N., Clayton, R., and Jones, C. (2008). The origin of deep ocean microseisms in the North Atlantic Ocean. *Proceedings of the Royal Society A: Mathematical, Physical and Engineering Sciences*, 464(2091):777–793.

Kelly, E. J. (1967). Response of seismic signals to wide-band signals. *Lincoln Lab. Tech. Note*, 30.

Kennett, B. (2005). Seismological tables: ak135. *Research School of Earth Sciences, The Australian National University, Australia*.

Kennett, B. L. N., Stipčević, J., and Gorbatov, A. (2015). Spiral-arm seismic arrays. *Bulletin of the Seismological Society of America*, 105(4):2109–2116.

Kimman, W. P., Campman, X., and Trampert, J. (2012). Characteristics of seismic noise: Fundamental and higher mode energy observed in the northeast of the Netherlands. *Bulletin of the Seismological Society of America*, 102(4):1388–1399.

Kinoshita, S., Fujiwara, H., Mikoshiba, T., and Hoshino, T. (1992). Secondary Love Waves Observed by a Strong-Motion Array in the Tokyo Lowlands, Japan. *Journal of Physics of the Earth*, 40(1):99–116.

Köhler, A., Weidle, C., and Maupin, V. (2011). Directionality analysis and Rayleigh wave tomography of ambient seismic noise in southern Norway. *Geophysical Journal International*, 184(1):287–300.

Koper, K. D. and Burlacu, R. (2015). The fine structure of double-frequency microseisms recorded by seismometers in North America. *Journal of Geophysical Research: Solid Earth*, 120(3):1677–1691.

Koper, K. D. and de Foy, B. (2008). Seasonal anisotropy in short-period seismic noise recorded in South Asia. *Bulletin of the Seismological Society of America*, 98(6):3033–3045.

Koper, K. D., de Foy, B., and Benz, H. (2009). Composition and variation of noise recorded at the Yellowknife Seismic Array, 1991-2007. *Journal of Geophysical Research*, 114(B10):1–13.

Koper, K. D. and Hawley, V. L. (2010). Frequency dependent polarization analysis of ambient seismic noise recorded at a broadband seismometer in the central United States. *Earthquake Science*, 23:439–447.

Koper, K. D., Seats, K., and Benz, H. (2010). On the composition of Earth's short-period seismic noise field. *Bulletin of the Seismological Society of America*, 100(2):606–617.

Krim, H. and Viberg, M. (1996). Two decades of array signal processing research. *IEEE Signal Process. Mag*, 13(4):67–94.

Kværna, T. and Doornbos, D. (1986). An integrated approach to slowness analysis with array and

three-component stations. *NORSAR Semiannual Technical Summary*, 2(85/86):60–69.

Kværna, T. and Ringdal, F. (1986). Stability of various f-k estimation techniques. *Norsar Scientific Report*, 1(86/87):29–40.

Lacoss, R., Kelly, E., and Toksöz, M. (1969). Estimation of seismic noise structure using arrays. *Geophysics*, 34(1):21–38.

Landès, M., Hubans, F., Shapiro, N. M., Paul, A., and Campillo, M. (2010). Origin of deep ocean microseisms by using teleseismic body waves. *Journal of Geophysical Research*, 115(B5):1–14.

Li, H., Bernardi, F., and Michelini, A. (2010). Surface wave dispersion measurements from ambient seismic noise analysis in Italy. *Geophysical Journal International*, 180(3):1242–1252.

Lin, F.-C., Moschetti, M. P., and Ritzwoller, M. H. (2008). Surface wave tomography of the western United States from ambient seismic noise: Rayleigh and Love wave phase velocity maps. *Geophysical Journal International*, 173(1):281–298.

Liu, Q., Koper, K. D., Burlacu, R., Ni, S., Wang, F., Zou, C., Wei, Y., Gal, M., and Reading, A. M. (2016). Source locations of teleseismic P, SV, and SH waves observed in microseisms recorded by a large aperture seismic array in China. *Earth and Planetary Science Letters*, 449:39–47.

Longuet-Higgins, M. (1950). A theory of the origin of microseisms. *Philosophical Transactions of the Royal Society of London. Series A. Mathematical and Physical Sciences*, 243(857):1–35.

Lucy, L. B. (1974). An iterative technique for the rectification of observed distributions. *The Astronomical Journal*, 79(6):745.

Manchee, E. B. and Weichert, D. H. (1968). Epicentral uncertainties and detection probabilities for the Yellowknife Seismic Array data. *Bulletin of the Seismological Society of America*, 58:1359–1377.

Matsuzawa, T., Obara, K., Maeda, T., Asano, Y., and Saito, T. (2012). Love- and Rayleigh-Wave Microseisms Excited by Migrating Ocean Swells in the North Atlantic Detected in Japan and Germany. *Bulletin of the Seismological Society of America*, 102(4):1864–1871.

Menon, R., Gerstoft, P., and Hodgkiss, W. S. (2014). On the apparent attenuation in the spatial coherence estimated from seismic arrays. *Journal of Geophysical Research: Solid Earth*, 119:3115–3132.

Miche, A. (1944). Mouvements ondulatoire de la mer en profondeur croissante ou décroissante. Première partie. Mouvements ondulatoires périodiques et cylindriques en profondeur constante. *Annales des Ponts et Chaussés*, 114:42–78.

Miron, S., Le Bihan, N., and Mars, J. I. (2005). Vector-Sensor MUSIC for Polarized Seismic Sources Localization. *EURASIP Journal on Advances in Signal Processing*, 2005(1):74–84.

Miron, S., Le Bihan, N., and Mars, J. I. (2006). Quaternion-MUSIC for vector-sensor array processing. *IEEE Transactions on Signal Processing*, 54(4):1218–1229.

Mitchell, B. J. (1995). Anelastic structure and evolution of the continental crust and upper mantle from seismic surface wave attenuation. *Rev. Geophys.*, 33(95):441–462.

Myers, S., Walter, W., Mayeda, K., and Glenn, L. (1999). Observations in support of Rg scattering as a source for explosion S waves: Regional and local recordings of the 1997 Kazakhstan depth of burial experiment. *Bulletin of the Seismological Society of America*, 89(2):544–549.

Ng, M. K., Chan, R. H., and Tang, W. (1999). A fast algorithm for deblurring models with Neumann boundary conditions. *SIAM Journal on Scientific Computing*, 21(3):851–866.

Nishida, K., Kawakatsu, H., Fukao, Y., and Obara, K. (2008a). Background Love and Rayleigh waves simultaneously generated at the Pacific Ocean floors. *Geophysical Research Letters*, 35(16):L16307.

Nishida, K., Kawakatsu, H., and Obara, K. (2008b). Three-dimensional crustal S wave velocity structure in Japan using microseismic data recorded by Hi-net tiltmeters. *Journal of Geophysical Research*, 113(10):1–22.

Obrebski, M., Ardhuin, F., Stutzmann, E., and Schimmel, M. (2013). Detection of microseismic compressional (P) body waves aided by numerical modeling of oceanic noise sources. *Journal of Geophysical Research: Solid Earth*, 118(8):4312–4324.

Obrebski, M. J., Ardhuin, F., Stutzmann, E., and Schimmel, M. (2012). How moderate sea states can generate loud seismic noise in the deep ocean. *Geophysical Research Letters*, 39(11).

Park, J., Lindberg, C., and Vernon, F. (1987). Multitaper spectral-analysis of high-frequency seismograms. *Journal of Geophysical Research*, 92(B12):12675–12684.

Patton, H. and Taylor, S. (1995). Analysis of Lg spectral ratios from NTS explosions: Implications for the source mechanisms of spall and the generation of Lg waves. *Bulletin of the Seismological Society of America*, 85(1):220–236.

Paulraj, A., Roy, R., and Kailath, T. (1985). Estimation of signal parameters via rotational invariance techniques 1- ESPRIT. In *Nineteeth Asilomar Conference on Circuits, Systems and Computers*, pages 83–89.

Picozzi, M., Parolai, S., and Bindi, D. (2010). Deblurring of frequency-wavenumber images from small-scale seismic arrays. *Geophysical Journal International*, 181(1):357–368.

Poggi, V. and Fäh, D. (2010). Estimating Rayleigh wave particle motion from three-component array analysis of ambient vibrations. *Geophysical Journal International*, 180:251–267.

Prieto, G. A., Parker, R. L., Thomson, D. J., Vernon, F. L., and Graham, R. L. (2007). Reducing the bias of multitaper spectrum estimates. *Geophysical Journal International*, 171(3):1269–1281.

Reading, A. M., Koper, K. D., Gal, M., Graham, L. S., Tkalčić, H., and Hemer, M. A. (2014). Dominant seismic noise sources in the Southern Ocean and West Pacific, 2000âĂŞ2012, recorded at the Warramunga Seismic Array, Australia. *Geophysical Research Letters*, 41(10):3455–3463.

Riahi, N., Bokelmann, G., Sala, P., and Saenger, E. H. (2013). Time-lapse analysis of ambient surface wave anisotropy: A three-component array study above an underground gas storage. *Journal of Geophysical Research: Solid Earth*, 118(10):5339–5351.

Richardson, W. (1972). Bayesian-based iterative method of image restoration. *Journal of the Optical Society of America*, 62(1):55–59.

Rost, S. and Thomas, C. (2002). Array seismology: Methods and applications. *Reviews of Geophysics*, 40(3):doi:10.1029/2000RG000100.

Rost, S. and Thomas, C. (2009). Improving seismic resolution through array processing techniques. *Surveys in Geophysics*, 30(4-5):271–299.

Sabra, K. G., Gerstoft, P., Roux, P., Kuperman, W. A., and Fehler, M. C. (2005). Surface wave tomography from microseisms in Southern California. *Geophysical Research Letters*, 32(14):1–4.

Saito, T. (2010). Love-wave excitation due to the interaction between a propagating ocean wave

and the sea-bottom topography. *Geophysical Journal International*, 182(3):1515–1523.

Samson, J. C. (1983). Pure states, polarized waves, and principal components in the spectra of multiple, geophysical time-series. *Geophysical Journal International*, 72(3):647–664.

Schimmel, M. and Gallart, J. (2003). The use of instantaneous polarization attributes for seismic signal detection and image enhancement. *Geophysical Journal International*, 155(2):653–668.

Schimmel, M. and Gallart, J. (2004). Degree of polarization filter for frequency-dependent signal enhancement through noise suppression. *Bulletin of the Seismological Society of America*, 94(3):1016–1035.

Schimmel, M., Stutzmann, E., Ardhuin, F., and Gallart, J. (2011). Polarized Earth's ambient microseismic noise. *Geochemistry, Geophysics, Geosystems*, 12(7):1–14.

Schisselé, E., Guilbert, J., Gaffet, S., and Cansi, Y. (2004). Accurate time-frequency-wavenumber analysis to study coda waves. *Geophysical Journal International*, 158(2):577–591.

Schmidt, R. (1986). Multiple emitter location and signal parameter estimation. *Antennas and Propagation, IEEE Transactions on*, AP-34(3):276–280.

Schulte-Pelkum, V., Earle, P. S., and Vernon, F. L. (2004). Strong directivity of ocean-generated seismic noise. *Geochemistry, Geophysics, Geosystems*, 5(3):1–13.

Schweitzer, J. (2001). Slowness corrections – One way to improve IDC products. *Pure and Applied Geophysics*, 158:375–396.

Schweitzer, J., Fyen, J., Mykkeltveit, S., and Kværna, T. (2002). Chapter 9: Seismic Arrays. In Bormann, P., editor, *IASPEI New Manual of Seismological Observatory Practice*. GeoForschungsZentrum, Potsdam. 52 pp.

Seligson, C. D. (1970). Comments on "High-resolution frequency-wavenumber spectrum analysis. *Proceedings of the IEEE*, 58:947–949.

Sergeant, A., Stutzmann, E., Maggi, A., Schimmel, M., Ardhuin, F., and Obrebski, M. (2013). Frequency-dependent noise sources in the North Atlantic Ocean. *Geochemistry, Geophysics, Geosystems*, 14(12):5341–5353.

Shapiro, N. M. and Campillo, M. (2004). Emergence of broadband Rayleigh waves from correlations of the ambient seismic noise. *Geophysical Research Letters*, 31(7):L07614.

Shapiro, N. M., Campillo, M., Stehly, L., and Ritzwoller, M. H. (2005). High-resolution surface-wave tomography from ambient seismic noise. *Science (New York, N.Y.)*, 307(5715):1615–1618.

Shepp, L. a. and Vardi, Y. (1982). Maximum likelihood reconstruction for emission tomography. *IEEE transactions on medical imaging*, 1(2):113–122.

Shumway, R. H., Smart, E., and Clauter, D. A. (2008). Mixed signal processing for regional and teleseismic arrays. *Bulletin Of The Seismological Society Of America*, 98(1):36–51.

Sijtsma, P. (2007). CLEAN based on spatial source coherence. *International journal of aeroacoustics*, pages 21–23.

Snieder, R. and Hagerty, M. (2004). Monitoring change in volcanic interiors using coda wave interferometry: Application to Arenal Volcano, Costa Rica. *Geophysical Research Letters*, 31(9).

Soares, C. and Jesus, S. M. (2003). Broadband matched-field processing: Coherent and incoherent approaches. *The Journal of the Acoustical Society of America*, 113(5):2587.

Stehly, L., Campillo, M., and Shapiro, N. M. (2006). A study of the seismic noise from its long-range correlation properties. *Journal of Geophysical Research*, 111(B10):1–12.

Stephens, C. and Isacks, B. L. (1977). Toward an understanding of Sn: Normal modes of Love waves in an oceanic structure. *Bulletin of the Seismological Society of America*, 67(1):69–78.

Stutzmann, E., Ardhuin, F., Schimmel, M., Mangeney, a., and Patau, G. (2012). Modelling long-term seismic noise in various environments. *Geophysical Journal International*, 191(2):707–722.

Stutzmann, E., Roult, G., and Astiz, L. (2000). GEOSCOPE Station Noise Levels. *Bulletin of the Seismological Society of America*, 90(3):690–701.

Stutzmann, E., Schimmel, M., Patau, G., and Maggi, A. (2009). Global climate imprint on seismic noise. *Geochemistry, Geophysics, Geosystems*, 10(11):doi:10.1029/2009GC002619.

Tanimoto, T., Hadziioannou, C., Igel, H., Wasserman, J., Schreiber, U., and Gebauer, A. (2015). Estimate of Rayleigh-to-Love wave ratio in the secondary microseism by colocated ring laser and seismograph. *Geophysical Research Letters*, 42(8):2650–2655.

Tanimoto, T., Hadziioannou, C., Igel, H., Wassermann, J., Schreiber, U., Gebauer, A., and Chow, B. (2016). Seasonal variations in the Rayleigh-to-Love wave ratio in the secondary microseism from colocated ring laser and seismograph. *Journal of Geophysical Research: Solid Earth*, 121(4):2447–2459.

Tanimoto, T., Ishimaru, S., and Alvizuri, C. (2006). Seasonality in particle motion of microseisms. *Geophysical Journal International*, 166(1):253–266.

Thomson, D. (1982). Spectrum estimation and harmonic analysis. *Proceedings of the IEEE*, 70(9):1055–1096.

Tkalčić, H., Rawlinson, N., Arroucau, P., Kumar, A., and Kennett, B. L. N. (2012). Multistep modelling of receiver-based seismic and ambient noise data from WOMBAT array: crustal structure beneath southeast Australia. *Geophysical Journal International*, 189(3):1680–1700.

Toksöz, M. and Lacoss, R. (1968). Microseisms: Mode structure and sources. *Science*, 159(December):872–873.

Tolman, H. (2009). User manual and system documentation of WAVEWATCH-III version 3.14. *NOAA/NWS/NCEP/MMAB Tech. Rep.*, 276:220 pp.

Traer, J., Gerstoft, P., Bromirski, P. D., and Shearer, P. M. (2012). Microseisms and hum from ocean surface gravity waves. *Journal of Geophysical Research*, 117(B11307).

Vernon, F., Fletcher, J., Carroll, L., Chave, A., and Sembera, E. (1991). Coherence of seismic body waves from local events as measured by a small-aperture array. *Journal of Geophysical Research*, 96(B7):11,981–11,996.

Vidale, J. E. (1986). Complex polarization analysis of particle motion. *Bulletin of the Seismological Society of America*, 76(5):1393–1405.

Wagner, G. (1996). Resolving diversly polarized, superimposed signals in three-component seismic array data. *Geophysical research letters*, 23(14):1837–1840.

Wagner, G. (1997). Regional wave propagation in southern California and Nevada : Observations from a three-component seismic array. *Journal of Geophysical Research*, 102(B4):8285–8311.

Wagner, G. and Owens, T. (1996). Signal detection using multi-channel seismic data. *Bulletin of the Seismological Society of America*, 86(1A):221–231.

Wang, H. and Kaveh, M. (1985). Coherent signal-subspace processing for the detection and estimation of angles of arrival of multiple wideband sources. *Acoustics, Speech and Signal Processing, IEEE Transactions on*, 33(4):823–831.

Wang, Y., Li, J., Stoica, P., Sheplak, M., and Nishida, T. (2004). Wideband RELAX and wideband CLEAN for aeroacoustic imaging. *The Journal of the Acoustical Society of America*, 115(2):757–767.

Wax, M. and Kailath, T. (1984). Determining the number of signals by information theoretic criteria. *ICASSP '84. IEEE International Conference on Acoustics, Speech, and Signal Processing*, 9:1–4.

Wax, M., Shan, T.-J., and Kailath, T. (1984). Spatio-temporal spectral analysis by eigenstructure methods. *Acoustics, Speech and Signal Processing, IEEE Transactions on*, 32(4):817–827.

Westwood, E. (1992). Broadband matched-field source localization. *The Journal of the Acoustical Society of America*, 91(5):2777–2789.

Wiechert, E. (1904). Verhandlungen der zweiten internationalen Seismologischen Konferenz. *Gerlands Beitraege zur Geophysik*, Ergaenzungsband. II: 41-43 (in German).

Woods, J. and Lintz, P. (1973). Plane waves at small arrays. *Geophysics*, 38(6):1023–1041.

Yang, Y. and Ritzwoller, M. H. (2008). Characteristics of ambient seismic noise as a source for surface wave tomography. *Geochemistry Geophysics Geosystems*, 9(2).

Yardibi, T., Li, J., Stoica, P., and Cattafesta, L. N. (2008). Sparsity constrained deconvolution approaches for acoustic source mapping. *The Journal of the Acoustical Society of America*, 123(5):2631–2642.

Yoon, Y. S., Kaplan, L. M., and McClellan, J. H. (2006). TOPS: New DOA estimator for wideband signals. *IEEE Transactions on Signal Processing*, 54(6):1977–1989.

Young, M. K., Rawlinson, N., Arroucau, P., Reading, A. M., and Tkalčić, H. (2011). High-frequency ambient noise tomography of southeast Australia: New constraints on Tasmania's tectonic past. *Geophysical Research Letters*, 38(13):doi:10.1029/2011GL047971.

Zhang, J., Gerstoft, P., and Bromirski, P. D. (2010). Pelagic and coastal sources of P -wave microseisms: Generation under tropical cyclones. *Geophysical Research Letters*, 37(15).

Zhang, J., Gerstoft, P., and Shearer, P. M. (2009). High-frequency P-wave seismic noise driven by ocean winds. *Geophysical Research Letters*, 36(9):1–5.

Zhang, T. and Lay, T. (1995). Why the Lg phase does not traverse oceanic crust. *Bulletin of the Seismological Society of America*, 85(6):1665–1678.